Repair welding of carbon steel pipe that has experienced partial graphitization during elevated temperature service

By

Kristian Johan Kruger

Submitted in partial fulfilment of the requirements for the degree
Master of Engineering (Metallurgical Engineering)

In the

Department of Materials Science and Metallurgical Engineering

Faculty of Engineering, Built Environment and Information Technology

UNIVERSITY OF PRETORIA

September 2016

Supervisor: Prof. PGH Pistorius

Abstract

Plain C-Mn steels such as SA-516 Grade 65 are used as steam lines to transport high temperature steam under pressure. Plain carbon steels that are in service at elevated temperatures (typically 400-450°C) for prolonged periods of time (typically in excess of 20 years) may experience an undesirable microstructural change in the form of secondary graphitization. Secondary graphitization of carbon steels is classically defined as the decomposition of cementite into carbon (present as the graphite phase) and iron (ferrite). Many cases have been documented where the decomposition reaction occurs more readily in a region closely associated to welds. The resultant graphite is often referred to as Heat Affected Zone (HAZ) graphite.

This study aimed to evaluate whether or not it would be possible to weld on graphitized material and if so, to recommend viable repair procedures. In addition to this, it was critical to study the effects of HAZ graphite on the mechanical properties of plain C-Mn steels after in-service exposure of approximately 35 years at 420°C. Additional work was also performed that supplemented the tests necessary to qualify a procedure qualification record (PQR) in the form of several prolonged heat treatments and detailed metallography. This was done in an effort to understand the process of graphitization and the subsequent effects that its formation in the HAZ would have on the mechanical properties of not only a single sample, but also on welded joints with varying degrees of graphitization.

It was concluded that the HAZ graphite had no effect on the tensile strength, impact toughness, hardness or ductility as characterised by the total elongation. Several tensile tests failed through the graphite plane associated with the HAZ. The samples that failed through the graphitized HAZ displayed a tensile strength, yield strength and total elongation similar to material that failed in the base material (away from the graphitized HAZ). However, failure in the graphitized HAZ resulted in a decrease in reduction in area from 72% to 44%. In spite of the change in reduction in area, the total elongation of samples that exhibited failure in the graphitized heat affected zone was acceptable.

It was concluded that it is possible to perform repair welding on graphitized material using conventional welding procedures. Based on a procedure that used GTAW to perform the root run, followed by SMAW to fill and cap the joint, two PQRs were produced for graphitized plain carbon steel welding. A number of repair techniques were considered, of which the most viable that was recommended was to wrap the graphitized joints that are at highest risk of failing with a reinforcing metal band and to fillet weld the band in place.

It was concluded that the presence of HAZ graphite was unlikely to affect the capacity of the steam line to resist plastic collapse. Future work on the influence of the presence of heat affected zone graphite on other failure mechanisms (such as thermal fatigue, mechanical fatigue and creep) is recommended.

Contents

List of Figures

List of Tables

Chapter 1 – Literature Review

Carbon manganese steel grades are often used for the construction of pipes for transporting superheated steam, and several of these grades are classified as pressure vessel steels (1). The elevated temperatures associated with superheated steam increases the rate of carbide decomposition which becomes more pronounced at lengthy service. The inherent tendency for cementite to transform to its most thermodynamically stable form (α-iron and graphite) is accelerated by exposing the material to elevated temperatures for prolonged periods of time (Samuels, 1999). The decomposition reaction of iron carbides are commonly referred to as graphitization.

Large diameter steam pipelines often have an extended service life, and it is common for such lines to be in service in excess of 30 or 40 years. It is sometimes necessary to cut into the pipeline and weld in new pipe inlets and outlets. Additionally, it may become necessary to remove old, damaged sections of the pipeline and replace these sections entirely. The implication of such repair work is that some of the base material may have experienced partial graphitization and such graphite could potentially complicate the welding of new inserts. In many cases the length of an affected pipe often makes it impractical to replace it in its entirety in a short period of time and therefore it may be necessary to extend the life of the pipeline while steady replacement of affected material is conducted. However if the material would rapidly approach its end of life, current welding procedures will not qualify for this material to be welded as stipulated in ASME IX (2) (pg. 96). This section of ASME states that a base material may not be indiscriminately substituted for a base metal that was used to qualify a procedure without consideration of the compatibility of the material in terms or metallurgical properties, post weld heat treatment, design mechanical properties and service requirements. Therefore, the effect of graphitization on the integrity of the material, as well its effects on the welding procedure, needs to be considered.

It is therefore critical to evaluate the feasibility of repair welding aging, graphitized pipelines. Should welding be deemed a viable method of repair, procedure qualification records must be developed to allow for welding of these graphitized materials. Additionally, the effect of all welding related operations must be clearly understood to avoid unforeseen failures.

1.1. Materials of construction

The steel grade that was used to construct the pipeline was SA-672 Grade C65 (3). In this ASTM specification, there are three areas that must be considered: the SA-code, the grade, and the class. In this case, the SA-code dictated that the pipe be constructed from a plate material that was fusion welded using an electric-fusion-welding process with filler metal. The grade refers to a specific plate material grade that must be used. The class defines the required heat treatment, non destructive testing (NDT) in the form of radiography, and pressure testing. No record of the class could be obtained for the material that was used in the current study.

Pipe conforming to SA-672 Grade C65 is manufactured from plate conforming to SA-516 Grade 65. This material is a plain carbon, killed, fine grained steel (4) that is most often used for moderate and lower temperature service (5). This grade was used in petro-chemical plants that were constructed in the mid 1900s for transporting gases and liquids at elevated temperatures and pressures and possesses enhanced impact properties when compared to a similar grades (SA-515 Grade 65). The chemical composition of SA-515 grade 65 and SA-516 grade 65 can be seen in Table 1.

Table 1: Chemical composition of steel grades SA-515 Grade 65 and SA-516 Grade 65. [1] Single values refer to maximum limits

Steel Grade	%C	%Mn	%P	%S	%Si
SA-515 Grade 65	0.33[1]	0.90	0.035	0.04	0.15-0.40
SA-516 Grade 65	0.29	0.85-1.20	0.035	0.04	0.15-0.40

Carbon steels display a tendency to graphitize when they were placed in service at elevated temperature and pressure for prolonged periods of time (6). Due to the widespread use of these grades in the service conditions mentioned above (elevated temperature and pressure) it became relevant to consider appropriate repair welding procedures that may be used on graphitized material.

SA-516 Grade 65 is a material that is currently in operation in several petrochemical plants and the slightly higher carbon content and coarser grain structure variant of this material, SA-515 Grade 65, has historically been used to transport superheated steam in petro-chemical plants. The mechanical properties of the above two steels can be found in Table 2 (5), note that neither material specifies properties as part of the standard requirements. While there are no substantial differences in chemistry between SA-515 and SA-516, ASME II-A describes SA-515 as material used in "moderate to high temperature applications" while SA-516 is described as material used in "moderate to low temperature applications".

Table 2: Material properties of the two steel grades relevant to this study

	SA-516 Grade 65	SA-515 Grade 65
Yield strength (MPa)	240	240
Tensile strength (MPa)	450-585	450-585
Minimum elongation (50mm wall thickness)	23%	23%

18

1.2. Graphitization

There are two mechanisms of graphite formation in ferrous, carbon containing alloys: primary graphitization and secondary graphitization.

Primary graphitization refers to the formation of graphite from a liquid material and it is most commonly witnessed in the solidification of cast iron such as grey and nodular cast iron.

Secondary graphitization refers to the formation of graphite in the solid phase. Secondary graphitization in medium and low carbon steel typically occurs during exposure to elevated temperatures for prolonged periods of time. Secondary graphitization is defined as the decomposition of iron carbide to graphite. This reaction may have deleterious effects on the mechanical properties of the steel and therefore an effort must be made to understand the mechanism by which secondary graphitization occurs. By understanding this mechanism, it would be possible to better understand and estimate the remnant life of components that have experienced some degree of secondary graphitization (6).

The strength and comparatively low cost of carbon steels made them an attractive material for use in elevated temperature and pressure pipeline applications. The critical drawback to this material, graphitization, was only realised once many plants and facilities had already constructed pipelines from this material. For any medium to large facility, replacement of such a large pipeline system would have proven to be economically unviable and thus the focus was shifted from replacement to management of the pipeline.

1.2.1. Thermodynamic Driving and Retarding Forces for Graphitization

The most pronounced driving force for graphitization is the chemical driving force in which the system attempts to reduce to more stable phases. This chemical driving force is the most likely candidate for the dissolution of iron carbides.

Graphite, in combination with ferrite, is a by-product of the decomposition of iron carbides such as cementite. Thermodynamic principles state that in order for a reaction to occur, the sum of the driving forces (forces that reduce the energy of a system) must be larger than the retarding forces (forces that increase the energy of a system). The major retarding force that must be considered is the strain energy due to the difference in volume between iron carbide, and ferrite and graphite. This volume difference is substantial enough to have made many researchers believe that the retarding forces that the reaction experiences are large enough to entirely suppress the reaction. While this assumption has since been proven erroneous, it does indicate that the graphitization process is very slow due to the large retarding forces (7). The change in volume (published as 205%) applies a large retarding force on the nucleation and growth of graphite from cementite in the form of strain energy ($\Delta G\varepsilon$) (8). The strain energy that is introduced into the system due to the misfit of the new phases that form is always positive and this in turn increases the internal energy in the system. Because all systems seek to reduce their energy, it was thought that the amount of energy introduced into the system as strain energy due to the increase in volume associated with the transformation of Fe_3C to ferrite and graphite

(positive retarding force) out-weighed the driving forces, which indicates that it is highly unlikely for this reaction to occur.

The following calculation was performed in order to determine the theoretical volume change as a result of cementite transforming to ferrite and graphite, as well as to theoretically verify the results obtained from literature.

Iron (α-Fe) has a published density of 7.87g/cm³ (9).

Cementite has a unit cell with lattice parameters:

A = 0.45165 nm, 0.50837 nm, 0.67297 nm.

A cementite unit cell contains 12 iron atoms and 4 carbon atoms (10). Based on this data, it is possible to calculate a theoretical density for cementite of 7.7186g/cm³.

Graphite has a theoretical density of 2.26g/cm³ (11).

Consider 1 mole of Fe₃C.

$$Mass = 3 \times 55.85_{Molar\ mass\ of\ Fe} + 1 \times 12.011_{Molar\ mass\ of\ C}$$

$$Mass = 179.561\ g$$

$$\rho_{Fe_3C} = \frac{Mass_{Fe_3C}}{Volume_{Fe_3C}}$$

$$\frac{Mass_{\ 1\ mol\ Fe_3C}}{\rho_{Fe_3C}} = Volume_{\ 1\ mol\ Fe_3C}$$

$$V_{Fe_3C} = \frac{179.561}{7.7186} \left(cm^3 \big/ mol\ of\ Fe_3C \right)$$

$$V_{Fe_3C} = 23.2634 \left(cm^3 \big/ mol\ of\ Fe_3C \right)$$

This calculation was repeated for ferrite and graphite and Table 3 was constructed from the results.

Table 3: Theoretically calculated densities, masses, and volumes for cementite, ferrite and graphite.

Variable	Reactant	Product 1	Product 2
Species	1 Fe₃C	3 Fe (Ferrite)	1 C (Graphite)
Density	7.7186 g/cm³	7.87 g/cm³	2.26 g/cm³
Mass as number of moles	179.561 g/mol	167.55 g/3 moles	12.011 g/mol
Volume per mole of reactant	23.3 cm³/ mol Fe₃C	21.3 cm³/3 moles of ferrite	5.3 cm³/mol of graphite

$$\Delta\,Volume = \sum(Volume_{products}) - \sum(Volume_{reactants})$$
$$\Delta\,Volume = (21.3 + 5.3) - 23.3$$
$$\Delta\,Volume = 3.3\left(cm^3/mol\ of\ Fe_3C\ transformed\right)$$
$$\%\Delta\,Volume = \frac{3.3}{23.3}\times100 = 14.2\%$$

Thus the net change in volume when cementite transforms to ferrite and graphite is an increase of 3.3 cm^3 per mol of Fe$_3$C transformed. This translates to a 14.2% increase in volume if pure cementite transforms to ferrite and graphite. Using the Fe-C binary phase diagram (9), it is possible to calculate that for a steel containing a maximum of 0.3% carbon (which is the case in the present study), the maximum cementite content is 4.2%. It is also possible to predict the maximum amount of pearlite that will be present the microstructure. The maximum pearlite content for a 0.3% carbon steel is 37.7%. This means that assuming all the carbon is present in the steel in the form of cementite, 11.1% of the pearlite will consist of cementite.

The implications of this are that if all the cementite in the steel transformed to ferrite and graphite, the net bulk volume increase would be 14.2 X 4.2% = 0.6%. If only the pearlite is considered, there would be a net volume increase in the pearlite phase of 1.6%.

However, the theoretical density of graphite is typically much higher than measured values in cast irons. This can most likely be attributed to the fact that graphite in cast irons is one of the solidification products (primary graphitization) and is therefore not dimensionally restricted as would be the case in a solid state transformation that occurs during secondary graphitization. In order to establish the effect of porous – or low density – graphite, a calculation can be made where 30% porosity is assumed in the graphite phase. Table 4 was constructed from the same calculations as Table 3, taking into consideration that the density of graphite was reduced to 70% of the theoretically calculated values.

Table 4: Theoretically calculated densities, masses, and volumes for cementite, ferrite and graphite assuming 30% porosity in the graphite phase.

Variable	Reactant	Product 1	Product 2
Species	1 Fe$_3$C	3 Fe (Ferrite)	1 C (Graphite)
Density	7.7186 (g/cm^3)	7.87 (g/cm^3)	1.58 (g/cm^3)
Mass as number of moles	179.561 (g/mol)	167.55 (g/3 moles)	12.011 (g/mol)
Volume per mole of reactant	23.3 (cm^3/ mol Fe$_3$C)	21.3 (cm^3/3 moles of ferrite)	7.6 (cm^3/mol of graphite)

$$\Delta\,Volume = \sum(Volume_{products}) - \sum(Volume_{reactants})$$
$$\Delta\,Volume = (21.3 + 7.6) - 23.3$$
$$\Delta\,Volume = 5.6\left(cm^3/mol\ of\ Fe_3C\ transformed\right)$$
$$\%\Delta\,Volume = \frac{5.6}{23.3}\times100 = 24.0\%$$

The implications of this are that if all the cementite in the steel transformed to ferrite and graphite, the net bulk volume increase would be 24.0 X 4.2% = 1.0%. If only the pearlite is considered, there would be a net volume increase in the pearlite phase of 2.7%.

The results of these calculations are interpreted to indicate that the net volume change of cementite transforming to ferrite and graphite is much smaller than originally expected, and suggests that the retarding forces are not as large as what was initially expected.

Irrespective of the magnitude of the volume change associated with the formation of graphite, the fact that its formation is associated with an increase in volume implies that compressive stresses will develop in the matrix surrounding the graphite particles. Furthermore, the formation of graphite is likely to be sensitive to the stress conditions.

1.2.2. Mechanisms of graphitization

Graphitization is a complicated process that is not fully understood. This is further complicated by the very slow kinetics that is associated with the reaction. This makes studying the reaction difficult and slow. Graphitization has classically been perceived as the decomposition of cementite into a combination of graphite and ferrite. While this argument was generally accepted, several adaptations of the standard model were analysed within this section, which include:

Decomposition theories

1. The decomposition of Fe_3C to form $C_{(Graphite)} + \alpha_{(Fe)}$. This is known as homogeneous base metal graphitization (12).

2. Preferential decomposition of higher order, metastable carbon containing phases that originate from rapid heterogeneous thermal cycles. These higher order carbon containing phases then decompose to form the final decomposition products $C_{(Graphite)} + \alpha_{(Fe)}$. This is known as heterogeneous weld HAZ graphitization (13).

Nucleation theories

1. The nucleation of graphite onto impurity particles such as inclusions (14).

2. The nucleation of graphite by forming an amorphous core that grows and forms an ordered structure as the particle increases in size (15).

The theories presented here are not the only theories that have been hypothesised and there are many minor variations to every graphitization mechanism.

1.2.2.1. *Carbide decomposition theories*

There have been two documented locations that graphite is commonly witnessed in carbon steels: randomly distributed (homogeneously) through base material (6); and heterogeneously distributed along a weld (12). The formation of graphite is closely linked to the decomposition of carbides, and thus two decomposition theories are proposed to explain homogeneous and heterogeneous nucleation.

Homogeneous nucleation is defined as the nucleation of graphite through the bulk of the material and occurs at random in the material. When homogeneous nucleation occurs, it is generally accepted that this is as a result of the iron carbide Fe_3C decomposing (16). In contrast to this, heterogeneous nucleation is often observed in the heat affected zone. This indicates that due to the process of welding, this region becomes a favourable nucleation, and most likely decomposition site of iron carbides.

When carbon steel is rapidly heated and cooled such as in a weld cycle, there is a particular region in the heat affected zone (HAZ) that will become heated to just above the Ac_1 temperature. This will result in a transformation of the pearlitic structure to austenite. However because of the rapid heating and subsequent cooling cycle, the carbon content in the austenite does not have enough time to homogenise which results in an 'austeno-martensite' structure, which is reported to contain Chi-phase (χ-phase, Fe_5C_2), upon cooling. Upon reheating the material, higher carbon containing carbides such as Chi-phase (17) and other metastable phases decompose to cementite and the free carbon atoms report to graphite (13). The concept that the material microstructure prior to subcritical temperature exposure has a substantial effect on the rate of graphitization has been stated as early as 1945 (18). Figure 1 shows the effect that the microstructure has on the tendency of steel to graphitize, and indicates that spheroidization and graphitization are competing mechanisms.

An alternative theory suggests that the nucleation positions for HAZ graphite forms during the weld thermal cycle. The particulates form from isolated carbides or from cementite in pearlite at positions corresponding to a peak temperature below the Ac_1 (19).

Normalized structure   Reheated structure (Spheroidized structure)

Quenched structure (Martensite)   Reheated structure (Graphitized structure)
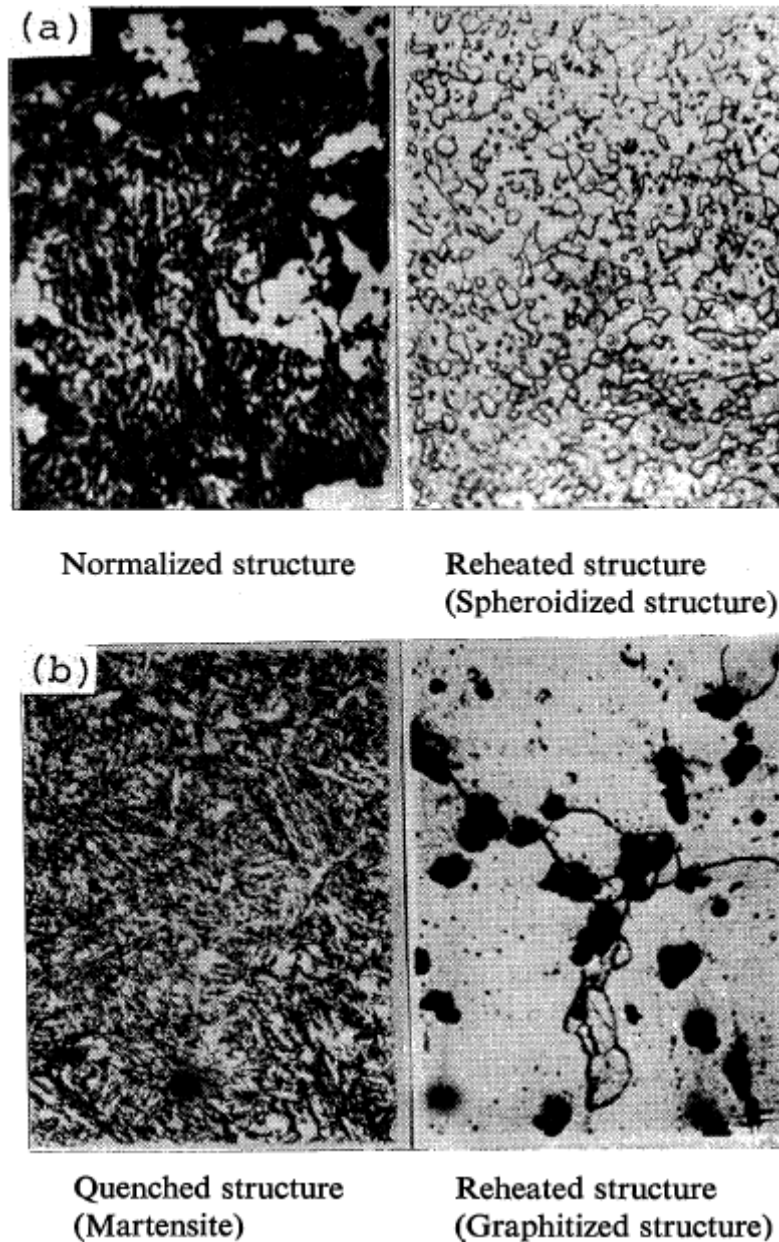
Figure 1: Effects of the microstructure prior to prolonged heat treatment on the tendency of a carbon steel (0.7%C, 0.2%Si, 0.33%Mn, 0.015%P, 0.018%S) to graphitize (a) Normalized and Reheated (b) Quenched and Reheated. Samples were either normalised or quenched from 1100°C after 10 min of soaking time at the austinitizing temperature (13).

1.2.2.2. Graphite nucleation and growth theories

There are two distinct types of graphite nucleation mechanisms which give rise to two distinct morphologies of graphite (15).

The first and more commonly accepted mechanism is that of a nucleation site in the form of an inclusion such as an aluminium oxide or nitride. This mechanism of nucleation results in large graphite particles with irregular morphology. This irregular morphology could be explained by the shape of the nucleation particle which gives rise to several graphite crystals that grow simultaneously and non-uniformly on the same particle in different directions as can be seen in the Figure 2. When observed

24

using a light microscope, it is expected that the resultant graphite nodule that nucleated on oxide or nitride particles will have an irregular shape such as the nodule which can be seen in Figure 3.
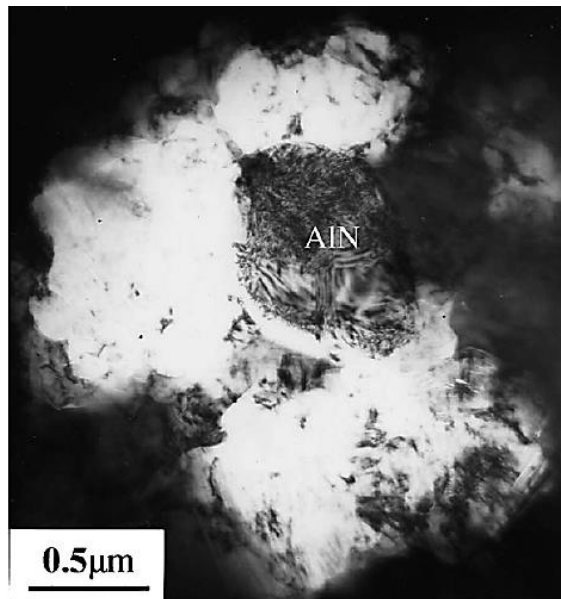
Figure 2: TEM bright field image of a graphite nodule with irregular morphology formed around an aluminium nitride particle after a 0.5h anneal at 680°C (He, 2007).
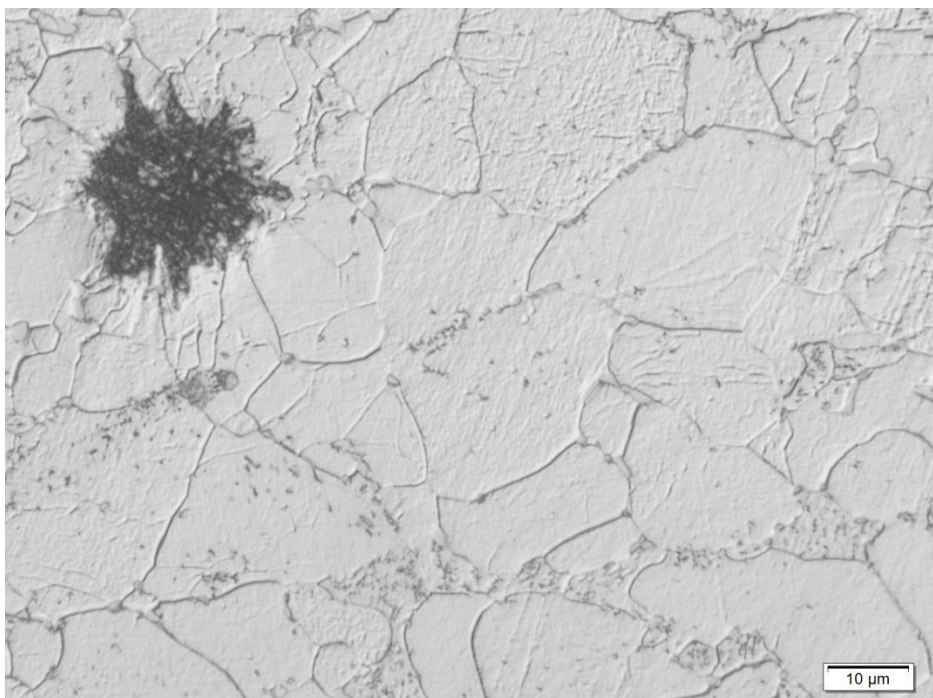
Figure 3: Irregularly shaped graphite nodule obtained after 200h heat treatment at 620°C of material identified as W 23 DS that has been in service at temperatures ranging from 425-435°C for 35 years.

Several instances of graphite particles have also been documented on ferrite-ferrite grain boundaries (14). There are several theories that attempt to explain the grain boundary graphite.

Dennis performed several long heat treatments on steel in either atmospheric conditions or in a pure nitrogen atmosphere, ranging from 500-1750 hours at 600°C. He found that with samples that were tested under atmospheric conditions, the material experienced greater graphitization at a position that was 3 mm away from the edge of the plate. He proposed that this was due to the difference in solubility of aluminium in austenite and ferrite (see Figure 4). Austenite has a much lower solubility for aluminium than ferrite. Therefore, if a carbon steel containing aluminium in solution is heated to above the Ac_1 temperature, local high concentrations of aluminium that exceed the solubility limit of austenite will segregate to the grain boundaries. If the steel is quenched fairly rapidly (by a normalizing process), the aluminium will remain heterogeneously distributed along the grain boundaries. However, if the steel is cooled slowly, as the bulk of the material transforms to ferrite, the aluminium will distribute through the grains more evenly. The aluminium is expected to finally oxidize and produce nucleation sites for graphite formation. The location of the aluminium upon oxidation will determine the shape and position of the graphite that forms (grain boundary graphite or graphite nodules within the grains) (20).
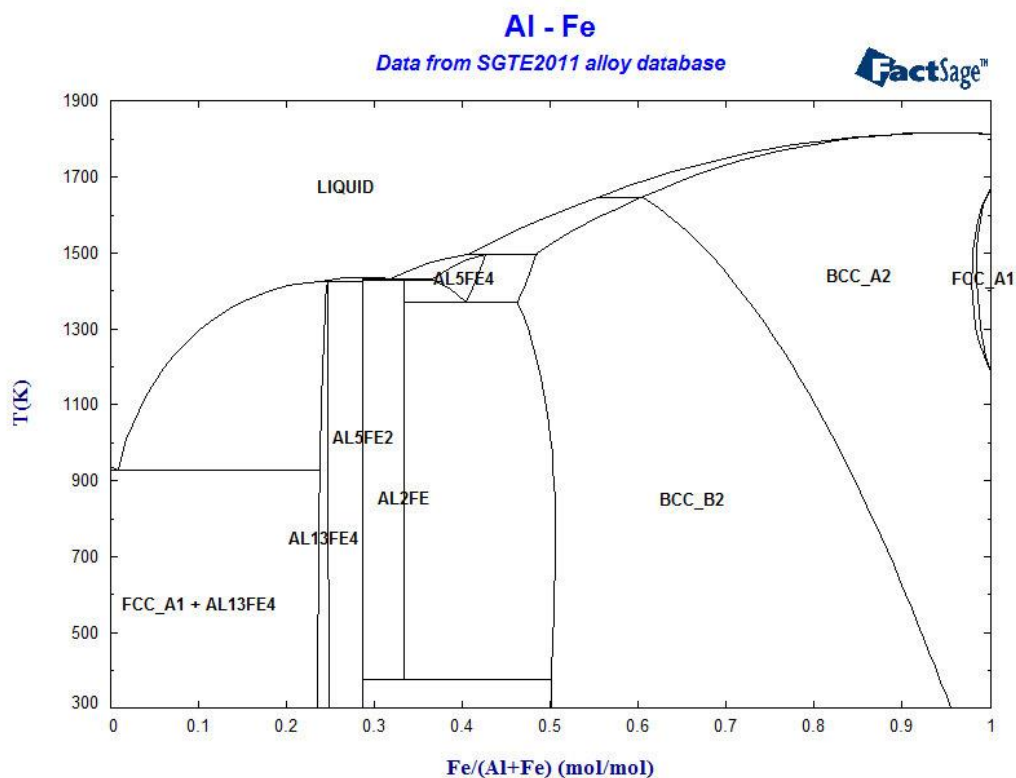
Figure 4: Al-Fe binary phase diagram produced using FactSage

Another interpretation of the grain boundary nucleation mechanism was proposed by Foulds. A basic requirement for the nucleation and growth of graphite is that there must be mechanisms whereby the material will accommodate the volume change resulting from the graphitization reaction. The volume change is then successfully accommodated by large quantities of defects such as vacancies and dislocations. These are commonly associated with grain boundaries, inclusions and strain induced defect clusters (12).

It has been demonstrated experimentally by several authors that an increase in aluminium in the steel (which is usually introduced in the deoxidizing process during steel making) leads to an increase in

graphite nucleation (20). While aluminium in solution is thought to have a benign effect of graphite nucleation, aluminium in the form of aluminium oxides could be one of the nucleation sites of graphite (20). According to Dennis, the graphite nucleates on alumina particles and this explains the 'incubation period' before the graphitization process accelerates. Dennis argued that the aluminium in solution must first react with oxygen that diffuses from the atmosphere into the steel to form alumina before graphite nucleation can begin. However, Foulds argued that while aluminium might have an effect on the initial nucleation rate of graphite, a study on the long term (in excess of 30 years) effects concluded that added aluminium and silicon has no significant effect on the overall graphite content of steels. Foulds concluded that chemistry has little to no effect on the activation energy of secondary graphitization of carbon steels (12). In a more recent paper, Foulds indicates that the presence of silicon and aluminium in typical C and C-Mo steels does not increase the total volume of graphite in the steel after prolonged periods of time in service. The presence of these elements only provide additional nucleation sites for the initial nucleation stage of the graphitization process (17).

The second nucleation mechanism has been observed by other researchers and occurs at the ferrite-cementite interface (14). This particle contains a Mn rich cementite side and a carbon rich, amorphous region which later grows to form the crystalline structure of graphite (15). As the particle grows, it becomes crystalline in structure and its bulk structure assumes the shape of a sphere. The growth pattern of this particle could be described by the cone-helix model of Double and Hellawell as can be seen in Figure 5.

Figure 6 shows the results of a 21 image montage where a spherical particle is analysed using Electron Energy Loss Spectroscopy (EELS) and energy filtered TEM (EFTEM) (known as the plasmon ratio method). The grey scale of the image is calibrated in such a way that low intensity (near-amorphous) material appears darker while high intensity (near-graphitic) material appears lighter. The low intensity core is indicative of near-amorphous material. The use of this method also suppresses any intensity variation arising from diffraction contrast.
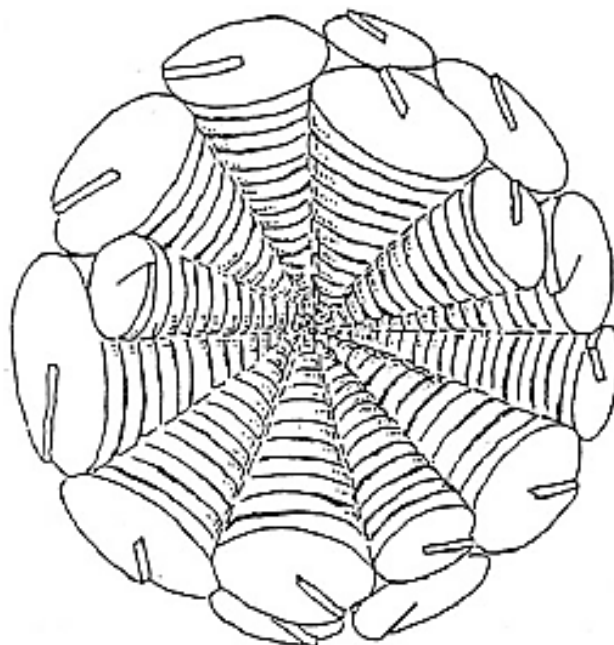
Figure 5: Cone-Helix model proposed by Double and Hellawell (15)
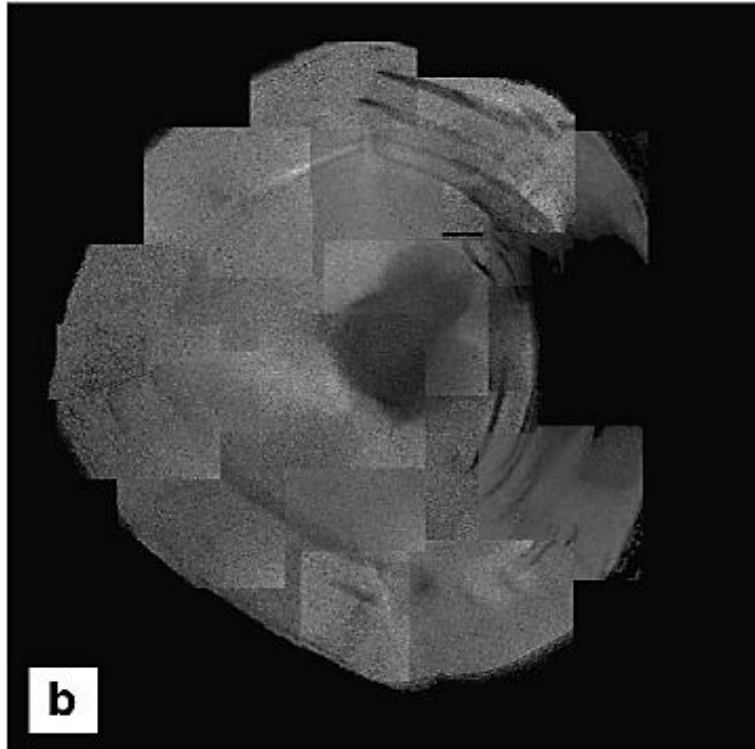
Figure 6: Plasmon ratio maps of a graphite spheroid (15)

Additionally, He mentions that some phases are more susceptible to graphite formation that others. His findings state that bainite is most resistant to graphitization while martensite is most susceptible to graphite formation (15).

Another case of heterogeneous nucleation of graphite in the intercritical zone was documented in the United State where a technical report documents the formation of graphite in the partially transformed zone of the HAZ of a welded joint (21). This indicates that graphite could form through the thickness of the welded joint at the temperature where material has experienced a very specific peak temperature (correlating with temperatures only several degrees above the Ac_1 temperature of the specific steel) and rapidly quenching. The findings of graphite forming in the partially transformed region of the HAZ are supported by Foulds (12).

This nucleation theory is further supported by Okada in a report where a study was performed on the formation of graphite in the heat affected zones on low carbon steel welded structures (13).

The effect of cold work on the tendency for a material to undergo graphitization must also be considered. In a study performed by Harry, it was discovered that in low carbon silicon steels, graphitization would be accelerated by performing small amounts of cold work to a material prior to prolonged heat treatments at 600°C (22). While the finding were reported qualitatively, it can be concluded that as the silicon content in the steel increases, so does the rate of graphitization. Additionally, the rate of graphitization was at a maximum when the amount of cold work was reported to be 10%.

Table 5 is a summary of the authors, steel chemistries used, heat treatment employed and graphite mechanism reported by each author. In early literature, it was widely accepted that the presence of aluminium, silicon and carbon increase the rate at which graphite forms in steel.

Table 5: List of authors, which steel chemistries were used, as well as the heat treatment that was used. The morphology and position of the graphite that was reported has been recorded.

Author	Steel Chemistry				Heat treatment	Graphite position and morphology
	%C	%Mn	%Al	%Si		
R. Charles 1939 (23)	1.0	0.35	0.01	-	72h anneal ranging from 760-880°C	Homogeneous, irregular shaped graphite
W.E. Dennis 1952 (20)	0.2	0.55	0.15	0.23	Austenitized at 1250°C for 15min, annealed at 600°C for up to 1500h	Higher concentration of graphite close to the surface of the material, irregular shaped graphite
E.D. Harry 1954 (22)	0.06-0.09	0.10-0.30	0-0.01	1.8-3.4	Cold worked, then heat treated at 600°C for between 3 and 110h	Graphite position and morphology not stated
F. Brown 1954 (14)	Not specified				Up to 110h anneal ranging from 600-760°C	Homogeneous, irregular shaped graphite
H. Thielsch 1954 (21)	Not specified (It may be assumed that due to the fact that this is a technical report, the grade is most likely a carbon manganese steel)				Not specified (It may be assumed that due to the fact that this is a technical report, heat treatment involved a PWHT followed by years of service at temperature which is most likely to fall within the range of 400-450°C)	Heterogeneous in the macrostructure, associated with material that heated to just above the Ac_1 temperature during welding. Graphite was both spherical and irregular in shape.
M. Okada 1982 (13)	0.7	0.33	Not specified	0.20	Samples dipped in 1000-1100°C lead bath for 5-7 sec, annealed at 670°C for 200-300h	Heterogeneous in the macrostructure, associated with material that displayed a martensitic microstructure prior to heat treatment below the Ac_1 temperature. Graphite was spherical in shape.
L.E. Samuals 1999 (6)	1	0.34	Al Treated	0.23	Austenitized at 1000°C for 1h, annealed at 650°C for 1-350h	Homogeneous, irregular shaped graphite
K. He 2007 (15)	0.38	0.07	1.44	1.82	Homogenized at 1150°C for 70h, annealed at 680°C for15min-91 hours	Homogeneously distributed through samples, both irregular and spherical graphite was witnessed.

Many authors that have produced graphite in hypo-eutectoid steel achieved this by using a large amount of silicon and aluminium. While these experiments resulted in forming graphite, the chemistry of the steels used in laboratory experiments are generally not representative of the steel grades used in industry. The heat treatment of most samples fell within the temperature range of 600 to 700°C. According to Foulds the graphitization to spheroidization transition temperature is 552°C, and as the temperature rises, spheroidization becomes more favoured at the expense of the graphitization process. The choice of 552°C was not explained in the paper that was available during this study. Foulds admitted that the graphitization to spheroidization transformation temperature could vary significantly and unpredictably (12). It should be noted that any attempt to replicate the graphitization process in a lab using conventional steel grades has been largely unsuccessful and inconsistent at best (24) with the exception of Wells. In a study by Wells on the graphitization of high purity C-Fe alloys, there was very little indication that any difficulty was encountered while trying to produce graphite in even low carbon (as low as 0.13%) steels (16). This leads to the conclusion that the alloying elements such as Mn and Mo must stabilize the Fe_3C phase significantly.

Figure 7 shows an example of the kinetics of the graphitization and spheroidization time-temperature graph.
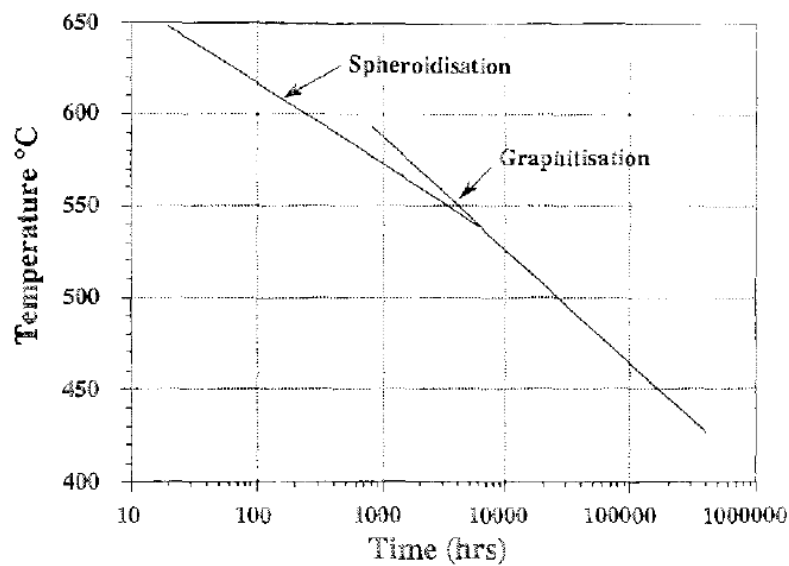
Figure 7: Comparison of the kinetics of spheroidization and graphitization. Time taken for half of the carbon in a 0.15% C steel to spheroidized, and for half of the carbon to transform to nodular graphite in an aluminium deoxidized 0.5% Mo steel (25).

It can be seen that graphitization is favoured at lower temperatures whereas spheroidization is favoured at higher temperatures. Additionally, at higher temperatures, the rate at which graphitization occurs is much lower than spheroidization. In the case of the steel used in Figure 7, graphitization is favoured at temperatures ranging from approximately 430°C to 540°C. At the peak temperature where graphitization takes place, the time for half of the material to undergo graphitization is still in excess of 3000 hours. Temperatures above 540°C favour the spheroidization process.

The volume increase associated with the formation of graphite from cementite will be favoured by tensile residual stresses. Such tensile residual stresses are present in a welded joint as a result of the thermal contraction of metallic materials during cooling (26). At high service temperatures, all residual stresses, including the tensile residual stresses will be reduced by creep. The reduction in residual tensile stresses at high service temperatures will favour spheroidization rather than graphitization, consistent with Figure 7.

Interpretation of published work on graphitization

Based on the sources discussed in the literature, it is possible to draw the following conclusions.

- It is possible to form graphite in hypo-eutectoid carbon steel at elevated operating temperatures (see Table 5).

- The graphite is formed from a decomposition reaction of carbon containing phases such as cementite and other carbon containing phases which are less stable than cementite (13). This reaction is drastically accelerated by increasing the temperature of the material but keeping the material below the Ac_1 temperature in order to prevent carbon from going into solution in austenite.

- During welding there appears to be preferential graphitization of the HAZ in a very narrow band corresponding to a relatively precise temperature range (typically 720 - 775°C) along the extremity of the HAZ (21) known as the partially transformed region. This temperature range is generally associated to Ac_1 and Ac_3 temperatures for C-Mn steels respectively, however this was never explicitly mentioned by Thielsch. This temperature range is associated with a partial transformation as the peak temperature exceeds the Ac_1 temperature of the steel by several degrees during welding, and subsequently cools down to below the Ac_1 temperature. The result of this unique thermal cycle is the transformation from $Fe_3C+\alpha \rightarrow \alpha + \gamma \rightarrow Fe_3C+\alpha$. However due to the rapid transformation from pearlite to austenite and back to pearlite, there is not enough time for the carbon that is present in the carbide to distribute evenly through the prior pearlitic microstructure before the austenite $\rightarrow$ pearlite transformation occurs during cooling. This ultimately would result in metastable phases other than Fe_3C to form that more readily dissociate and form iron and free carbon in the form of α iron and graphite (13). This clearly indicates that the phase transformation that occurs in the partially transformed region of the HAZ plays an important role in producing free carbon that is then readily available for the graphitization reaction.

- It has been demonstrated that there is no significant long term effect of aluminium and silicon with the overall graphite content in carbon and C-Mn steels. However, it is possible to chemically inhibit the graphitization reaction by adding alloying elements that will form stable carbides. A popular addition to steels that operate under elevated temperature conditions is chromium. By adding 0.5% chromium to the steel, any carbon that is present as free carbon forms chromium carbides instead of graphite (12).

1.2.3. Effects of graphitization on the mechanical properties of steel

There have been several documented cases of failures directly attributed to the graphitization of hypoeutectic steels. The first reported failure occurred in the Springdale Generation Station in the United States of America in 1943 where a high temperature steam pipe failed due to graphitization. Other noted cases of equipment failures due to graphitization include Oak Ridge Gaseous Diffusion Plant in 1957, as well as the Williamsburg Station failure in 1977 (12). Over the course of 30-40 years following the first major incident (Springdale) several papers were published regarding graphitization, however the findings were often "confusing and contradicting" (20). Additionally, factors that govern the graphitization reaction were often poorly defined (6).

Graphite was the reported cause of several failures of high temperature pressurised pipelines and was considered to have a negative effect on the mechanical properties of hypo-eutectic steels by negatively affecting the tensile strength, ductility and creep resistance (27). The severity of the loss of strength associated with graphite was strongly linked to the geometry and concentration of the graphite. Graphite that manifested through randomly distributed nodules (Figure 8) in the steel had a much less severe impact on the above mentioned mechanical properties (17). If the nodules were orientated on a preferred plane, or in a specific direction (Figure 9 & Figure 10), then the effects on the mechanical properties should be severe (28), although no quantitative effect on tensile properties, impact toughness or hardness were reported (29). Due to the differences in orientation of graphite in microstructures, attempts to obtain numerical data with regards to the loss in strength and impact toughness were largely unsuccessful. The tensile strength of graphite is anisotropic and if the samples are tested in a favourable direction, tensile strengths can be as high as 70 MPa, and as low as 6 MPa if tested in unfavourable directions (30).

As a result, cracks tend to propagate and grow extremely easily in graphite and this allows cracks to reach a critical size with minimal stress required if the graphite is orientated in a critical direction.
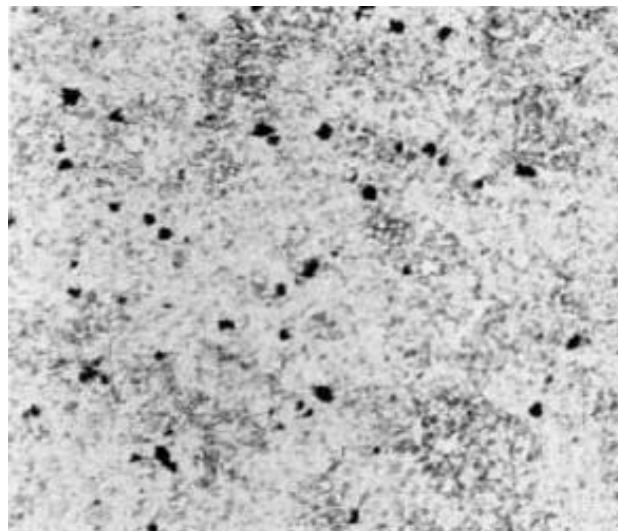
Figure 8: Randomly distributed graphite in a 1C-0.23Si-0.34Mn steel that has been austenitized at 1000°C, quenched and heat treated in air at 650°C for 100 hours (Samuels, 1999)
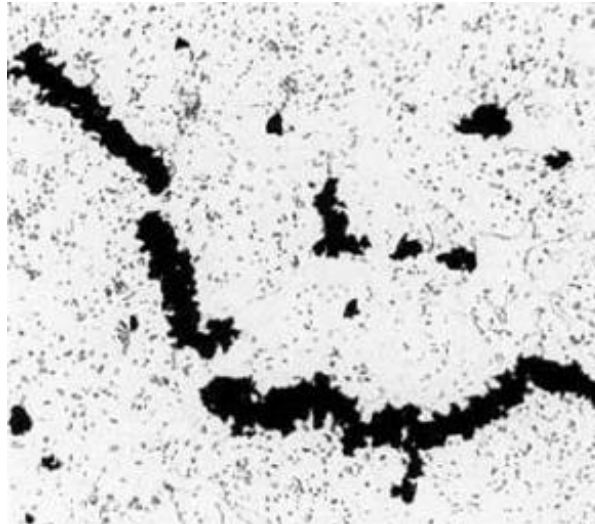
Figure 9: Chain of graphite in a 1C-0.23Si-0.34Mn steel that has been austenitized at 1000°C, quenched and heat treated in a vacuum at 650°C for 235 hours (Samuels, 1999)
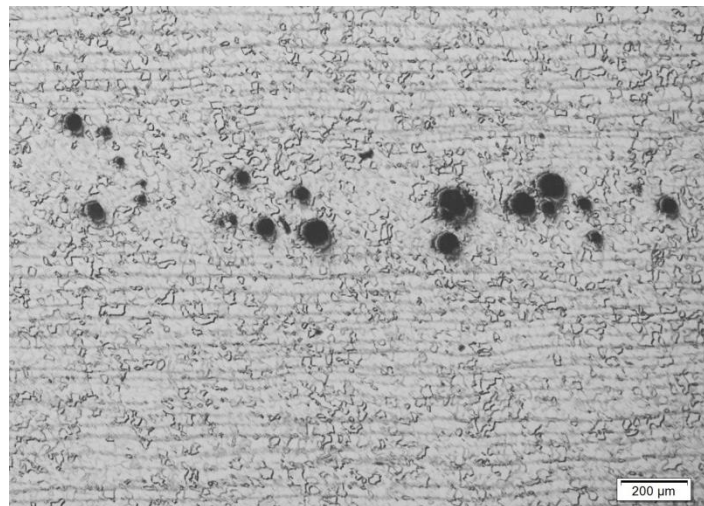
Figure 10: Nodules orientated in preferred plane from a 0.2% carbon steel that has been in service for 35 years at a temperature between 425-435°C. Sample was from the current study and can be identified as W23 DS after 500 hours of additional heat treatment at 625°C.

One of the most commonly used methods to characterise the degree of graphitization is by means of performing a bend test (27). The results on the degree of graphitization are then qualitatively measured according to Table 6. The results are often largely skewed and inconsistent with the true degree of graphitization due to the fact that no standardised test methods have been developed to test the effects of graphitization in the HAZ (31).

Table 6: Degree of graphitization of the HAZ as a function of the bend angle (27)

Bend Angle	Qualitative degree of graphitization
>90º	Mild
45-90º	Moderate
30-45º	Heavy
15-30º	Severe
<15º	Extremely Severe

The test method is largely left to the researcher and this inevitably results in variations in test procedures. One common example in the variation of testing procedure is the orientation of the test piece when placed in the bend test jig. Figure 11 shows the difference in orientation of the sample, this simple variation in orientation could drastically affect the results of a bend test (31).
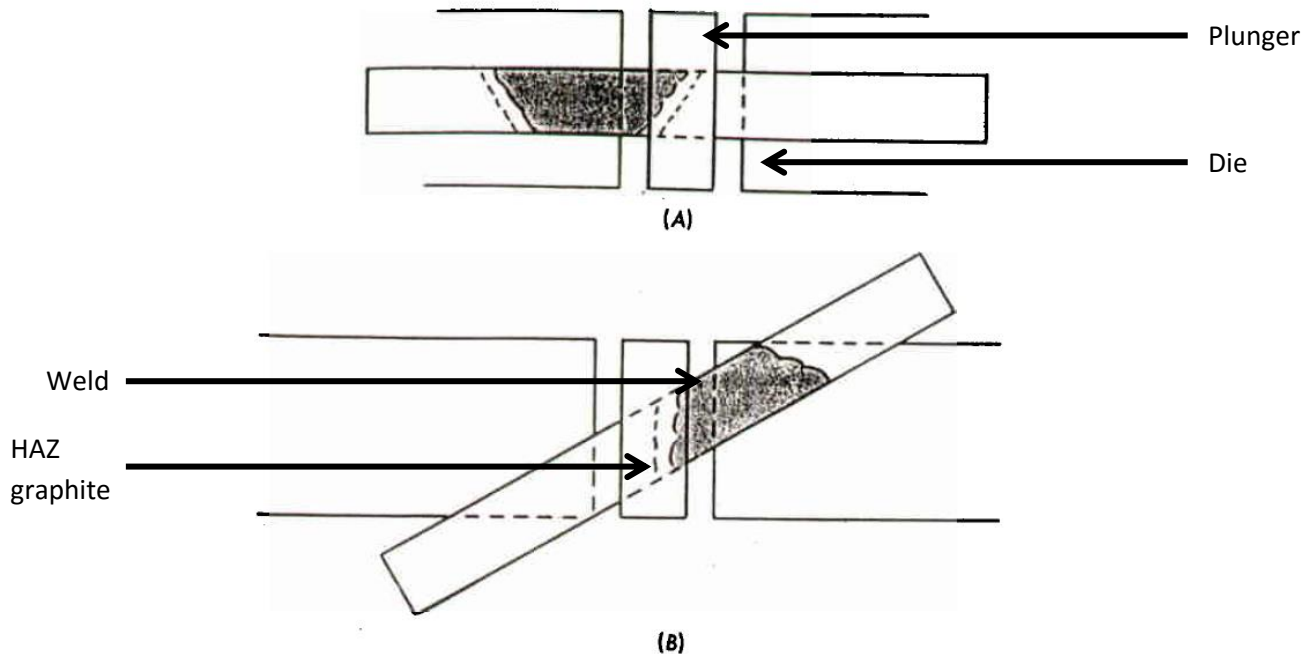
Figure 11: Test method variation with regards to the orientation of the bend test plunger with regards to the graphitized region of the HAZ during a side bend test (31).

Other variations to the recording of the results of the bend test include:

1. Recording the angle at which the sample starts to crack vs. recording the angle at which the sample cracks across its entire length.
2. Recording the bend angle vs. recording the elongation.
3. Aligning the graphitized region with the plunger of the bend test vs. aligning the short axis with the plunger (See Figure 11).

Interpretation

It was concluded from the above literature that the bend tests did not conform to a standard test method and therefore, results could be variable. This makes analysing the severity of graphite difficult and thus, the quantity and orientation of the graphite and the resultant deleterious effects of graphite are generally poorly understood. These two factors drastically increase the degree of uncertainty in terms of understanding the effects of graphite position (and orientation) and graphite quantity.

1.2.4. Estimating the position of HAZ graphite formation using the Rosenthal equation

It is likely that the graphite forms preferentially from metastable phases. Furthermore, these metastable phases are produced in all carbon steel welded joints due to the inevitability that at some position away from the heat source, there will be a point where the peak temperature that the material is exposed to will result in the rapid partial transformation from cementite and ferrite to carbon rich austenite and ferrite. Once this reaction occurs just above the Ac_1 temperature, the material will subsequently cool down to below the Ac_1 temperature and transform again to form a metastable, carbon rich phase as indicated in Figure 12. Therefore it would be possible to estimate at which position graphite is likely to form in the HAZ by using the Rosenthal heat flow equation to determine at what distance away from the heat source the last material will experience a peak temperature equal to the Ac_1 temperature. This will be possible provided the welding data be available as follows.

The Rosenthal equation for thick plate is:

$$T - T_0 = \frac{q/v}{2\pi\lambda t} e^{-r^2/4at}$$

The Rosenthal equation for thin plate is:

$$T - T_0 = \frac{q/v}{d\sqrt{4\pi\lambda\rho ct}} e^{-r^2/4at}$$

Symbols:

T	instantaneous temperature K
T_0	preheating temperature K
(q/v)	heat input J/m
t	time s
r	distance from heat source m
ρ	volume thermal capacity $J.m^{-3}.K^{-1}$
a	thermal diffusivity $m^2.s^{-1}$
λ	thermal conductivity $J.m^{-1}s^{-1}.K^{-1}$

The plate condition (thick or thin plate) may be established using the equation:

$$d' = \{\frac{\left(\frac{q}{v}\right)}{2\rho}(\frac{1}{773 - T_0} + \frac{1}{1073 - T_0})\}^{1/2}$$

If the plate thickness is greater than d', the thick plate solution is valid, whereas if the plate thickness is less than d', the thin plate mode is valid. During the current study, the thick plate solution was used.

It is possible to determine the distance at which the last material will be exposed to a peak temperature equal to the Ac_1 temperature. This sequence effectively produces non equilibrium material that is likely to graphitize preferentially to the rest of the microstructure.

The Ac_1 temperature of carbon steel may be approximated using the empirical relationship below (32).

$$Ac_1(°C) = 723 - 10.7(\%Mn) - 16.9(\%Ni) + 29.1(\%Si) + 16.9(\%Cr) + 290(\%As) + 6.38(\%W)$$

The results of the calculation of temperature as a function of time, for a position where graphed in Figure 12. The figure was generated using the Rosenthal equations and typical carbon steel material constants and welding parameters obtained from a PQR and the distance that was chosen (12.6mm) is the distance at which the material furthest away from the heat source is exposed to the Ac_1 temperature.
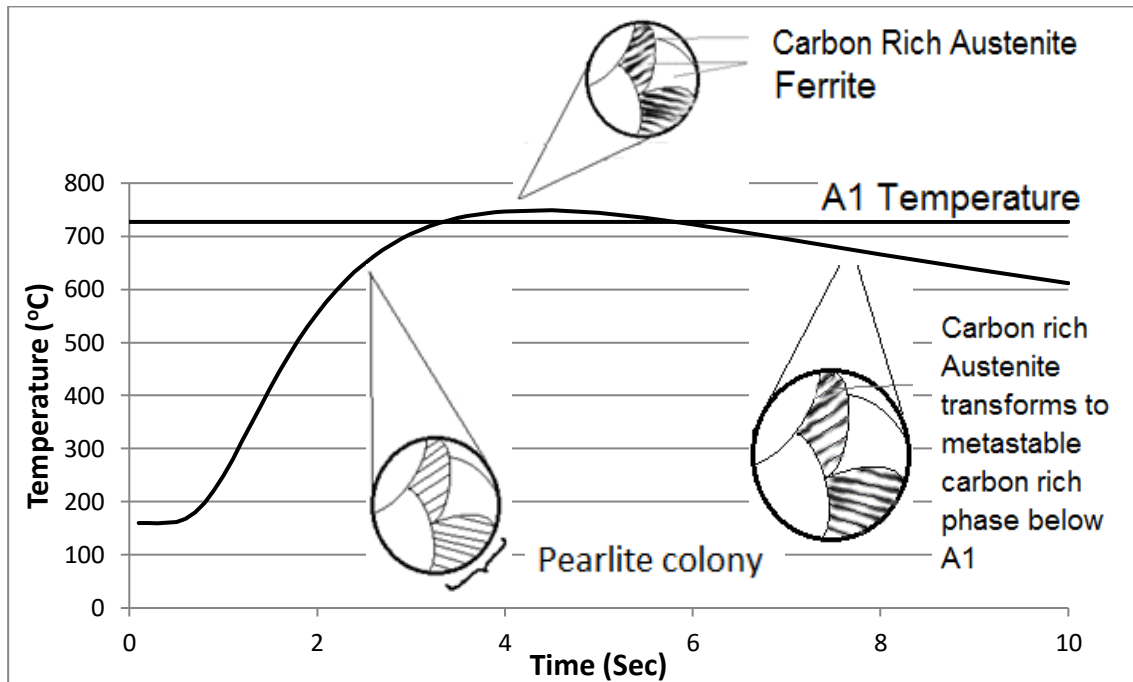
Figure 12: Proposed visual representation of none-homogeneous distribution of carbon in a pearlitic structure during rapid pearlite ➔ austenite ➔ pearlite transformations as seen at the extremities of weld HAZ in carbon steel. The graph was constructed with the following parameters: Heat input 1.8 kJ.mm⁻¹; Preheat 160°C; Thermal conductivity 41 J.m⁻¹.s⁻¹.K⁻¹; Distance from heat source 12.6 mm: Distance from fusion line 4.4 mm; Thermal diffusivity 9.1 X 10⁻⁶ m².s⁻¹.

Figure 12 shows the change in temperature of material that is 12.6 mm away from the heat source. Note that the material at this position remains above the Ac_1 temperature for approximately 2 seconds, and in this time, the pearlite will presumably transform into alternating bands of ferrite and carbon rich austenite. On cooling, the carbon rich austenite could transform to a metastable carbide other than Fe_3C which could more readily decompose to form graphite as seen in Figure 13.
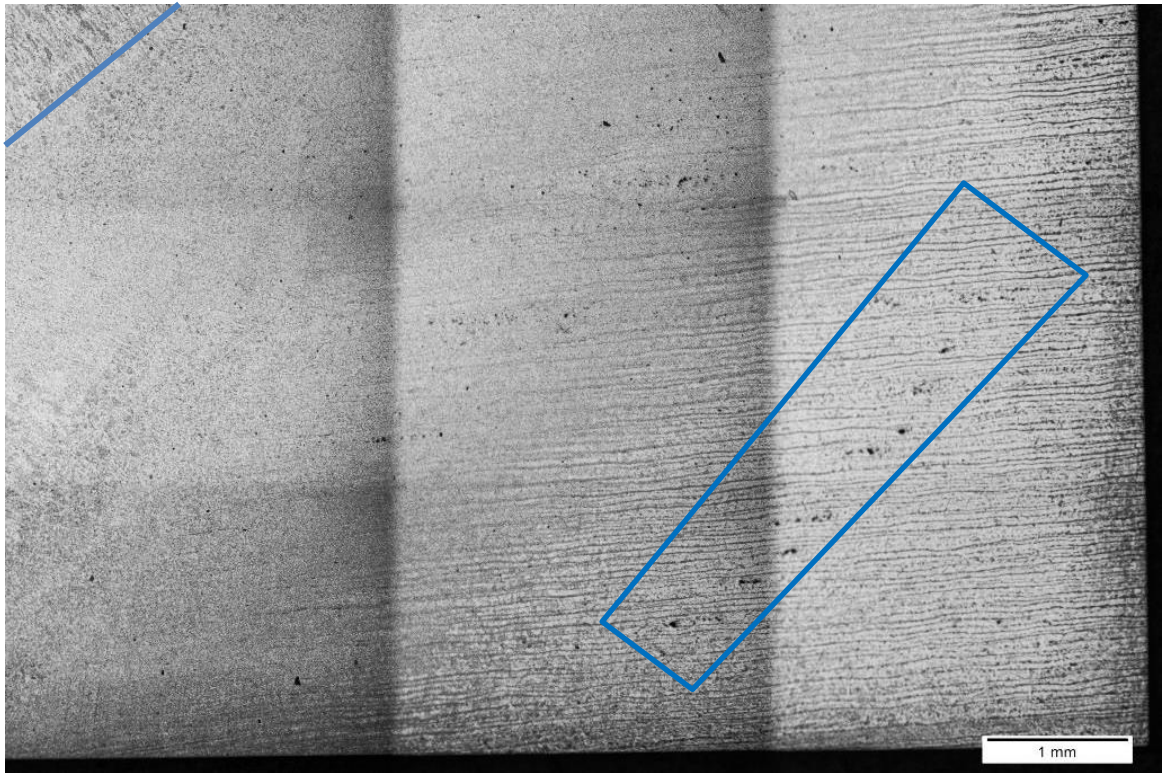
Figure 13: Montage of the heat affected zone of material that has been in service at elevated temperatures for 35 years from sample W 23 DS in the as-received condition. Note the line of graphite (As many small black dots outlines by the rectangle) forming in the partially transformed zone. The fusion line is demarcated by the line at the top left of the image. Note that the fusion line has a distance of approximately 5 mm from the graphite indicated.

1.2.3. Proposed repair techniques

Several repair techniques have been proposed for graphitized pipelines to date, however each proposed technique to date has had major limitations. The following provides a list of previously proposed repair techniques.

Solution heat treatment

A solution heat treatment process was proposed and implemented as a possible repair procedure for several years. This treatment involves heating the material to between 927°C and 954°C for between 2 – 4 hours before cooling the material down. It was found that the heat treatment was successful in removing the graphite from the microstructure, however it was discovered several years later that this was a temporary solution. The graphite that had previously been dissolved by the heat treatment had reformed within 5 years of continued operation. The heat treatment is now believed to leave sub microscopic voids that still act as stress concentrators. As a consequence, the solution heat treatment process has been largely discredited (31). Additionally, a solution heat treatment will not be a practical rehabilitation technique for a large diameter pipeline.

Removal of the graphitized region and rewelding

Due to the fact that almost all the documented cases of graphite related failures have been caused by preferential graphitization of the low temperature HAZ (12), a repair strategy that was considered viable was to remove the preferentially graphitized plane of material and reweld it.

While this may appear to be an elegant solution, there are numerous drawbacks to this repair technique such as: It is extremely labour intensive and joint preparation as well as welding can only be performed while the pipe is not in operation. Edge preparation of the pipe that remains intact will be very difficult to perform in practice.

Replacement of the section

This method is the most effective means of ensuring no graphite is present in the pipe section, joint preparation can be performed prior to taking the pipeline out of operation, and welding can be minimised provided that the correct joint preparation was performed. Many detection methods are currently in development and large efforts are being made in early detection techniques such as high temperature ultrasonic testing and radiographic testing (33).

While this solution is clearly the safest one, it is not cost effective if a large number of pipe sections require replacement.

1.3. Conclusions drawn from available literature regarding graphite formation in carbon steel as well as the effect perceived effects of graphite on the mechanical properties of carbon steel

Secondary graphite forms in C-Mn steels due to the inherent metastable nature of iron carbides. The exact nucleation sites of graphite, dissolution rates of iron carbides, nucleation rate of graphite, and all the associated influencing factors are poorly understood. This makes the prediction of graphite formation in terms of volume and location very difficult.

Due to a lack of uniformity in the test methods used to evaluate the effects of graphite on the mechanical properties of graphitized carbon steel, there is a large variance in test results. There are few points which are agreed upon with regards to the effects of graphitization on carbon steels. The most important consensus that exists is that planar graphite is more deleterious to the mechanical properties of graphitized carbon steel than randomly distributed nodules (31).

There are numerous theories that attempt to explain graphite nucleation and growth, and to date there is still no clear consensus regarding this topic ((14), (20), (12), (22), (27), (13), (31)). The reason for this is that every attempt at generating a guideline for the nucleation and growth of graphite has been dismissed due to contradicting evidence. An example of this would be the theory that steel chemistry will determine the graphite nucleation and growth rate as has been proven by several authors under specific conditions (20). This is in direct contradiction to the results obtained in the graphitization study performed in this project as seen in Table 7 and Figures 24 - 29. Therefore it must be concluded that not one or two factors determine the tendency for a material to graphitize, but rather a complex matrix of variables. The variables that appear to increase the nucleation and growth rate of graphite ultimately need to fulfil three requirements: provide free carbon to form graphite; provide graphite with space to grow within the material; and provide energy to drive the reaction.

Steel chemistry is now used to inhibit graphite formation by alloying with small amounts of chromium to form more stable chromium containing carbides. When the carbon is locked in the chromium containing carbide it is much less metastable than the Fe_3C carbide which is more readily available for the graphite reaction.

The thermal history – especially rapid heating and cooling cycles – effect the formation of metastable iron carbides. These carbides more readily decompose and provide free carbon for the graphite reaction.

The service temperature is a strongly debated topic, while there is a general consensus in the literature that graphitization and spheroidization are competing reactions, there is still much uncertainty as to which temperature range favours graphitization, and which favours spheroidization (12).

In service tensile strain and pre-service plastic strain, provides a driving force for graphitization. Tensile strain in service is generally observed in positions on a pipeline where a bend is required (expansion loops for example).

Material defects, on a smaller scale provide the material with high energy positions. The energy of these positions can be minimized by filling them with graphite.

Time is an important variable that is coupled to the graphitization rate. If the other factors that affect graphite nucleation and growth rate could be resolved, the factor of time would be a valuable output variable.

Conditions that allow these variables to overlap significantly will determine the location and severity of graphitization. There appears to be a strong correlation between the heat affected zones produced through welding and graphitization. It is likely that the effects that the thermal cycle from welding has on the material is of significant importance with respect to graphitization. Thermal history, specifically, rapid heating and cooling associated with the weld thermal cycle, and tensile strain appears to be the most important features of the heat affected zone resulting in graphitization. As discussed in 1.2.2.2, the temperature range (720-730°C) that results in the partial transformation from pearlite to carbon rich austenite and ferrite, and subsequent rapid cooling to below the Ac_1 temperature is hypothesised to result in less stable, higher carbon containing phase(s) other than cementite. It is this phase(s) that provides the carbon for the graphite reaction, and the associated tensile stress in the HAZ associated with the contraction of the weld metal on cooling that provides favourable conditions for graphitization. This also explains the highly heterogeneous and predictable graphite morphology in the low temperature HAZ near welded joints.

Chapter 2 – Experimental design

2.1. Aim

The aim of this study was to determine the feasibility of performing repair welding on a graphitized C-Mn steel steam pipe. If the repair welding was found to be feasible, a Procedure Qualification Record (PQR) had to be compiled that conforms to ASME (2) requirements that will allow the welding of carbon steel that has undergone graphitization.

Additionally the effect of graphitization on the mechanical properties of a welded joint was investigated, taking into account the orientation and severity of the graphitization.

2.2. Outline of Work

The experiments were constructed in such a way so as to answer specific questions surrounding the formation of graphite, as well as the possible steps that could be taken in order to successfully repair weld graphitized material. Thus two important outcomes had to be obtained from the experiments.

- It was important to be able to accurately predict which material was likely to graphitize preferentially, thus the theory of graphitization based on steel chemistry was tested. This was performed by using a range of steel chemistries and analysing the response (in terms of graphite formation) to temperature.
- Based on the results obtained from the steel chemistry evaluation, the material that displayed the highest tendency to graphitize was then used to perform the subsequent mechanical tests on possible repair weld scenarios.

2.3. Initial Graphitization Study

The material that was available for this project consisted of a number of pipe sections that were removed from a pipeline. This pipeline had been in service for 35 years at temperatures ranging from 417-435°C throughout its service life and reportedly exhibited secondary graphitization, with the degree of graphite varying significantly from one pipe section to the next. It had been previously been concluded that the presence of graphite in a pipe that operates at any appreciable pressure could have catastrophic consequences if the graphite was present in large enough quantities and orientated in a deleterious direction such as in the through thickness direction of the pipe wall. Based on the evidence obtained in this study, all in-service failures related to graphite occurred when graphite formed in large amounts along a planar direction, rather than when the bulk graphite content becomes large (28). The aim of the initial study was to identify the most severely graphitized pipe section so as to perform further work with the most severely deteriorated material. For this reason, it was desirable to produce a 'worst case scenario' by attempting to artificially graphitize unwelded parent material from a number of heats.

Based on the information presented in the literature study (Table 5), it was concluded that it would be possible to further graphitize the material through a prolonged heat treatment. The heat treatment

parameters that were chosen, were based on the general consensus in the literature regarding the temperature at which graphitization appears to occur at the highest rate, i.e. 620°C. Additionally, three samples were selected based on the information provided in the literature based on how the sample chemistry affects its sensitivity to graphitization. The material chemistries selected can be seen in the Table 7. Based on the literature, chemistries that included high C, Al and Si contents, and low Mn (due to Mn reportedly being a strong carbide stabilizer rendering the carbon unavailable for the graphite reaction (14)) contents are most vulnerable to graphitization. Therefore, a 'sensitive', 'moderately sensitive', and 'insensitive' sample was selected. All samples obtained had been from decommissioned pipe sections that had been in service for approximately 35 years at a service temperature of 420°C (3).

The samples were heat treated in a laboratory furnace. The temperature was measured once a minute via a K-type thermocouple. These samples were mounted, polished and etched in the as-received condition, as well as at 3 intervals during the heat treatment at 620°C (100h, 200h and 500h).

Table 7: Sample chemistries of samples selected for graphitization study

Sample Number	%C	%Si	%Al	%Mn	Rationale
W 23 DS (Insensitive)	0.25	0.19	0.009	0.85	Low C, Si, Al
W 13 DS (Moderately Sensitive)	0.28	0.22	0.003	0.90	High C. Average Si. Low Al
W 24 US (Sensitive)	0.30	0.23	0.061	0.87	High C, Si, Al.

2.4. Experimental Welds

2.4.1. Sample selection

The samples were selected according to material that was deemed most likely to display severe graphitization. For this reason, samples were obtained from a pipe section identified as W23 (3). This refers to a section near to circumferential weld number 23 both upstream and downstream as seen in Figure 14.

Longitudinal weld

Circumferential weld
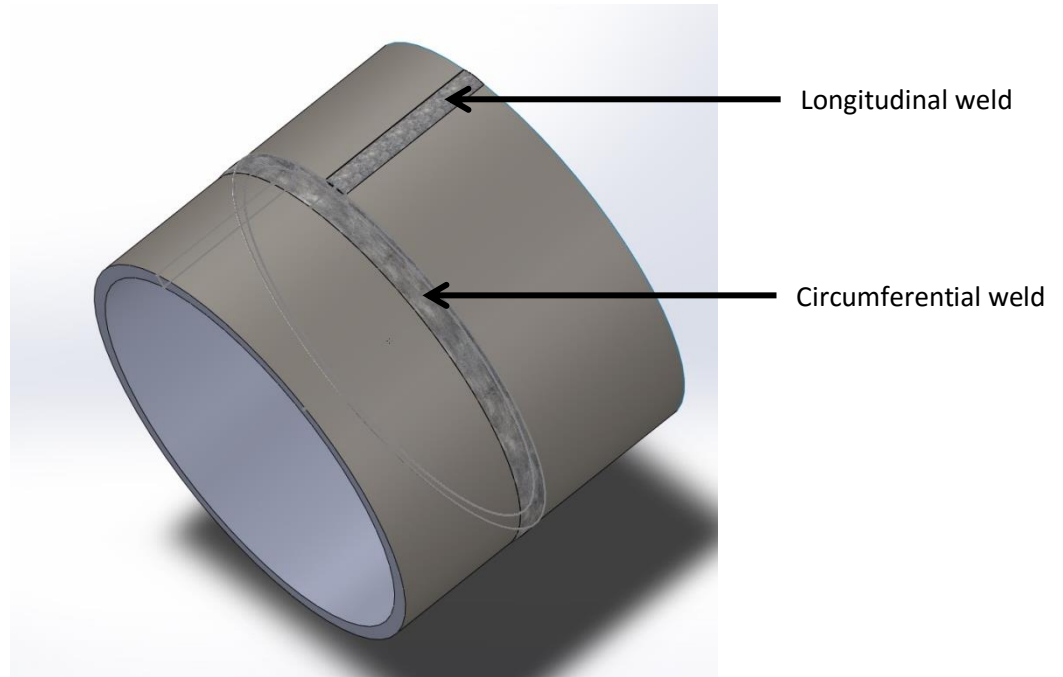
Figure 14: Schematic representation of material used (W 23 DS) in the current study where the circumferential as well as the positions of welds discussed.

Two sections of circumferentially welded pipe were obtained as well as two sections of material that did not contain any welds but were also cut from the material designated as W 23 DS.

When pipeline material is formed, it is usually rolled plate material that is welded longitudinally to produce a pipe section. The rolling direction dictates the orientation of the typical alternating layers of pearlite and ferrite in the material as seen in Figure 15. The orientation of these alternating bands could have an effect on the mechanical properties of the material. Due to the geometry of the material that is available for the current project, it was not possible to orientate all the samples in the same rolling direction. Thus samples 1 and 2 were orientated in such a way so that the rolling direction is parallel to the welding direction, while samples 3 and 4 were orientated so that the rolling direction is perpendicular to the welding direction.

Rolling direction

Through thickness direction

400 µm
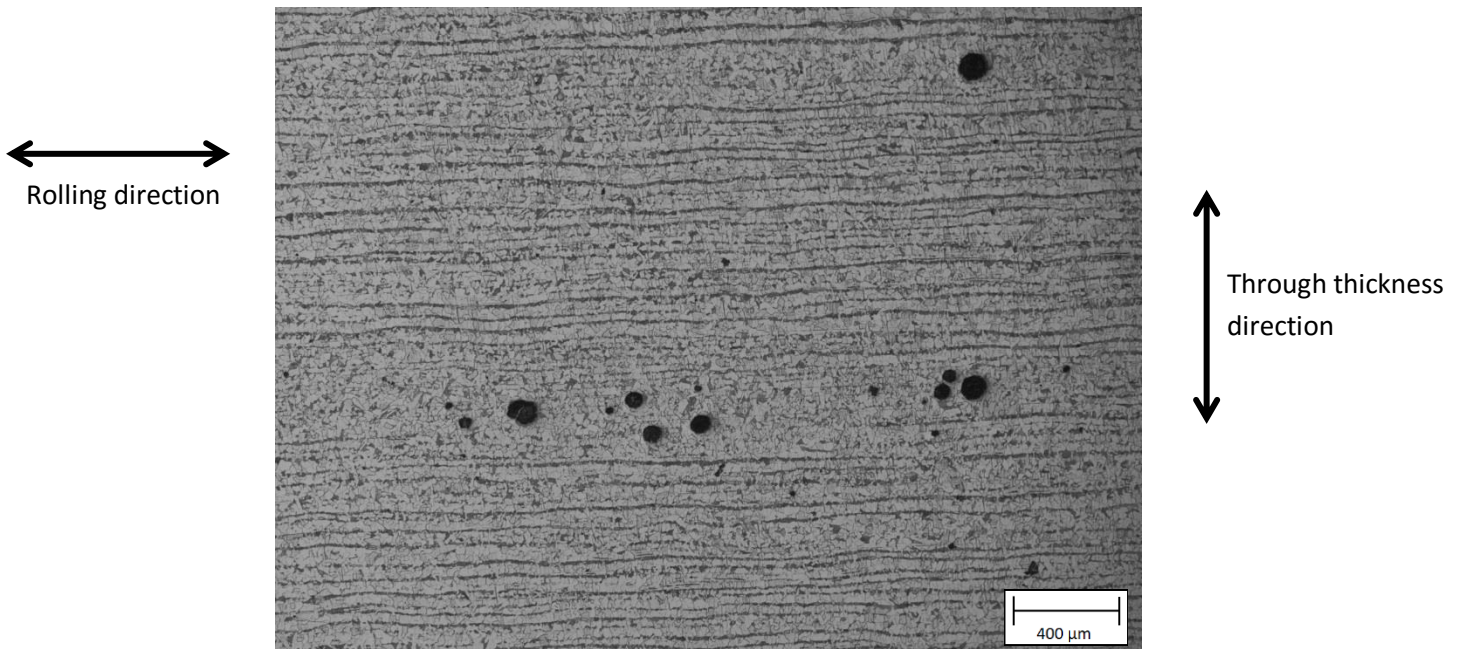
Figure 15: Light microscope image of a cross section of service exposed material (sample W 23 DS) to illustrate the effect of the rolling direction during the forming process on the microstructure. Note the pearlite-ferrite banding parallel to the rolling direction. The dark spots are graphite particles.

2.4.2. Processing Routes

These sample processing routes were selected to answer the following questions:

1.   What is the effect of welding on the mechanical properties of already graphitized base material? (Sample 1 & 2)

2.   Can graphite be selectively formed in a specific region in the material through subjecting it to a specific welding cycle followed by a 600 hour heat treatment? (Sample 1 & 3)

3.   Can pre-welded joint geometry affect the mechanical properties of the welded joint by altering the geometry of the graphite formation? (Sample 3)

All these samples were compared to a reference sample (Sample 4) which was a service exposed section of pipe that contained graphite and was tested as received from the pipeline. This reference sample allowed the experimental repair welds to be compared to the material that is currently in the pipeline.

The experimental procedure included four sets of samples that were processed in different ways so as to extract as much information for the final mechanical testing and micrographs as possible.

Table 8 summarised the differences in processing routes for samples 1, 2 and 3, with sample 4 acting as a baseline sample. These processing routes determined which of the three processes resulted in more favourable mechanical properties when compared to the mechanical properties of the material that is currently in service.

Table 8: Material processing routes that were performed for the current study as well as their respective rationales.

Sample No.	Rationale	Preweld heat treatment	Joint preparation[1]	Welding[2]	Post weld heat treatment
1	Replacement and graphitization study	600h at 635°C	Double V-groove	GTAW & SMAW	600h at 635°C
2	Replacement	600h at 635°C	Double V-groove	GTAW & SMAW	12h at 635°C
3	Rehabilitation	None	Two single V-groove	SMAW	600h at 635°C
4	Service exposed	None	None	None	None

All samples were produced from W 23 DS and underwent identical mechanical testing as specified in section 0.

2.4.3. Pre- and post-weld heat treatment

The initial graphitization study demonstrated that it was possible to artificially increase the volume fraction of graphite in a sample to a more severe level in a much shorter period of time by increasing the temperature significantly above the operating temperature of 417°C (3). In the case of the initial graphitization study, it was concluded that 500 hours at 620°C was sufficient to induce additional graphitization in the sample within the time frame that was available.

In the subsequent sample graphitization, it was decided that the samples would be exposed to 635°C for 600 hours. The temperature was increased by 15°C and the time was increased by 100 hours when compared to the initial graphitization study. The graphitization heat treatment temperature 635°C still fell well below the Ac_1 temperature of 719°C (according to the Ac_1 equation in section 0, and the chemistry of W 23 DS in Table 7). It was thought that raising the temperature will aid in accelerating the graphitization of the sample. The heat treatment time was increased by 100 hours in order to accommodate any power failures during the heat treatment period. By increasing the time at temperature, the effects that would be witnessed are an increase in graphite as well as an increase in spheroidization of pearlite in the material. Both graphitization and spheroidization deteriorates the mechanical properties of steel and thus, a worst case scenario was established. The samples would not be heat treated for longer than 600 hours due to time constraints. Two samples were placed in the furnace at a time and the sample temperature was recorded by two K-type thermocouples (one placed on each sample, and an average was recorded) and the same data collector that was used in the initial graphitization study was used in the pre- and post-weld heat treatments.

The furnace that was used was an electrical furnace with resistive heating elements with furnace dimensions of: length (1130mm) X height (580mm) X width (620mm). The furnace was fitted with a Toho Electronics PTM4 PID controller. This is a Proportional-Integral-Derivative (PID) controller and

---

[1] For a schematic of the joint preparations, see 2.4.4
[2] For a schematic of the welding procedure, see 2.4.6

the PID controller assists the furnace in reaching temperature at the desired rate and allows it to very accurately maintain the temperature without overshooting the set point value (in this case 635°C).

The furnace underwent a temperature uniformity survey as defined in ASTM A991/A991M-98 (34). The purpose of the survey was to define a working zone in the furnace where the temperature that is defined by the controller set point correlated as closely as possible to the temperature that is recorded by the independent thermocouples within the furnace. Figure 16 briefly illustrates the placement of the stages that were used to perform the temperature uniformity survey. The furnace working zone was established at heights between 65 and 405 mm within the furnace and the minimum sample thickness sample qualified is 6 mm.
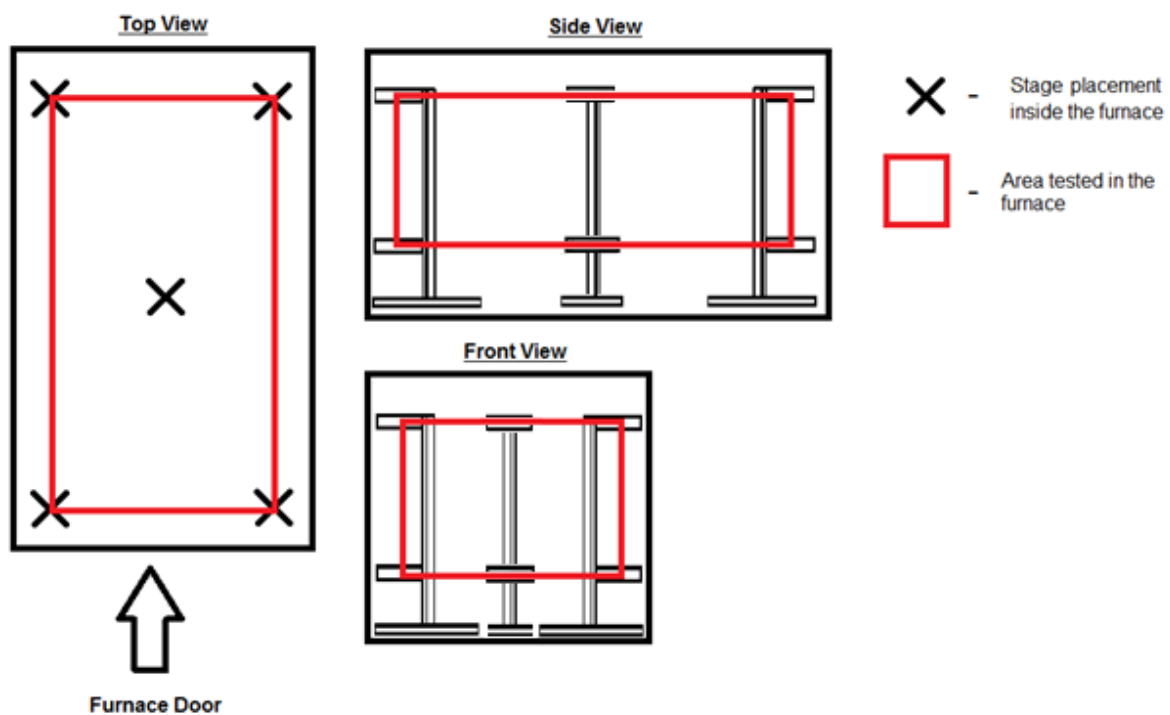
Figure 16: Stage placement inside the furnace for the temperature uniformity survey

Table 9 contains the results of the temperature uniformity survey.

Table 9: Results from the temperature survey performed on 2 March 2015 (T in °C)

	Bottom position	Top position
Left rear	624	590
Right rear	598	619
Centre	584	605
Left front	623	623
Right front	596	622

The results of the uniformity survey showed general temperature conformity within the furnace however there were several zones that were colder than desired. These zones were avoided when the furnace was loaded with the samples. The maximum recorded temperatures occurred at the left front of the furnace, while the minimum temperature recorded occurred at bottom centre of the furnace. Both these areas were avoided in order to minimize the temperature gradient that developed within the material due to the difference in temperature within the furnace. The estimated maximum temperature gradient that was expected to occur within any one sample was calculated to be less than 15 degrees Celsius. This was based on the temperatures generated by the furnace temperature uniformity survey and the positions that the samples were placed inside the furnace during heat treatment. The results also showed that the furnace ran approximately 5°C colder than the controllers' thermocouple indicated. For this reason, the furnace was set to 640°C in order to achieve the set point of 635°C that was required. The furnace was used once to perform a temperature uniformity survey.

The furnace was used an additional three times during the current study as described in Table 8 for heat treatments: the pre-weld heat treatment of samples 1 and 2 (600 hours); the post weld heat treatment of sample 2 (12 hours); the prolonged post weld heat treatment of samples 1 and 3 (600 hours).

2.4.4. Joint preparation

Two weld preparations were used:

<u>Full thickness asymmetrical double V preparation</u>

The full thickness asymmetrical double V preparation was performed on base material that was far enough away from any welded regions in order to remain thermally unaffected by previous welding. This welding preparation was based on a previously qualified WPS. The joints were prepared using a milling machine. These joints were welded in order to witness the effects of welding on material that has already graphitized. Additionally, it was hypothesised that heterogeneous graphite will form along the low temperature HAZ if the material is exposed to elevated temperature for a prolonged period of time (15). The orientation of the graphite is therefore expected to be parallel to the fusion line.
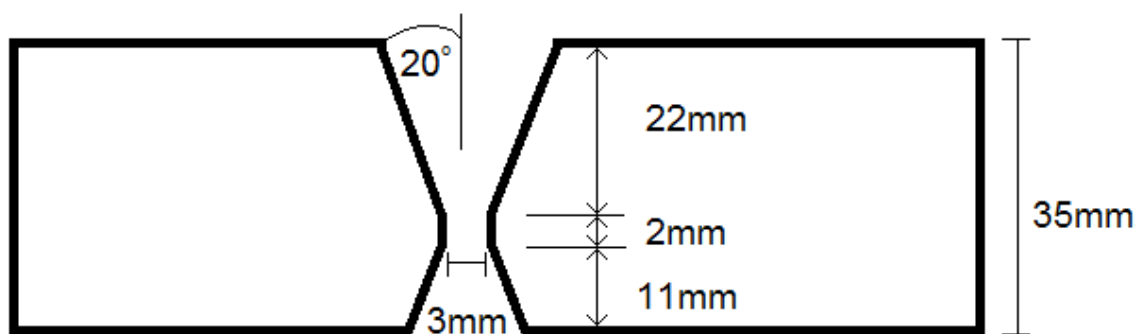
Figure 17: Full thickness groove preparation for graphitized carbon steel (joint preparation of samples 1 & 2).

Half thickness groove preparation

The half thickness groove preparation was performed so that 17.5 mm of the groove was excavated from the weld metal in the horizontal direction and 17.5 mm of the groove was excavated from the base material in the horizontal direction, finally the groove was ground 17.5 mm deep to form a triangular joint preparation as seen below as seen in Figure 18. This is similar to a joint preparation that was proposed by Thielsch a technical report in 1954 (21) and can be seen in Figure 19. The joint preparation was performed using grinding only so as to avoid further thermal cycles being induced into the material via the alternative methods such as carbon electric arc-air gouging. Grinding was used as this is the method that would be used in industry. These joints were welded with the intention of performing an additional heat treatment of 600 hours in an attempt to induce graphitization in the low temperature HAZ. As mentioned above, the graphite is expected to form in the low temperature HAZ, in a plane parallel to the fusion line. The intention of this joint preparation is to create a staggered low temperature HAZ in the through thickness direction which will in turn stagger the formation of the graphite in the low temperature HAZ. By staggering the graphite, it was expected that the risk of failure in the through thickness direction should be reduced. In addition to this, the material that would experience the highest bending stresses would be found on the outside of the pipe and by removing the graphitized outer edge, it is likely that crack initiation as a result of graphite would not occur at this area of maximum bending stress.
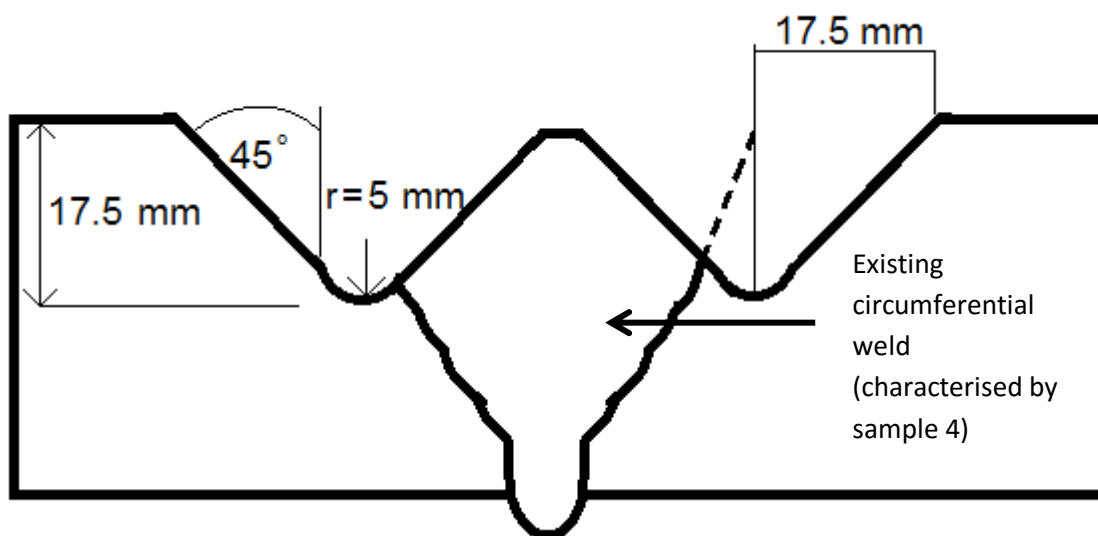
Figure 18: Half thickness groove preparation superimposed on pre-existing circumferential weld (joint preparation of sample3).
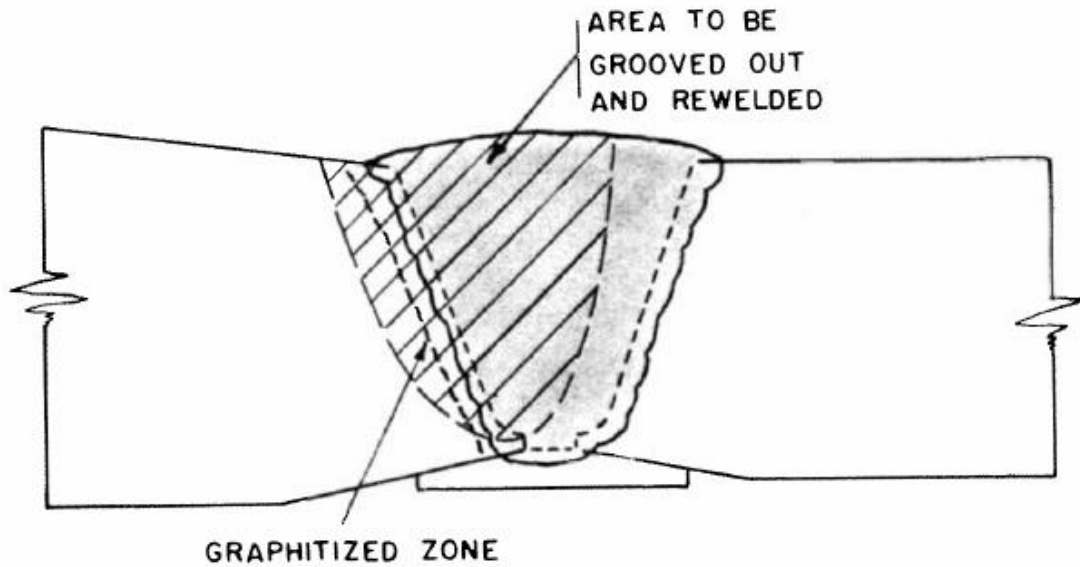
Figure 19: Partial removal of graphitized HAZ in pipe applications (21).

2.4.5. Non destructive testing

It was important to determine whether or not the surfaces that were prepared for welding, as well as whether the finished welds were defect free. The presence of a defect could affect the results of the mechanical tests that were performed on the samples. For this reason, non destructive testing (NDT) was employed in order to determine whether or not there were any defects present. There were two NDT techniques that were employed in this study, namely magnetic particle testing (MT) and ultrasonic testing (UT)

Magnetic particle testing was used to determine whether or not there were surface, or near surface cracks on an edge preparation or on the surface of the finished weld. MT was employed on all edge preparations and finished weld surfaces to check for any surface cracks.

UT was used to detect subsurface defects. These include but are not limited to: lack of side wall fusion, porosity and slag inclusions. UT was performed on all finished welded joints to check for weld soundness.

2.4.7. Welding

During the welding of each sample, the following welding parameters were recorded for every SMAW electrode that was used. Additionally, recording the welding parameters for the GTAW runs was completed whenever possible. The welding parameters that were recorded were:

- Maximum and minimum voltage
- Maximum and minimum current
- Welding time
- Bead length
- Stub end length
- Preheat/interpass temperature

Full thickness welding sequence

Figure 20 below indicates the welding sequence used for the full thickness groove preparation in 2.3.3. and included the electrodes used and thickness of material used for each section in the sequence. For the complete set of welding parameters, refer to appendix A. The welding parameters were based on a pre-existing WPS. At least 980 mm of full thickness welded joint was required in order to complete all the test work.
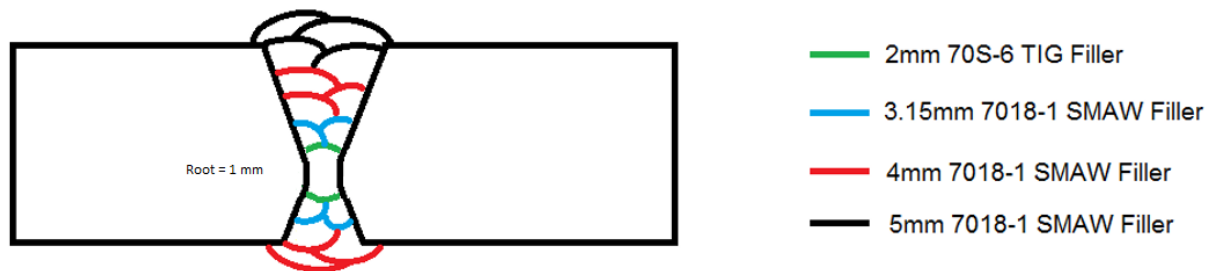
Figure 20: Schematic illustration of a full thickness welding sequence based on WPS 1-1-D-21-1 Rev 2a

Half thickness welding sequence

Figure 21 below indicates the welding sequence for the half thickness groove preparation in 2.3.3. and includes the electrodes used and thickness of material used for each section in the sequence (note that in the illustration, only the groove on the right indicates welding, however this sequence was be performed on both grooves that were machined). For the complete set of welding parameters, refer to appendix A. The welding parameters were based on a pre-existing WPS. At least 490 mm of half thickness weld was needed in order to complete all the test work that was required.
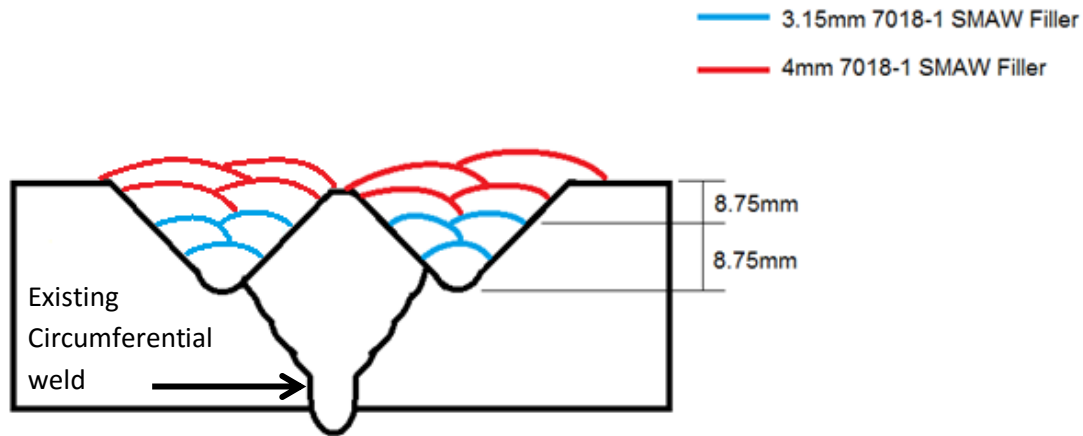
Figure 21: Schematic illustration of a half thickness welding sequence based on WPS 1-1-D-21-1 Rev 2a

2.4.8. Mechanical testing and microstructural analysis

The mechanical properties of all the welded joints were tested. Figure 22 illustrates the amount of material required from each sample. (35)
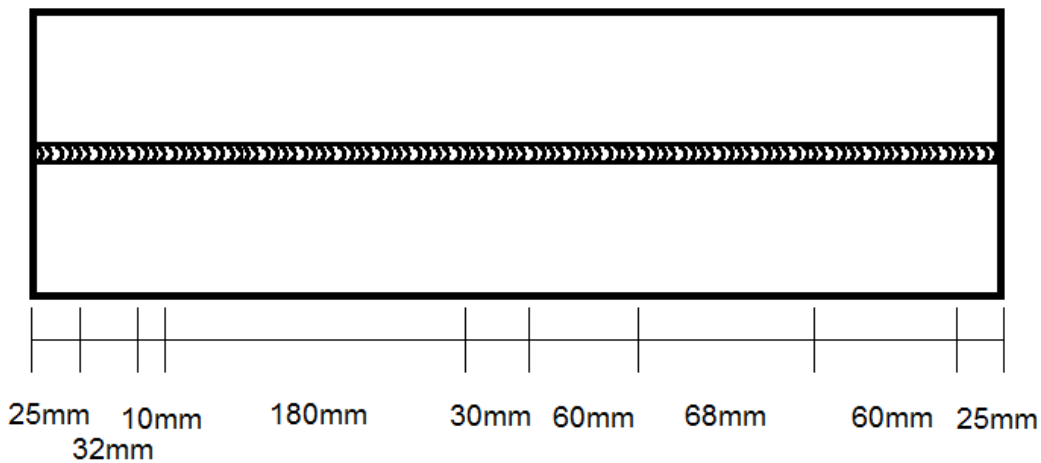
Figure 22: Illustration of the amount material required for each mechanical test out of the original 400mm welded joint (1:2.67 scale).

- 25mm was cut from both extremity and discarded.
- 60mm was designated for the production of 2 full section rectangular tensile samples.
- 60mm was designated for the production of 2 reduced section, round tensile samples.
- 30mm was designated for the production of 1 reduced section, round, hot tensile sample.
- 68mm was designated for the production of 4 side bend samples.
- 180mm was designated for the production of 6 Charpy V-notch samples.
- 10mm was designated for microstructural analysis and hardness testing

32mm of welded joint was designated as additional material to be used as required. Table 10 lists the number of tests that were performed as well as the requirements as per ASME IX guidelines in order to qualify a PQR (QW-451.1).

52

Table 10: List and quantity of tests to be performed on the welded samples, as well as the ASME requirements in order to qualify a WPS

	Welded samples	ASME
Full section tensile tests	2	2
Reduced section round tensile test	2	Not required
Reduced section round hot tensile test	1	Not required
Side bend tests	4	4
Weld metal Charpy	3	Not required
HAZ Charpy	3	Not required
Hardness	HAZ and weld metal	Not required

2.4.8.1.   Tensile testing

Test Significance

The tensile test produces a large amount of useful information with regards to the load bearing capabilities of a sample. Information that was extracted from a tensile test include the ultimate tensile strength, yield strength, elongation to failure, percentage reduction in area, stress strain diagrams and the location and mode of fracture (35). Due to the uniform nature in which round tensile samples neck and fail, it was more convenient to determine the reduction in area of a sample using these samples. Hot tensile testing was used to determine the mechanical properties of the material at the service temperature.

In a weld, the fracture surface could provide important information with regards to the effects of defects that result in discontinuities such as lack of fusion, inclusions, cracking and porosity. The fracture surface was particularly important to this study as it aided in understanding the effects of graphite on mechanical properties of graphitized carbon steel.

Test sample as per ASME

According to ASME, the rectangular tensile sample must have a gauge length of 60mm, gauge width of 25mm, and enough material on either side of the gauge so as to clamp the sample.

ASME also stipulates that the reduced section round tensile test samples must have a gauge length of 50mm, diameter of 12.5mm, and enough material on either side of the gauge so as to clamp the sample.

The reduced section round hot tensile test samples must have a gauge length of 40mm, diameter of 10mm, and enough material on either side of the gauge so as to machine threads in the ends by which the sample is held in place as prescribed by ASME.

2.4.8.2. Bend Testing

Test Significance

Bend tests were used in order to determine ductility of the welded joint in the presence of defects.

Test procedure

The test sample was placed on two shoulders or rollers and a plunger was used to bend the sample into a gap between the stationary rollers. The test sample was then inspected for any defects or tears on the tension side.

Test sample as per ASME

According to ASME, the side bend sample must have a through wall thickness that is the largest thickness achievable that results in a flat profile on the top and bottom of the weld. The width of the sample must be 10mm, and the total length of the sample must be 150mm.

2.4.8.3. Charpy impact toughness test

Test Significance

Fracture testing is used to determine whether a material will fracture in a brittle manner as well as to establish the ductile to brittle transition temperature (DBTT). The energy per unit volume of material that a material can absorb at a specific temperature is referred to as the impact toughness (35). This test is significant for welded joints due to the fact that the rapid thermal cycles could drastically change the mechanical properties of the material. In order to ensure that the welding process has not degraded the impact properties of the material, impact testing is necessary, especially for materials operating at low temperatures.

Test procedure

The test sample was placed on an anvil and the notch that was machined into the sample was facing away from the point of impact. The sample was then impacted by a hammer and the energy absorbed by the sample was recorded. The fracture surfaces could also be analysed further. The current study made use of room temperature tests in order to evaluate the impact properties of the steel

Test sample as per ASME

Note that ASME does not require Charpy impact tests for the PQR, the addition of Charpy impact tests are purely for supplementary information. According to ASME, the sample must have a height of 10mm, width of 10mm and length of 55mm. The notch is machined into the sample and is 2mm deep, has a tip radius of 0.25mm, and an open angle of 45°. Charpy impact tests are taken in sets of 3 and will be taken from both the weld metal (3 samples from weld metal) as well as from the HAZ (3 samples from the HAZ) as specified in EN 15614-1.

2.4.8.4. Hardness

Test Significance

The Micro-Vickers hardness test provides qualitative information that can be used in evaluating welding procedures.

Test procedure

Note that ASME does not require hardness tests for the PQR, the addition of hardness tests are purely for supplementary information. The sample was prepared in the same manner as in section 2.3.5.4. The sample was then manually tested with a Micro-Vickers testing apparatus and tested 3 times across the transverse direction to the weld using the HV 2 scale (2 kg load). A 2 kg load was selected because this load is relatively low and the resultant indentation is small (typically 160-180 µm diagonals) and therefore tests could be conducted 1mm (5 diagonals distances) apart. By performing the hardness tests close to one another, it was possible to measure the effects of graphite on the hardness of the material as the indentations moved across the graphitized HAZ in the cases of samples 3 and 4.

2.4.9. Microstructural analysis

Test Significance

Microstructural analysis yields valuable information regarding the position, orientation and size of structures within the material. The use of microstructural analysis aided in justifying many of the findings made with the mechanical tests.

Test procedure

Note that ASME does not require microstructural analysis for the PQR, the addition of microstructural analysis are purely for supplementary information. Samples of material was mounted in Bakelite resin, ground and polished to mirror finish. The samples were then etched with 3% nital solution and analysed using an optical microscope (Olympus BX51M) as well as a scanning electron microscope (Zeiss Crossbeam540 Ultra High resolution FEC). Fracture surfaces were observed using a stereoscope (Olympus SZX7) and the SEM.

The metallographic sample preparation method for polished samples was as follows:

- Samples were cut to sizes no larger than 20x20mm using an abrasive cutting disc.
- Samples were hot mounted in Bakelite resin.
- Samples were ground using 80, 240, 400, 600, 800, and 1200 grit silicon carbide grinding paper and running water for rinsing away debris and for lubricating the grinding process.
- Samples were then polished using 9µm, 3µm, 1µm, and 0.25µm diamond suspension polishing medium and an alcohol based lubricant.
- The samples were then etched for between 13-20 seconds using a 3% Nital etchant. 3% Nital consists of 3% Nitric acid and 97% ethanol (36).

In the preliminary stages of metallographic sample preparation, an additional polishing step using 50nm colloidal silica was used after the 0.25µm diamond suspension. However once samples that were prepared in this manner were viewed in a SEM, it became clear that the 50nm sized particles were embedding themselves into the soft graphite as seen in Figure 23. This rendered it impossible to observe the structure of graphite clearly and therefore it was decided to omit the final polishing step using 50nm sized colloidal silica.
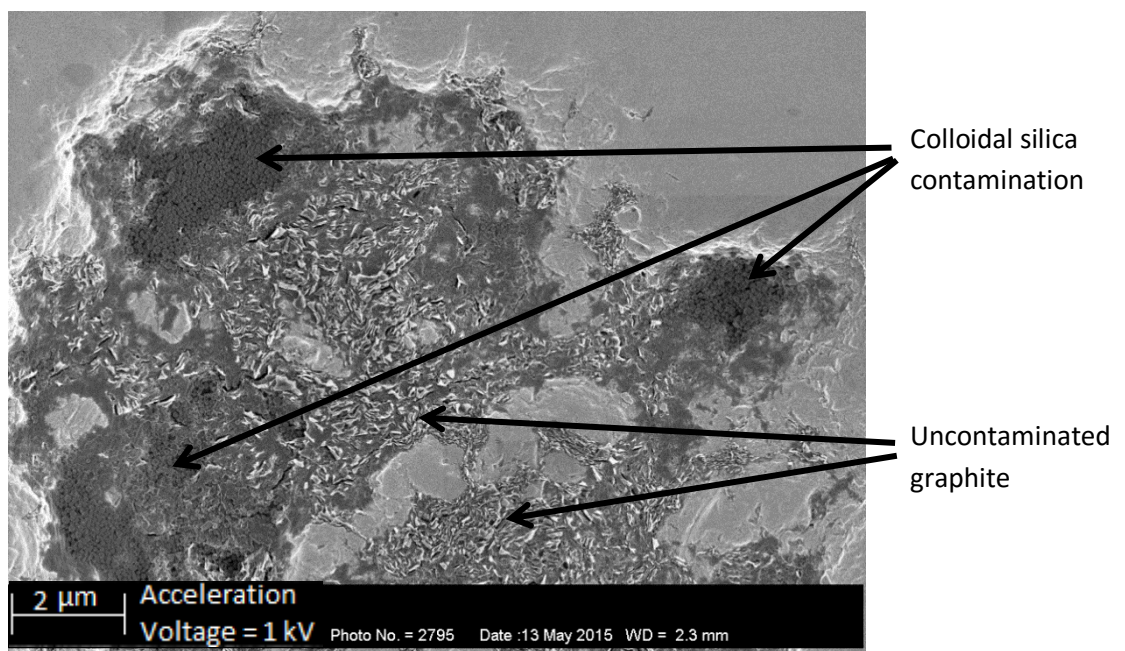
Figure 23: Colloidal silica embedded in sections of the graphite particle of a polished cross section.

Fracture surface samples that were of metallographic interest were first cleaned of petroleum jelly (originally used for protecting fracture surfaces from oxidation) by dissolving the jelly in petroleum spirits or petroleum ether and then washed with ethanol.

By making use of a program called ImageJ (37), it was possible to perform quantitative metallography in the form of a point count in the HAZ to determine the amount of graphite that is present in the HAZ. This was made possible by superimposing a grid over an existing image and using the grid to perform a point count to determine the volume fraction of graphite present in a section of the HAZ.

ImageJ was also used to approximate the percentage of the tensile fracture surfaces that was covered in graphite. In the binary black and white image that resulted from the analysis, the black areas of the

image indicate areas of the fracture surface that were covered in graphite while the white areas are graphite free areas. The total percentage of graphite that is present on the fracture surface could then calculated by performing a pixel count in the ImageJ program. The images were processed so as to approach the most accurate conclusion of the graphite content on each surface, however where it was unclear as to whether or not an area contained graphite, it was then assumed that the unknown area was graphite.

ImageJ was also used to perform quantitative metallography in the form of a point count in order to estimate the volume fraction of graphite present in the base metal of each sample as well as in the partially transformed region of the HAZ (38).

Chapter 3 – Results

This section details the actual procedure and execution of the experimental design, as well as the results obtained from the experiments that were performed.

3.1.   Initial heat treatment study

The initial heat treatment study was performed in order to determine whether it would be possible to increase the volume fraction of graphite within aged material by performing a prolonged heat treatment on decommissioned material. Additionally, three sections of material were selected with the intention of verifying the effect of chemistry on the tendency for a material to graphitize as well as to select the most graphitized final sample to perform further work on.

Figure 24 - Figure 29 compares the images obtained using optical microscopy of the three samples at the four time intervals selected.

W 23 DS (as-received)

W 23 DS (100h)
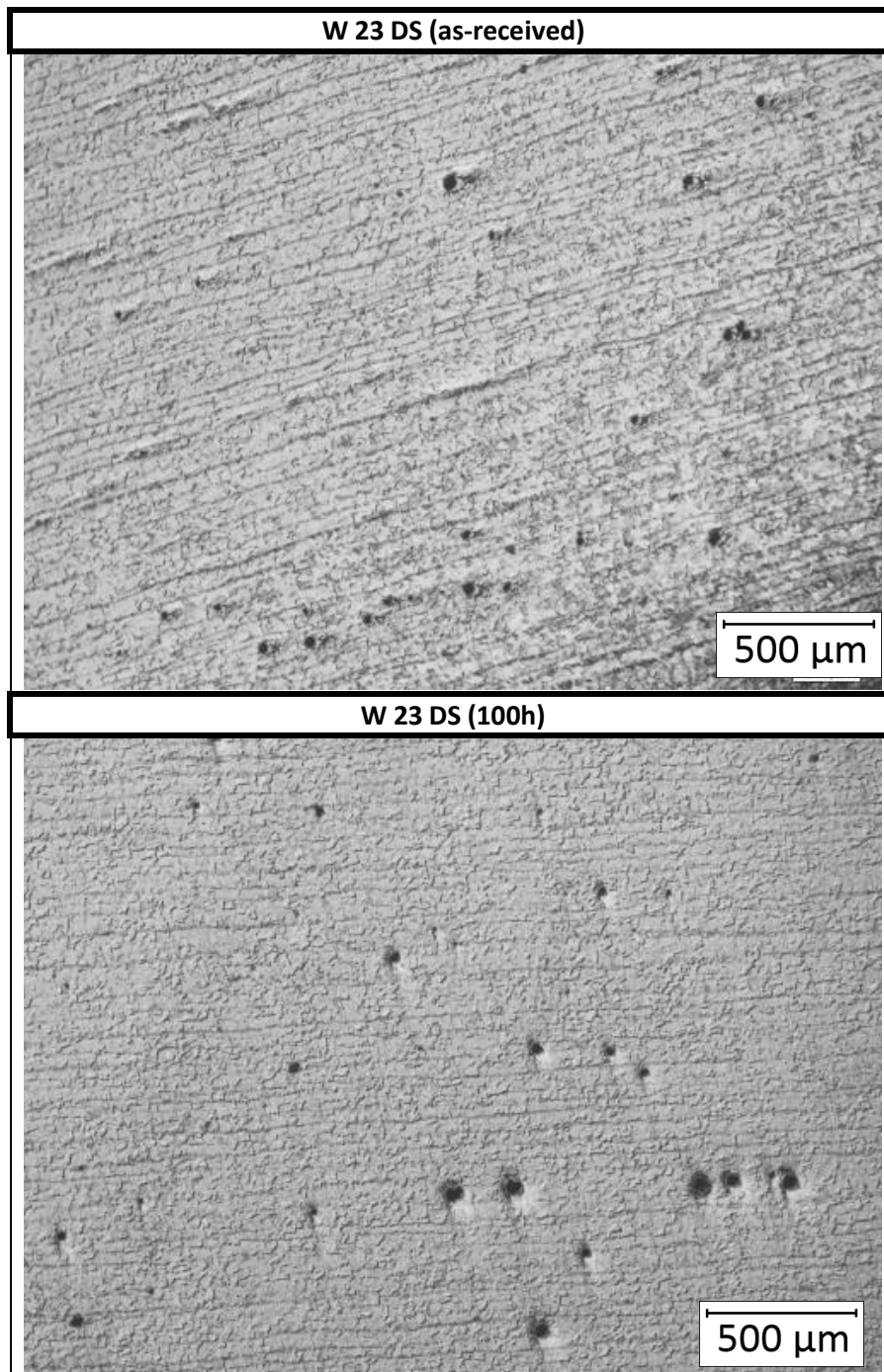
Figure 24: Microstructures of sample W 23 DS in the as-received condition (0h heat treatment) as well as after 100h, heat treatment. Images are of the most severe graphite that could be found in each sample

W 23 DS (200h)

W 23 DS (500h)
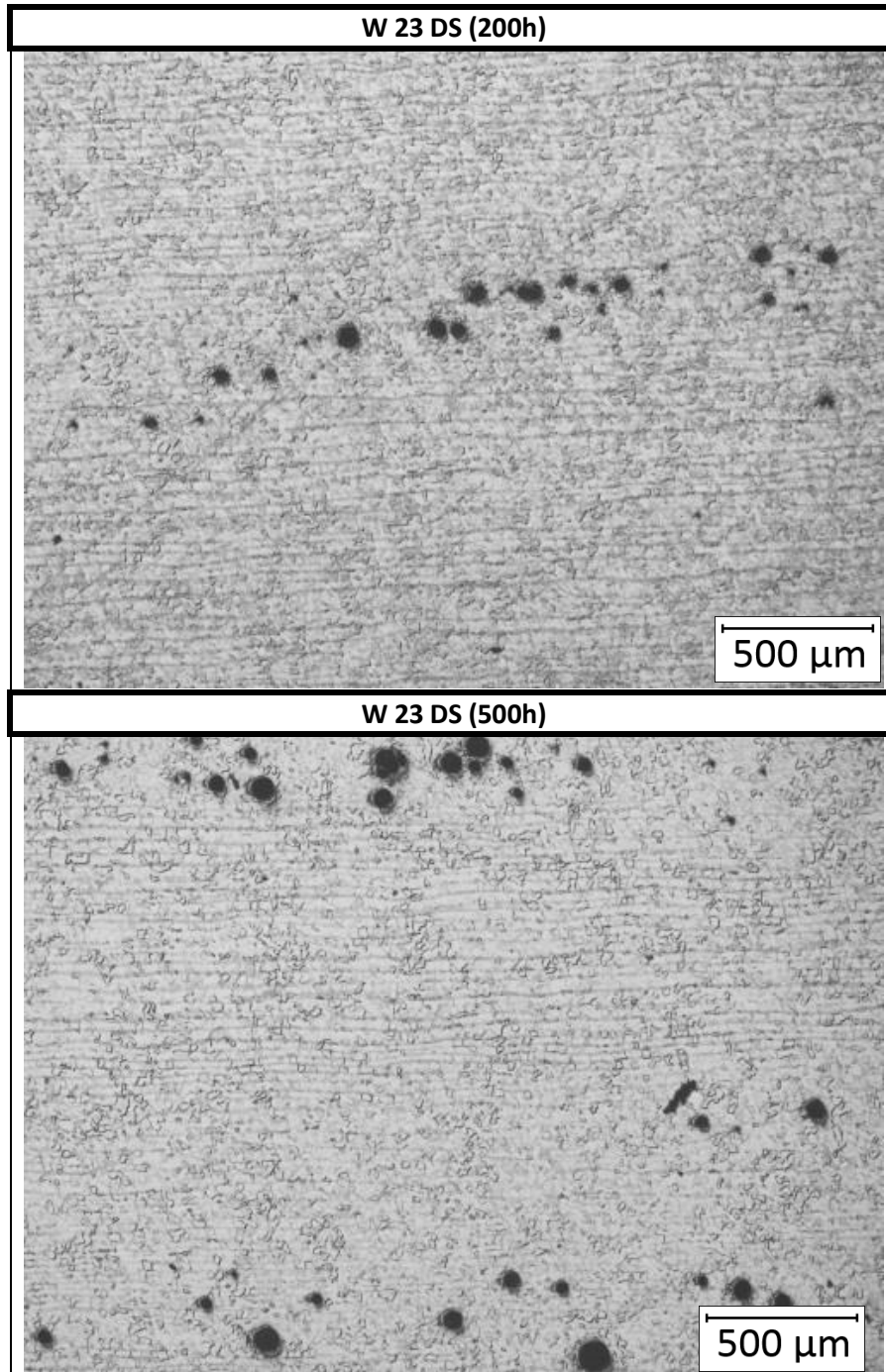
Figure 25: Microstructures of sample W 23 DS after 200h and 500h of heat treatment. Images are of the most severe graphite that could be found in each sample

W 13 DS (as-received)

500 µm

W 13 DS (100h)

500 µm
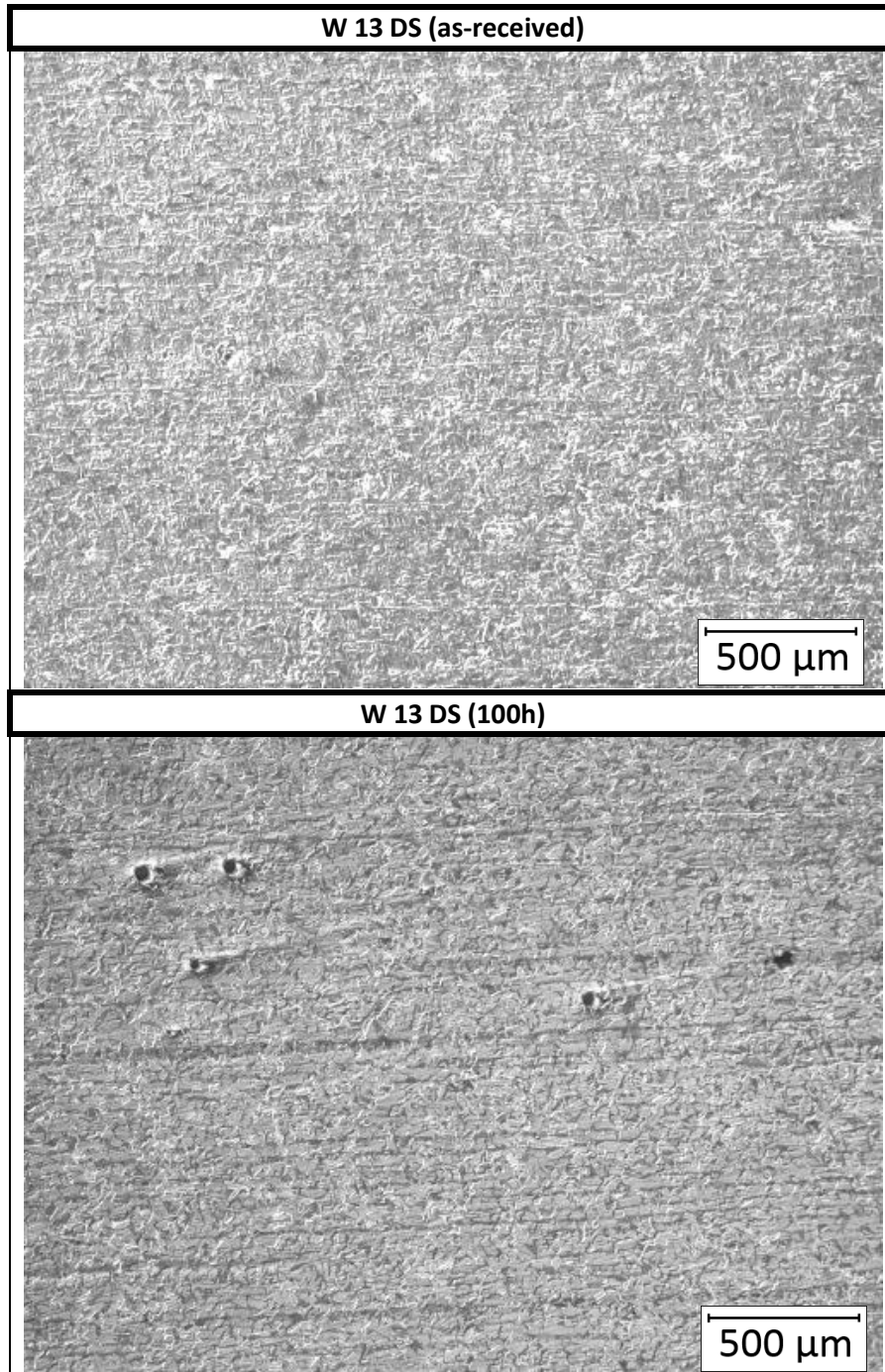
Figure 26: Microstructures of sample W 13 DS in the as-received condition (0h heat treatment) as well as after 100h, heat treatment. Images are of the most severe graphite that could be found in each sample
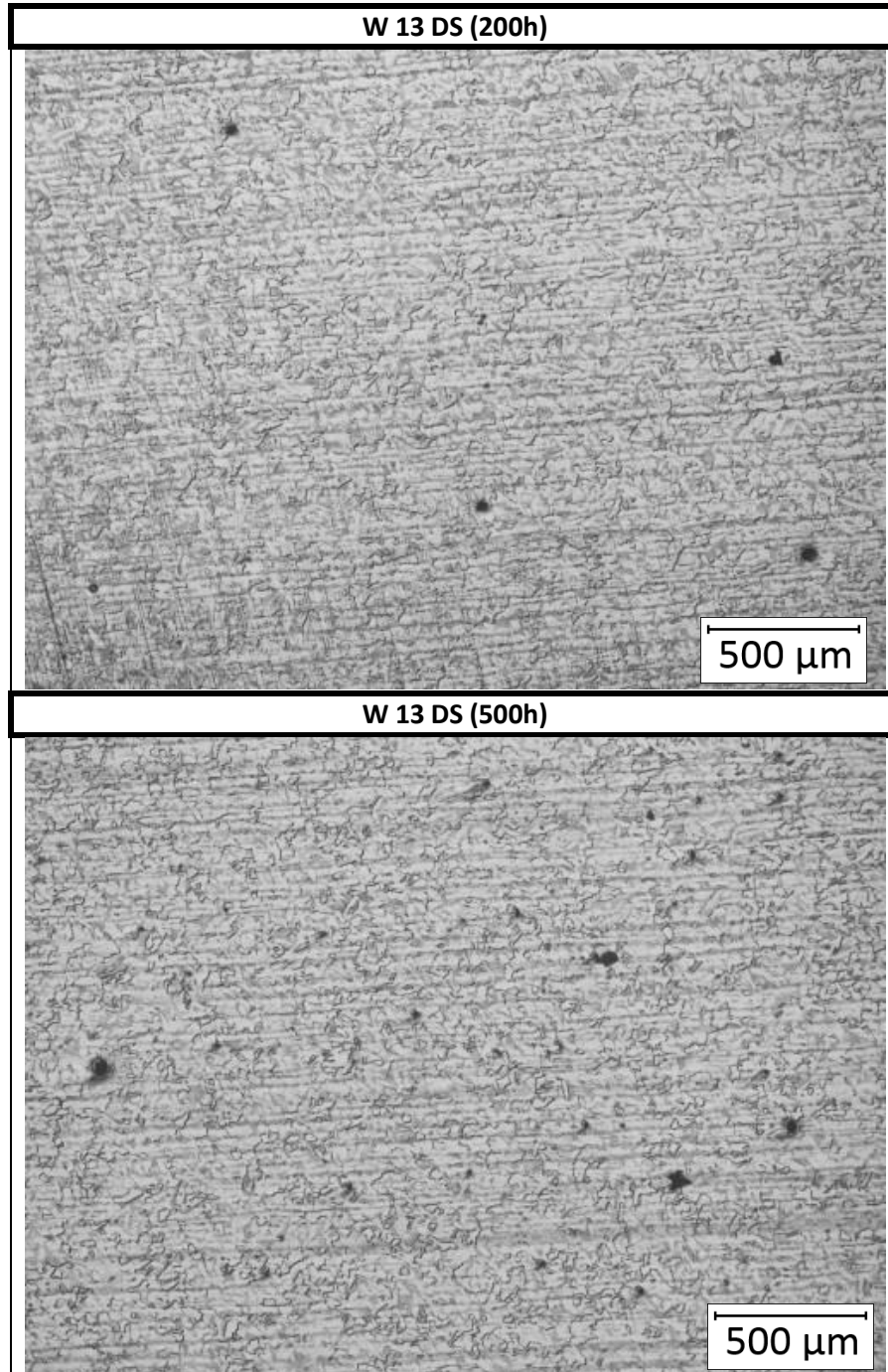
Figure 27: Microstructures of sample W 13 DS after 200h and 500h of heat treatment. Images are of the most severe graphite that could be found in each sample.

W 24 US (as-recieved)

W 24 US (100h)
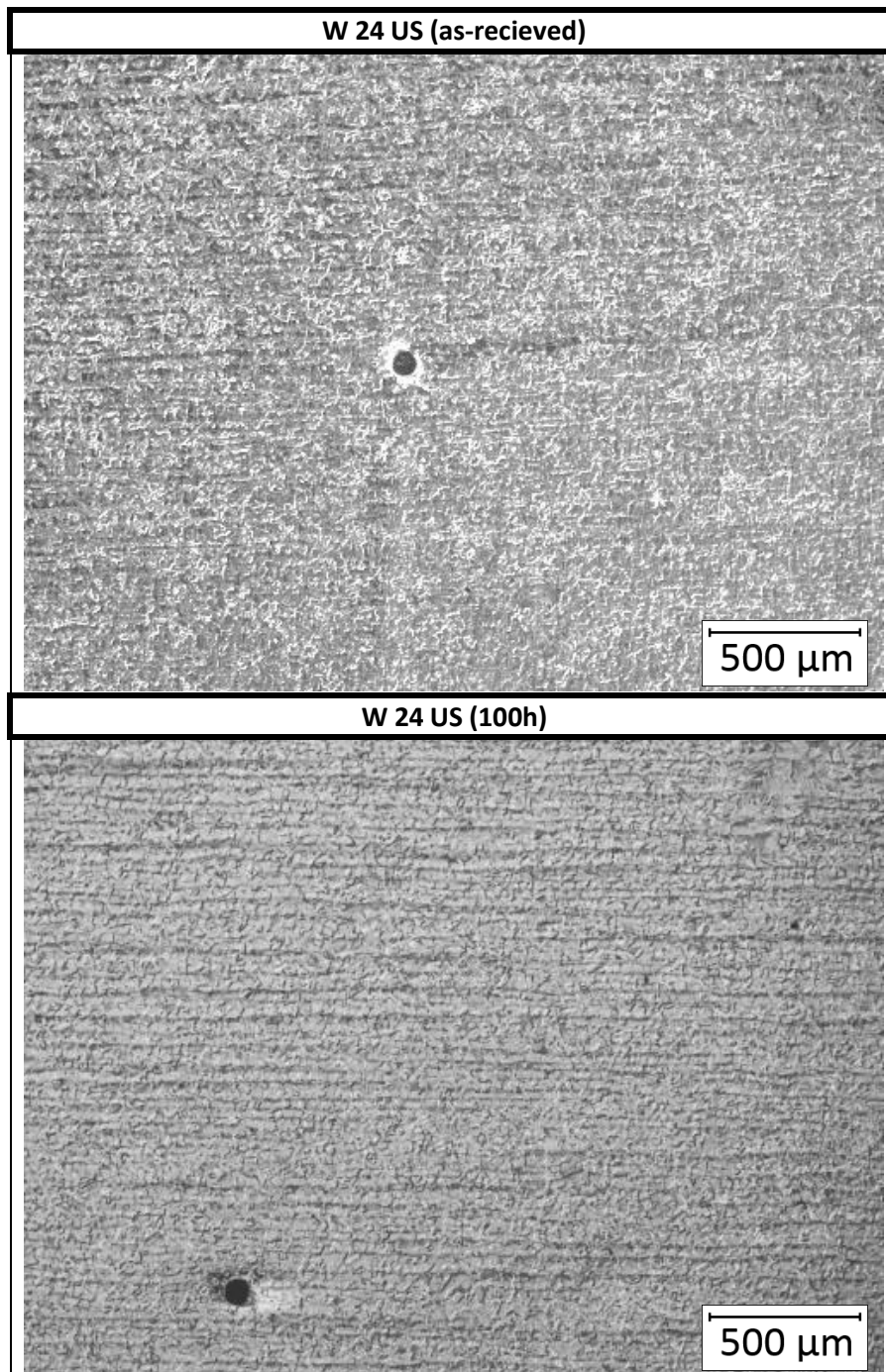
Figure 28: Microstructures of sample W 24 US in the as-received condition (0h heat treatment) as well as after 100h, heat treatment. Images are of the most severe graphite that could be found in each sample

W 24 US (200h)

500 μm

W 24 US (500h)

500 μm
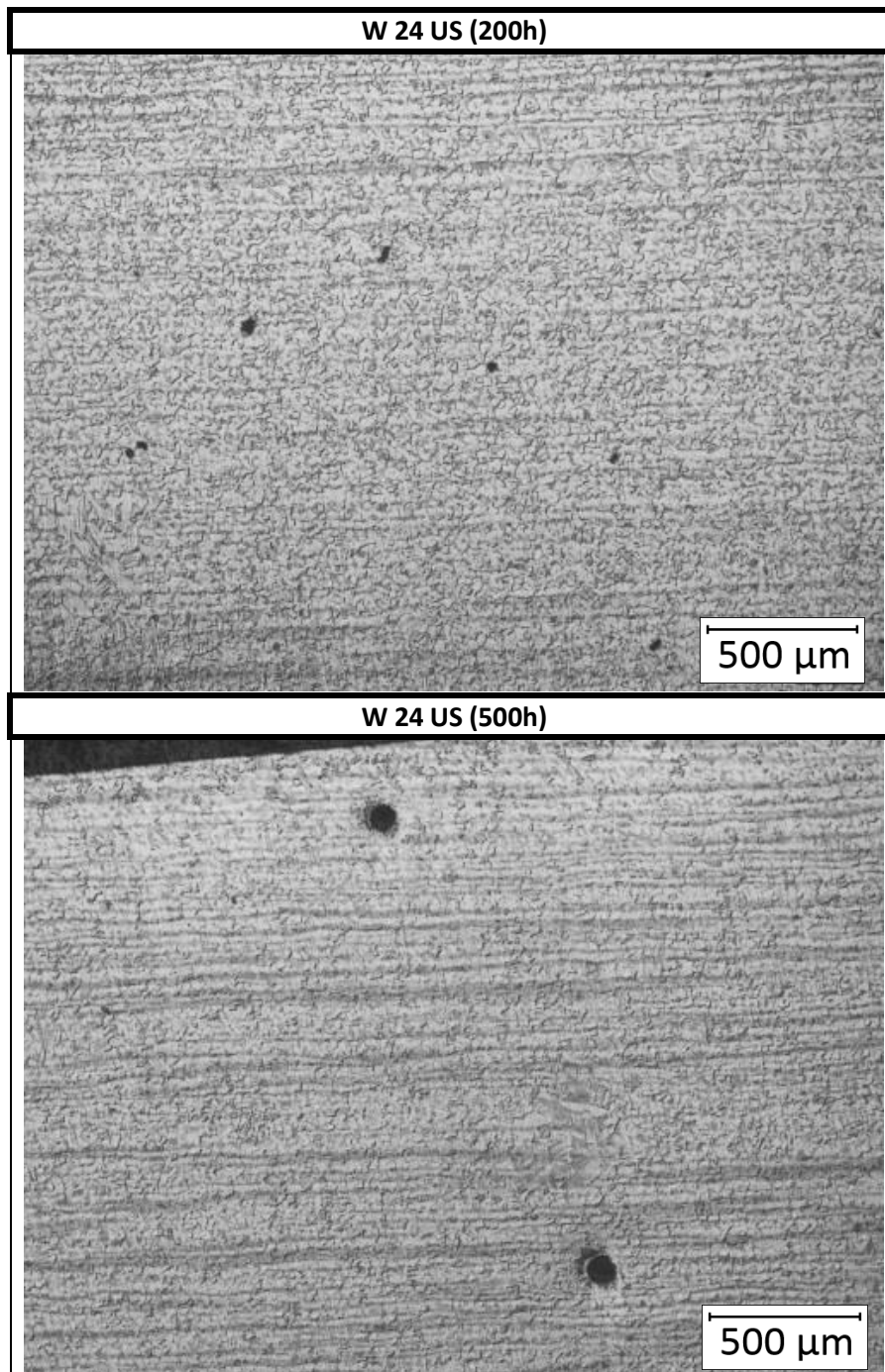
Figure 29: Microstructures of sample W 24 US after 200h and 500h of heat treatment. Images are of the most severe graphite that could be found in each sample

Based on the micrographs shown in Figure 24 - Figure 29, two important conclusions can be drawn.

1. The chemistry of the steel within the range used in this study with regards to the above mentioned elements, according to the micrographs, is not a contributing factor to the tendency for steel to graphitize. However based on the evidence presented in the literature review, the influence of the chemical composition (specifically the C, Si, and Mn content) must not be disregarded. It is likely that the steel chemistry that determines whether the material will be sensitive to graphitization or not only becomes relevant once some elements in the

steel (such as aluminium) are increased significantly (20). It is clear that based on these results, the chemistry of the steel is not the determining factor in commercially manufactured steels.

2. The graphitization heat treatment was successful in increasing either the size of the graphite nodules that are already present, or increasing the number of graphite nodules present in the microstructure, or both.

    Based on the initial graphitization study, it was clear that the sample which would be used to perform subsequent research would be sample denoted as W 23 DS in the initial graphitization study. This material showed the most severe graphitization out of the three samples (in terms of graphite particle size and quantity) that were considered during the initial graphitization study, both in the as-received condition and after 500 hours of heat treatment. Therefore if a repair welding procedure could be developed with this sample successfully, it will qualify all repair welding of graphitized C-Mn steel up to the severity of the sample used in this study. Graphitized base material was used to produce samples 1 & 2 while graphitized HAZ material was used to produce sample 3 and 4.

3.2. Heat Treatment

The material underwent its first stage of heat treatment as detailed in section 2.3.2. Table 11 details the thermal history of the samples used for the study. Each thermocouple wire was placed on top and in the centre of the samples that were in the furnace. The temperature as measured by two thermocouples was averaged to obtain the heat treatment temperature.

Table 11: Thermal history of the material that was used in this study.

Sample #	Rationale	Original PWHT	Service at temperature	Graphitization heat treatment	PWHT after repair welding
1	Replacement and graphitization study	Up to 15h at 635°C	35 Years at 425°C	579h at 635°C	672h at 635°C
2	Replacement	Up to 15h at 635°C	35 Years at 425°C	579h at 635°C	12h at 635°C
3	Rehabilitation	Up to 15h at 635°C	35 Years at 425°C	None	672h at 635°C
4	Service exposed	Up to 15h at 635°C	35 Years at 425°C	None	None

Approximately 440 hours of sample temperature can be seen in Figure 30 below. The temperature was recorded every one minute. There were three disruptions to the power in the furnace during the time that data was being captured. The effect that the power disruptions had on the temperature within the furnace are summarised in Table 12.

Table 12: Effects of power loss to the furnace on the internal temperature of the furnace.

Event #	Time that furnace was below acceptable temperature	Minimum temperature (°C)	Maximum Temperature (°C)
1	58 Minutes	602	633
2	9 Hours and 24 Minutes	467	633
3	13 Hours and 52 Minutes	356	630

The furnace temperature was very stable during steady operation. Table 13 lists the relevant statistical data that was obtained during the graphitization heat treatment. The data below excluded the data taken during the times in which the furnace lost power in order to determine the furnace consistency during steady state operation.

Table 13: Relevant statistical data during the steady state operation of the furnace

Temperature Set Point	**635°C**
Maximum Temperature	642°C
Minimum Temperature	618°C
Average Temperature	633°C
Standard Deviation of Temperature	2°C
Number of Points Captured	26320

The second prolonged heat treatment (PWHT) experienced multiple prolonged power failures, and thus it was not possible to capture the data from the thermocouples accurately. The previous heat treatment displayed the close temperature control that the furnace controller was capable of executing. Therefore, power failures were recorded (in terms of duration) and additional time was added to the PWHT in order to ensure that the minimum heat treatment time of 600 hours was obtained.
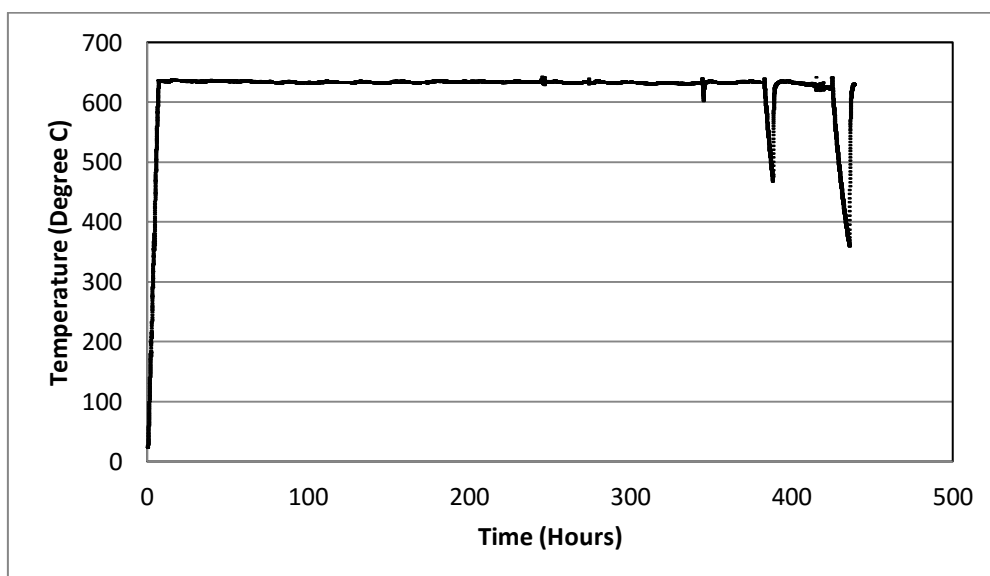
Figure 30: Initial 600h graphitization heat treatment temperature log (Samples 1 & 2)

3.3. Non Destructive Testing

Non destructive testing (NDT) was performed on the circumferentially welded sample before welding in order to ensure that there were no defects in the material prior to welding. The NDT methods employed were magnetic particle inspection (MPI) and ultrasonic testing (UT). Several surface cracks were detected and were caused by excessive force being applied to the sample during grinding (grinding cracks). These cracks had no effect on subsequent welding or testing, this is because the grinding cracks that occurred were melted away during the welding process, and this was also confirmed by metallography. No other defects were detected prior to welding.

All samples were tested using NDT after welding had been completed in order to ensure that failure of a test piece during mechanical testing would not be as a result of welding defects. The NDT results showed several defects, however all defects were within allowable limits as defined by BS EN ISO 17640:2010 (39), and no detailed information on the flaws were given. Samples that were removed from the welds for the purposes of mechanical testing were cut so as to avoid any defects that were detected by the NDT inspection. No indications of the grinding cracks (as noted in the previous paragraph) that occurred prior to welding were detected in the NDT inspection after welding, or during subsequent destructive testing.

3.4. Welding

The welding was performed as detailed in section 2.3.5 with respect to the two types of joint preparations mentioned above. The preheating method was flame heating, and both preheat and interpass temperatures were maintained between 150°C and 280°C as defined in CAT 24 (SP-1-1-D-21-1) and the temperature was measured using a handheld pyrometer. Table 14 lists the statistics regarding preheat. A list of essential, supplementary essential and nonessential variables as defined in ASME IX can be seen in appendix A in Table 40 and Table 41 for Gas Tungsten Arc Welding (GTAW) and Shielded Metal Arc Welding (SMAW) respectively (2).

Table 14: Statistical data relevant to the recorded preheat values

Statistical parameter	Statistical value (°C)
Minimum	140
Maximum	280
Average	208
Standard deviation	34
95% Confidence interval	208 ± 6

A complete set of welding data (including minimum and maximum current and voltage per run, run time, run speed, length of consumable consumed per run, tab length remaining, and heat input per run) may be viewed in appendix B. No abnormalities were detected during welding.

Figure 31 graphically represents the consistency of the measurements taken by calculating the heat input into the material using the two available methods (one method based on the electrical

characteristics, and the other based on the run out length of the weld). Table 15 lists the relevant statistical data pertaining to the heat input calculations.

Method 1: Heat input equation based on electrical characteristics

$$Heat\ Input = \frac{\eta VI}{v}$$

Where: η =   Arc efficiency (0.8 for SMAW and 0.6 for GTAW)
    V =   Average Voltage
    I =   Average Current
    v =   Welding speed

Method 2: Heat input equation based on run out length

$$Heat\ Input = \frac{d^2 LF}{ROL}$$

Where: d =   Electrode diameter
    L =   Length of consumed electrode
    F =   Electrode efficiency factor
    ROL =   Weld bead length
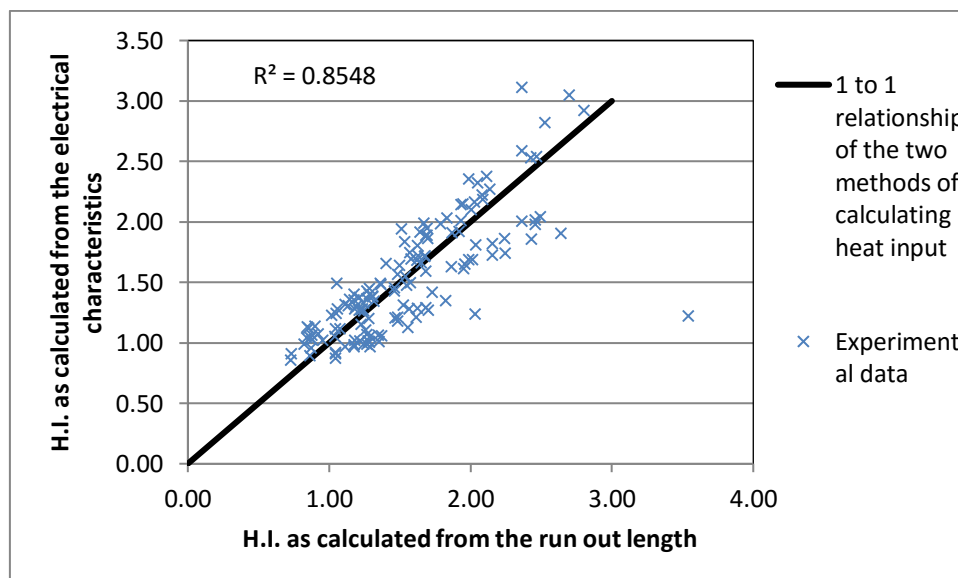
Figure 31: Graphical representation of the calculated heat input based on the two available methods of calculating heat input, from the electrical characteristics and from the run out length.

Table 15: Statistical data of the heat input into the material based on the two methods of calculating heat input, from the electrical characteristics and from the run out length.

Statistical parameter	Heat input based on electrical characteristics	Heat input based on run out length
Maximum	3.12	3.54
Minimum	0.86	0.73
Average	1.53	1.56
Standard deviation	0.48	0.50
95% Confidence interval	1.53 ± 0.08	1.56 ± 0.08

The Rosenthal equation was used to calculate the areas in the HAZ that are most likely to graphitize. The calculations (which can be seen in appendix C) are designed to determine which material was the material furthest from the weld centre to experience a temperature of 719°C. The results from the Rosenthal equation showed that graphitization is most likely to occur between 4 and 6 mm from the fusion line.

3.5. Tensile test

Three types of tensile tests were performed: The full section tensile test, the reduced section round tensile test, and the reduced section round hot tensile test.

3.5.1. Full Section Tensile Tests

Full section tensile tests were performed because they most closely approximate the full thickness welded joint loaded in the transverse direction. Table 16 summarises the results of the full section tensile tests as well as the passing criteria for the two steel grades considered, please note that each sample underwent 2 tensile tests.

Table 16: Summary of the full section tensile test results

Sample #	Yield strength 0.2% offset (MPa)	Tensile strength (MPa)	Total elongation (%)	Location of failure
1	263	410	42	Base material
	245	416	38	Base material
2	268	416	45	Base material
	269	418	44	Base material
3	259	418	52	Base material
	277	419	47	Base material
4	272	451	48	HAZ
	277	450	46	HAZ

The stress versus strain graph for samples 1-4 can be seen in Figure 32.
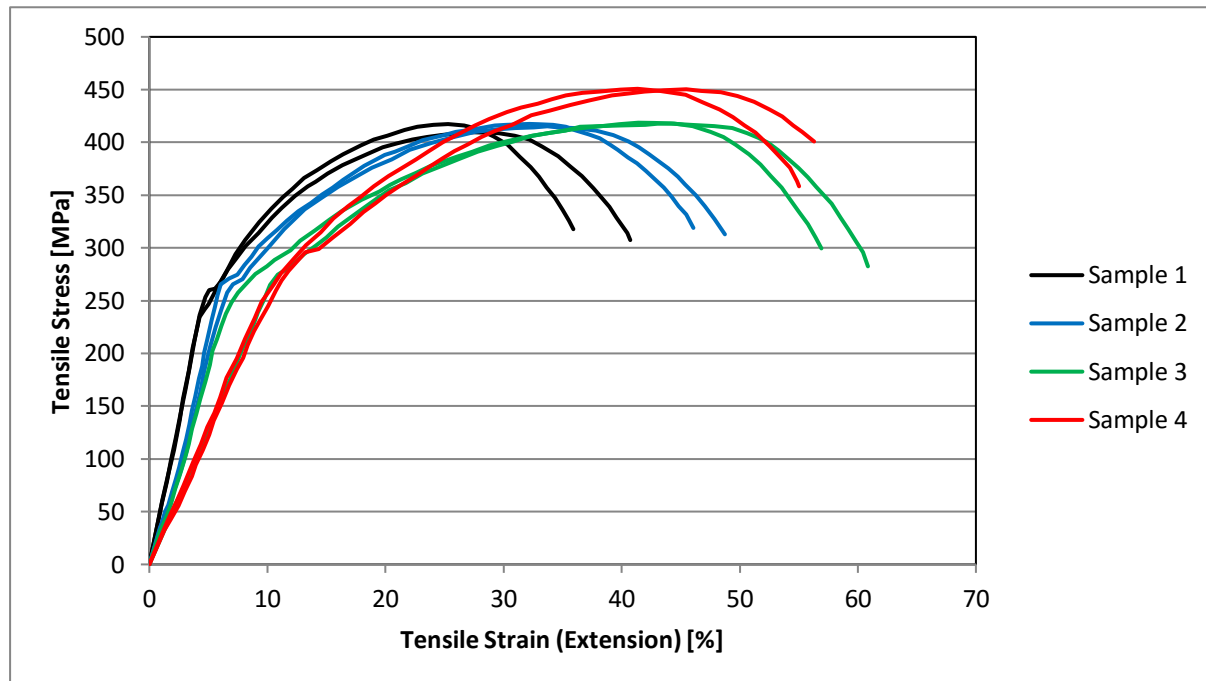
Figure 32: Engineering stress vs. engineering strain for the full section tensile test of samples 1-4

Sample 1 failed in the base metal. This is despite the prolonged PWHT that sample 1 experienced in an attempt to produce HAZ graphite. Two small indications were present in the root which would suggest a lack of fusion. However, despite this defect, the material failed in the base metal far from the weld.

Sample 2 failed in the base metal. This was an expected result due to the sample experiencing a short PWHT and new weld metal was used to weld the joint.

Sample 3 failed in the base metal. Despite having only half the old weld ground out and rewelded, the addition of new weld metal and removal of a section of the graphitized HAZ provided enough additional strength to prevent the sample from failing through the HAZ.

Sample 4 failed in the graphitized HAZ. The region where failure occurred displayed very little plastic deformation and the reduction in cross sectional area was much less than in the other three samples. Figure 33 in an images of a tensile test sample after the test had been completed.

It should also be noted that the elastic modulus of samples appear to differ between sample sets. The difference in the apparent elastic modulus were probably due to slight bending of the full section tensile samples. Therefore the elastic modulus observed in the full section tensile test results are not a true representation.
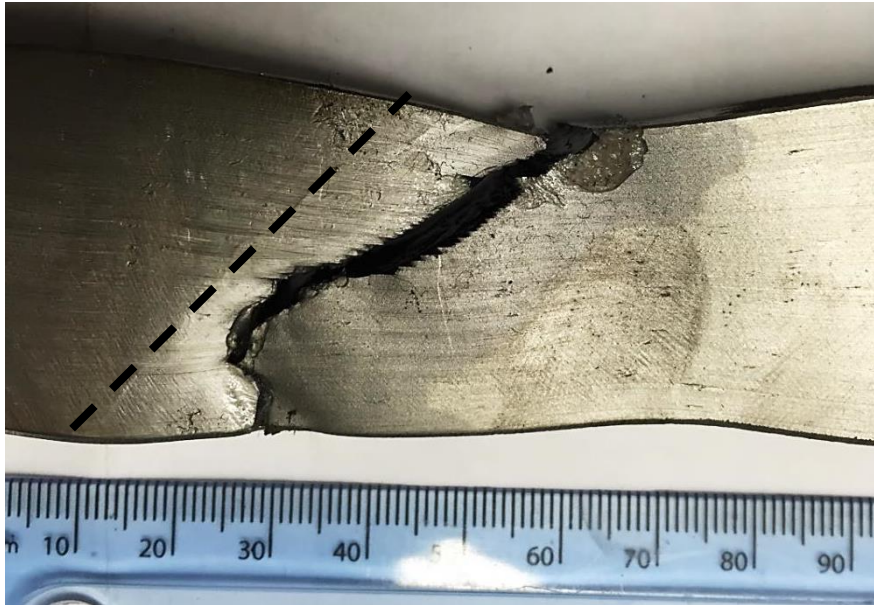
Figure 33: Tensile test of sample 4. The fusion line is marked by a dotted line with weld metal to the left of the dotted line (Material was tested in the service exposed condition and experienced no new thermal conditions prior to testing).

Under closer inspection, this sample failed in the HAZ at a distance from the weld which is consistent with graphite formation as can be seen in Figure 34. Note the fusion line (on the left hand side of the fracture) as well as the step like fracture edge. It will be shown later (in section 3.9 – Metallography) that such steps are indicative of failure due to graphite.
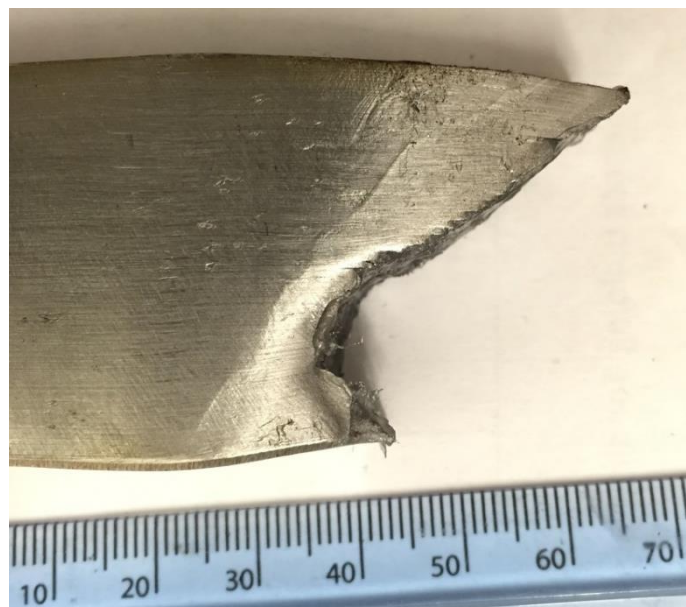
Figure 34: Closer inspection of sample 4 reveals that the weld remains intact however, failure occurred in the HAZ (Material was tested in the service exposed condition and experienced no new thermal conditions prior to testing).

3.5.2. Reduced Section Round Tensile Tests

Two reduced section round tensile tests were machined from each sample (1-4) and tested. The purpose of these tests was to obtain a more accurate result for total reduction in cross sectional area. Table 17 summarises the results of the reduced section round tensile test. For all round tensile specimens, except for one tensile specimen from Sample 3, the reduction in area was between 69 and 74%. The second test from Sample 3 displayed a reduction in area of 44% due to the fracture occurring through a graphitized HAZ.

Table 17: Summary of the reduced section round tensile test results

Sample No.	Yield strength 0.2% offset (MPa)	Tensile strength (MPa)	Reduction in cross sectional area (%)	Location of failure
1	276	407	70	Base material
	302	410	69	Base material
2	297	421	70	Base material
	283	412	71	Base material
3	297	415	70	Base material
	286	412	44	HAZ
4	292	452	74	Base material
	293	447	69	Base material

The stress versus strain graphs for samples 1-4 can be seen in Figure 35.
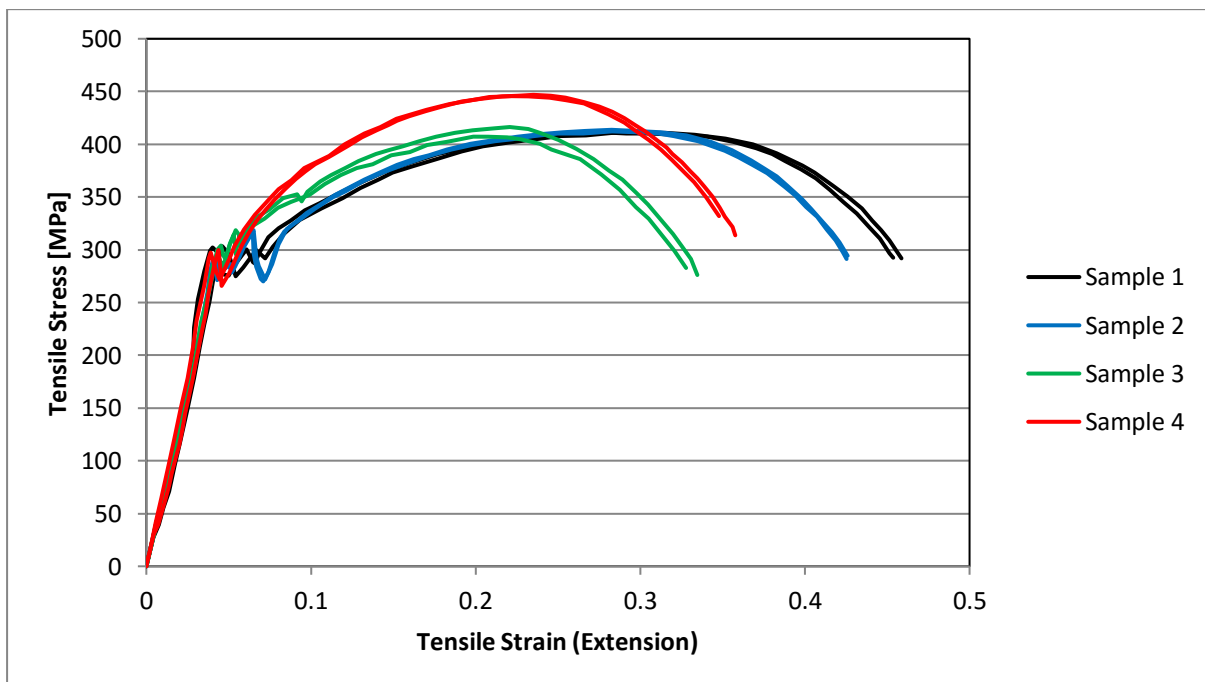
Figure 35: Engineering stress vs. engineering strain graph for the reduced section round tensile test samples 1-4

It can be seen that as with the full section tensile tests, graphite appears to have no effect on the tensile strength of the material. This is demonstrated by sample 4 which failed in the HAZ during the full section tensile tests and failed in the base metal in the reduced section tensile tests. Despite the difference in failure location, there was at most a 4 MPa difference in tensile strength between the HAZ failures and base metal failure, for Sample 4 specifically. This is again demonstrated by sample 3 which experienced one HAZ failure from the round tensile tests and none in the full section tests. The difference in tensile strength between the HAZ failure and base metal failures of sample 3 was at most 7 MPa.

Additionally, there appears to be a significant change in elongation for all the samples when compared to the full section samples. This can be explained as a result of the amount of weld metal that was sampled during the full section and reduced section tensile tests. The reduced section tensile tests have a significantly shorter gauge length than that of the full section samples. Therefore, it can be expected that if the ratio of weld metal to base metal that is sampled during the respective tensile tests change, so will the elongation to failure.

Figure 36 is an image of the reduced section round tensile test of sample 2 after the test was completed. In each case, the sample diameters were measured at 5 mm intervals along the gauge length. One image was superimposed over the graph to illustrate the reduction in area vs. position. This was performed in order to more clearly observe the reduction in cross sectional area versus distance to the fracture surface and locations of the fracture surface (i.e. in base material or HAZ). In all cases, the slight increase in diameter near the centre of the graph is the position of the weld, and indicates that the weld did not plastically deform as much as the base material. The near uniform diameter to the right of the weld corresponds to the uniform elongation of the sample and the final small incline at the extremities of the graph was an indication that the shoulder of the gauge was being measured.
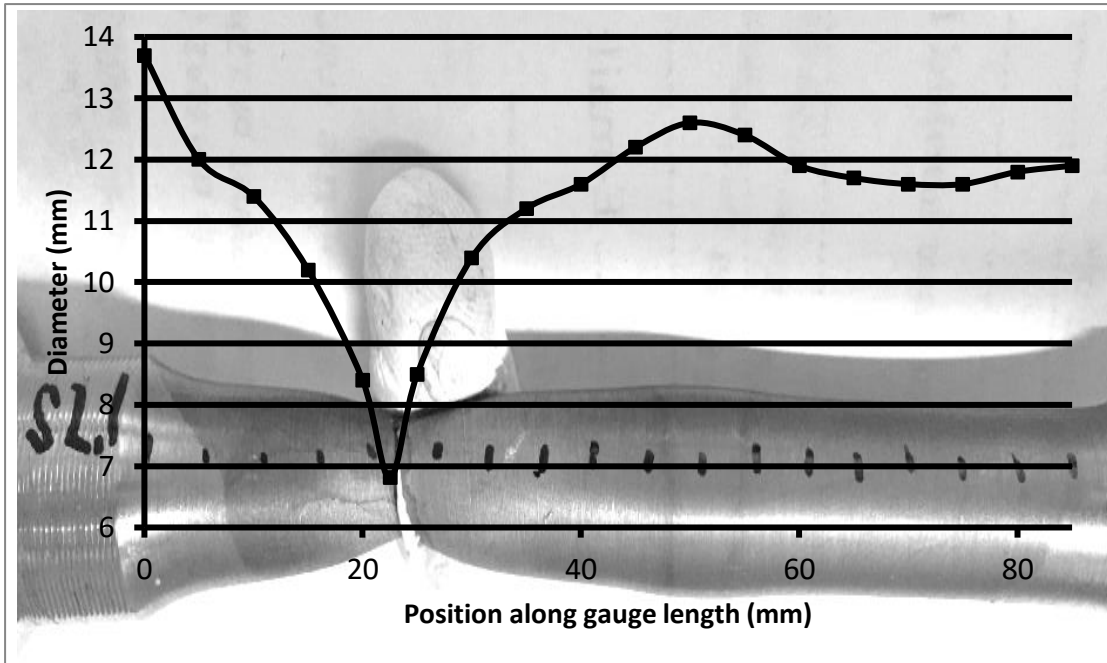
Figure 36: Image of test 1 sample 2 reduced section round tensile sample with diameter readings superimposed. Failure occurred in the base material
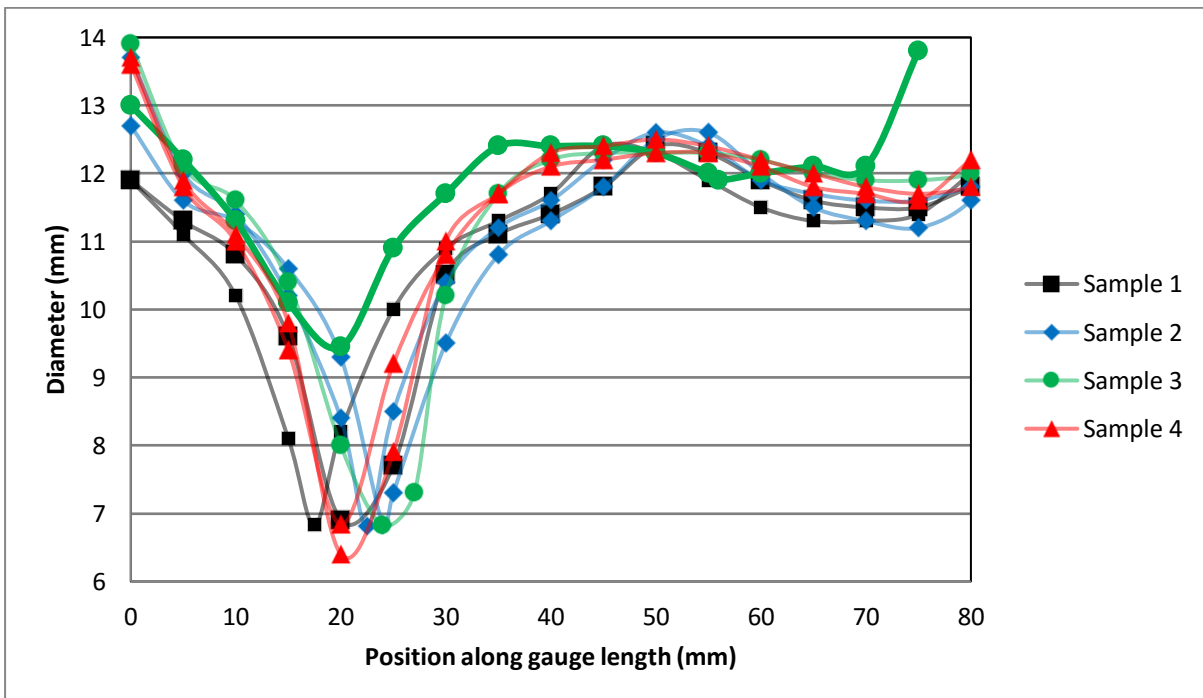
Figure 37: Reduced section round tensile sample diameter readings vs. the position of each reading for all 8 round tensile samples.

3.5.3. Reduced Section Hot Round Tensile Tests

One reduced section hot tensile test was performed for each sample (1-4). The purpose of the test was to gain a more accurate understanding of the tensile properties of the material at its service temperature. The service temperature of the material is currently 417°C while the samples were tested at 420°C. Table 18 summarises the results obtained from the hot tensile test.

Table 18: Summary of the reduced section round hot tensile test results.

Sample No.	Yield strength 0.2% offset (MPa)	Tensile strength (MPa)	Reduction in cross sectional area (%)	Location of failure
1	212	351	78	Base material
2	236	355	76	Base material
3	230	371	77	Base material
4	251	374	78	Base material

Figure 38 is the engineering stress vs. engineering strain graphs of sample 1-4. It was suspected that the reduced section round tensile tests did not fail in the same consistent manner as the full section tensile test samples due to the strain rate being too high. Thus the laboratory was instructed to stop straining the material for a period of five minutes after the sample experienced necking, and if no fracture had occurred by this point, to continue the test until fracture. The test showed that the failure location (base metal or graphitized HAZ) is not dependant on the strain rate when low strain rates are considered. The four straight lines that extend from the x-axis and connect with each respective curve past the tensile strength indicates the elastic strain that was reapplied once each sample was placed under tension for the second time.
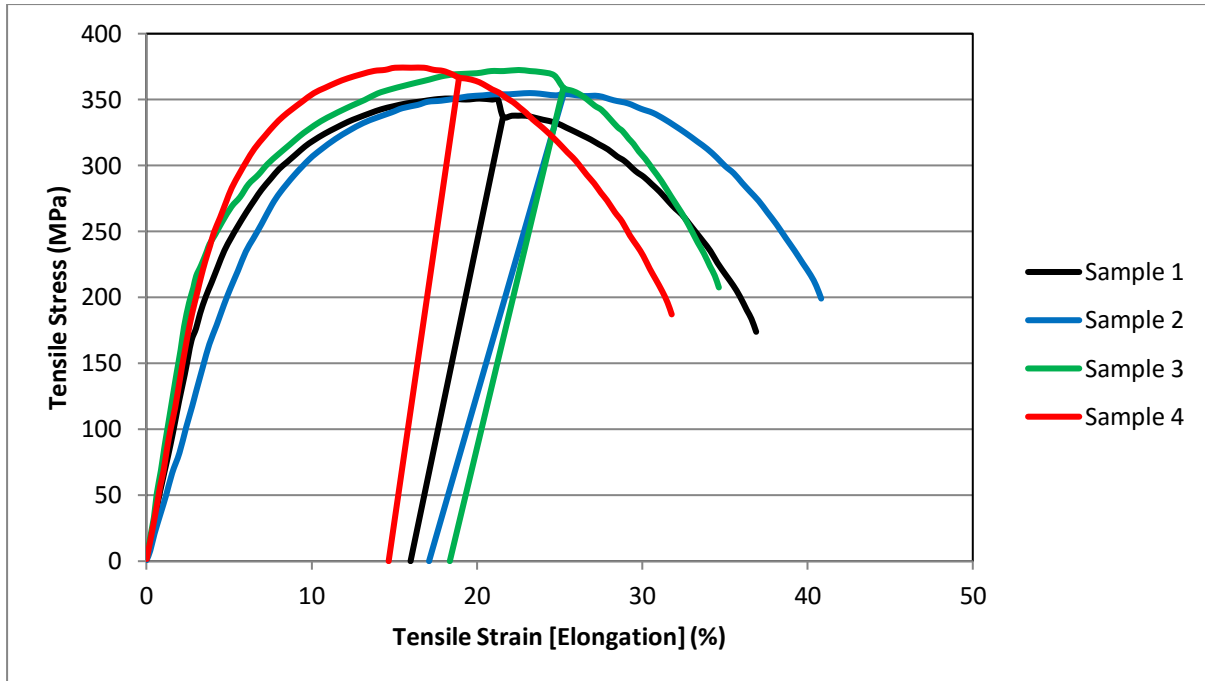
Figure 38: Engineering stress vs. engineering strain for the reduced section round hot tensile test of samples 1-4

3.6.   Bend test

All samples underwent four guided bend tests as prescribed by ASME IX section QW-162 Guided-bend test procedure (2).

All four bend tests performed on material from sample 1 were bent through 180º with three of the four samples showing no cracks or failures. One sample experienced a tear approximately 5 mm away from the root during the test, however this tear was 1 mm in length which is below the maximum allowable defect size of 3 mm during a bend test as specified in ASME IX QW-163 Acceptance Criteria – Bend Tests (See Figure 39). Therefore all samples of material 1 performed satisfactorily in the bend tests.

All four bend tests performed on material from samples 2 to 4 were bent though 180º with no cracks or failures. Therefore all samples of material 2 performed satisfactorily in the bend tests (Figure 40 - Figure 42).
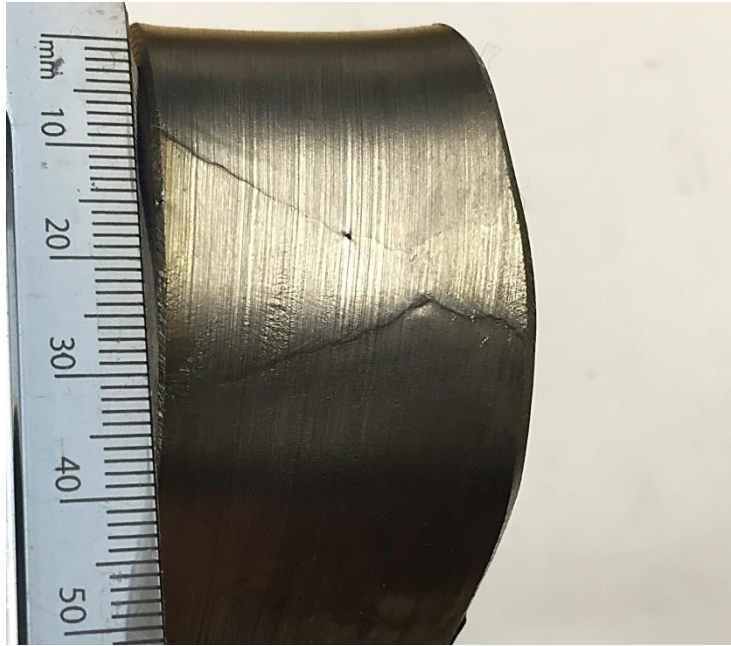
Figure 39: Sample 1 side bend test, face view. Small tear 5 mm away from the root (Heat treated for 579h at 635°C prior to welding and a 672h PWHT at 635°C).
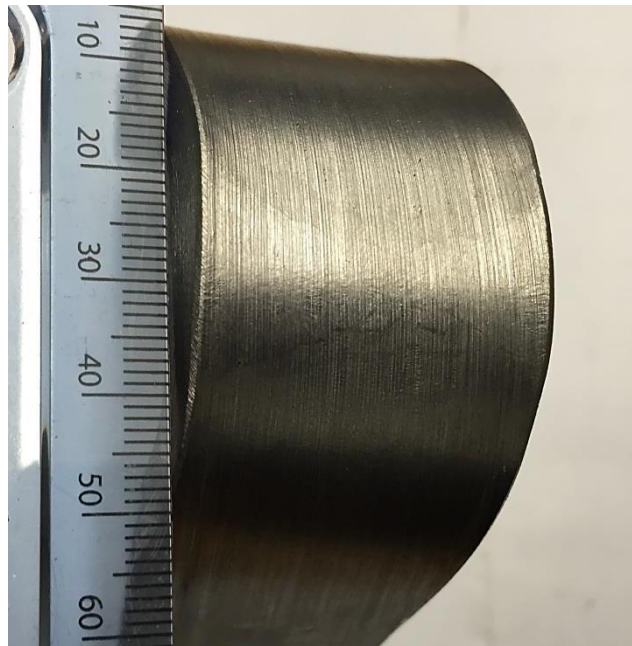
Figure 40: sample 2 side bend test, face view (Heat treated for 579h at 635°C prior to welding and a 12h PWHT at 635°C).
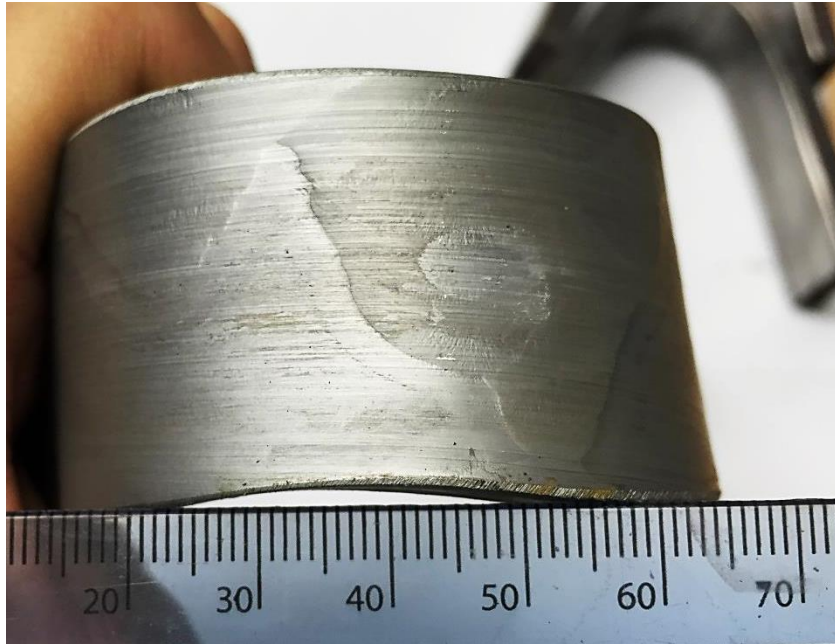
Figure 41: Sample 3 side bend test, face view (No heat treatment prior to welding and a 672h PWHT at 635°C).
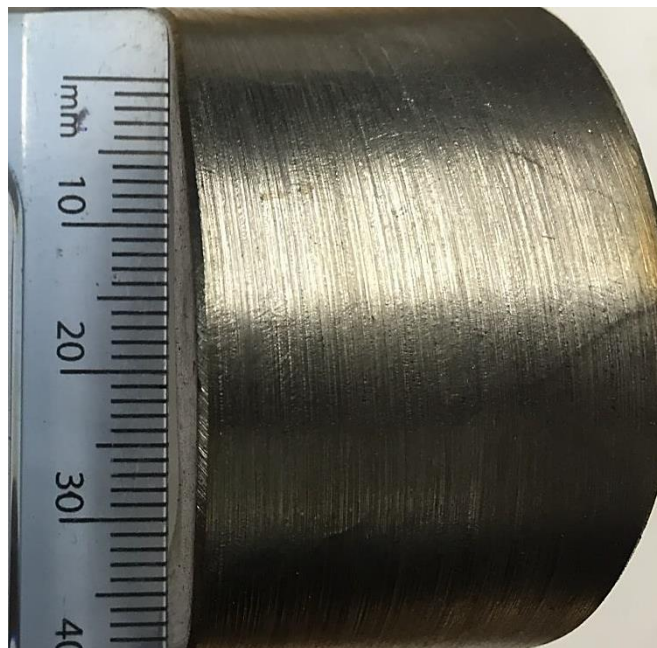
Figure 42: Sample 4 side bend test, face view (Material was welded in the service exposed condition and experienced no new thermal conditions prior to testing).

3.7. Charpy impact test

Six Charpy impact tests were performed per sample; three samples were taken from the weld metal and three samples were taken from the HAZ. All samples were V-notched and tested in the direction transverse to the weld as seen in Figure 43.
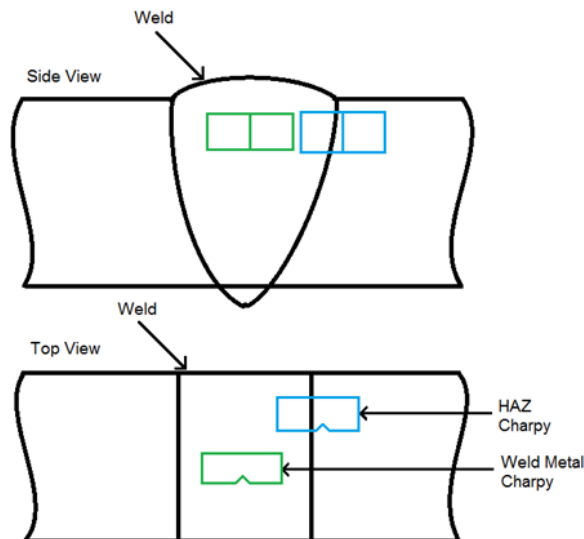
Figure 43: Schematic representation of position and orientation of the Charpy Impact Test samples

Table 19 shows the results obtained from the Charpy impact test.

Table 19: Tabulated results from all the Charpy tests performed

			1	2	3	Average
Sample 1	Weld	Impact toughness (J)	182	252	208	214
		% Shear	90	100	100	
	HAZ	Impact toughness (J)	104	90	104	99
		% Shear	80	70	70	
Sample 2	Weld	Impact toughness (J)	293	268	268	276
		% Shear	100	100	100	
	HAZ	Impact toughness (J)	96	82	136	105
		% Shear	70	60	70	
Sample 3	Weld	Impact toughness (J)	264	272	260	265
		% Shear	100	100	100	
	HAZ	Impact toughness (J)	220	182	176	193
		% Shear	100	100	100	
Sample 4	Weld	Impact toughness (J)	102	134	118	118
		% Shear	60	70	70	
	HAZ	Impact toughness (J)	170	140	140	150
		% Shear	90	90	80	

In all newly welded sample (1-3) the weld metal displays better toughness characteristics than that of the base metal. Sample 4 is the only sample that deviates from this trend and can most likely be attributed to the ±35 years of in-service degradation that has occurred.

3.8.   Hardness test

The purpose of the hardness tests was to determine whether or not there were any abnormalities in hardness caused by the graphitization that could indicate a possible future graphitization site. All four samples were tested using the Vickers hardness test. Each sample was tested up to 5 mm into the weld metal and then up to 10 mm into the base material. Table 20 shows the results from the Vickers hardness tests for the base metal and Table 21 shows the test results for the HAZ of each sample, where samples were tested using a spacing of 1mm and a load of 2kg (HV_2). No indentations were closer than 3 indentation diameters to one another in order to avoid interference between adjacent indentations.

Table 20: Vickers hardness test results for the hardness of the base metal of each sample tested (30 hardness measurements per sample)

Sample No.	Average Base Metal Hardness (HV)	Maximum Hardness	Minimum Hardness	Standard Deviation of the Sample	95% C.I
1	114	138	105	114 ± 9	114 ± 3
2	115	127	108	115 ± 4	115 ± 2
3	122	149	113	122 ± 9	122 ± 3
4	138	173	122	138 ± 11	138 ± 4

Table 21: Vickers hardness test results for the hardness of the HAZ of each sample tested (15 test points per sample)

Sample No.	Average HAZ Hardness (HV)	Maximum Hardness	Minimum Hardness	Standard Deviation of the Sample	95% C.I
1	124	134	115	124 ± 5	124 ± 3
2	130	154	118	130 ± 11	130 ± 6
3	134	147	117	134 ± 10	134 ± 5
4	158	170	146	158 ± 7	158 ± 4

The hardness results are well within acceptable ranges and therefore it can be concluded that the graphite did not have any deleterious effect on the bulk material hardness.

In an effort to determine whether graphite contributed any strength to the matrix, the hardness of the graphite nodules were measured using the Vickers hardness test with a 10 g load. The results can be seen in Table 22.

Table 22: Vickers hardness HV$_{0.01}$ test results for the hardness of graphite nodules of sample 4 (5 test points)

Sample No.	Average Graphite Hardness (HV)	Maximum Hardness	Minimum Hardness	Standard Deviation of the Sample	95% C.I
4	33	39	27	33 ± 5	33 ± 4

As can be seen, the hardness of the nodules is extremely low and it is highly likely that the soft phase that is observed in these nodules is graphite. Additionally, no real strength can be expected (in terms of tensile strength) to be contributed to the steel by these nodules.

Figure 44 to Figure 47 shows the hardness profiles of the four samples as indicated by each respective accompanying schematic. The legend in the graph also makes reference to important points with respect to the data plotted on the graph.
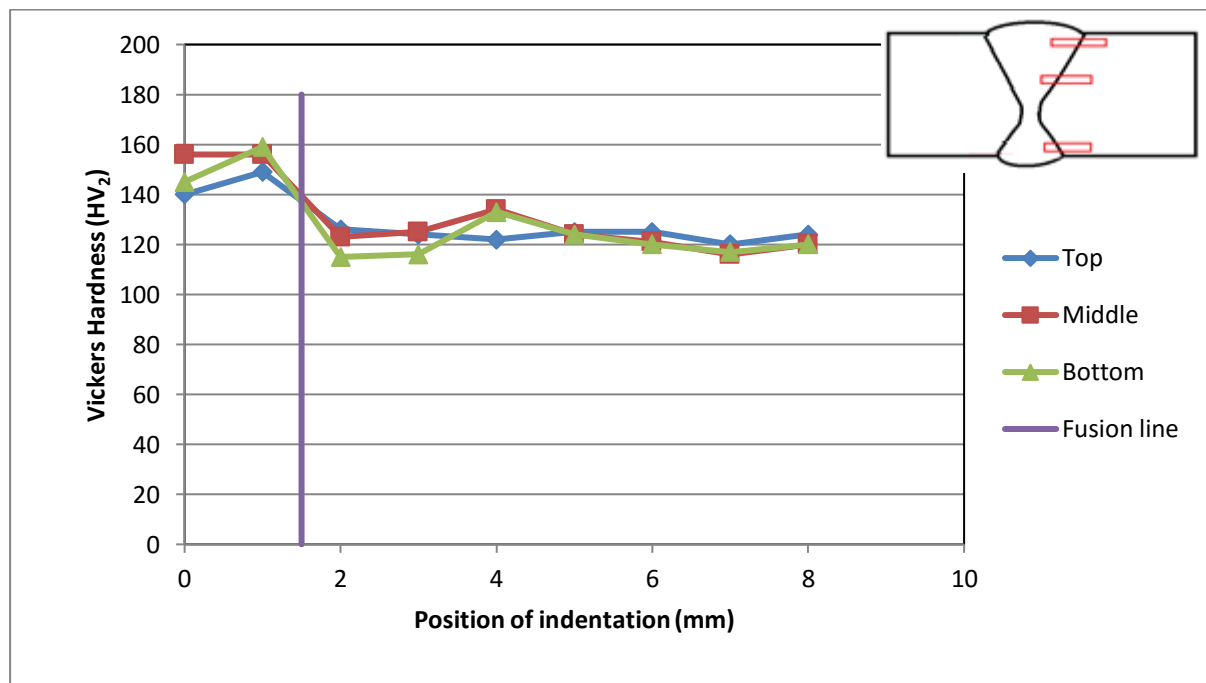
Figure 44: Hardness profile of sample 1 across the regions indicated in the schematic at the top right hand side of the graph. Note that the vertical line indicates the position of the fusion line. The weld metal is to the left of the fusion line.
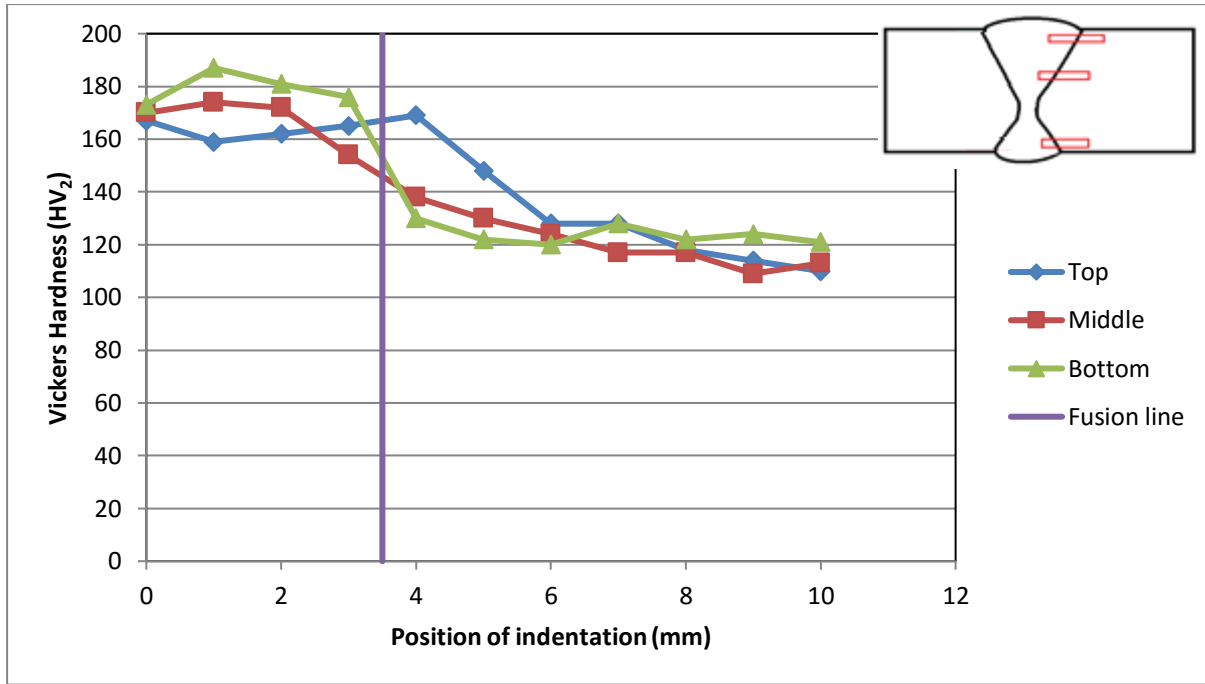
Figure 45: Hardness profile of sample 2 across the regions indicated in the schematic at the top right hand side of the graph. Note that the vertical line indicates the position of the fusion line. The weld metal is to the left of the fusion line.
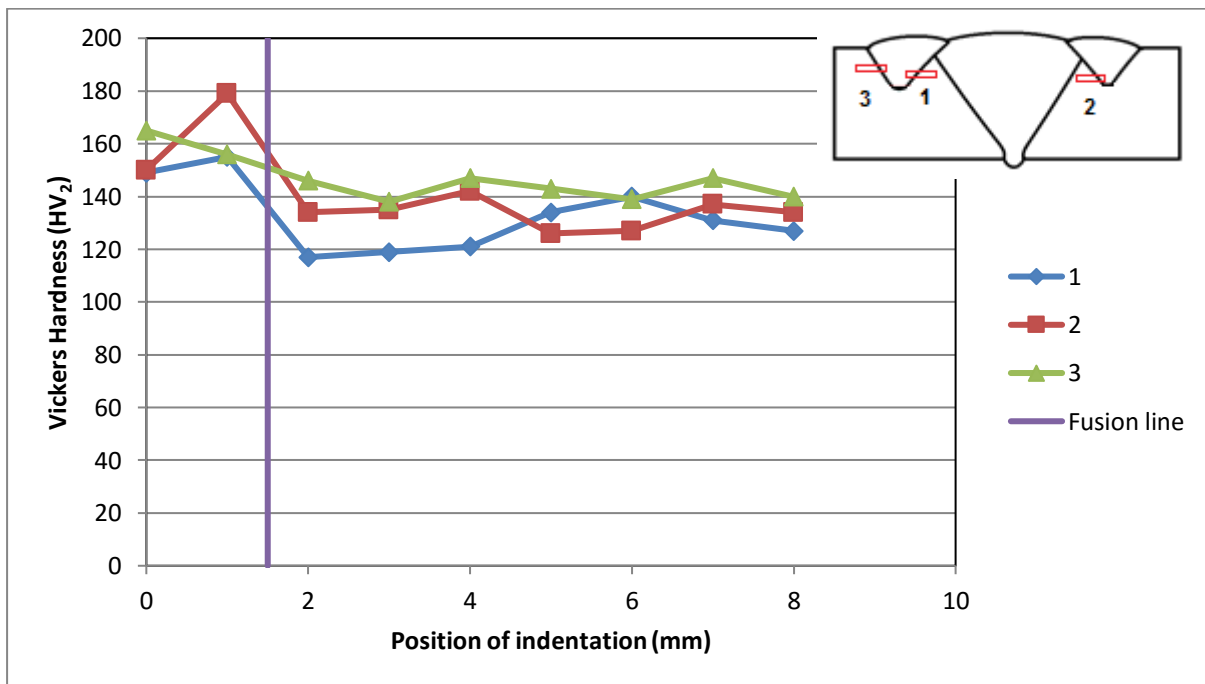
Figure 46: Hardness profile of sample 3 across the regions indicated in the schematic at the top right hand side of the graph. The weld metal is to the left of the fusion line.
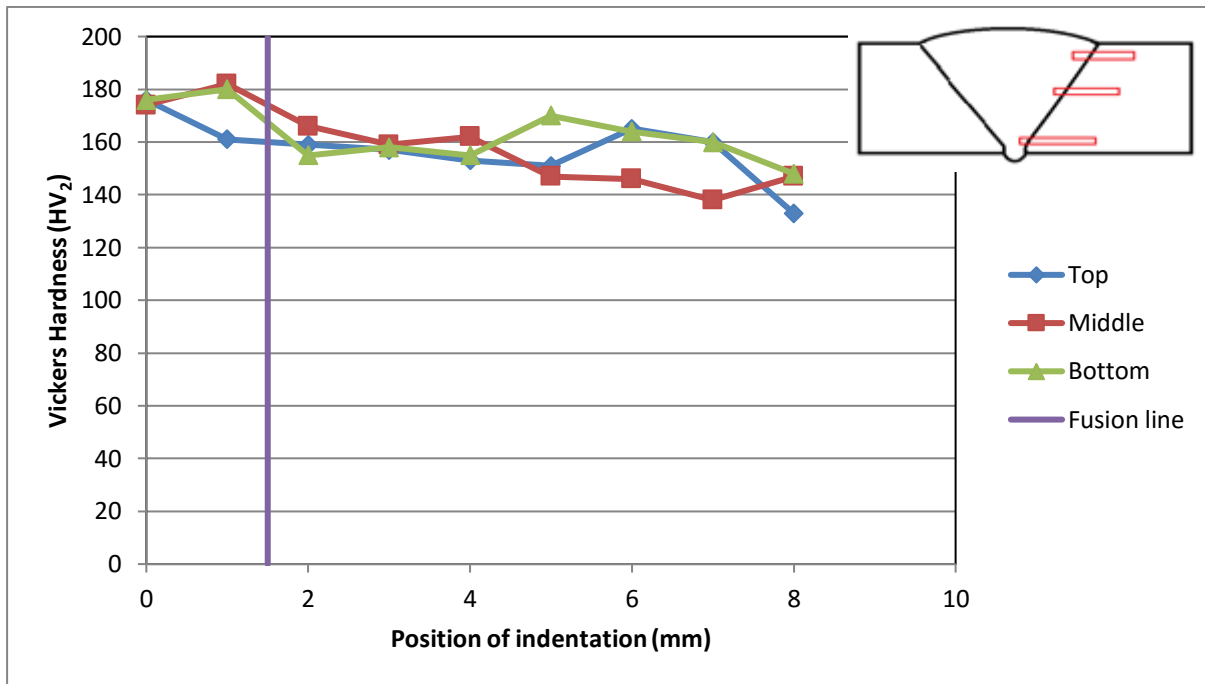
Figure 47: Hardness profile of sample 4 across the regions indicated in the schematic at the top right hand side of the graph. Note that the vertical line indicates the position of the fusion line. The weld metal is to the left of the fusion line.

3.9.   Metallography

Table 23 details the samples that were observed and which techniques were used to do so. The full section tensile fracture surface was considered to be the test that would most accurately represent the behaviour of the entire welded joint and therefore both the fracture surface as well as a polished cross section of the fracture surface was evaluated using a SEM and light microscope, while a stereoscope was used for the fracture surface as well. Only samples that displayed abnormalities in subsequent tests were also analysed. Thus, the reduced section round tensile samples 3 and 4 were analysed using all three techniques due to the unexpected HAZ failure of the reduced section round tensile sample 3 and the absence of HAZ failure in sample 4. Due to no HAZ failures in the reduced section round hot tensile tests, sample 3 and 4 were again analysed using all techniques.

Please take note of the following pertaining to Table 23:

- 'Round tensile' refers to the reduced section round tensile samples
- 'Hot round tensile' refers the reduced section hot round tensile samples
- 'FS' refers to fracture surfaces

'PCS' refers to polished cross sections.

Table 23: list of microscopic evaluations used to analyse the samples

Weld sample	Test sample	Analytical technique		
		Stereoscope	Light microscope (Polished section)	Scanning electron microscope
Sample 1	Full section tensile sample	FS	PCS	FS PCS
	Full section tensile sample HAZ	None	PCS	PCS
	Round tensile sample	FS	None	None
	Hot round tensile sample	FS	None	FS
	Charpy impact sample	FS	None	None
Sample 2	Full section tensile sample	FS	PCS	FS PCS
	Full section tensile sample HAZ	None	PCS	PCS
	Round tensile sample	FS	None	None
	Hot round tensile sample	FS	None	FS
	Charpy impact sample	FS	None	None
Sample 3	Full section tensile sample	FS	PCS	FS PCS
	Full section tensile sample HAZ	None	PCS	PCS
	Round tensile sample	FS	None	PCS
	Hot round tensile sample	FS	PCS	FS PCS
	Charpy impact sample	FS	None	None
Sample 4	Full section tensile sample	FS	PCS	FS PCS
	Full section tensile sample HAZ	None	PCS	PCS
	Round tensile sample	FS	None	PCS
	Hot round tensile sample	FS	None	FS PCS
	Charpy impact sample	FS	None	None

The model of stereoscope that was used was the Olympus SZX7 and the model of light microscope used was the Olympus BX51M. The model of scanning electron microscope that was used was the Zeiss Crossbeam540 Ultra High resolution FEC. This particular SEM is able to use extremely low acceleration voltages, and as a result of this, the beam penetration depth into the material is greatly reduced. By using low acceleration voltages and reducing the penetration depth, the resolution of secondary images was greatly increased (40).
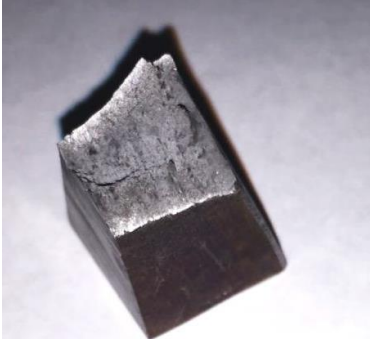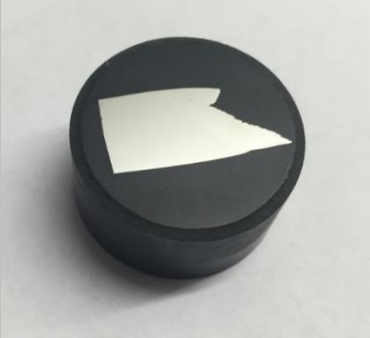
Several micrographs appear to be severely scratched. These micrographs appear so for two reasons:

1. Very high magnification images (50,000 – 75,000X magnification) tend to pronounce metallographic sample preparation imperfections.

In general, metallographic samples are viewed in a SEM at acceleration voltages ranging from 10 – 20 kV which result in the electrons penetrating 1-3 μm into the sample generating a smoothed micrograph. At an acceleration voltage of 1 kV (the typical acceleration voltage used in most of the SEM images in the following sections) an electron penetration depth of several nanometres is achieved. This results much more topographical information and therefore revealing the very fine metallographic sample preparation imperfections on a polished sample surface.

Table 24 was constructed to clarify the terms used in the subsequent sections. 'Fracture surface' refers to the viewing of the rough fracture edge where the crack formed that ultimately led to the failure of the sample. 'Polished cross section of the fracture surface' refers to a smooth polished surface that has been mounted and is viewed in a direction that is perpendicular to the viewing direction of the 'fracture surface' samples.

Table 24: Graphical representation of the terms used in the metallography section

85

3.9.1. Guidelines for the interpretation of the metallographic images

This section discusses observations that were used to identify phases within the microstructure, orientation of the sample and plastic strain directions for plastically deformed samples.

It is generally accepted that the phases in order of decreasing hardness are as follows: iron carbide, ferrite, and lastly graphite. Thus, when polished cross sections are observed under high magnification, the phases that contain the deepest and highest concentration of scratch marks were likely to be graphite, while the phase that contains the most shallow and fewest scratch marks were likely to be iron carbides as seen in Figure 48.
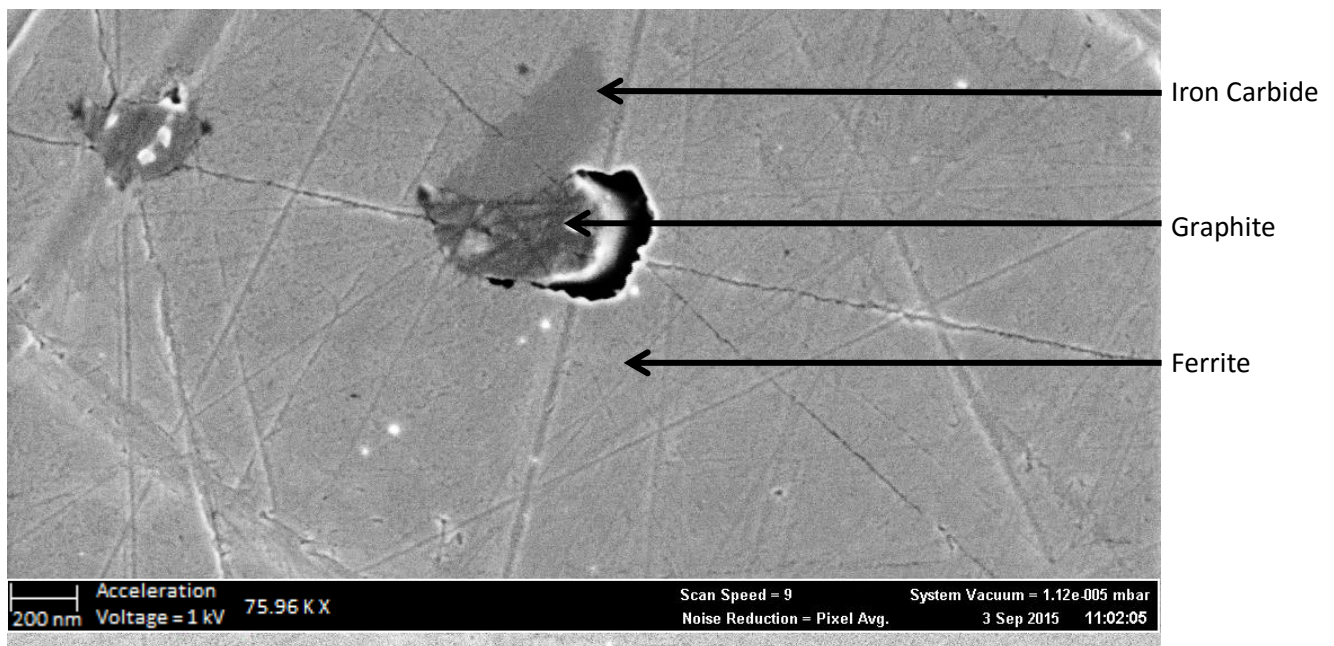
Figure 48: SEM image of a polished cross section from the full section tensile test of sample 3 near the weld. This image illustrates the effects of hardness of individual phases on the depth and number of observed scratch marks under an original magnification of approximately 76 000 X using the inlens detector.

Larger graphite nodules in polished cross sections can easily be identified using a SEM by looking for the characteristic layers of graphite that tend to form in layers or plates as seen in Figure 49 (left hand image). Only large graphite nodules can be observed using a light microscope, and appear as black marks in the microstructure as seen in Figure 49 (right hand image).
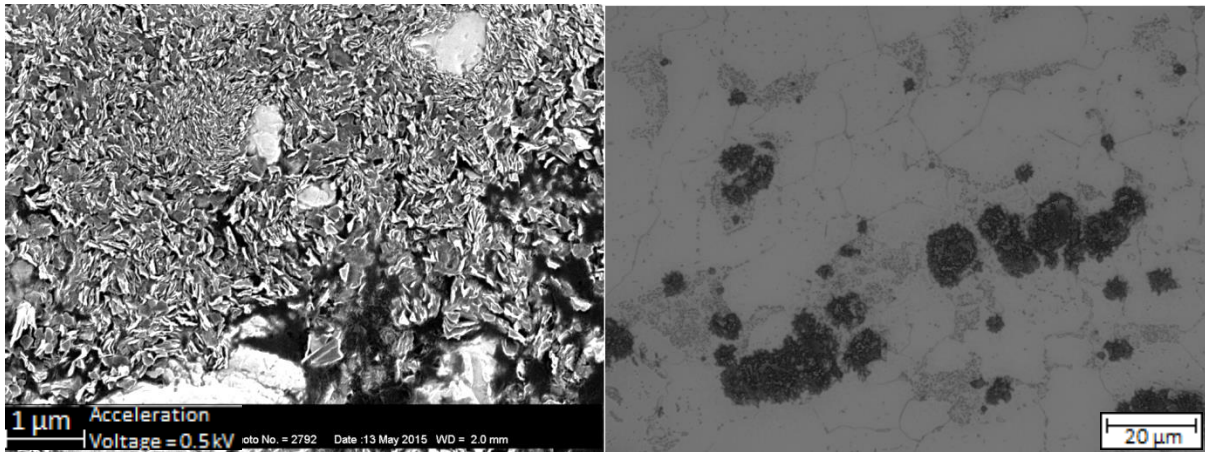
Figure 49: SEM image of graphite displays the layer formation of graphite in sample 4 which was left in the service exposed condition (Left). Graphite is observed black marks in the microstructure when using an optical microscope (Right).

When samples that have been tensile tested, and samples have been prepared from the material after testing, graphite nodules will no longer assume a generally round shape, but rather elongate in the direction of the tensile load as seen in Figure 50.
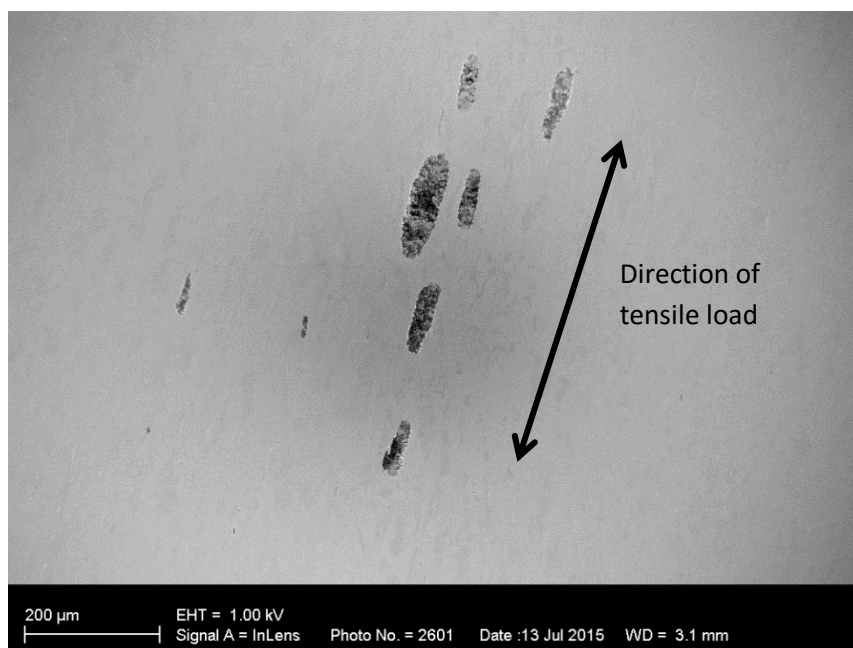
Figure 50: SEM image of elongated graphite nodules of the full section tensile test of sample 4. The direction of elongation indicates the direction of the tensile load (indicated by arrow).

Figure 51 compares the use of the InLens detector and the Secondary electron (SE) detector on the SEM. It can be seen that the SE detector shows greater depth of field which is used when the topography of a sample is important. Therefore this detector adds value to fracture surface analysis while is it does not provide much added value when observing unetched polished samples. The InLens detector provides little to no depth of field, however is exceptionally good at distinguishing differences in materials. Therefore this detector is used when it is important to distinguish between different phases that are present in the material.
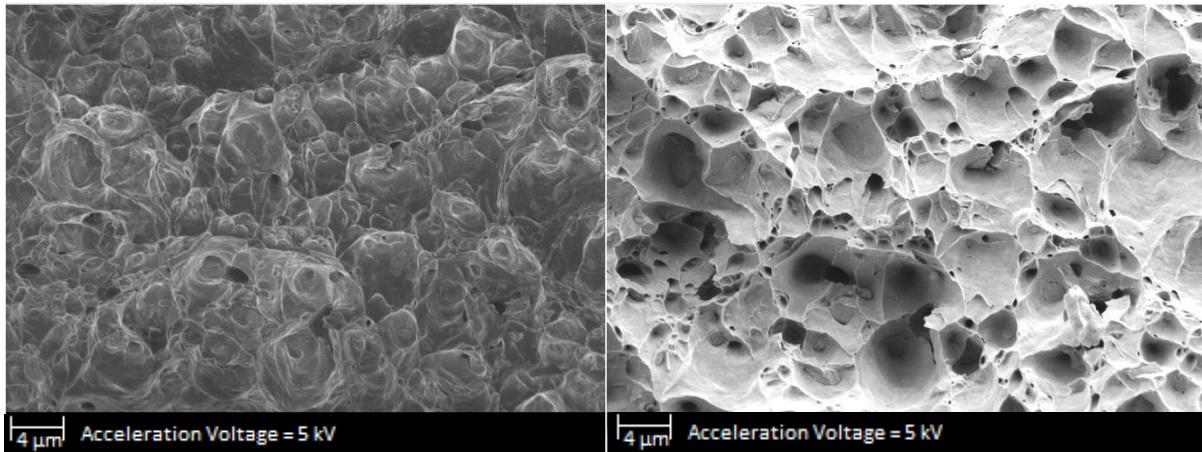
Figure 51: SEM image of the fracture surface of the tensile sample of sample 3. Image is of the same location and all parameters are the same. Left image was taken using the InLens detector while the right image was taken using the Secondary electron detector. (No heat treatment prior to welding and a 672h PWHT at 635°C).

3.9.2. General observations

Using a light microscope it was possible to inspect a polished section of the tensile fracture surfaces. The light microscope revealed that the prolonged exposure to elevated temperatures that was experienced by sample 1 (and all other samples that experienced prolonged exposure in excess of 600 hour at 635°C) had either spheroidized, or graphitized all the carbides that were previously present in the microstructure as pearlite. Figure 52 shows that the structure has fully spheroidized.
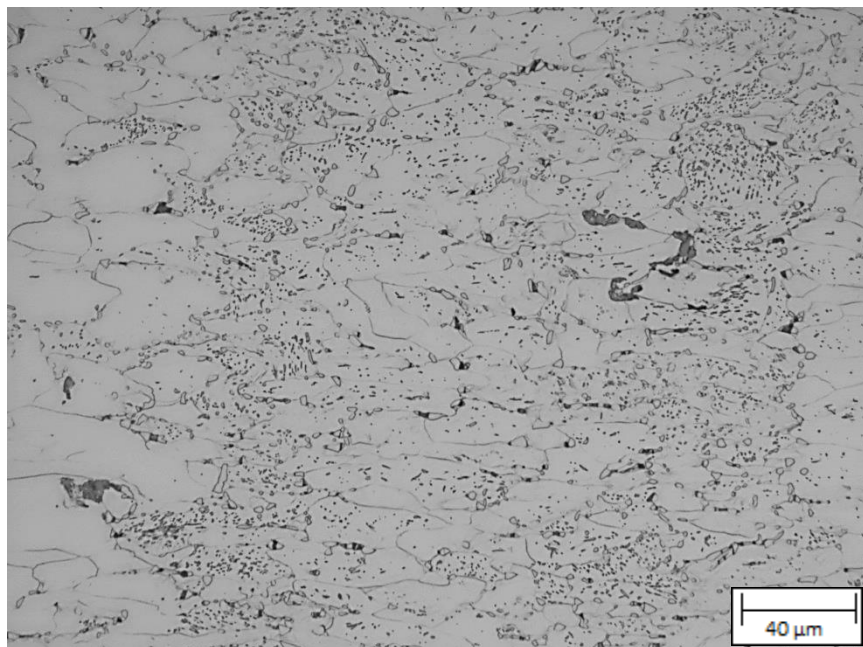
Figure 52: Light microscope image of the microstructure of sample 1 far from any fracture surfaces where the applied tensile load was applied in a horizontal direction in the case of this image (Heat treated for 579h at 635°C prior to welding and a 672h PWHT at 635°C).

Several polished cross sections of weld and HAZ material from the full section tensile test that remained intact was inspected using a SEM. It was discovered that all samples contained very narrow

88

unidentified inclusions (particles smaller than 1 µm in width) that appeared elongated in shape, often 10-20 times their width in length. All the elongated particles were orientated in the same direction within each sample, and aligned with the rolling direction. Figure 53 shows the elongated phase that formed adjacent to a dark phase in the polished section. The shape of the particle could be due to plastic deformation that occurred during the tensile test or during original forming. Closer inspection of the scratch marks present reveal that the elongated particle is soft due to the deep scratch marks. The light phase that makes up the bulk of the image is ferrite while the darker phase adjacent to the inclusion particle is most likely cementite due to the relatively shallow scratch marks in this phase. The shallow scratch marks indicate that this adjacent phase has high hardness; this is consistent with the characteristics of cementite.
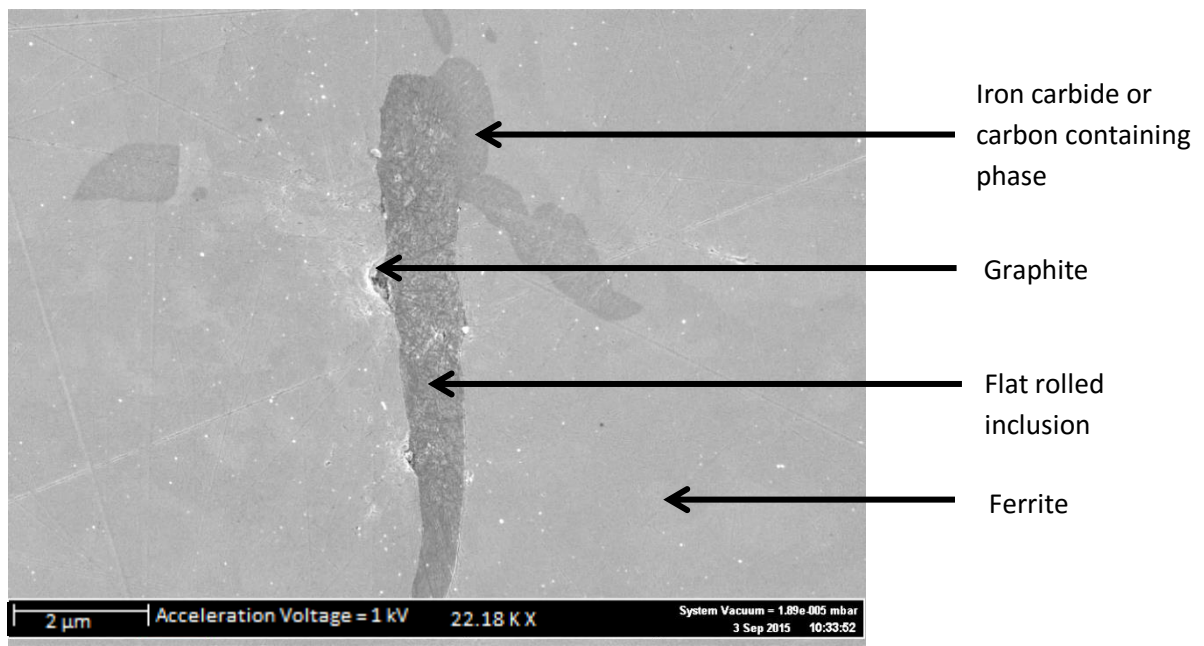
Figure 53: Elongated graphite particle contacting a phase that is darker than the matrix from sample 1 full section tensile test. (Heat treated for 579h at 635°C prior to welding and a 672h PWHT at 635°C)

It was considered advantageous to attempt to liberate the graphite particles from the matrix through chemical etching in order to observe the graphite shape more precisely. Because graphite is substantially more acid resistant than ferrite, a 3% Nital solution was used to etch the sample. The sample was immersed in Nital for approximately 5 minutes and not swabbed in order to prevent the graphite particles from dislodging or being damaged due to mechanical action. Once the etching process was completed, the sample was observed under the SEM. Figure 54 shows an elongated particle as seen in Figure 53, and this strengthens the argument that these particles are inclusions.

Figure 54: Inclusion from sample 4 reduced section round tensile test (Tested in the As-received condition) that was revealed by etching with 3% Nital for 5 minutes.

In all observed cases of samples that fractured through the HAZ graphite, it was noted that not only the quantity, but also the size of the graphite nodules present on the fracture surface was large. This can be seen in Figure 55 and Figure 56.
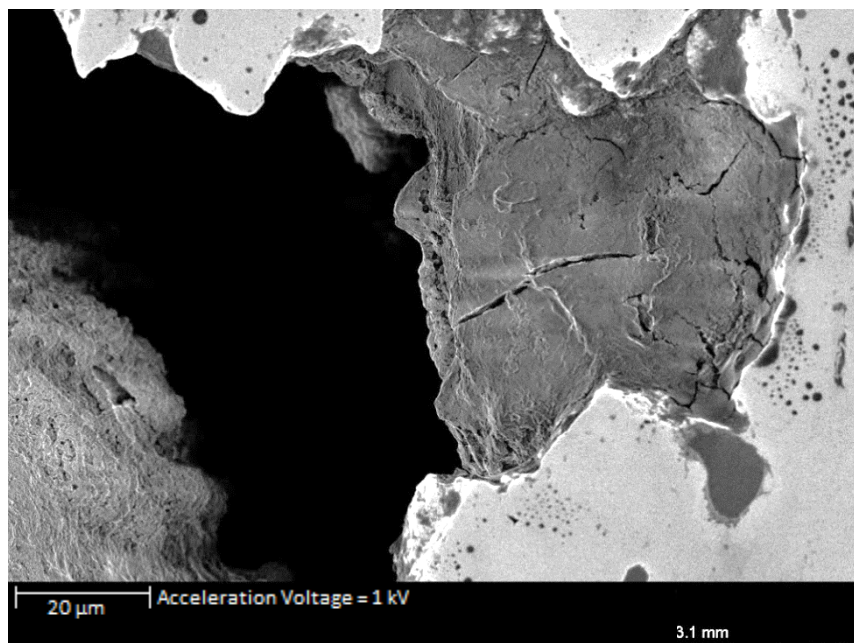
Figure 55: SEM image of a large graphite particle present on the fracture surface from the full section tensile test of sample 4 (Material was tested in the service exposed condition and experienced no new thermal conditions prior to testing).
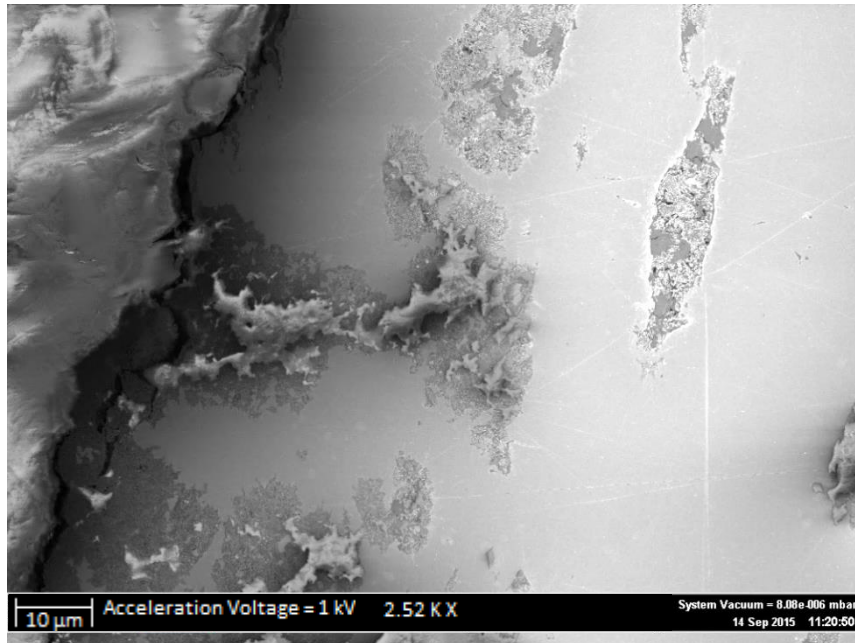
Figure 56: SEM image of the polished fracture surface of the reduced section tensile test of sample 3. The left lower region of the image displays the fracture surface containing graphite (No heat treatment prior to welding and a 672h PWHT at 635°C).

Figure 57 shows graphite growing on ferrite-ferrite grain boundary regions. This indicates that graphite may grow on the ferrite-ferrite grain boundaries.
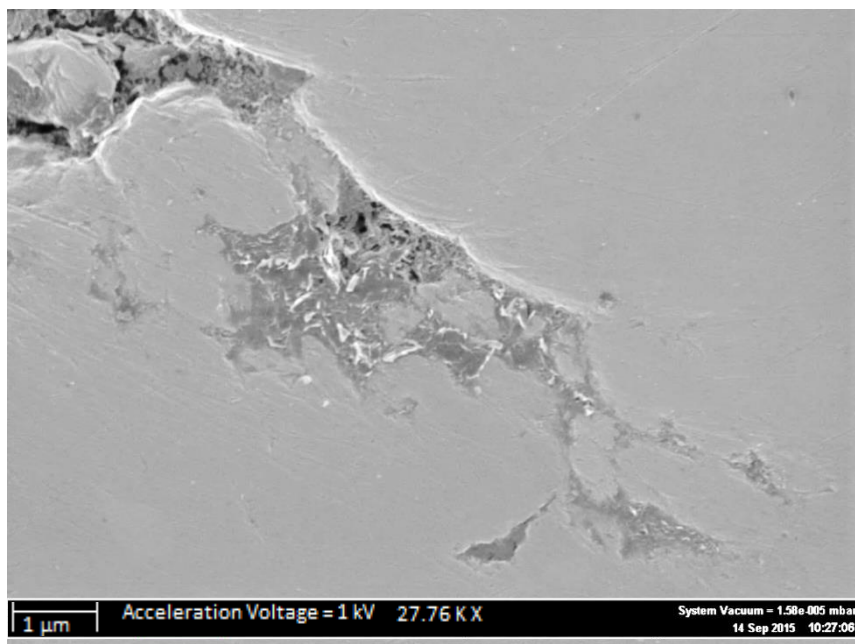
Figure 57: SEM image of grain boundary graphite forming on ferrite-ferrite grain boundaries in the polished reduced section tensile test of sample 4 (Material was received in the as welded condition and experienced no new thermal conditions prior to testing).

The following sections (labelled sample 1 – sample 4) will discuss sample specific details.

91

Sample 1

Full section tensile test sample (Fracture surface)

Stereoscopic evaluation of the full section tensile test fracture surface revealed a relatively high fraction of graphite. The particles were randomly distributed across the fracture surface. There was no evidence of 'chaining' where a continuous line or chain of graphite formed to generate a preferential failure direction. The fracture surface can be seen in Figure 58.
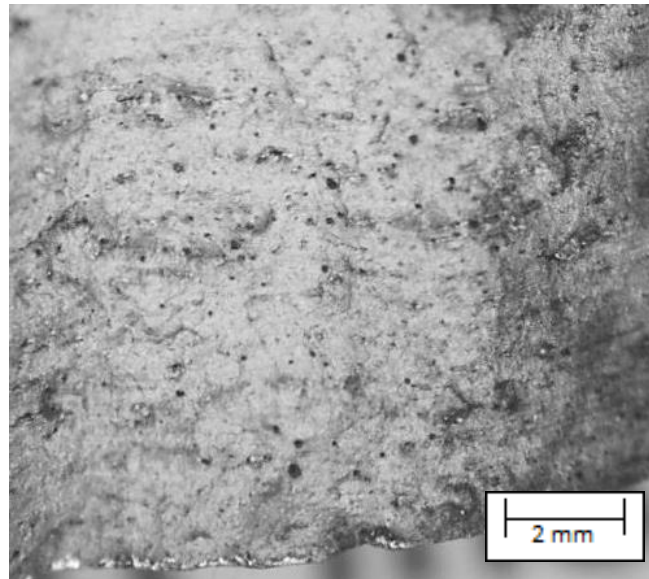
Figure 58: Stereoscopic image of the ductile fracture surface of the full section tensile test sample 1. The surface contains an appreciable amount of graphite which can be identified as the black dots in the image (Heat treated for 579h at 635°C prior to welding and a 672h PWHT at 635°C)

ImageJ was used to determine the percentage of the fracture surface that was covered in graphite. The binary black and white image that resulted from this can be seen in Figure 59. In Figure 59, the black areas of the image indicate areas of the fracture surface that is covered in graphite while the white areas are graphite free areas. The total percentage of graphite that is present on the part of the fracture surface presented in this image is 6%.
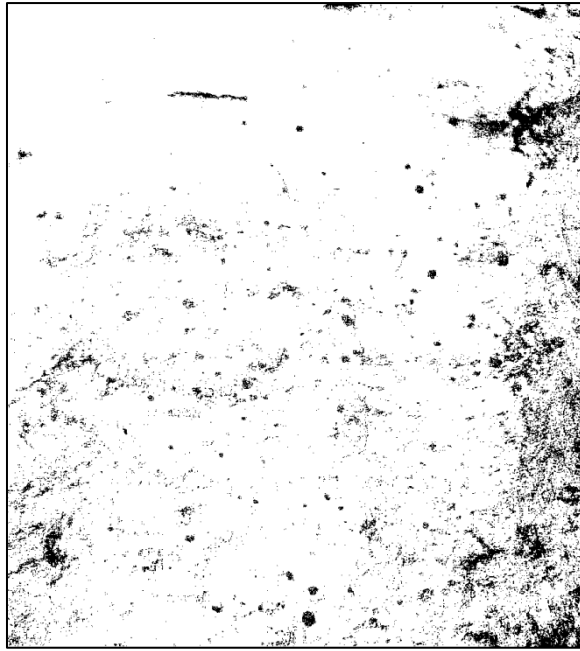
Figure 59: Processed stereoscopic image of the ductile fracture surface of tensile sample 1 using ImageJ to determine the percentage graphite present on the fracture surface. (Heat treated for 579h at 635°C prior to welding and a 672h PWHT at 635°C)

The polished section of a tensile sample also revealed that the graphite particles change shape due to plastic deformation that occurred during the tensile test. All particles previously displayed a roughly circular shape prior to tensile deformation however after the plastic deformation occurred, all the graphite particles appear oval in shape with the ovals being elongated in the direction of the tensile load as can be seen in Figure 60. The dark bands that run in the near vertical direction are as a result of the combination of strain experienced by the sample during the tensile test (known as strain lines), and of the ferrite pearlite microstructure being revealed by the etchant.
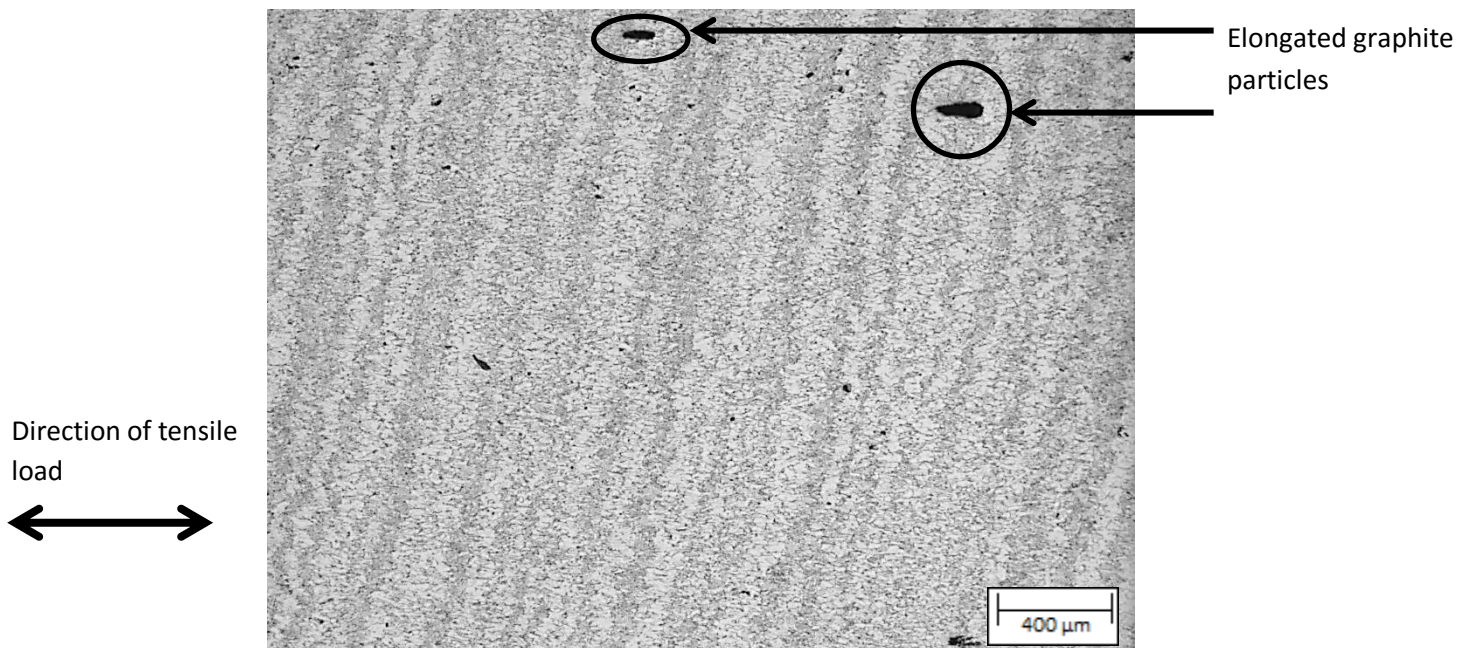
Figure 60: Light microscope image of elongated graphite particles from near the fracture surface of the tensile test of sample 1(Heat treated for 579h at 635°C prior to welding and a 672h PWHT at 635°C). The applied load from the tensile sample was orientated in the direction parallel to the elongated sides of the graphite particles. The banding observed is an etching effect as a result of plastic deformation and will be referred to as 'stain lines'.

Observation of the polished tensile fracture surface in Figure 61 shows that while there are several isolated graphite particles that form part of the fracture surface, there is no evidence of graphite chains that allow cracks to grow in a preferred direction. Additionally, there are even some graphite particles near to the fracture surface (indicated by an arrow on Figure 61) that the crack did not travel through.
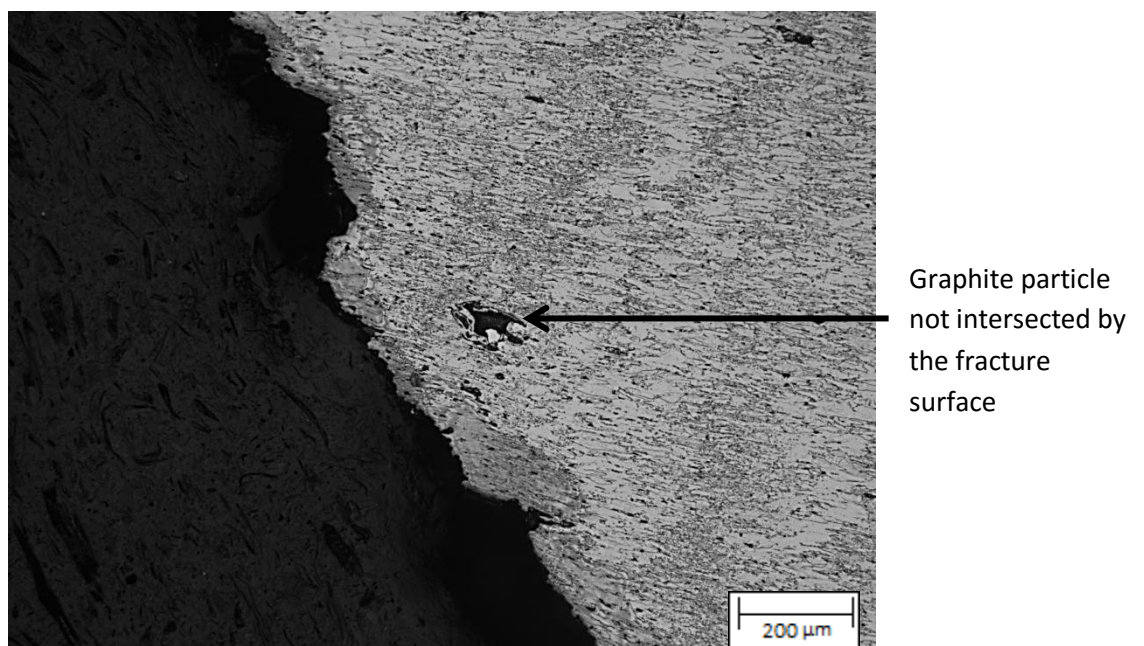
Figure 61: Light microscope image of the tensile fracture surface of sample 1 (Heat treated for 579h at 635°C prior to welding and a 672h PWHT at 635°C).

94

By making use of a high resolution Scanning Electron Microscope (SEM), it was possible to clearly observe the features of the graphite particles. Figure 62 shows that the colonies tend to form in roughly circular geometries where graphite 'cones' grow off of a steel wall so that the tips of the cones face inwards towards the centre of the graphite particle. Furthermore the individual particles within a graphite colony are not connected to one another after tensile fracture.
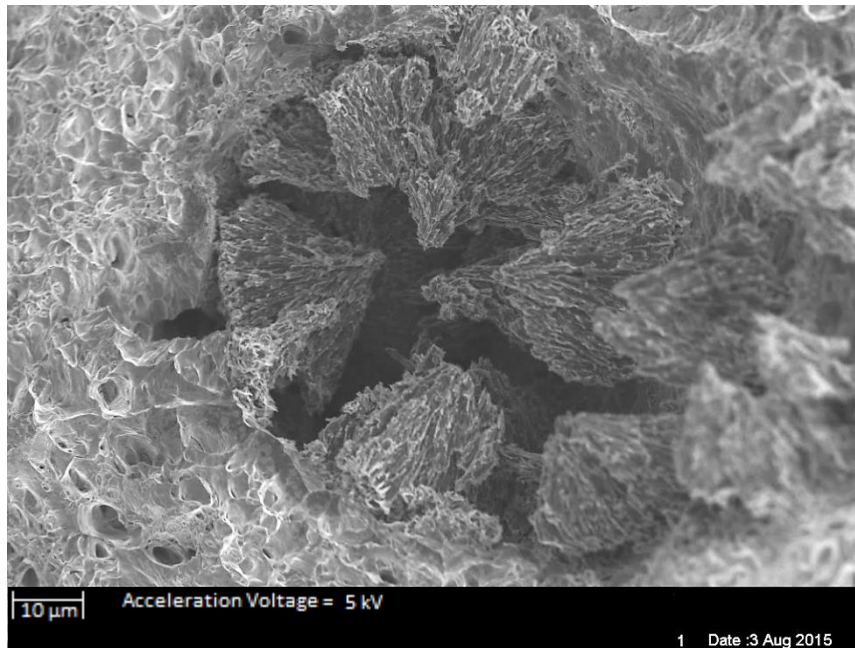
Figure 62: SEM image of graphite particle from the tensile fracture surface of sample 1 (Heat treated for 579h at 635°C prior to welding and a 672h PWHT at 635°C).

Closer inspection of the fracture surface using a SEM revealed further evidence of a ductile tearing with the characteristic dimpled surface when viewed under high magnifications as can be seen in Figure 63 which are possibly associated with non-metallic inclusions.
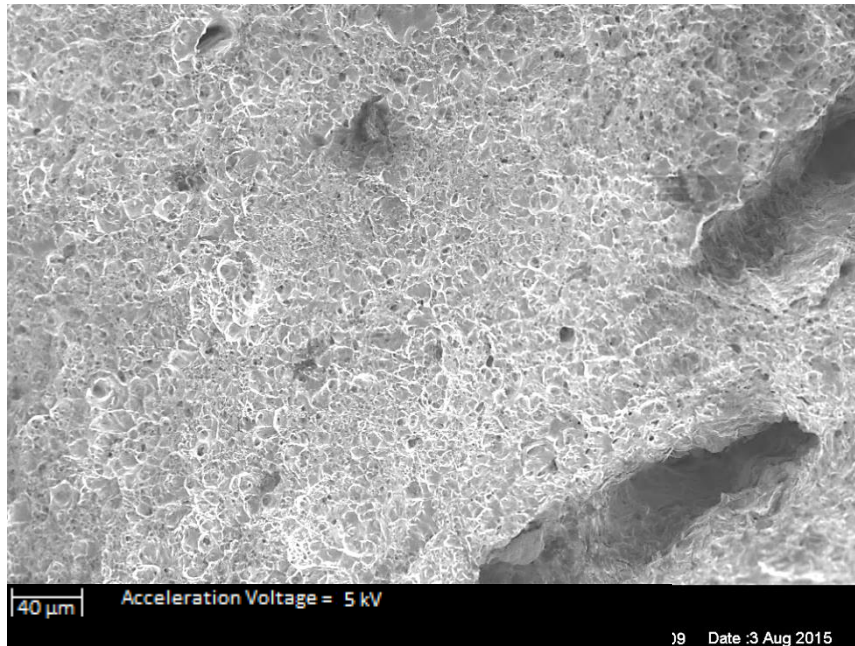
Figure 63: SEM image of the tensile fracture surface of sample 1. The surface displays a dimpled surface finish which is characteristic of ductile fractures (Heat treated for 579h at 635°C prior to welding and a 672h PWHT at 635°C).

Linear features were also observed, however it was concluded that no graphite was present in these locations and therefore the graphite present in the material played no role in producing the linear features observed in Figure 64 and Figure 65. It is considered likely that these linear defects formed when non-metallic inclusions were linked by ductile tearing during the tensile test.
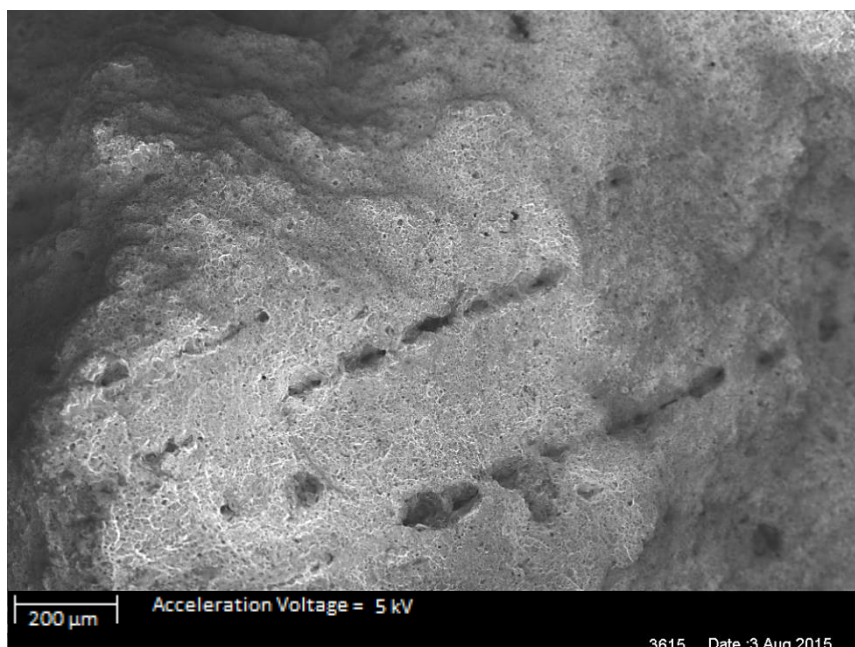
Figure 64: SEM image of linear features observed on the tensile sample fracture surface of sample 1 (Heat treated for 579h at 635°C prior to welding and a 672h PWHT at 635°C).

96
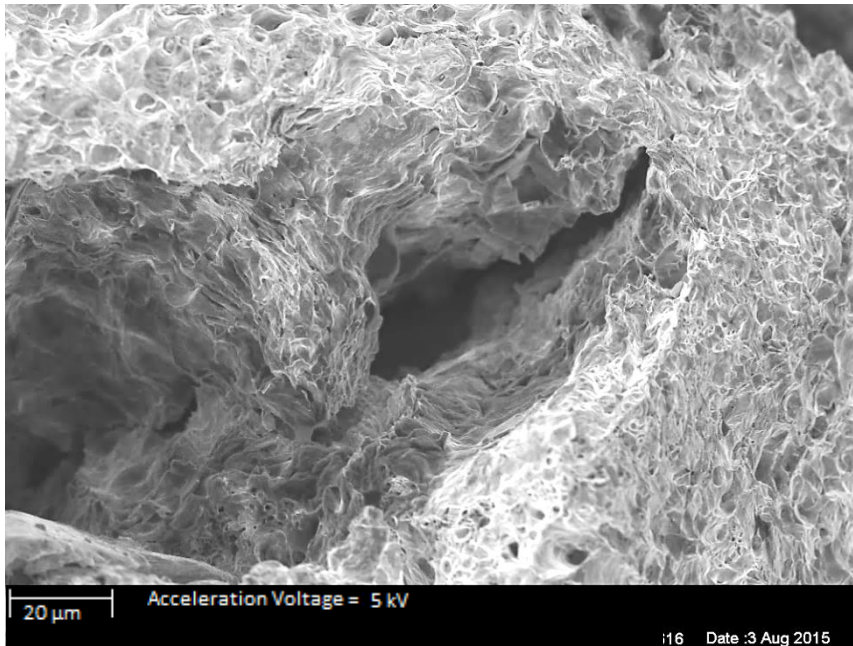
Figure 65: SEM image of linear features observed on the tensile sample fracture surface of sample 1 under higher magnification (Heat treated for 579h at 635°C prior to welding and a 672h PWHT at 635°C).

HAZ microstructure prepared from the full section tensile test sample

Figure 66 shows extremely small graphite particles starting to form in the HAZ. There are between 3 and 5 particles circled in Figure 66 and additionally, there is a relatively larger particle near to the particles that were circled. When the contrast was increased, it was possible to see that the formation of these small graphite particles are located in the ferrite-ferrite grain boundary region.
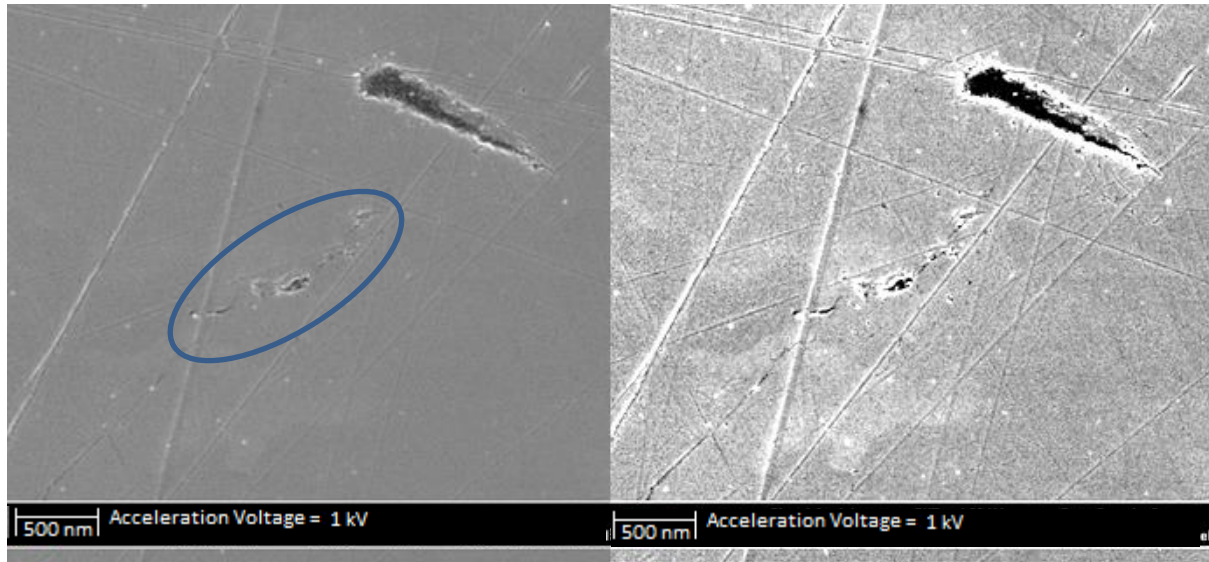
Figure 66: SEM image of HAZ region of the full section tensile test of sample 1 (Heat treated for 579h at 635°C prior to welding and a 672h PWHT at 635°C).

Note the discontinuities in the base metal in Figure 67 which are associated with all graphite particles. All polished sections that contained graphite displayed material damage at high magnifications (typically at magnifications greater than 25 000 X) in the base metal directly adjacent to the graphite nodule (Figure 66, Figure 67 and Figure 80) in both strained and unstrained material. This damage was characterised by what appears to be small circular voids and a spider web crack-like surface finish that radiates outwards from the nodule. This crack-like surface finish most likely contributed to plastic deformation associated with the growth of the graphite nodule. These images are significant because it indicates a mechanical interaction between the base metal and the graphite nodules.
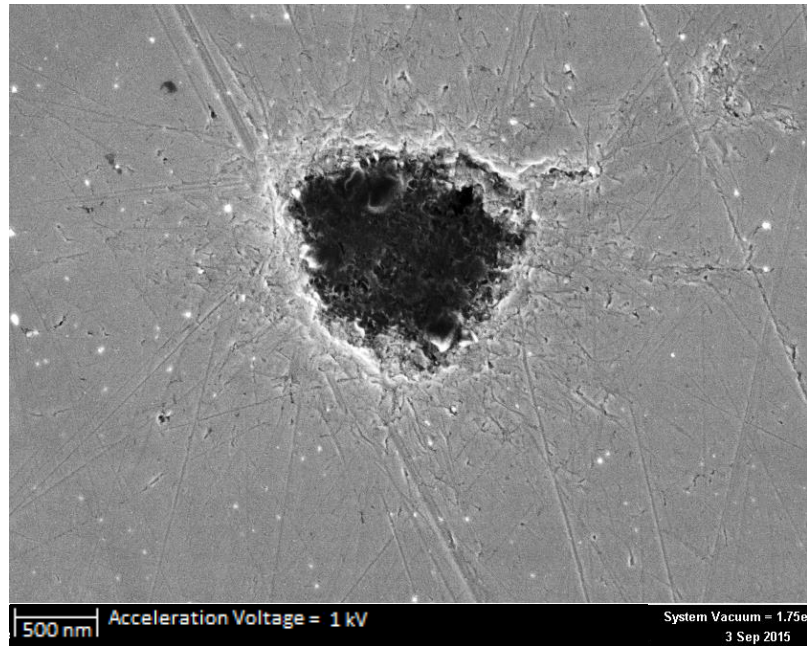
Figure 67: SEM image of HAZ region of the full section tensile test of sample 1. Note the damaged base material surrounding the graphite nodule. This damaged appearance was noted in several samples that were polished, un-etched, and observed at very high magnifications and was found in both strained and unstrained material.

Reduced section round tensile sample

The reduced section round tensile fracture surface was consistent with the full section tensile test fracture surface, displaying several non-connected round graphite particles on the fracture surface as well as the long linear discontinuities not associated with graphite.

Reduced section hot round tensile sample

Inspection of the ductile fracture surface using SEM revealed that the dark, round structures (which are generally found to be graphite) that appear in Figure 68 are not graphite but rather small holes which are thought to be ductile dimples as can be seen in Figure 69. The majority of the small dark spots in Figure 68 are not graphite particles, and only the larger spots (circled) are in fact graphite particles.

99
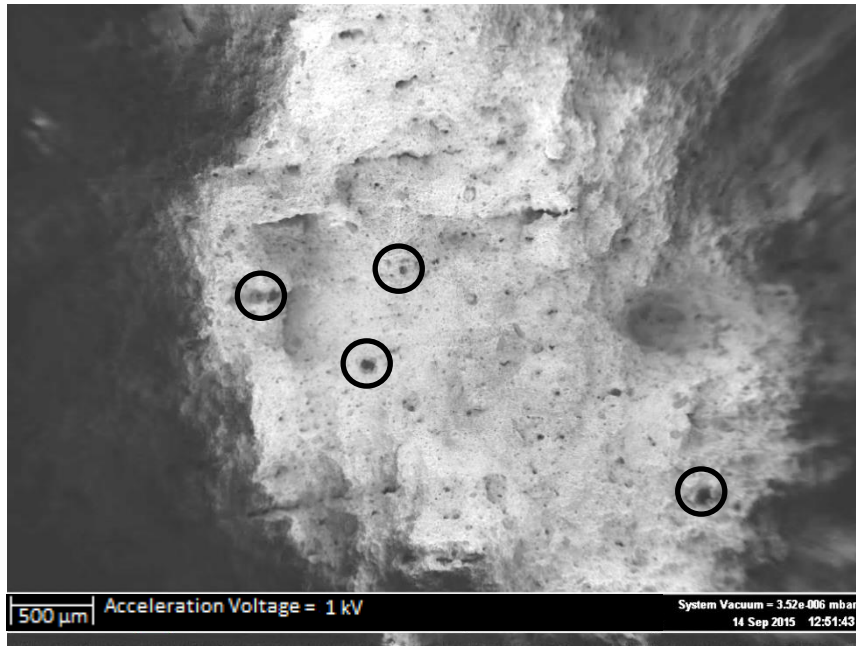
Figure 68: SEM image of reduced section hot round tensile fracture surface of sample 1 (Heat treated for 579h at 635°C prior to welding and a 672h PWHT at 635°C). RA = 78%
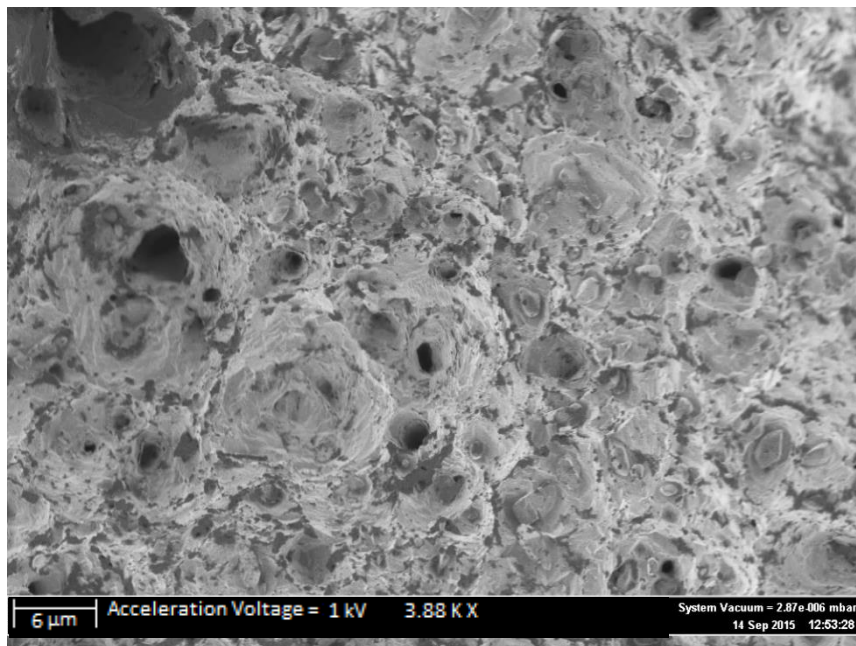
Figure 69: SEM image of reduced section hot round tensile fracture surface of sample 1 under higher magnification. Note the black holes contain no graphite and are likely ductile dimples (Heat treated for 579h at 635°C prior to welding and a 672h PWHT at 635°C). RA = 78%

100

Charpy impact test fracture surface

The Charpy impact fracture surfaces showed no abnormalities, Figure 70 and Figure 71 show the fracture surfaces of the weld metal and HAZ respectively.
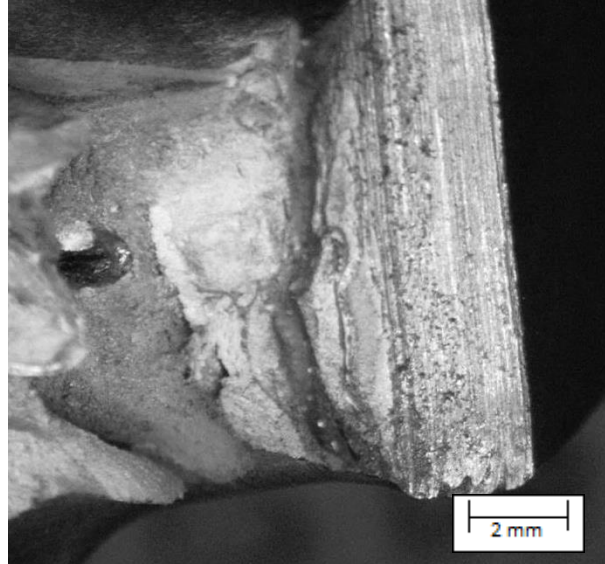
Figure 70: Stereoscopic image of the fracture surface of the weld of sample 1 (Heat treated for 579h at 635°C prior to welding and a 672h PWHT at 635°C).
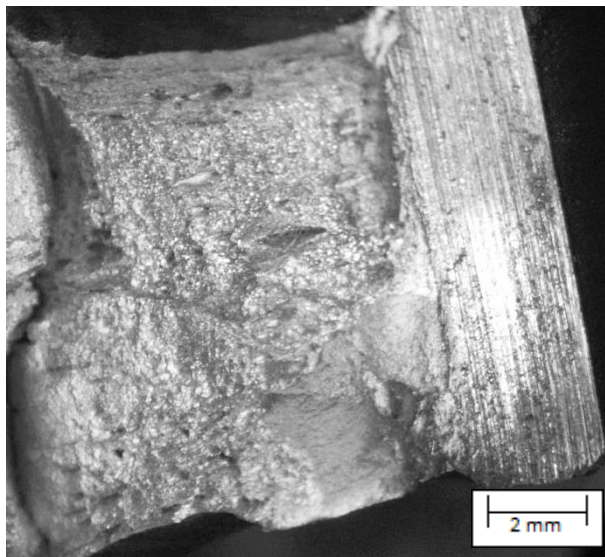
Figure 71: Stereoscopic image of the fracture surface of the HAZ of sample 1 (Heat treated for 579h at 635°C prior to welding and a 672h PWHT at 635°C).

The results obtained with regards to the mechanical properties of the samples from the Charpy impact test showed that all samples displayed ductile fracture characteristics, and that all samples absorbed a significant amount of energy during testing (all above 27J). In addition to this, the fracture surfaces showed no abnormalities and provided no additional information. Thus it was decided not to report the remainder of fracture surfaces of the Charpy impact tests (samples 2-4) in the metallography section.

Sample 2

Full section tensile test sample (Fracture surface)

Stereoscopic evaluation of the tensile test fracture surface revealed several graphite particles, however it is clear that the material did not experience a brittle fracture. The graphite particles that can be seen in Figure 72 are small and distributed randomly across the fracture surface.
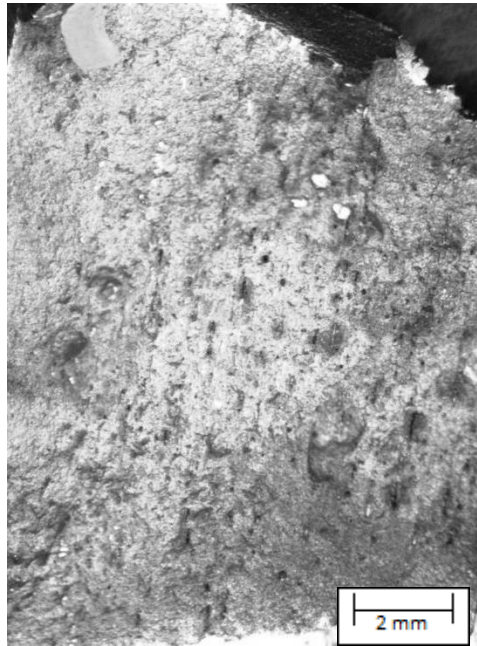
Figure 72: Stereoscopic image of the ductile fracture surface of sample 2 (Heat treated for 579h at 635°C prior to welding and a 12h PWHT at 635°C)

ImageJ was once again used to determine the percentage of the fracture surface that was covered in graphite. The binary black and white image that resulted from this can be seen in Figure 73. In Figure 73, the black areas of the image indicate areas of the fracture surface that was covered in graphite while the white areas represent graphite free areas. The total percentage of graphite that was present in this image was 3.5%.

Figure 73: Processed stereoscopic image of the ductile fracture surface of sample 2 using ImageJ to determine the percentage graphite present on the fracture surface (Heat treated for 579h at 635°C prior to welding and a 12h PWHT at 635°C)

The random distribution of the graphite through the sample resulted in no noticeable difference in material performance and no cracks were detected that resulted in the failure of the sample that could be directly linked to the graphite in the material. It can be seen in Figure 74 that cracks tend to grow between graphite particles that are close together. The crack path in this case was consistently intergranular.

Cracks forming between graphite particles

Direction of tensile load
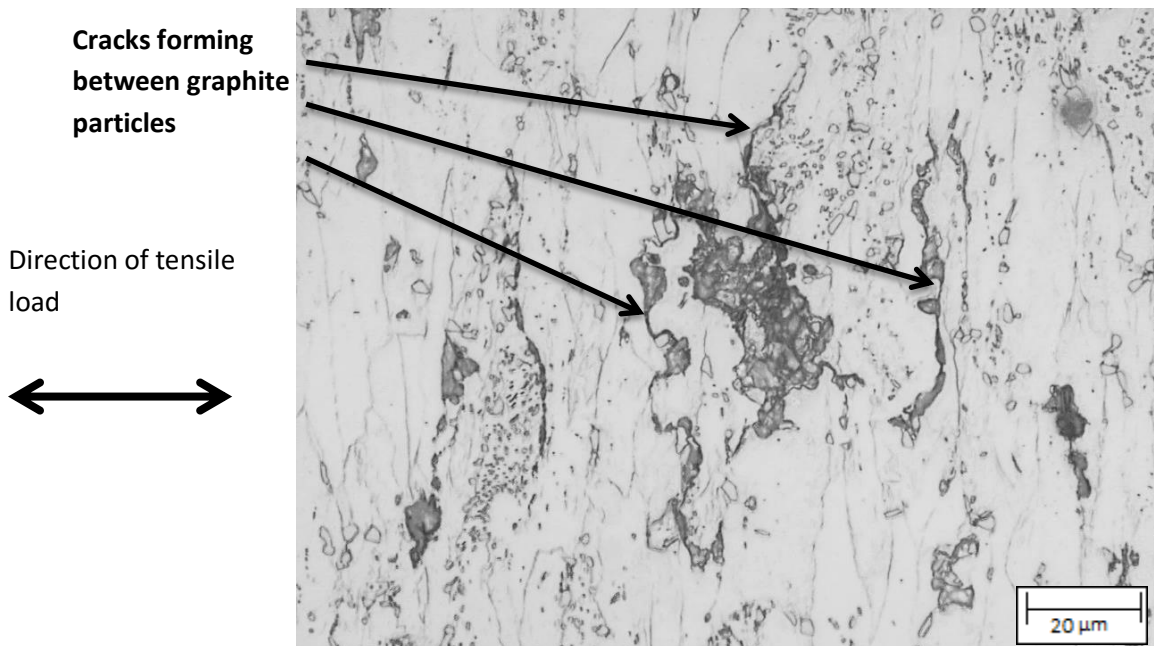
Figure 74: Light microscopy image of cracks forming between closely neighbouring graphite particles in full section tensile sample 2 (Heat treated for 579h at 635°C prior to welding and a 12h PWHT at 635°C)

Figure 75 shows a polished cross section of the fracture surface. It was observed that there are no graphite chains on the fracture surface that resulted in the failure of the sample.

Direction of tensile load
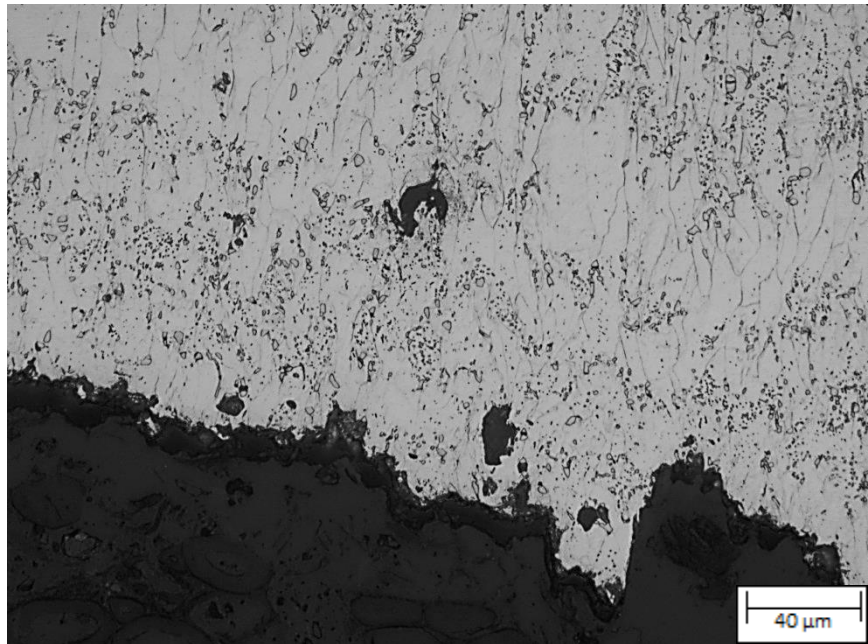
Figure 75: Light microscopy image of cross section of the fracture surface of the full section tensile test of sample 2 (Heat treated for 579h at 635°C prior to welding and a 12h PWHT at 635°C)

Scanning electron microscopy (SEM) images were also taken of the fracture surface under very low acceleration voltages (1 kV) in order to detect fine details on the fracture surface. Figure 76 shows a graphite particle that had been fractured by the tensile test. The surrounding material displayed the typical 'dimpled' surface of a ductile fracture while the graphite showed no deformation.
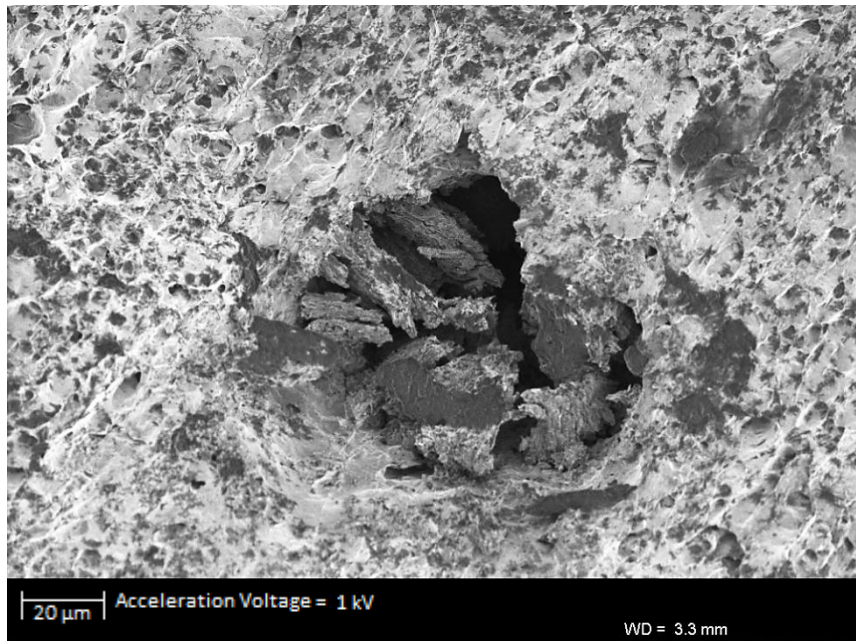
Figure 76: SEM image of the fracture surface of sample 2 graphite particle (Heat treated for 579h at 635°C prior to welding and a 12h PWHT at 635°C)

Figure 77 shows the weld, HAZ and region where graphite is expected to form in the joint. There is only one large graphite particle (circled) that, due to its size, was likely to be present in the base material prior to welding.
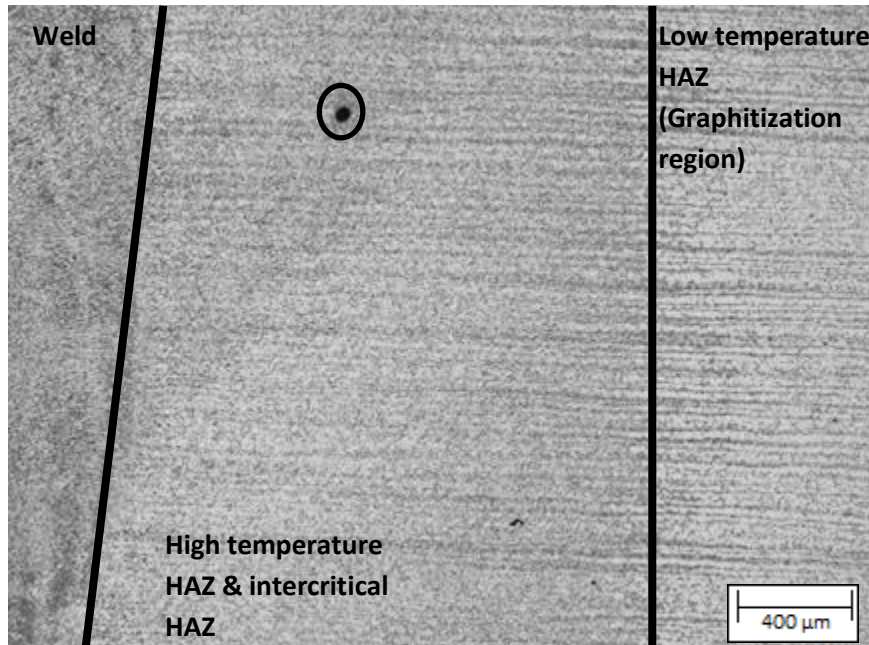
Figure 77: Light microscope image of the welded joint and HAZ of sample 2. Graphite nodule circled. (Heat treated for 579h at 635°C prior to welding and a 12h PWHT at 635°C)

Closer inspection of the partially transformed region reveals small graphite particles as seen in Figure 78. It was not possible to determine whether the graphite was present prior to welding, however it is unlikely that these particles formed during the PWHT due to the short PWHT time that sample 2 experienced (12 hours at 635°C) despite the fact that the location of the graphite seen in Figure 78 correlates very well with the region which experienced a peak temperature near to the Ac_1 temperature of the material.
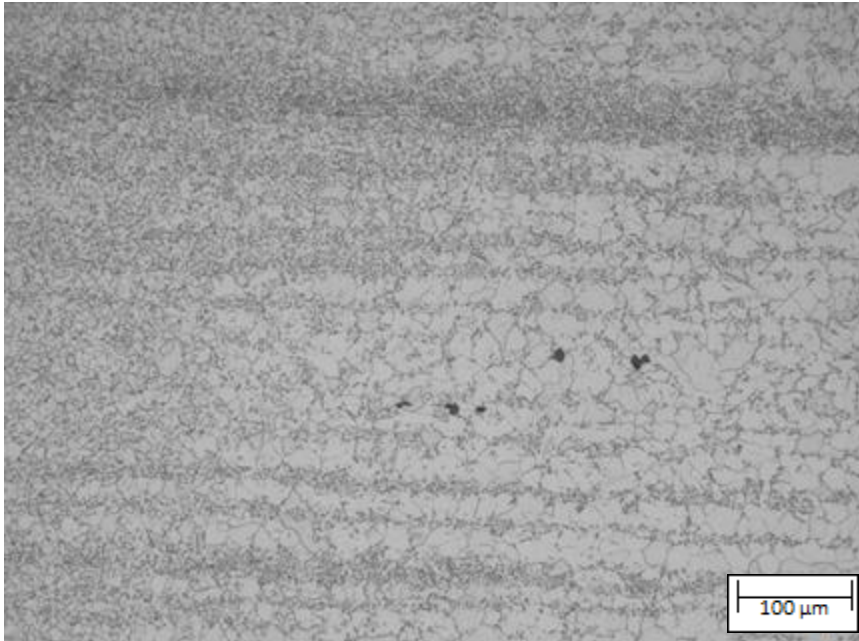
Figure 78: Light microscope image of the welded joint and HAZ of sample 2. (Heat treated for 579h at 635°C prior to welding and a 12h PWHT at 635°C)

Figure 79 shows a light microscope image of a rolled in inclusion that was discussed earlier in 'General observations' and in Figure 53 and Figure 54.
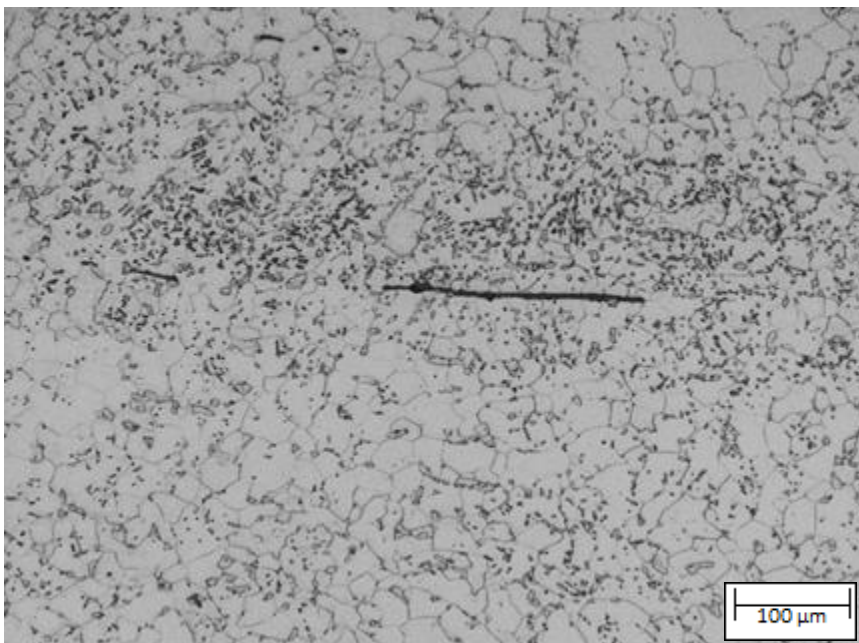
Figure 79: Light microscope image of inclusion in the base metal of sample 2. (Heat treated for 579h at 635°C prior to welding and a 12h PWHT at 635°C)

Closer inspection of these inclusions using a SEM shows that the inclusions are a favourable site for graphite to nucleate at as seen in Figure 80. While these inclusions were not chemically analysed, it is highly likely that these were MnS inclusions.
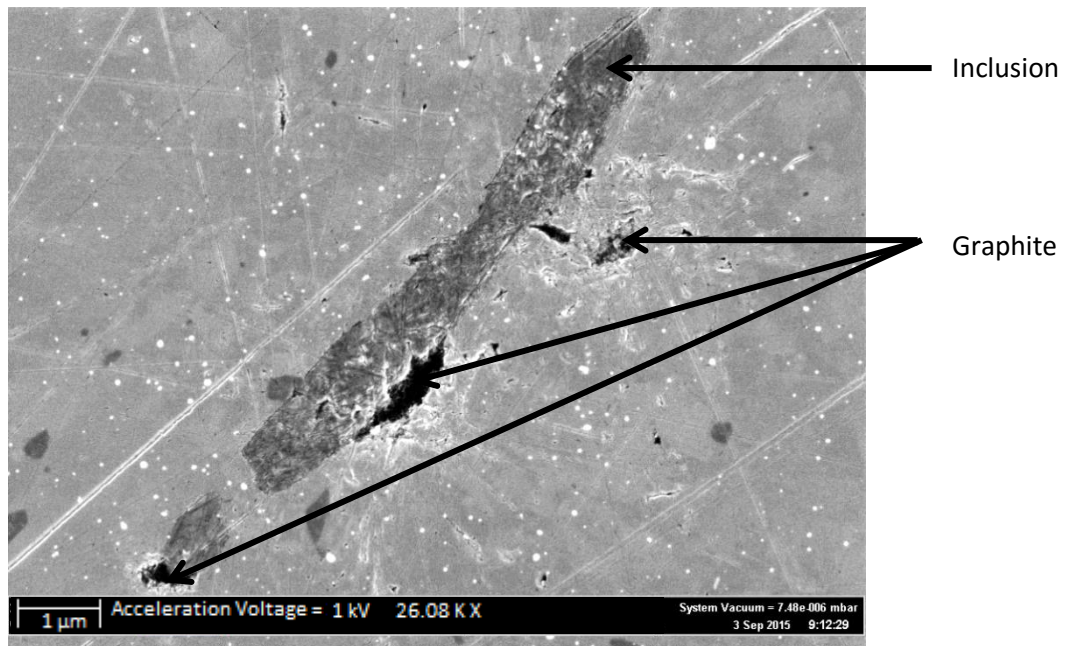
Figure 80: SEM image of inclusion from sample 2 full section tensile test. (Heat treated for 579h at 635°C prior to welding and a 12h PWHT at 635°C)

Figure 81 shows a fully developed graphite particle. It can be seen that the graphite is not separated from the ferrite, but instead there are small amounts of ferrite that were dispersed throughout the graphite particle. This observation was not an isolated case, and all graphite particles displayed the ferrite seen in Figure 81 and can be seen in all graphite nodules.
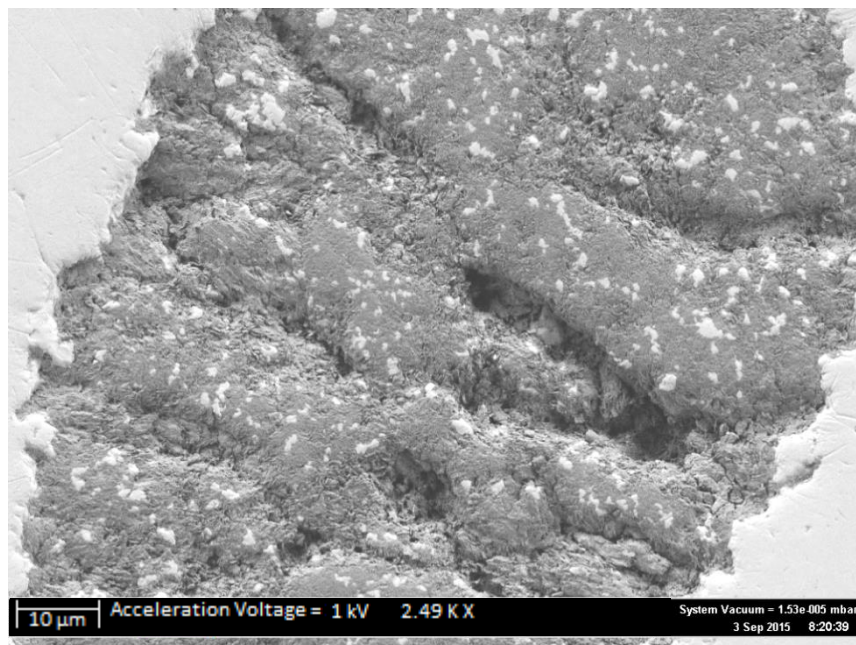
Figure 81: Polished SEM image of ferrite intespered between graphite from the full section tensile test HAZ (Heat treated for 579h at 635°C prior to welding and a 12h PWHT at 635°C)

Reduced section round tensile sample

Similarly to sample 1 and as seen in Figure 68, there was very little graphite on the fracture surface and relatively high quantities of linear defects.

Reduced section hot round tensile sample

SEM evaluation of the fracture surface were similar to that of sample 1. Only several larger dark circular structures were confirmed to be graphite while the majority of the smaller dark features appeared to be linear defects.
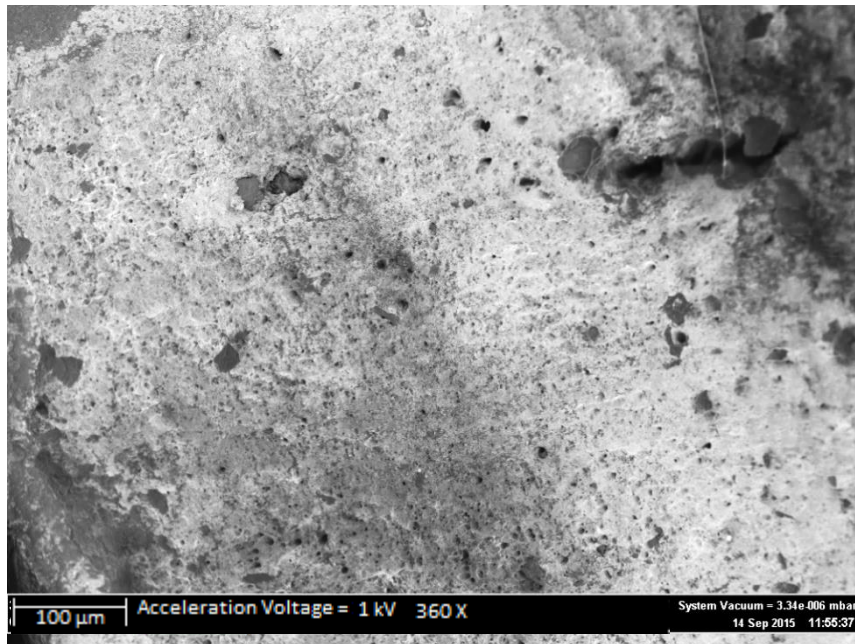
Figure 82: Low magnification SEM image of the ductile fracture surface of the reduced section hot round tensile test sample 2 (Heat treated for 579h at 635°C prior to welding and a 12h PWHT at 635°C). RA = 76%

Figure 83 shows several graphite particles that were present on the fracture surface. Several graphite particles appear to have experienced a partial combustion reaction once the fracture took place and the graphite came into contact with oxygen from the air.

Figure 83: SEM image of fractured graphite nodules on the fracture surface of the reduced section round hot tensile test of sample 2 (Heat treated for 579h at 635°C prior to welding and a 12h PWHT at 635°C). RA = 76%

Sample 3

Full section tensile test sample (Fracture surface)

Stereoscopic evaluation shows that the sample displays small quantities of graphite however the graphite was randomly distributed across the fracture surface as can be seen in Figure 84. The fracture was ductile in nature and large portions of the fracture surface appear to be free from graphite.
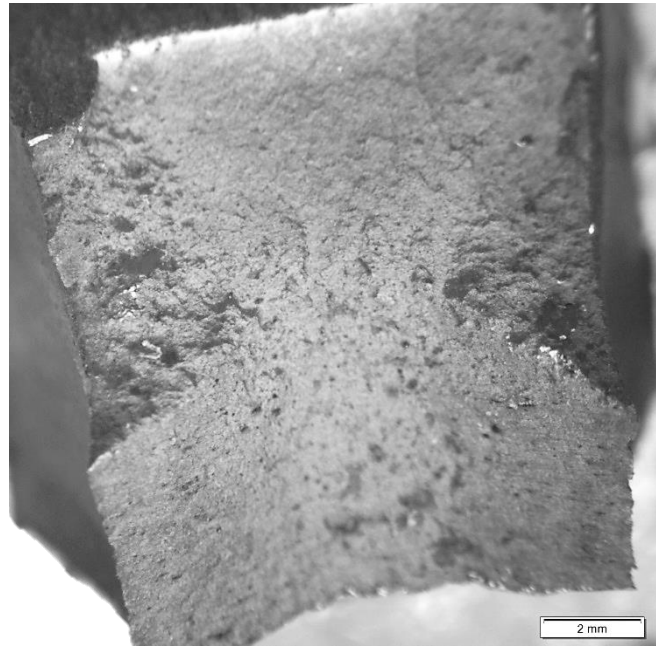
Figure 84: Stereoscopic image of the tensile fracture surface of sample 3 (No heat treatment prior to welding and a 672h PWHT at 635°C).

Under higher magnification it is clear that there were several areas with higher concentrations of graphite colonies. The circled area indicates the area of the fracture surface that contained high numbers of graphite colonies in relation to the rest of the fracture surface that appeared nearly free from graphite.

Figure 85: Stereoscopic image of the tensile fracture surface of sample 3 at higher magnification. Circled is the area of the fracture surface with the highest concentration of graphite colonies on the fracture surface (No heat treatment prior to welding and a 672h PWHT at 635°C).

ImageJ was used to determine the percentage of the fracture surface that was covered in graphite. The binary black and white image that resulted from this can be seen in Figure 86. In Figure 86, the black areas of the image indicate areas of the fracture surface that were covered in graphite while the white areas represent graphite free areas. The total percentage of graphite that is present in this image is 1%.
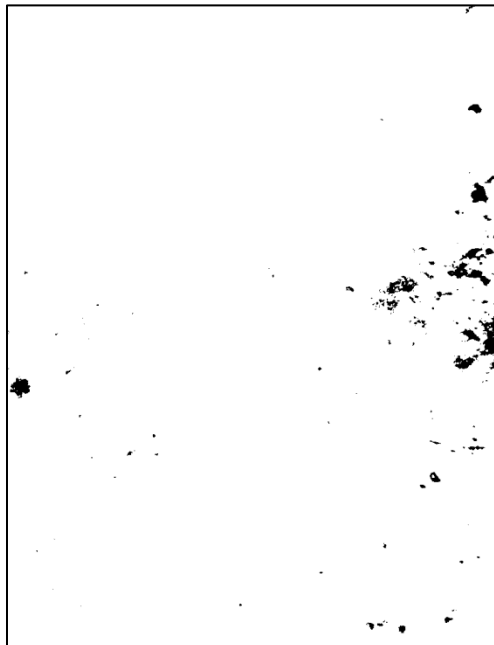
Figure 86: Processed stereoscopic image of the ductile fracture surface of sample 3 using ImageJ to determine the percentage graphite present on the fracture surface (No heat treatment prior to welding and a 672h PWHT at 635°C).

Figure 87 was taken using a light microscope from a polished section approximately 20 mm away from the fracture surface. Circled in this image are several small graphite colonies where a crack had formed between closely neighbouring graphite colonies.

Direction of tensile load

↔
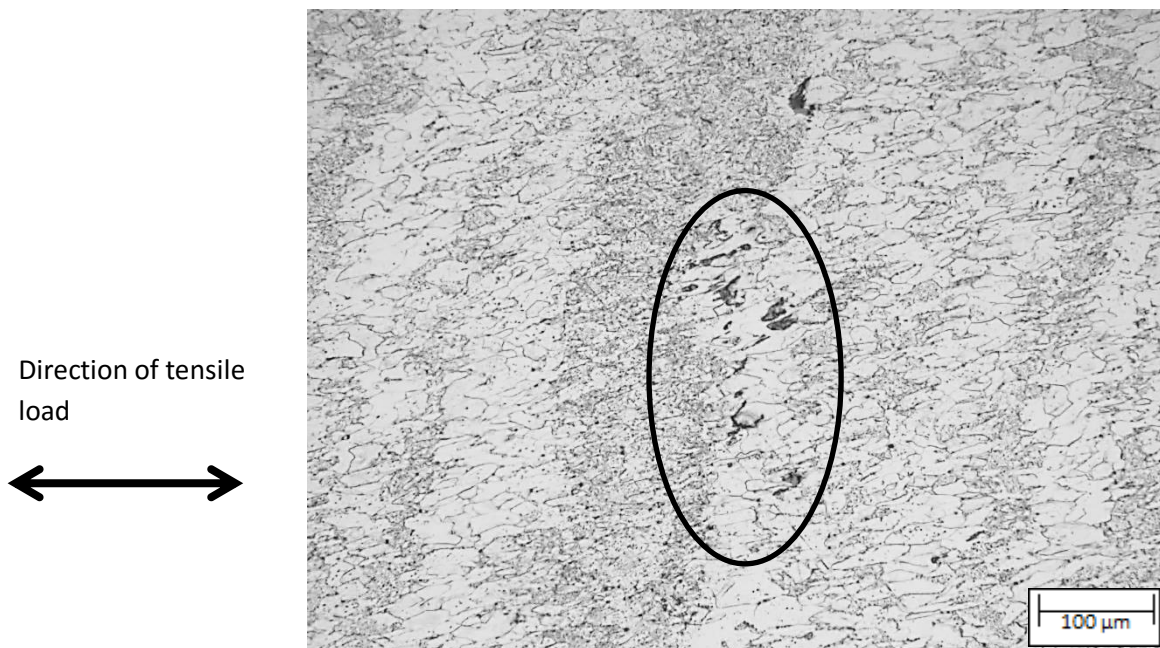
Figure 87: Light microscope image of a polished section of the tensile sample of sample 3 at far from the fracture location. Circled is the area where cracks would form between small clusters of graphite. (No heat treatment prior to welding and a 672h PWHT at 635°C).

It can be seen in Figure 88 that there were no chains of graphite that could be observed that were associated with the fracture surface. There were isolated graphite particles that were present on the fracture surface however all these particles were randomly distributed.

Direction of tensile load

←——————→
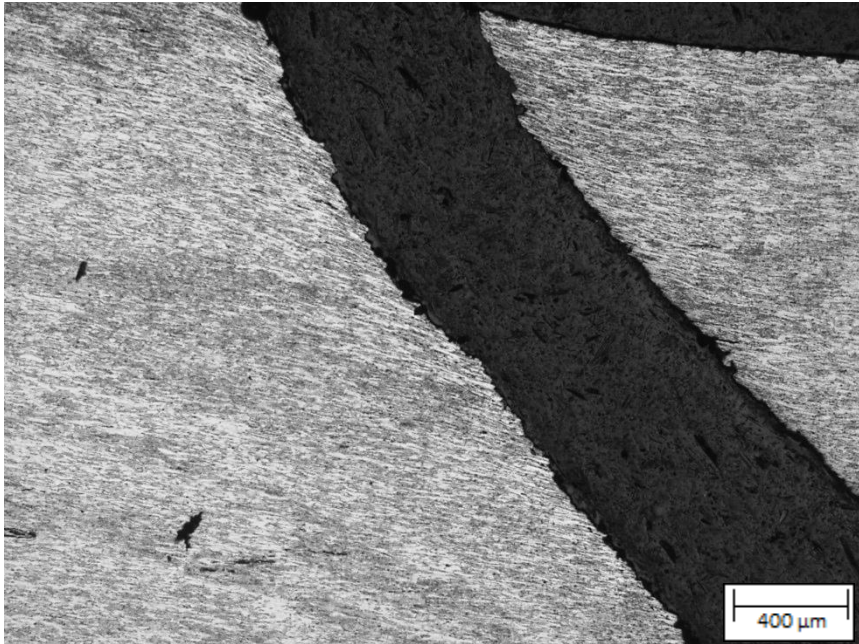
Figure 88: Light microscope image of a polished section of the tensile sample of sample 3 at the fracture location. There are no graphite clusters that are associated with the fracture surface and only randomly distributed graphite particles are present on the fracture surface. (No heat treatment prior to welding and a 672h PWHT at 635°C).

Using a SEM it was possible to study the fracture surface in greater detail. The SEM image in Figure 89 shows the characteristic dimpled surface associated with a ductile fracture. Additionally the surface contained several linear discontinuities (circled) which were not associated with any graphite.
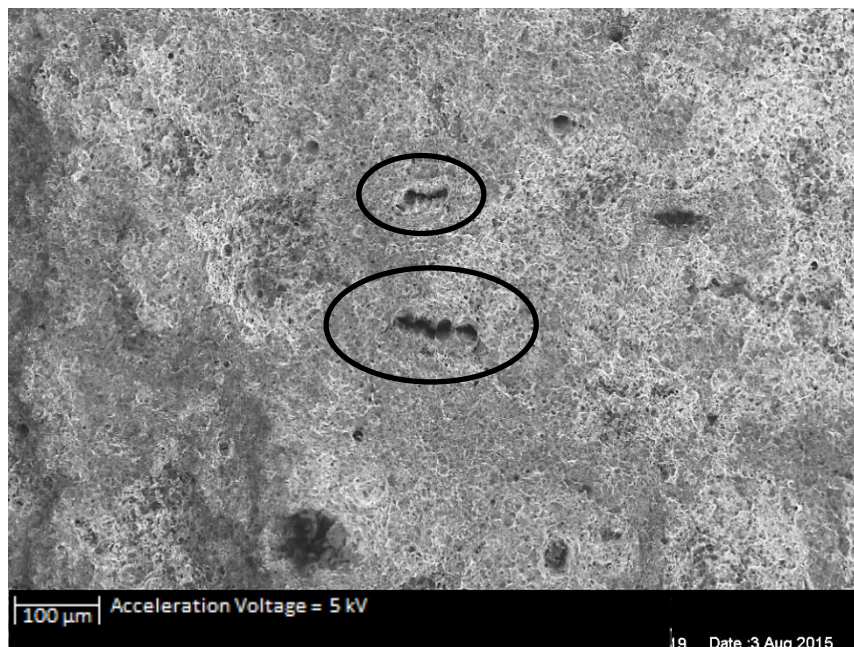
Figure 89: SEM image of the fracture surface of the tensile sample of sample 3. Linear discontinuities have been observed which are not associated with any graphite and the bulk of the material displays a dimpled surface finish indicative of ductile failure. (No heat treatment prior to welding and a 672h PWHT at 635°C).

Figure 90 was taking using the SE detector. The image shows the graphite-ferrite interface of a graphite particle that has detached from the steel.

113
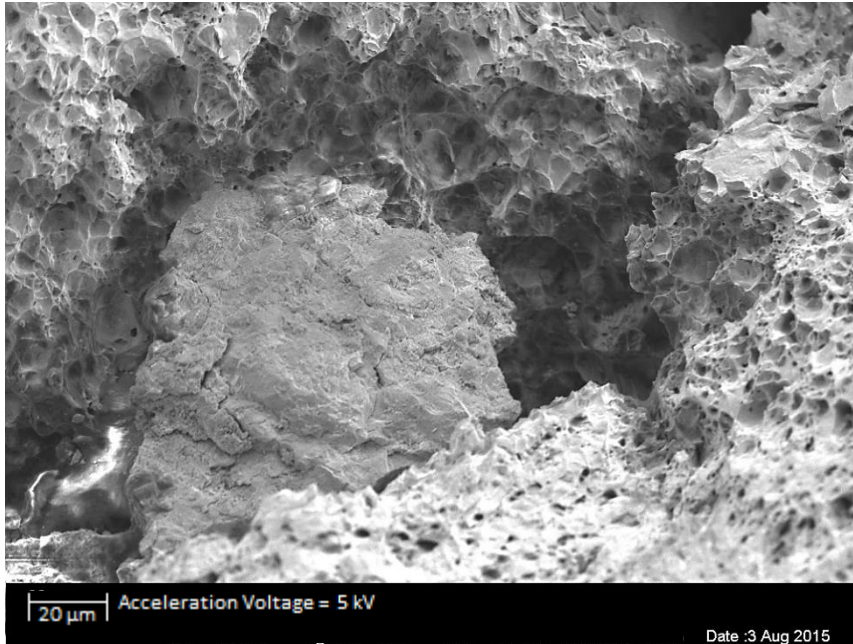
Figure 90: SEM image of the fracture surface of the tensile sample of sample 3. SE detector was used to photograph the steel-graphite interface where a graphite particle had detached from the steel. (No heat treatment prior to welding and a 672h PWHT at 635°C).

HAZ microstructure prepared from the full section tensile test sample

Figure 91 shows the graphitized region in the partially transformed HAZ. Due to the original joint design, the weld and subsequently the graphitized HAZ follows a path which is approximately 45° to the through thickness direction of the pipe.
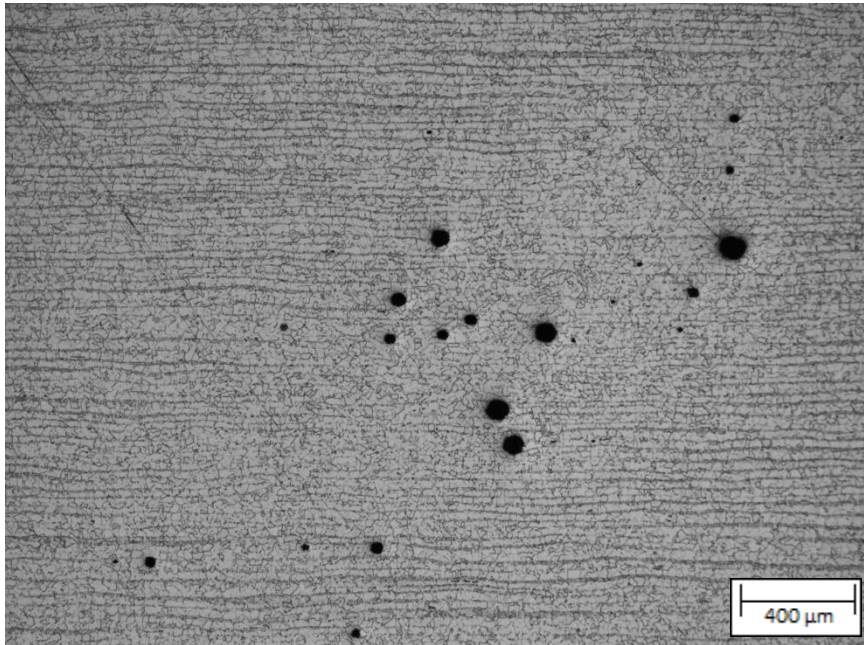
Figure 91: Light microscopy image of the polished section of the full tensile test sample HAZ (No heat treatment prior to welding and a 672h PWHT at 635°C).

Close inspection of the graphite nodules in Figure 91 shows that, as in Figure 81, the graphite and ferrite are closely associated and interspersed between one another rather than two spatially separate phases as seen in Figure 92.
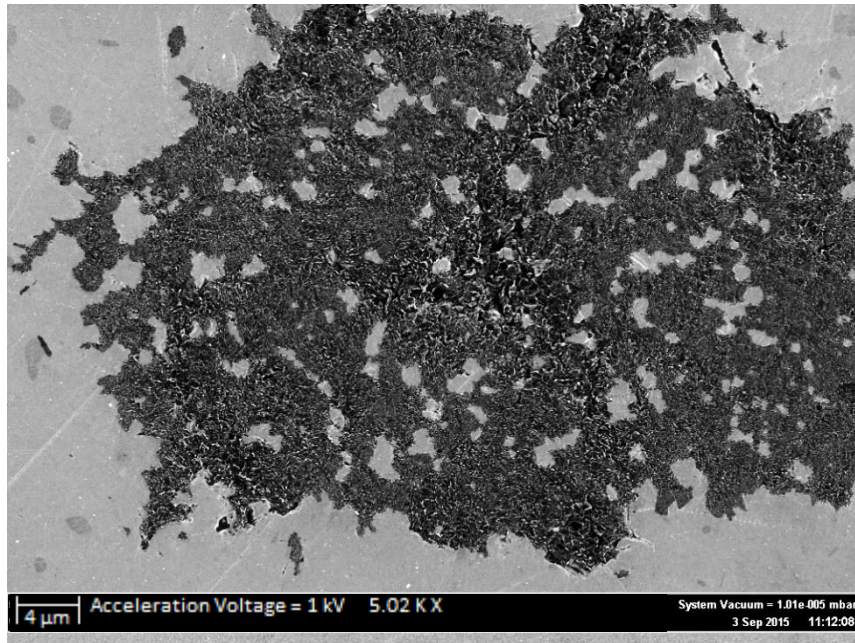
Figure 92: SEM image of the polished section of the HAZ graphite in the full section tensile test sample (No heat treatment prior to welding and a 672h PWHT at 635°C).

Reduced section round tensile sample

Sample 3 failed through a graphitized plane of the HAZ (Figure 93). The full section tensile samples of sample 3 did not fail through the HAZ. The reason for the unexpected failure of one of the reduced section tensile test samples is due to the position from which the reduced section was taken. Because the joint preparation that was used on sample 3 only made alterations to the top half of the welded joint, and because the sample in Figure 93 was taken in a position that did not receive the repair welding, there was a continuous plane of graphite that ran through the thickness of the sample which resulted in the HAZ failure.
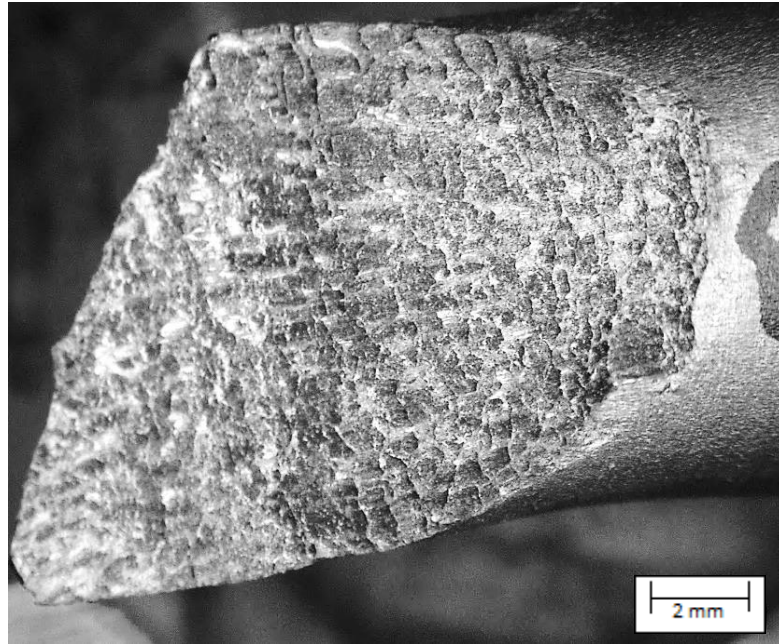
Figure 93: Stereoscopic image of the fracture surface of the the reduced section round tensile test sample (No heat treatment prior to welding and a 672h PWHT at 635°C). RA = 44%

Figure 94 is a polished cross section of the fracture surface and shows the stepwise fracture path of the fracture. This indicates that the sample ruptured along a preferred plane in the same direction as the axial load (the direction in which the graphite clusters are orientated) before stepping vertically upwards or downwards (perpendicular to the axial load) to the next horizontal discontinuity. Based on the planes of graphite that have formed, it can be concluded that the original joint preparation prior to welding was a 90° included angle joint. This resulted in, on a larger scale, a 45° fracture angle which is also the angle of the maximum shear stress. However, under closer inspection, it can be seen that this 45° angle is separated into a series of 0° and 90° fracture lines which correlate to the planes parallel to the graphite planes (shearing along graphite clusters) and perpendicular to the graphite plane (plain strain fracture conditions). A fracture plane orientated at an angle of 45° to the direction of principle stress is normally interpreted as indicating shear on the plane of highest shear stress. In contrast, Figure 94 indicates a fracture surface orientated at 45° as consisting of a series of fracture planes parallel to and transverse to the direction of principle stress. The orientation of 45° to the direction of the principle stress may be the consequence of the angle of the original weld preparation, that is 45 to 50° – see Figure 33.
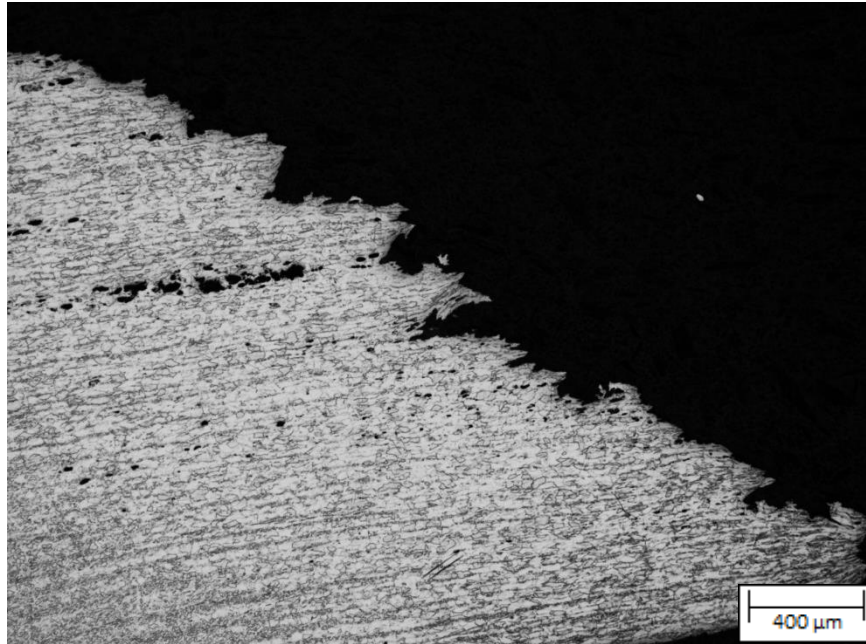
Figure 94: Light microscope image of the fracture surface of the reduced section round tensile test sample of sample 3 that failed through the graphitized HAZ (No heat treatment prior to welding and a 672h PWHT at 635°C). RA = 44%

Figure 95 shows the fracture surface at higher magnification. Previously it was noted that in samples that failed away from the graphite, as seen in Figure 60 and Figure 61, there are strain lines that appear when the samples are etched with Nital. In samples that failed in the graphitized HAZ, no such strain lines develop after etching. This suggests that there was little plastic flow near the fracture surface of samples that failed in the graphitized zone.
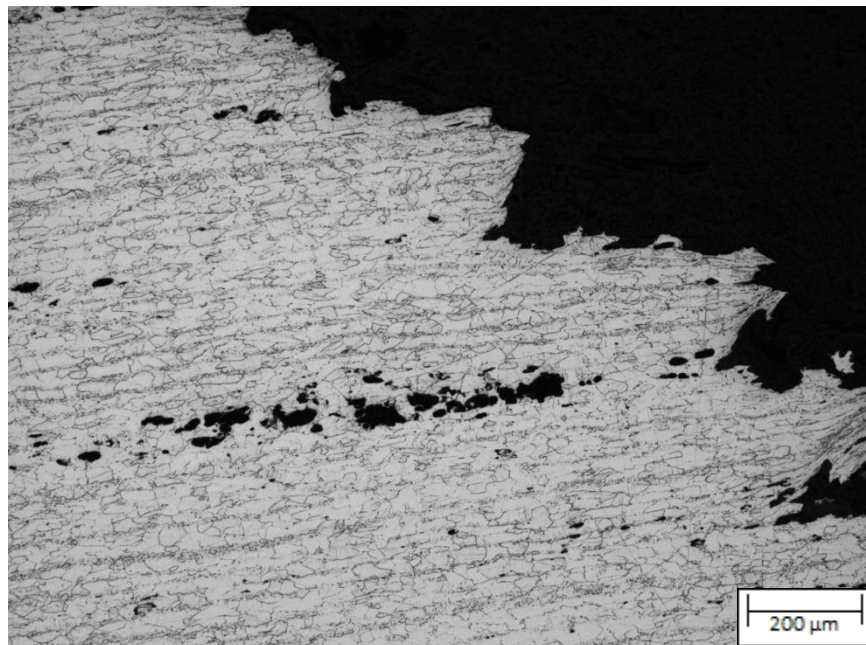
Figure 95 Light microscope image of the stepwise fracture surface of the reduced section round tensile test sample of sample 3 (No heat treatment prior to welding and a 672h PWHT at 635°C). RA = 44%

Close inspection of sample 3 in Figure 96 shows that there is a small amount of plastic deformation at the edge of the fracture surface. The direction of the plastic deformation is uniform and this suggests that during failure, the sample experienced a bending moment immediately before fracture.
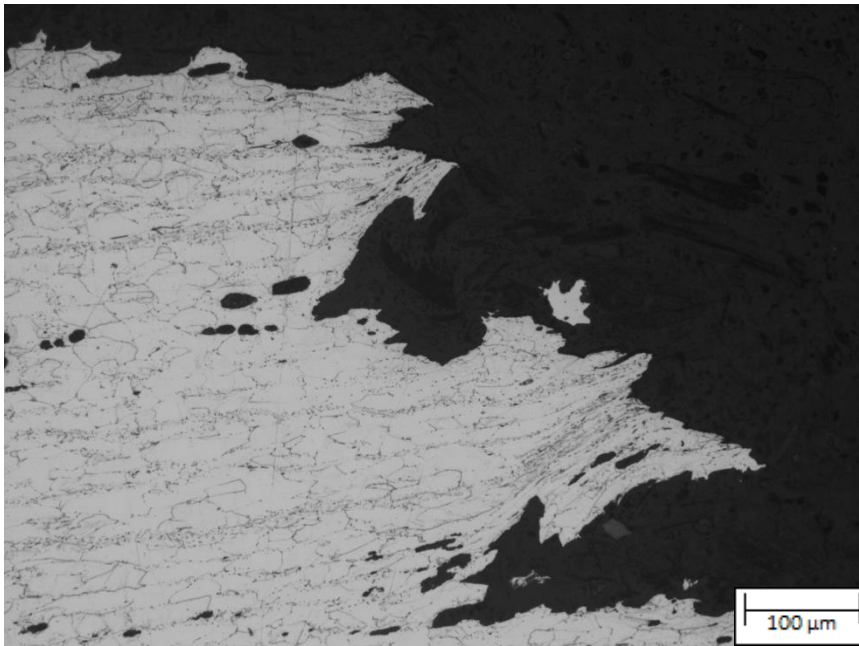
Figure 96 Light microscope image of the plastically deformed grains directly adjasent to the fracture surface of the reduced section round tensile test sample of sample 3 (No heat treatment prior to welding and a 672h PWHT at 635°C). RA = 44%

Figure 97 shows a typically elongated graphite particle near the fracture surface of the reduced section round tensile test of sample 3. The dimensions of this nodule are approximately 80 X 20 µm through the longest and thickest portions of the nodule.
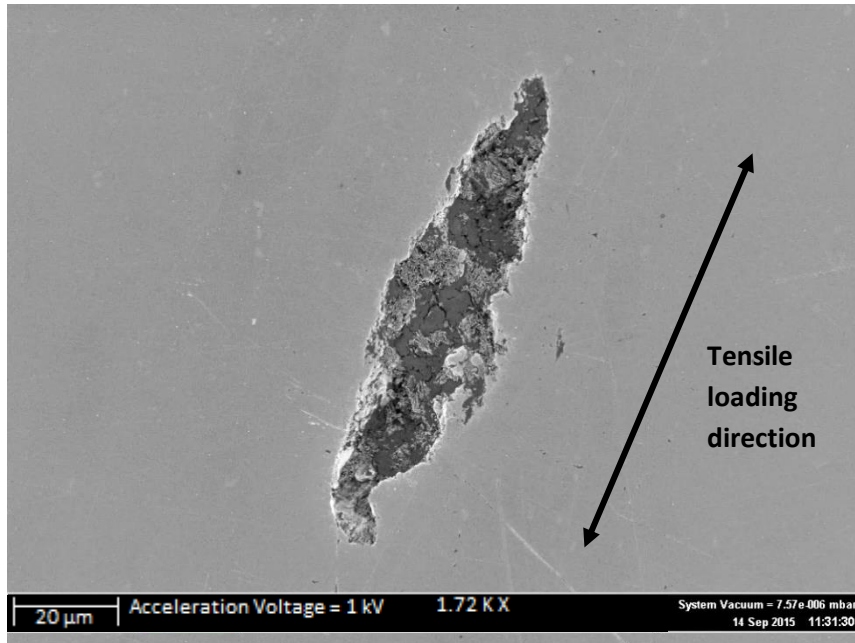
Figure 97: SEM image of an elongated graphite nodule near to the fracture surface of the reduced section round tensile test specimen of sample 3 (No heat treatment prior to welding and a 672h PWHT at 635°C). RA = 44%

Figure 98 shows a small section of a graphite nodule that still adhered to the fracture surface.
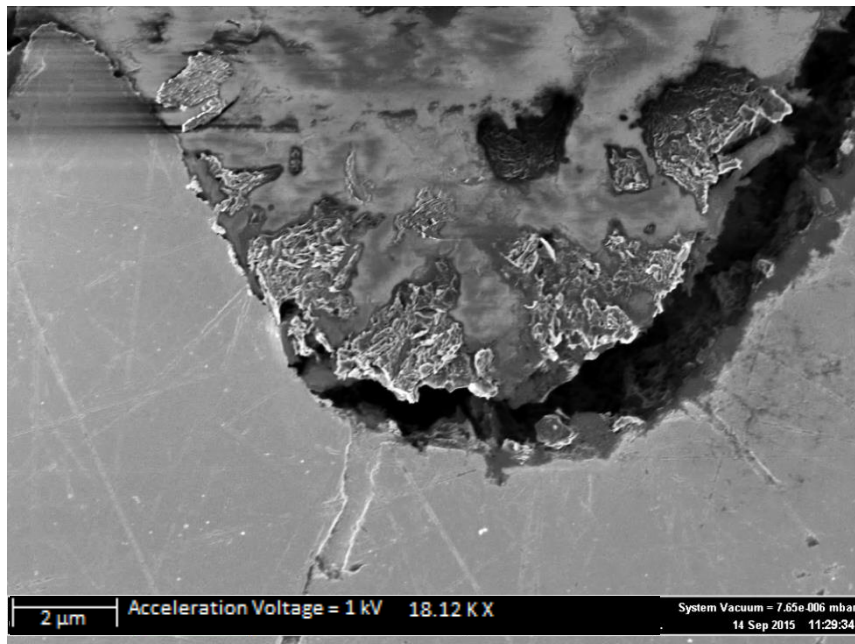
Figure 98: SEM image of a portion of a graphite nodule on the fracture surface of the reduced section round tensile test specimen of sample 3 (No heat treatment prior to welding and a 672h PWHT at 635°C). RA = 44%

Reduced section hot round tensile sample

The reduced section hot round tensile test fracture surface of sample 3 revealed a substantial amount of graphite on the fracture surface as seen in Figure 99.
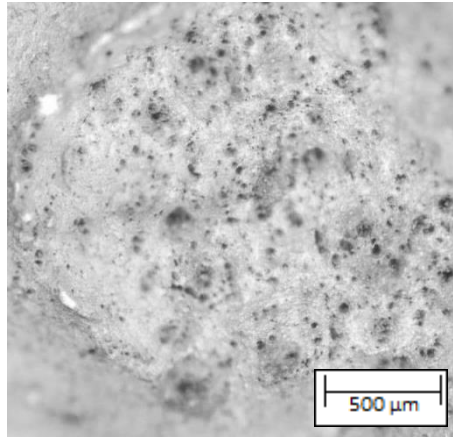
Figure 99: Stereoscopic image of the fracture surface of the reduced section hot round tensile test specimen of sample 3 (No heat treatment prior to welding and a 672h PWHT at 635°C). RA = 77%

Closer inspection of the fracture surface in Figure 99 reveals that the majority of the dark circles observed were graphite nodules as seen in Figure 100 and Figure 101 unlike that observed in the samples 1 and 2.
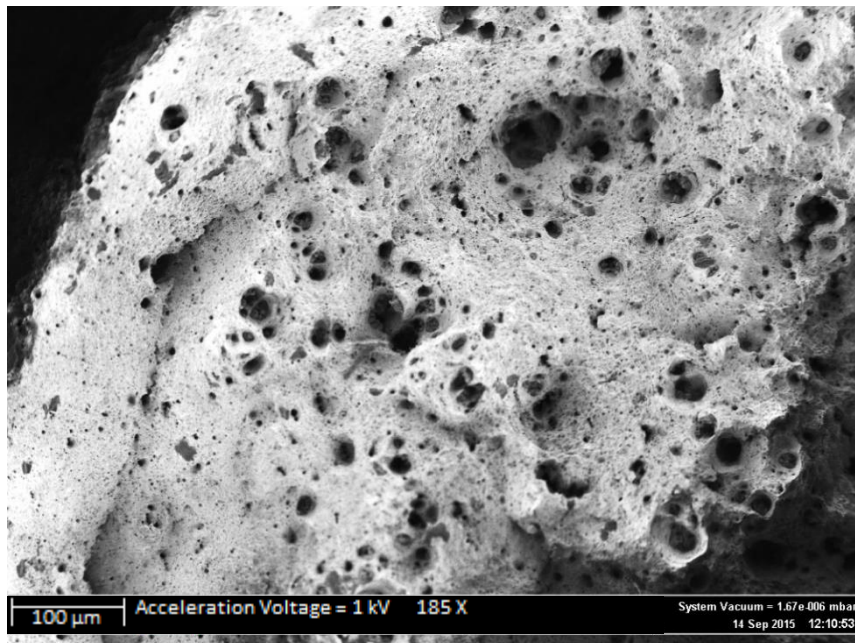
Figure 100: SEM image of the fracture surface of the reduced section hot round tensile test specimen of sample 3 (No heat treatment prior to welding and a 672h PWHT at 635°C). RA = 77%
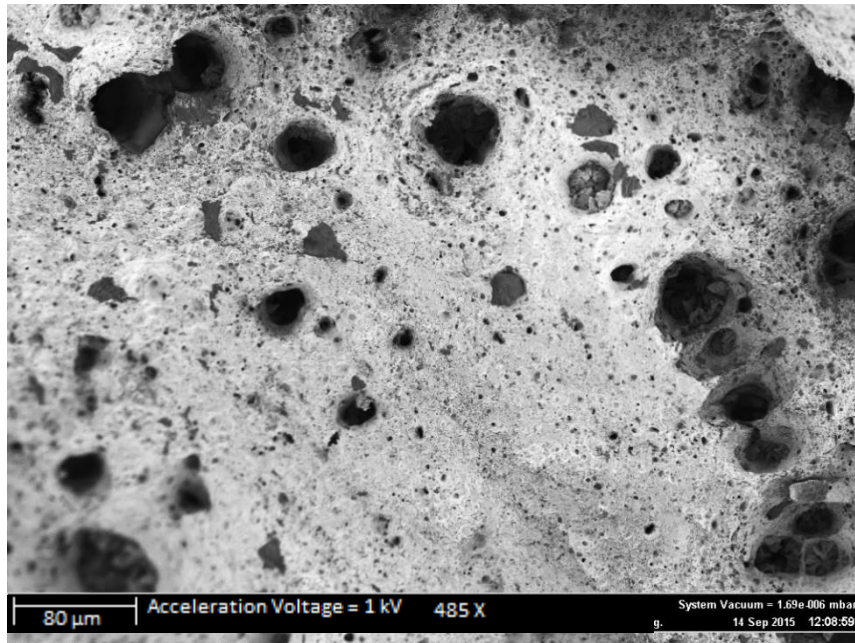
Figure 101: SEM image of the fracture surface of the reduced section hot round tensile test specimen of sample 3 using higher magnification than in Figure 100 (No heat treatment prior to welding and a 672h PWHT at 635°C). RA = 77%

A polished cross section of the fracture surface can be seen in Figure 102. It is clear that the fracture path did not follow any particular preferred plane.
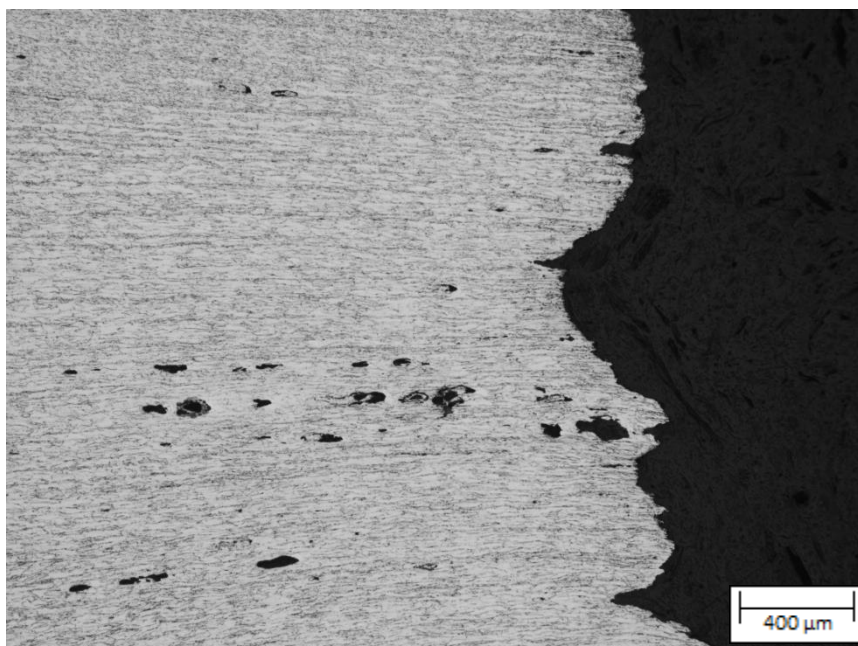
Figure 102: Light microscope image of a polished section of the fracture surface of the reduced section hot round tensile test specimen of sample 3 (No heat treatment prior to welding and a 672h PWHT at 635°C). RA = 77%

Sample 4

Full section tensile test sample (Fracture surface)

Stereoscopic evaluation of the fracture surface revealed long chains of graphite that run across the fracture surface. It can be seen from Figure 103 that a large amount of the fracture surface is covered in graphite. Sample 4 experienced failure in the HAZ in both full section tensile tests.
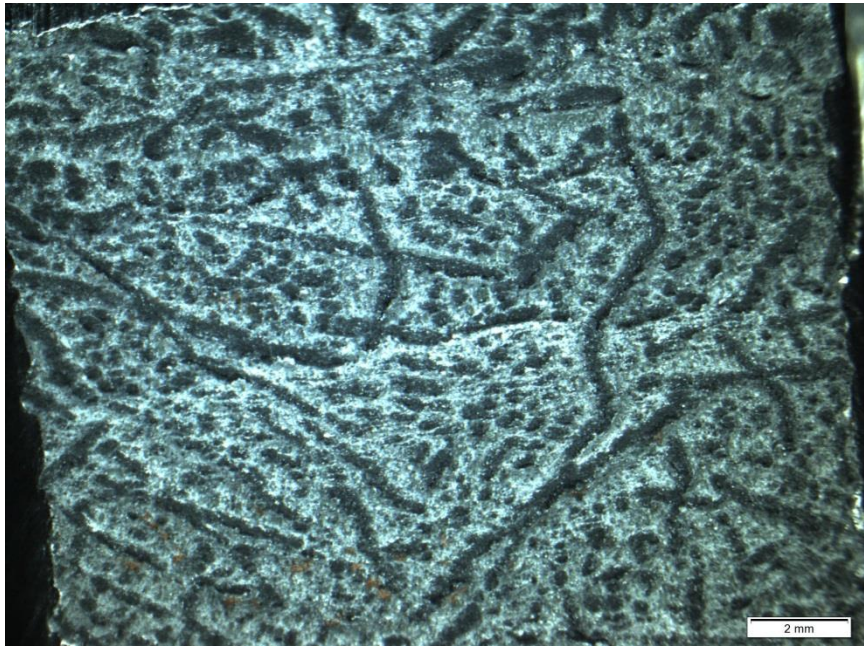
Figure 103: Stereoscopic image of the tensile fracture surface of sample 4 (Material was tested in the service exposed condition with no further welding or heat treatments performed in order to establish a test baseline). The surface contains large amounts of graphite.

ImageJ was used to determine the percentage of the fracture surface that was covered in graphite. The binary black and white image that resulted from this can be seen in Figure 104. In Figure 104, the black areas of the image indicate areas of the fracture surface that is covered in graphite while the white areas represent graphite free areas. The total percentage of graphite that was present in this image is 55%.
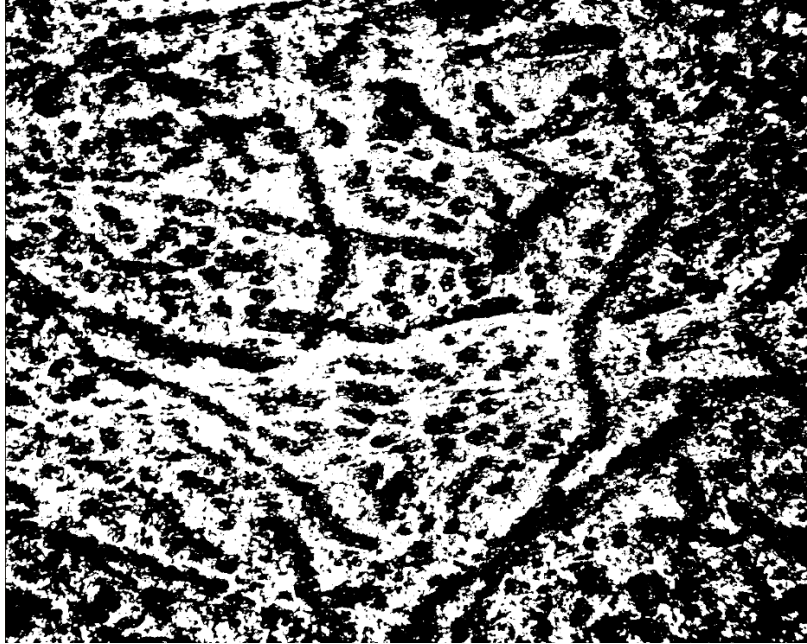
Figure 104: Processed stereoscopic image of the brittle fracture surface of sample 4 using ImageJ to determine the percentage graphite present on the fracture surface (Material was tested in the service exposed condition with no further welding or heat treatments performed in order to establish a test baseline)

Figure 105 is a polished section from the tensile test and pearlite was observed. No spheroidization of the pearlite was observed.
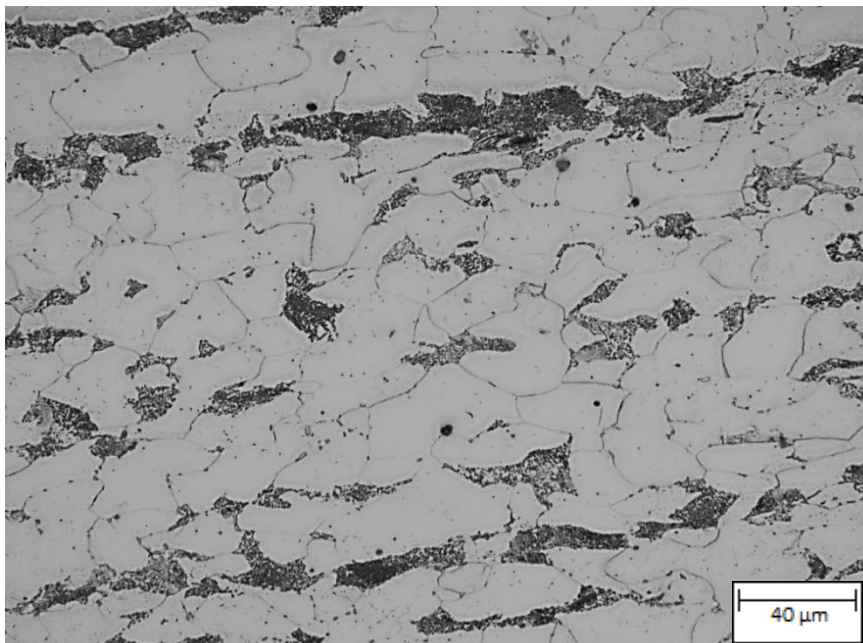
Figure 105: Light microscopy image of Sample 4 displays far less microstructural degradation than sample 2 (Material was tested in the service exposed condition with no further welding or heat treatments performed in order to establish a test baseline)

Once the sample was polished and etched, it was possible to more clearly observe the step-like crack that ran through the HAZ of the material in a preferred plane (17). Figure 106 is a montage of the edge of the fracture surface. Take note that every graphite cluster in the vicinity of the crack path has

ruptured, and in most cases the cracks have travelled exclusively through the graphite clusters when travelling in the direction parallel to the tensile load; this demonstrates the low mechanical strength of graphite.
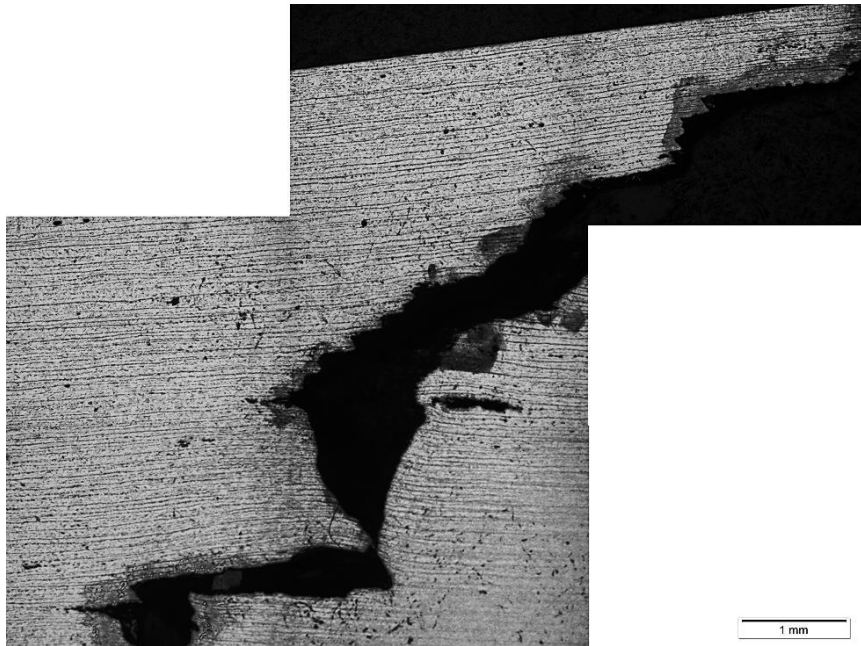
Figure 106: Light microscopy image of step like fracture of sample 4 (Material was tested in the service exposed condition with no further welding or heat treatments performed in order to establish a test baseline)

It can be seen in Figure 107 that cracks, as in sample 2, form between closely neighbouring graphite particles. However unlike sample 2, the graphite particles are not randomly distributed through the material, but rather concentrated in the partially transformed region of the HAZ of the material.

Figure 107: Light microscopy image of crack running through multiple graphite particles in sample 4 (Material was tested in the service exposed condition with no further welding or heat treatments performed in order to establish a test baseline)

125

Figure 108 reveals that the planar HAZ graphite forms in a cellular manner, where the iron acts to separate one graphite nodule from another. The shape and high concentration of graphite in this highly heterogeneous orientation almost certainly disproves the need for an inclusion to be present for the nucleation of graphite.
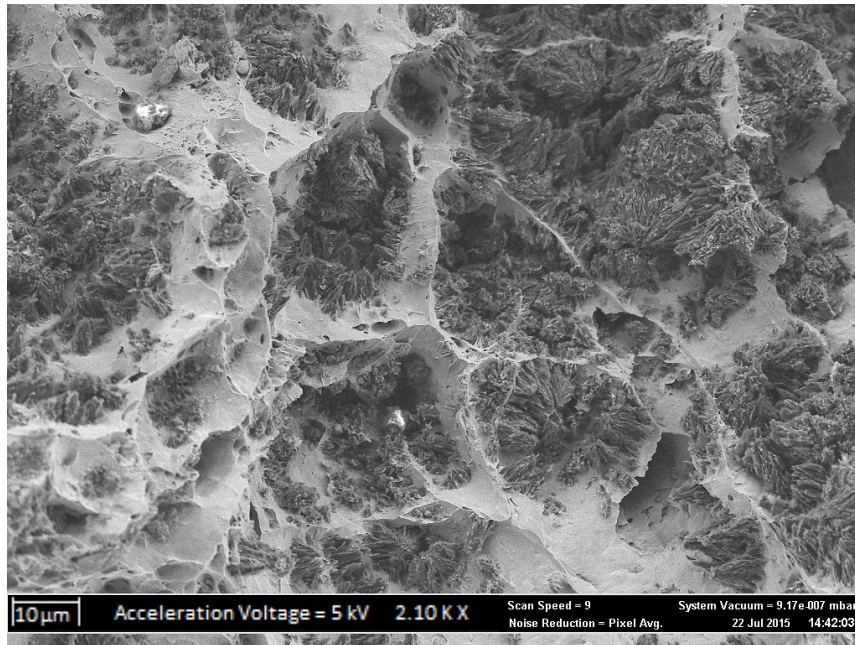
Figure 108: SEM image of graphite particles in the tensile fracture surface of sample 4 (Material was tested in the service exposed condition with no further welding or heat treatments performed in order to establish a test baseline)

Figure 109 shows the extent of the graphite colonies present in sample 4, and is a higher magnification of Figure 103.
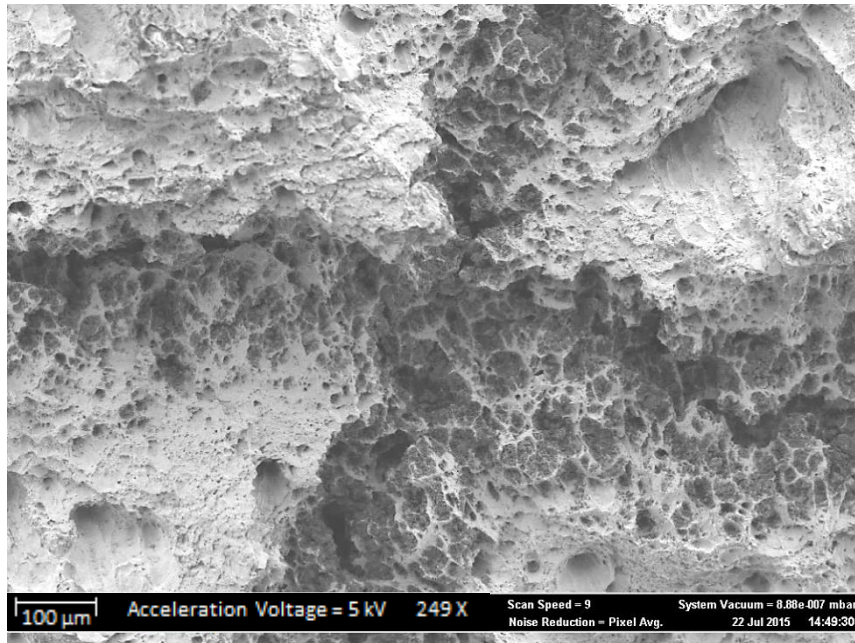
Figure 109: SEM image of graphite particles in the tensile fracture surface of sample 4 using the SE detector (Material was tested in the service exposed condition with no further welding or heat treatments performed in order to establish a test baseline)

HAZ microstructure prepared from the full section tensile test sample

Figure 110 shows the fully pearlitic structure of the material near the HAZ of sample 4. The cementite that is present in the microstructure as a lamellar structure is hard and highly resistant to plastic deformation. As a result, the structure is highly effective at arresting cracks in the through thickness direction and resisting plastic deformation, and thus the pearlitic structure present in sample 4 displayed the highest tensile strength of the samples that were tested.
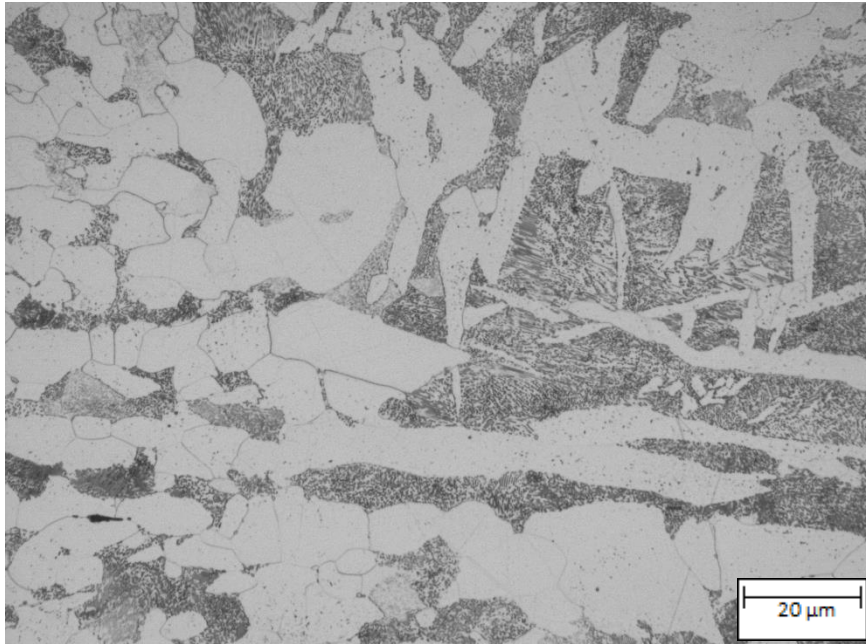
Figure 110: Light microscope image of the fully pearlitic structure of sample 4 near the HAZ of the full section tensile test specimen (Material was tested in the service exposed condition with no further welding or heat treatments performed in order to establish a test baseline).

Rolled in inclusions appeared to be present in all samples, with sample 4 being no exception as seen in Figure 111. These inclusions were clearly favourable graphite nucleation and growth sites due to the fact that graphite is often associated with such inclusions.

Figure 111: Rolled in inclusion in the HAZ region of the full section tensile test specimen of sample 4 (Material was tested in the service exposed condition with no further welding or heat treatments performed in order to establish a test baseline)

The following samples were cut at cross sections to the pipe thickness through the graphitized HAZ in a direction which is parallel to the welding direction as seen in Figure 112 and Figure 113.
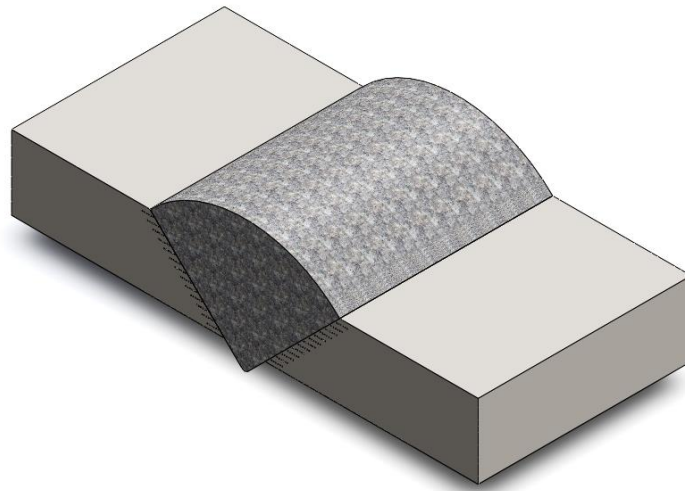
Figure 112: Isometric view of the as-received weld showing the graphitized HAZ
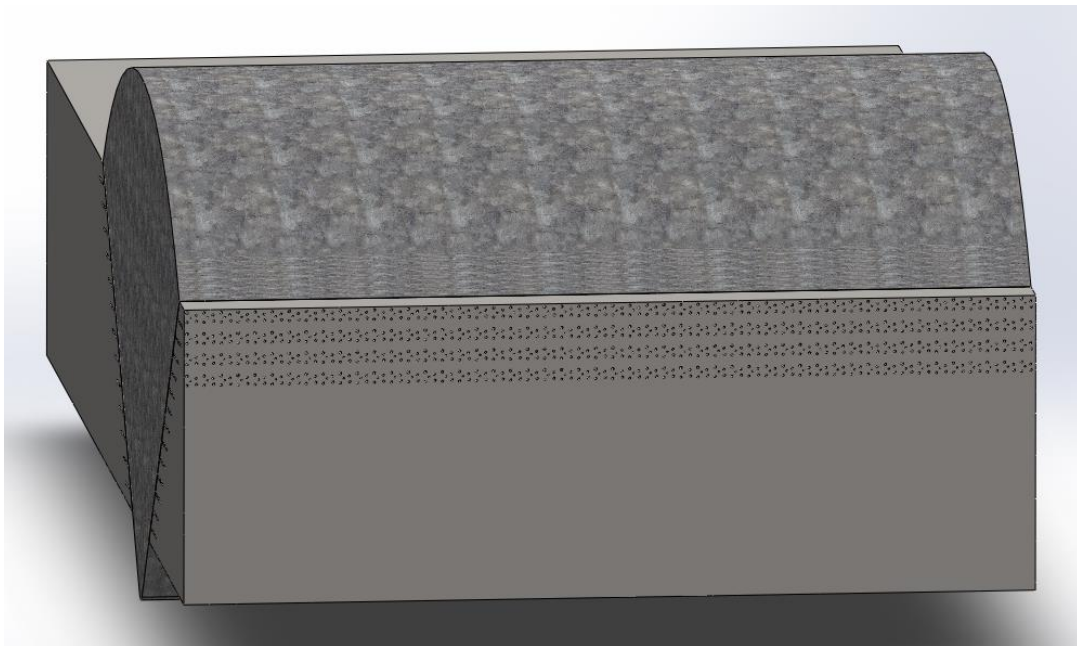
Figure 113: Section through which the sample was cut in order to reveal the microstructures as seen in Figure 114 and Figure 115.

Figure 114 shows the severity of the graphitized plane which can only be observed in the cutting direction explained in Figure 113. The image illustrates the graphite density in the direction running parallel to the weld pool and the resultant crack (from tensile overload) assumes a stepwise cracking sequence due to the geometry of the graphite formation.
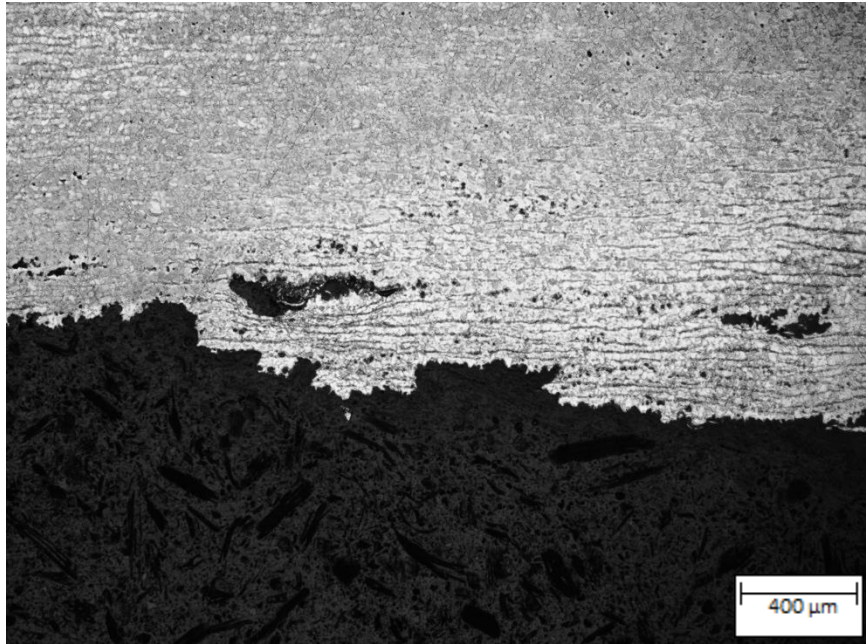
Figure 114: Light microscope image of the cross section of the pipe thickness which was cut through the fractured HAZ. (Material was tested in the service exposed condition with no further welding or heat treatments performed in order to establish a test baseline)

Figure 115 is a 9 image composite image that was constructed in order to illustrate the high concentration of graphite in unstrained material of the partially transformed region of sample 4. These graphite particles were orientated largely in the direction that ran parallel to the weld, however due to the large number of nodules, the graphite that formed parallel to the welding direction and to the rolling direction often lined up in the through thickness direction. This formed a graphite colony that was orientated in the through thickness direction of the pipe as indicated in Figure 115.
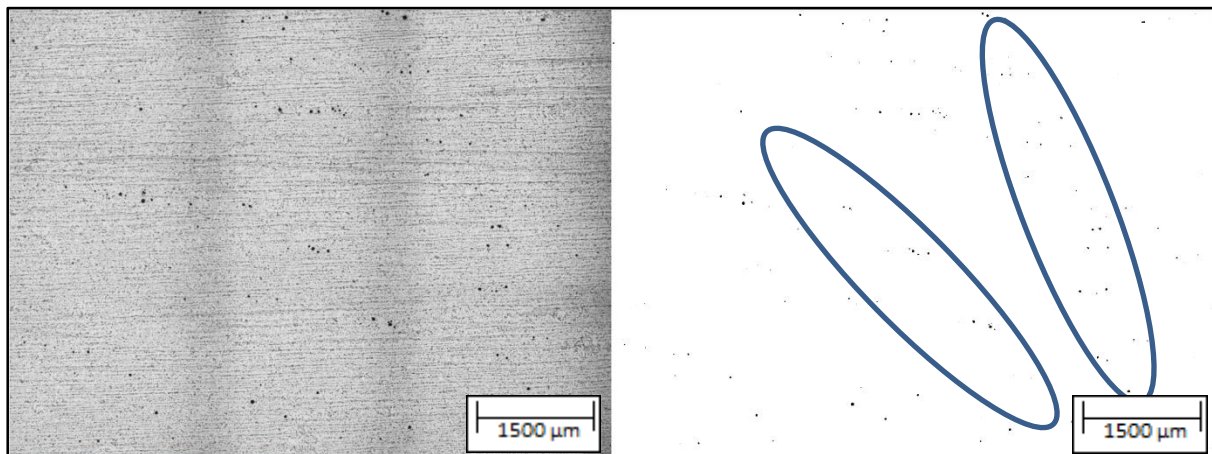
Figure 115: Light microscope image of the cross section of the pipe thickness which was cut through unstrained HAZ material. Left is the original image and the right image is an ImageJ processed image that highlights the graphite only. (Material was tested in the service exposed condition with no further welding or heat treatments performed in order to establish a test baseline)

Reduced section round tensile sample

Figure 116 shows the fracture surface of the reduced section round tensile test sample. There are no graphite planes running across the surface.
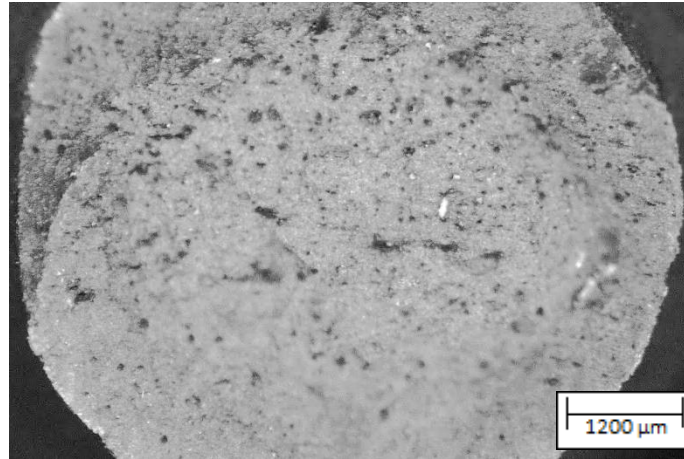
Figure 116: Stereoscopic image of the reduced section tensile test specimen of sample 4 (Material was tested in the service exposed condition with no further welding or heat treatments performed in order to establish a test baseline) RA = 74%

Figure 117 shows a graphite nodule on a polished cross section from the fracture surface. The graphite flakes that form at the extremities of the particle appear to be growing in preferred directions. This yet again suggests that there are some favourable growth directions within the material.
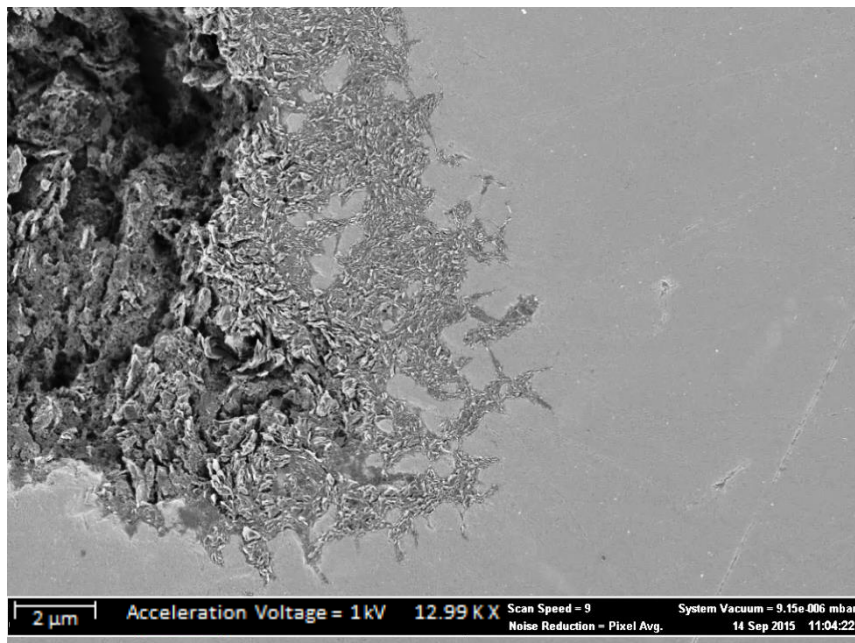
Figure 117: SEM image of a polished cross section of the fracture surface of of the reduced section round tensile test specimen of sample 4 (Material was tested in the service exposed condition with no further welding or heat treatments performed in order to establish a test baseline) RA = 74%

Reduced section hot round tensile sample

SEM analysis of the reduced round hot tensile 4 revealed linear tears and large graphite colonies that are present on the fracture surface as seen in Figure 118.
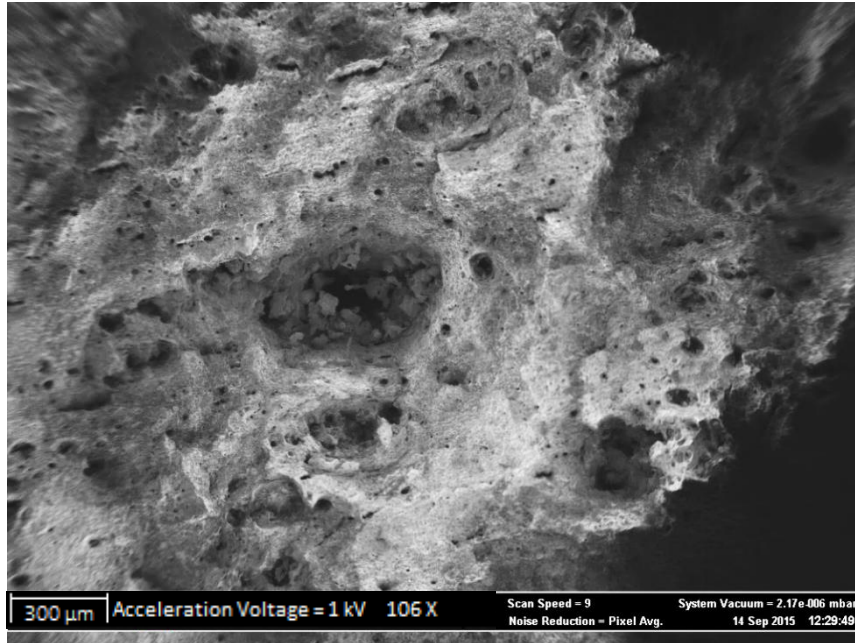
Figure 118: SEM image of large graphite colonies on the fracture surface of the reduced section hot round tensile test specimen of sample 4 (Material was tested in the service exposed condition with no further welding or heat treatments performed in order to establish a test baseline) RA = 77%

It can be seen in Figure 119 that there are deep tears in the hot sample in excess of 400 μm.
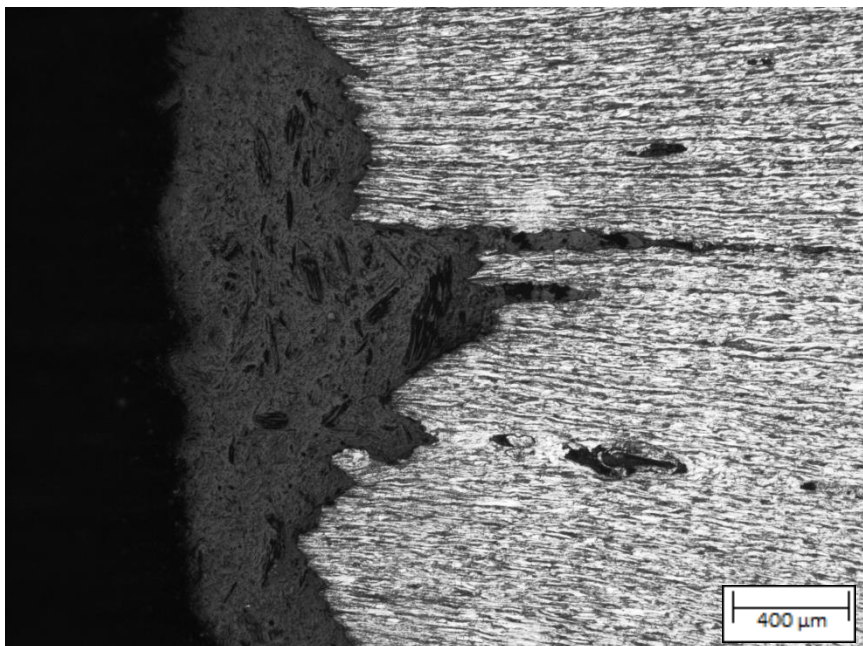
Figure 119: Light microscope image of polished cross section of the fracture surface of the reduced section hot round tensile test specimen of sample 4 (Material was tested in the service exposed condition with no further welding or heat treatments performed in order to establish a test baseline) RA = 77%

Figure 120 shows that there was a distinct absence of the large volumes of graphite that have commonly been associated with the partially transformed HAZ. It is not uncommon for there to be a degree of variation in terms of the graphite density throughout a welded joint. The partially transformed HAZ, while its chances of containing large amounts of graphite are higher, is no exception to the fluctuation in graphite concentration. This low graphite content would explain the failure of the base metal in the hot tensile test of sample 4 rather than the HAZ.
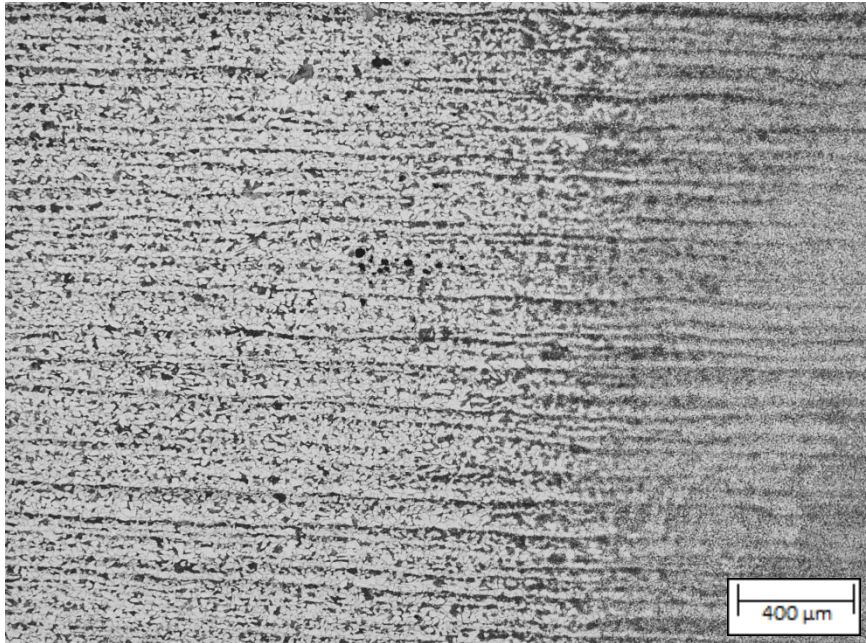
Figure 120: Light microscope image of the HAZ of the reduced section hot round tensile test specimen of sample 4 (Material was tested in the service exposed condition with no further welding or heat treatments performed in order to establish a test baseline) RA = 77%

3.9.3. Severely etched sample

Graphite nodules contain small iron particles that form as a result of carbide dissolution. In an effort to characterize the growth and shape of the layers of graphite within the nodules, one sample (sample 4) was severely etched using a 4% Nital solution by submerging the sample for 5 minutes.

It was possible to identify a nucleation site as seen in Figure 121 which shows a round inclusion associated with the graphite. It appears to be approximately in the centre of the nodule which suggests that this is the nucleating particle, and also indicates that the graphite has grown at approximately the same rate in all directions.
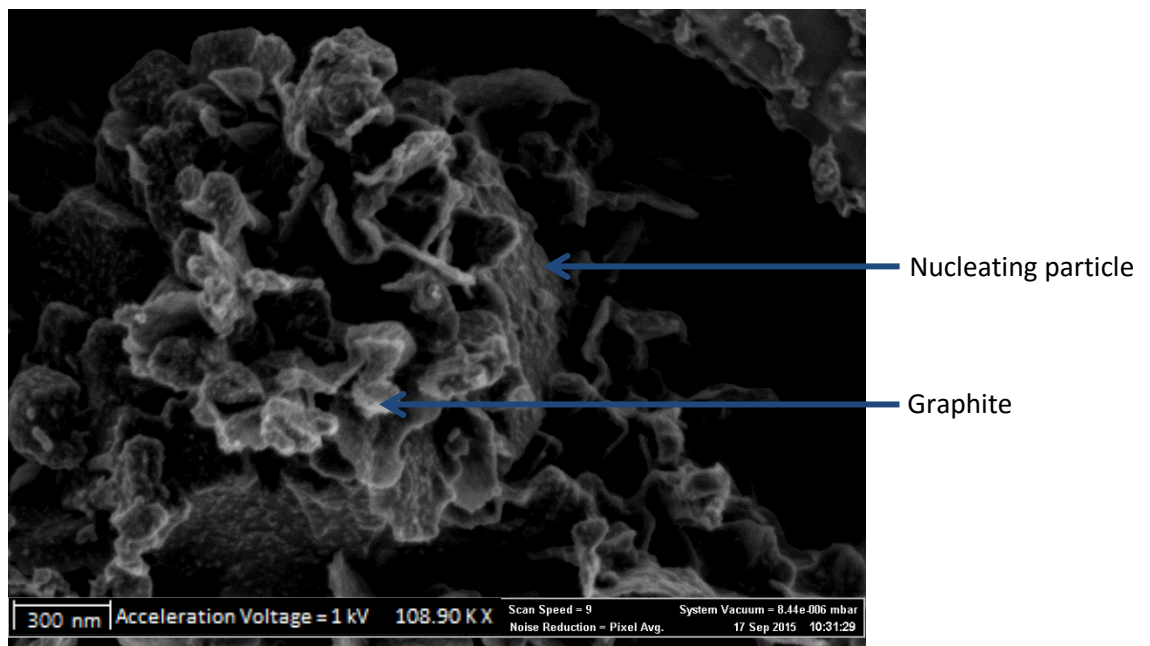
Figure 121: SEM image of a round inclusion that is partially concealed by graphite has nucleated onto in the inclusion. The sample was a polished cross section of the full section tensile test of sample 4 on the side of the weld where the HAZ remained intact. (Material was tested in the service exposed condition with no further welding or heat treatments performed in order to establish a test baseline).

In many small nodules, it can be seen that the growth of the graphite is extremely irregular. This can be seen in Figure 121, Figure 122 and Figure 123.
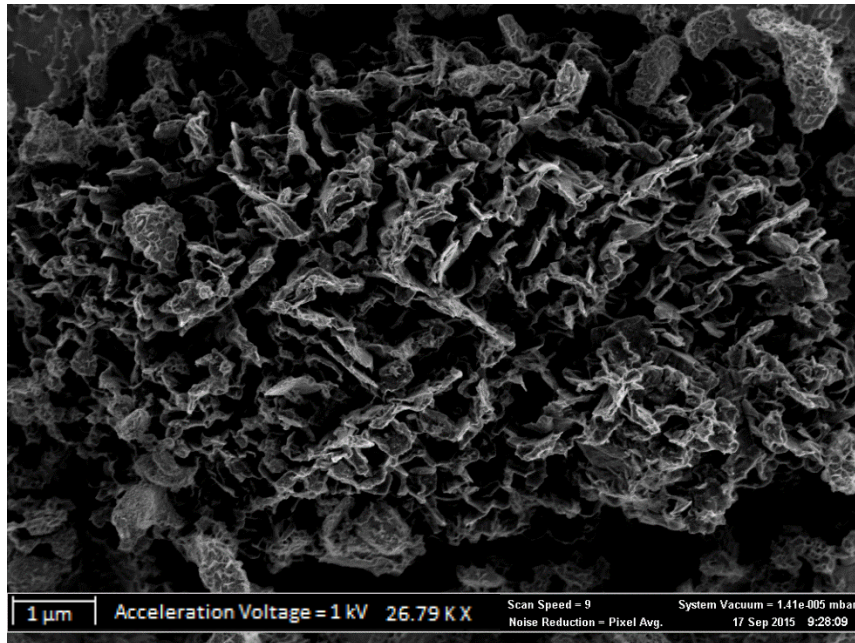
Figure 122: Highly irregular growth pattern of graphite.

Graphite

Elongated inclusion
(Nucleating particle)
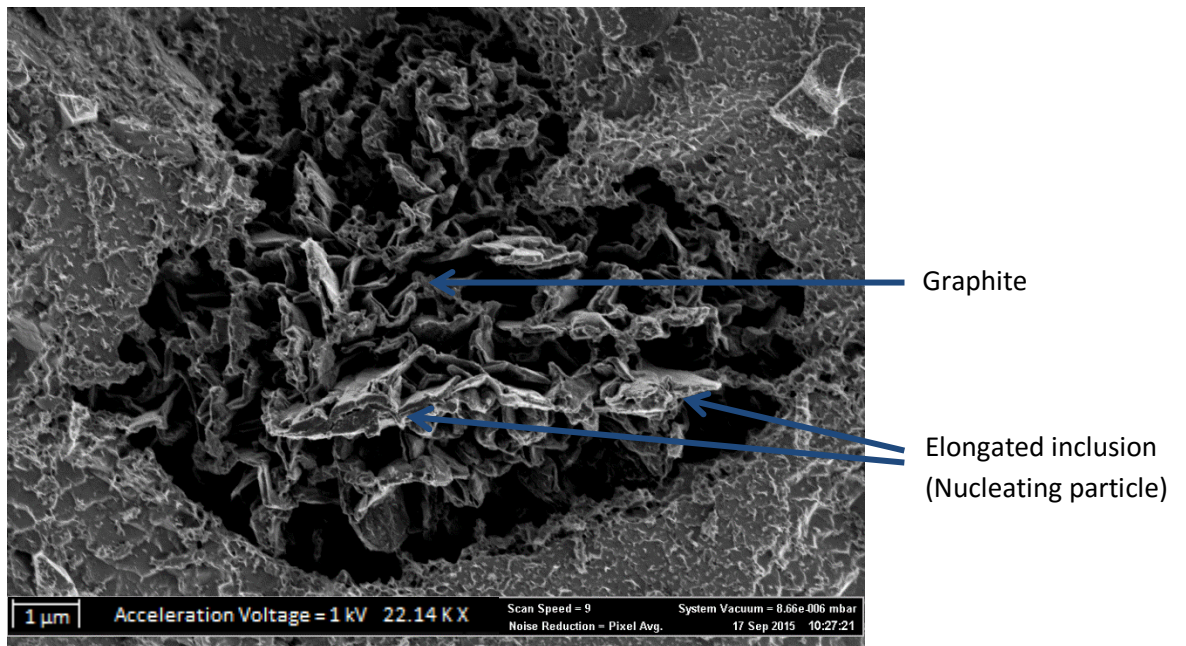
Figure 123: Elongated nucleating particle, with graphite growing in similar patterns as seen in Figure 121 and Figure 122.

135

3.9.4. Summary of the metallographic observations

Types of failure

It can be concluded that there are two distinct failure types: Base metal failure (Figure 124 & Figure 125); and HAZ graphite failure (Figure 126 & Figure 127).

Samples that failed through the graphitized HAZ displayed step like cracking where the crack would run in parallel to the graphite cluster until another graphite cluster became available in the direction which is perpendicular to the clusters. Once this occurred, the crack would run perpendicular to the first graphite cluster until it reached the next cluster where it would again run parallel as seen in Figure 124.
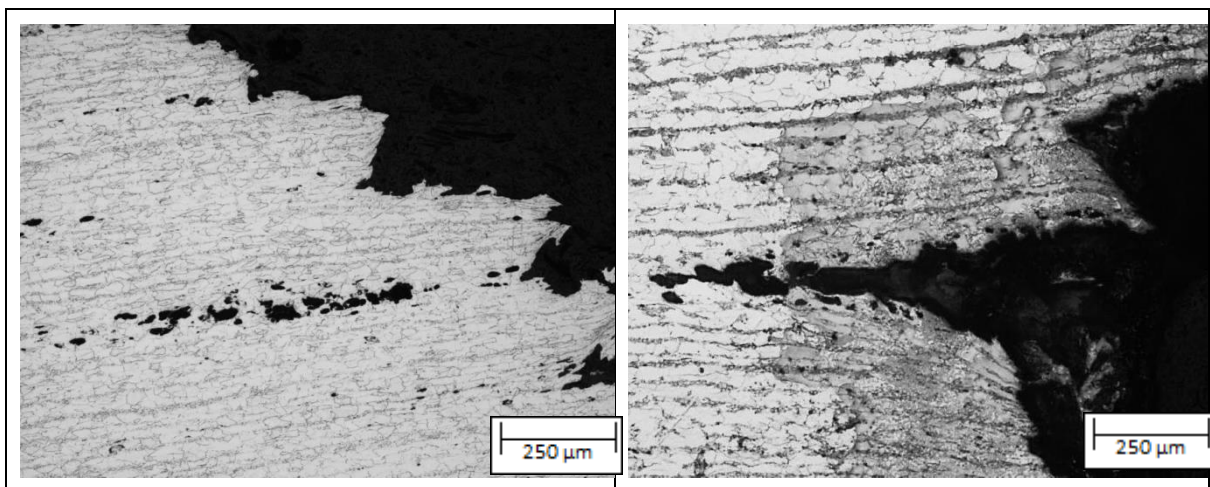
Figure 124: Light microscope images of tensile samples that experienced graphitized HAZ failures. The left hand image is of sample 3 while the right hand image is of sample 4

The resultant fracture surface also clearly shows the presence of large quantities of graphite as seen in Figure 125.
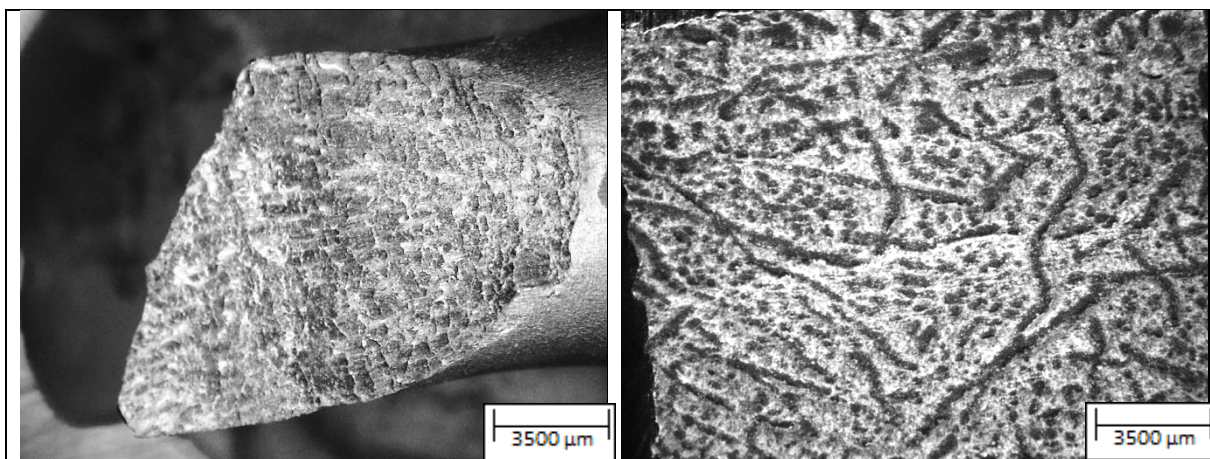
Figure 125: Stereoscopic images of graphitized HAZ tensile test fracture surfaces. The image on the left shows the graphitized fracture surface of sample 3 while the image on the right shows the graphitized fracture surface of sample 4.

Samples that failed through the base metal displayed no preferred plane on which fracture took place. This can be seen in Figure 126.

© University of Pretoria
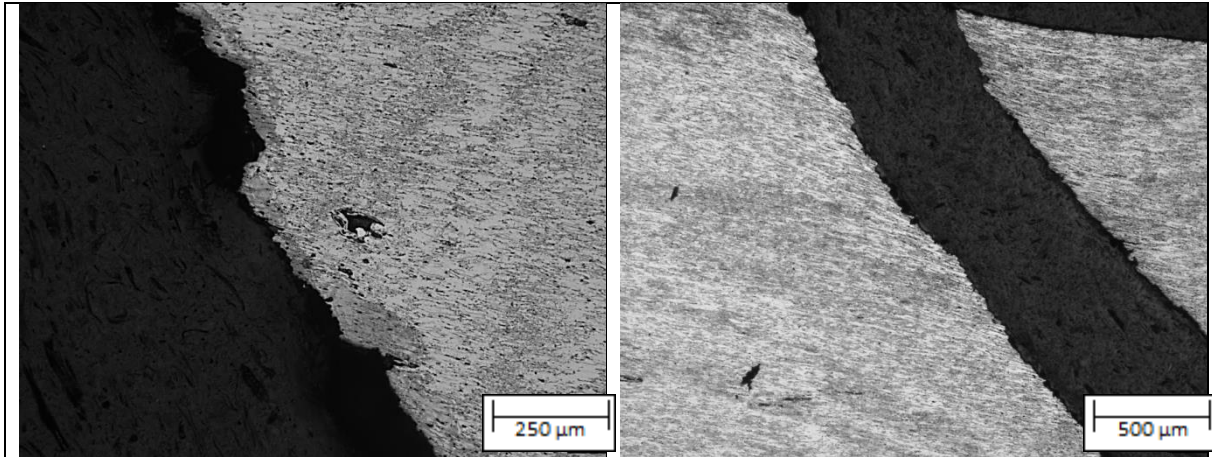
Figure 126: Light microscope images of tensile samples that fractured in the base metal. The left image is an image of sample 1 full section tensile test, while the right image is of sample 3 full section tensile test

The fracture surfaces of samples that failed in the base metal do not display any heterogeneous features as that seen in Figure 125. Figure 127 shows that there were several randomly distributed graphite nodules present on the fracture surfaces of samples that failed through the base metal, however the quantity of graphite on these fracture surfaces are insignificant in comparison to that seen in Figure 125.
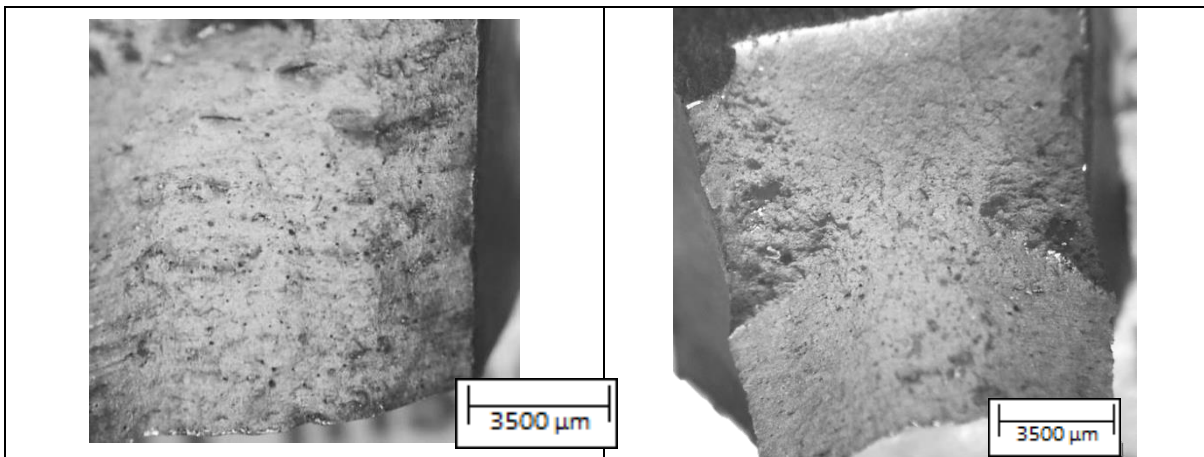
Figure 127: Stereoscopic images of tensile test fracture that failed in the base metal. the image on the left was taken from the full section tensile test of sample 1 while the image on the right was taken from the full section tensile test of sample 3

Loss of strength due to spheroidization

Samples 1-3 have all experienced at least 600 hours of heat treatment at 635°C while sample 4 did not experience this thermal treatment. The effects that this extended heat treatment had on the tensile properties of samples 1-3 were that all three of these sample sets experienced a reduction in tensile strength of approximately 35 MPa. This drop in tensile strength can be attributed to the complete spheroidization of the pearlite in samples 1-3. This is graphically represented in Figure 128 and compared to the microstructure of sample 4 which, despite have undergone approximately 35 years of service at 420°C, shows little to no spheroidization.

137
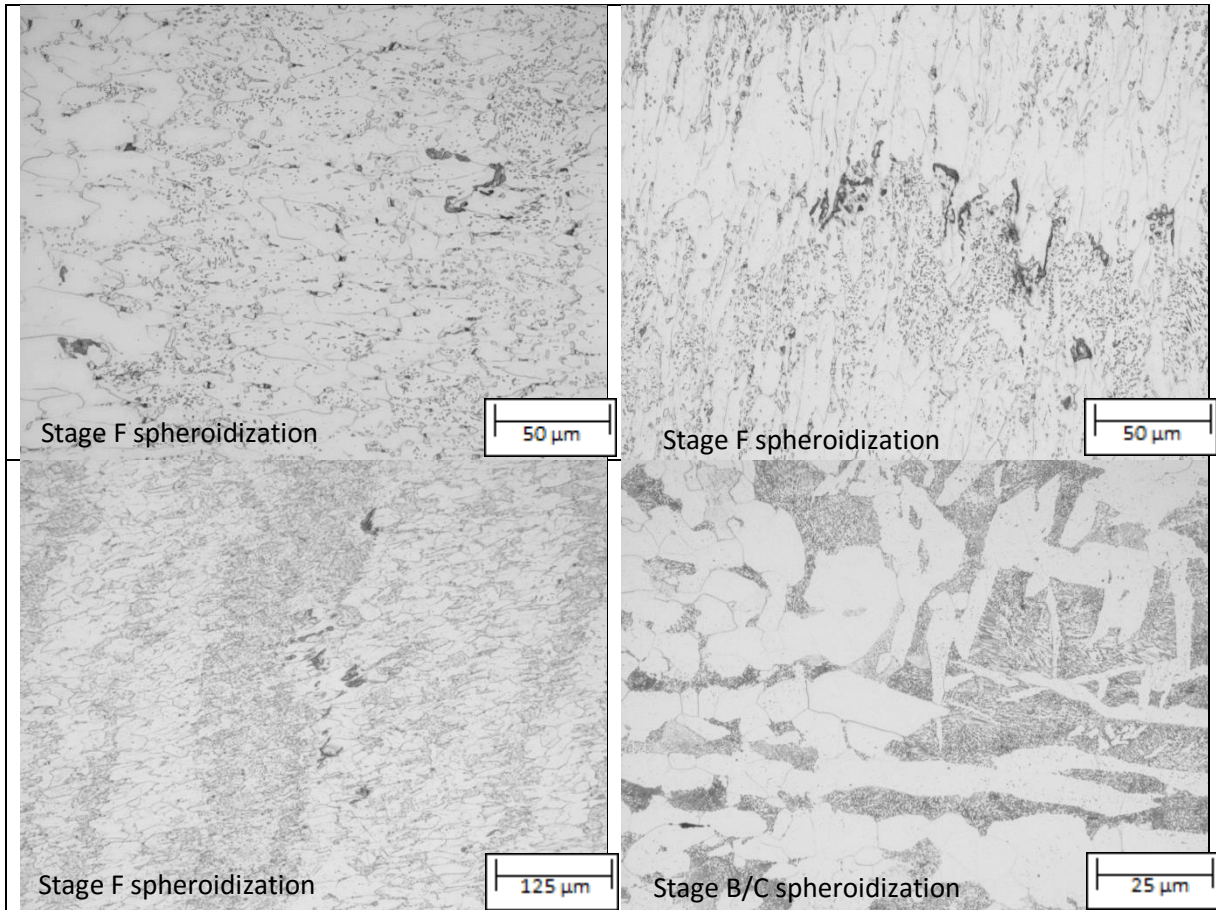
Figure 128: Light microscope image of the degree of spheroidization of sample 1 (top left), 2 (top right), 3 (bottom left) and 4 (bottom right)

3.9.5. Quantitative metallography

Quantitative metallography was used in the form of point counts in order to determine the volume fraction of graphite that is present in the base metal of each sample as well as in the partially transformed region of the HAZ of each sample (41).

Each sample was measured using 3 fields of view. Due to the erratic position of graphite, the fields of view were chosen in such a way so as to include a representative amount of graphite in each image. Table 25 shows the results of the quantitative metallography with confidence intervals included (42).

Table 25: Number of points that fell on graphite and the resultant volume fraction and 95% confidence intervals of graphite based on each sample undergoing 3000 point counts.

Region measured	Sample 1	Sample 2	Sample 3	Sample 4
Base metal	12 points 0.40% 0.40 ± 0.23	6 points 0.20% 0.20 ± 0.08	14 points 0.47% 0.47 ± 0.13	11 points 0.37% 0.37 ± 0.11
Partially transformed HAZ	10 points 0.33% 0.33 ± 0.11	3 points 0.10% 0.10 ± 0.06	3 points 0.10% 0.10 ± 0.06	66 points 2.20% 2.20 ± 0.27

The average amount of graphite that was present in base material remains low throughout all the samples. Sample 4 is the only sample that contained an original intact weld and thus is the only sample that displayed HAZ graphitization. It must be noted that sample 3 contains an original intact weld and HAZ, however this region was not evaluated and only the new welds of sample 3 were evaluated.

Table 26 indicates the apparent amount of graphite present directly adjacent to the fracture surface and its relation to the amount of graphite observed on the fracture surface. It can be seen that there is a sharp rise in both these values when a sample fails through the HAZ.

Table 26: Summary table correlating the amount of graphite observed on the fracture surface to the amount of graphite observed in the cross section on the material directly adjacent to the failure location. Data was obtained from rectangular cross section samples.

Sample no.	Failure location	Percentage graphite at failure location	Percentage graphite on fracture surface
1	Base metal	0.40 ± 0.23	6.00
2	Base metal	0.20 ± 0.08	3.50
3	Base metal	0.47 ± 0.13	1.00
4	HAZ	2.20 ± 0.27	55.00

3.9.6. Microstructural similarities and differences between graphite nodules, voids and inclusions

Due to the fact that nodules appear black on micrographs, these nodules could possibly be microstructural features other than graphite, such as creep voids or inclusions. The appearance of creep voids and graphite can be similar. See for example, French (43).

Creep voids

Due to the size and spherical shape of the feature, these black spots could be creep voids. At higher magnification, the circular features usually display an irregular interface with the surrounding matrix. The interface of a creep void is generally smooth (43). Additionally, under close inspection a substructure is observed, as seen in Figure 129 & Figure 130. Furthermore, under high resolution SEM analysis, no evidence of creep voids were detected on polished cross sections. EDS analysis of voids would result in a chemical response that would approximate the bulk chemical composition as seen

in the EDS results of section 3.10. The grade of material used in thus study typically displays high creep ductility and formation of creep voids occurs only shortly before creep failure (44). In summary, the presence of creep voids cannot be excluded, however it is the opinion of the author that most of the features are the product of graphitization, and not of the formation of creep voids.
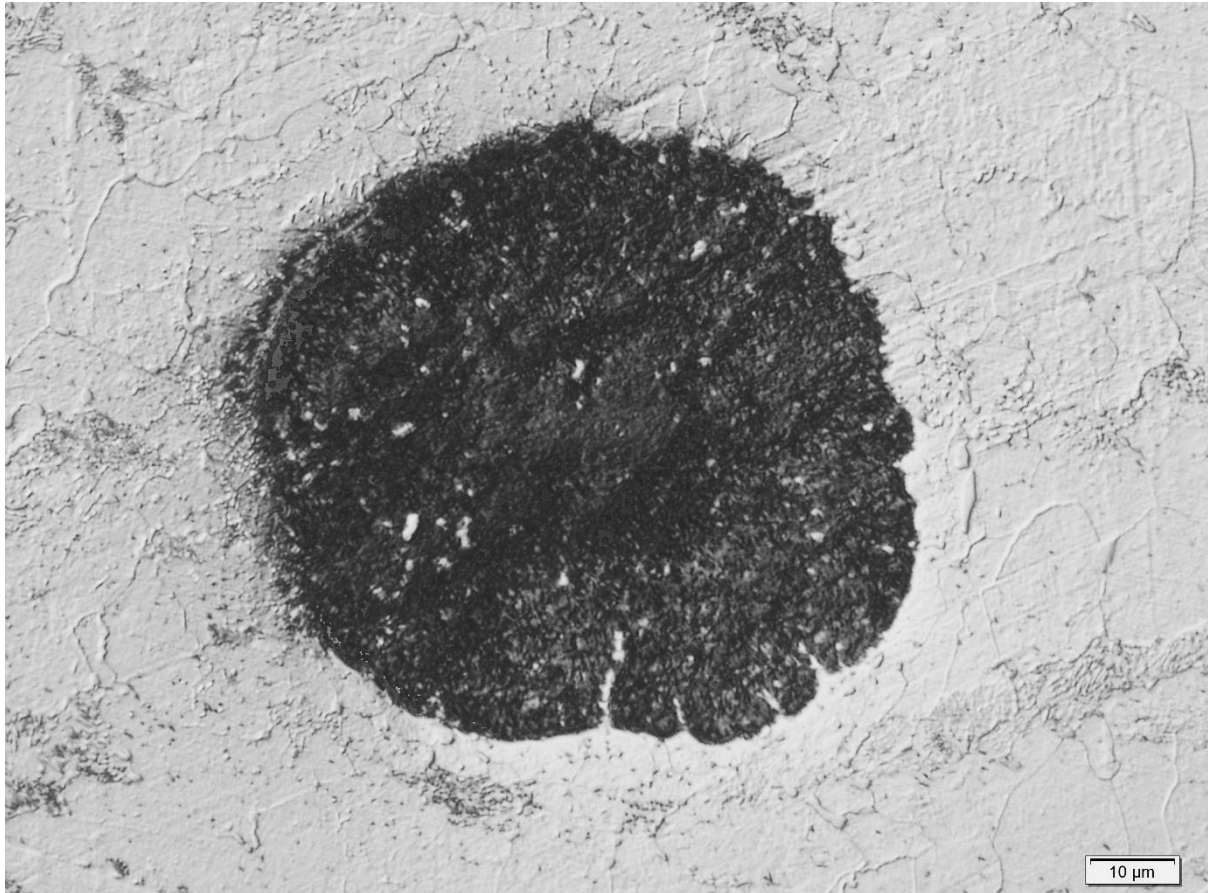
Figure 129: High magnification (1000X) of round black spot in the base metal of service exposed material (Material was in the service exposed condition with no further welding or heat treatments performed in order to establish a test baseline).

Notice slight colour variations indicating texture
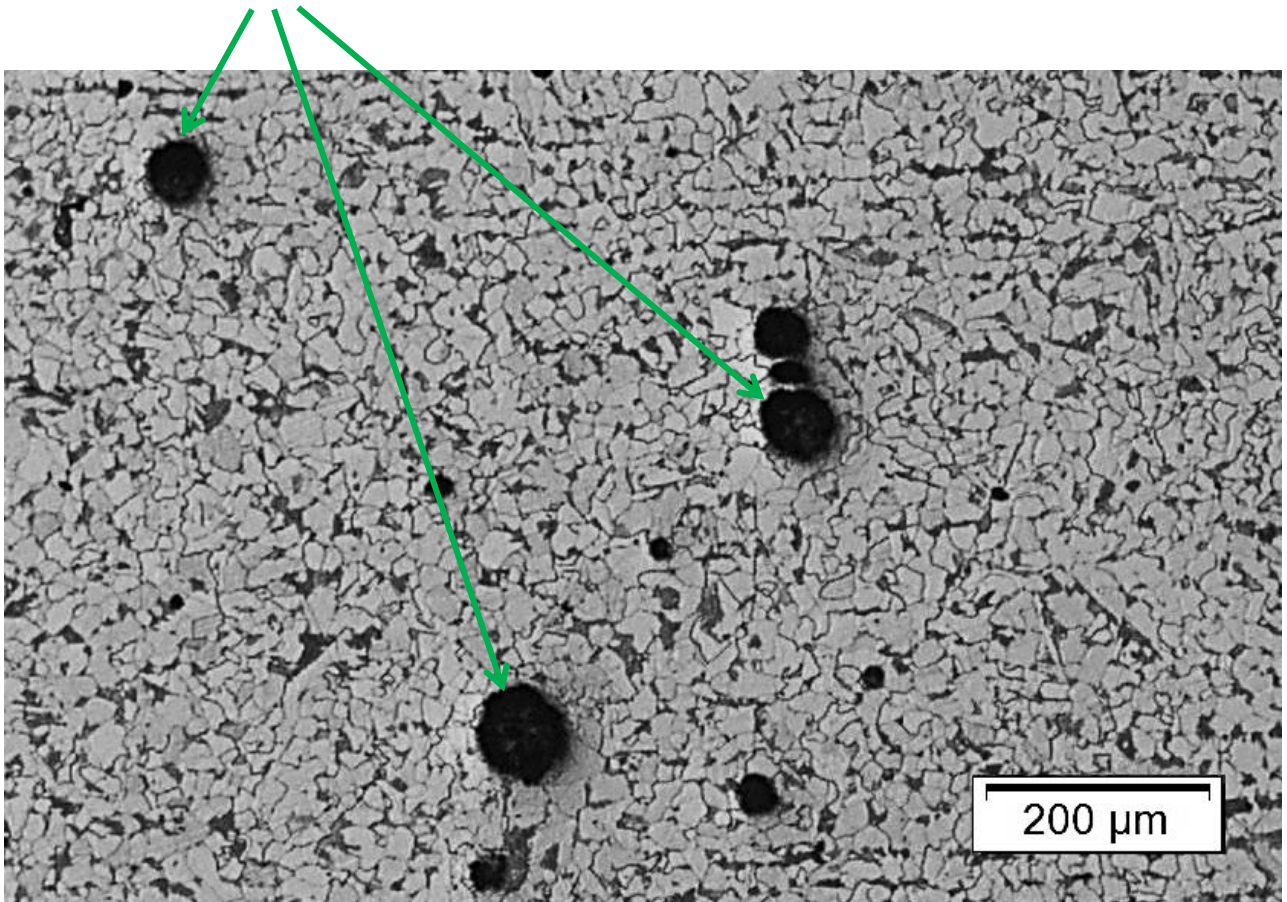
Figure 130: Low magnification (50X) of round black spot in the base metal of service exposed material (Material was in the service exposed condition with no further welding or heat treatments performed in order to establish a test baseline).

Inclusions

Inclusions have been detected (Figure 53, Figure 54, Figure 79, Figure 80 and Figure 111) and it has been demonstrated that the inclusions observed in the current study display morphology consistent with MnS stringers.

3.10. Chemical Analysis

The chemical composition of both the weld metal and the base material was checked for all four samples using Spark Emission Analysis (SEA). Each weld was tested once and the base metal on either side of the weld was tested once. Table 27 shows the results of the base metal test while Table 28 shows the results of the weld metal tests.

Table 27: Chemical analysis of the base metal of sample 1-4

Sample No.	% C	% Mn	% Cr	%Al
Requirement	0.30 (Max)	0.85-1.20	0.40 (Max)	-
1	0.22	0.81	0.009	0.006
	0.22	0.79	0.009	0.007
2	0.23	0.82	0.010	0.005
	0.20	0.80	0.010	0.010
3	0.14	0.79	0.030	0.050
	0.20	0.78	0.009	0.006
4	0.30	0.81	0.009	0.006
	0.14	0.77	0.030	0.040

Table 28: Chemical analysis of the weld metal of samples 1-4

Sample No.	% C	% Mn	% Cr	%Al
1	0.05	1.36	0.07	<0.002
2	0.04	1.38	0.05	<0.002
3	0.07	1.13	0.03	0.004
4	0.07	0.97	0.35	0.007

There were no abnormalities in the weld metal chemistries. The carbon content of sample 3-1 and sample 4-2 are lower than expected, however no evidence of low carbon contents were detected in the microstructures with regards to the amount of pearlite present in the material. It is possible that the low base metal carbon content reported for sample 4 (0.14% - Table 27) was the result of partial sampling of weld metal, that on average contained about 0.06% C (Table 28).

Additionally, Electron Diffraction Spectroscopy (EDS) was performed on the graphite nodules to confirm that the chemistry of the nodules. Figure 131 - Figure 135 shows the positions of four EDS scans as well as the spectrum results. The results confirm that the nodules, once etched, consist almost exclusively of carbon.
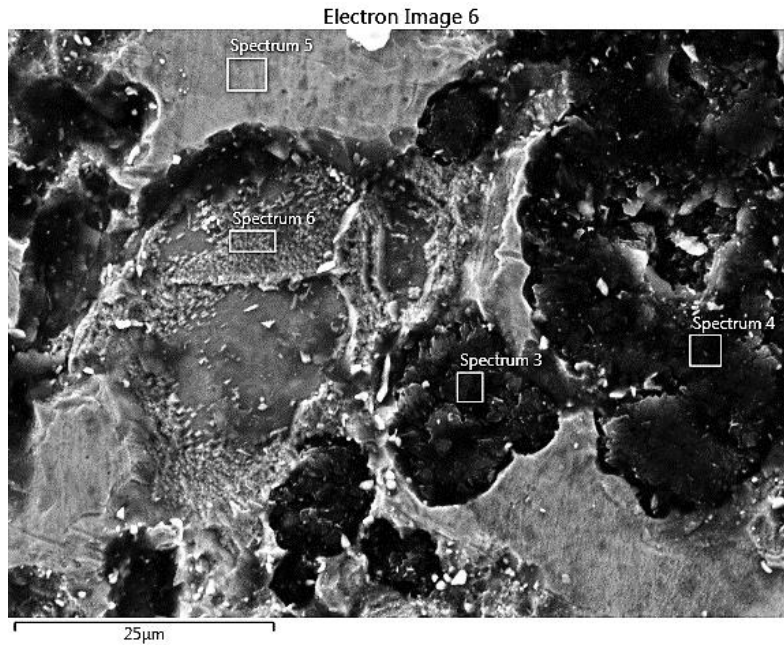
Figure 131: SEM image indicating the position of the four EDS scans. The sample was a polished severely etched cross section of the full section tensile test of sample 4 on the side of the weld where the HAZ remained intact
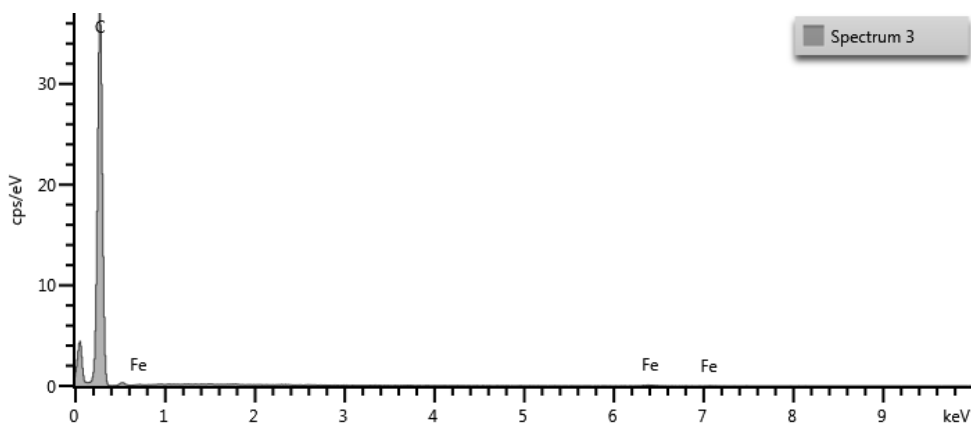
Figure 132: EDS results of nodule 1 indicating extremely high carbon content.
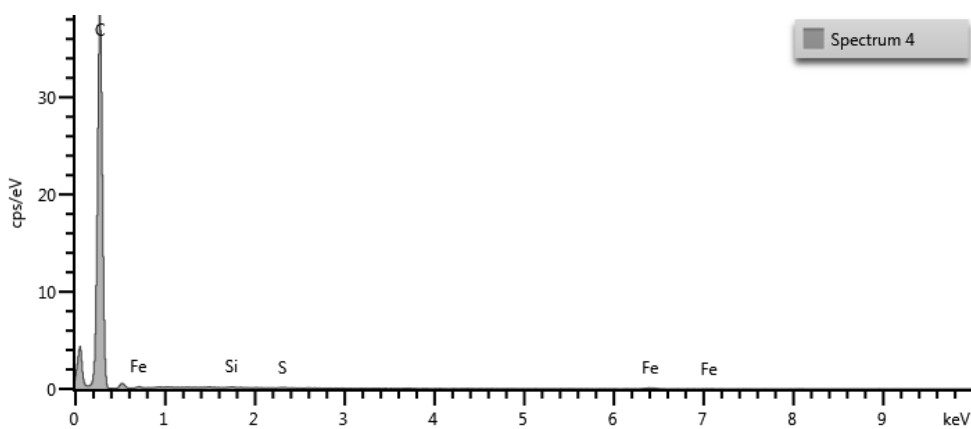
Figure 133: EDS results of nodule 2 indicating identical EDS results. This confirms the results obtained from nodule 1.

143
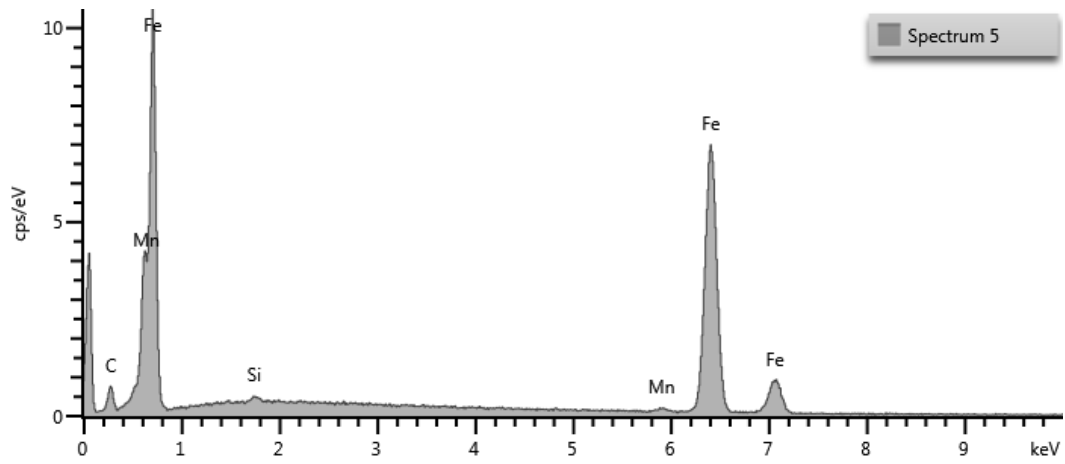
Figure 134: EDS results of metallic material near a graphite nodule.
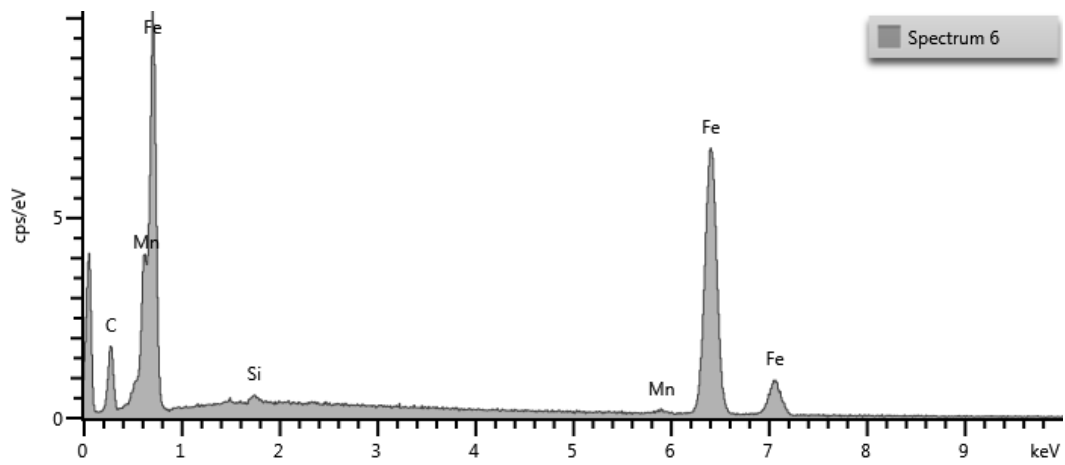
Figure 135: EDS results of carbide near the graphite nodule indicating appreciably higher carbon content than the metallic material.

Chapter 4 – Discussion

4.1. Base metal grade

Material grade is not only determined by chemistry, but also prior heat treatment, whether the material was formed hot or cold, as well as the material grain size. All these factors influence the final mechanical properties of material and therefore dictate the mechanical properties that the material must conform to in order to pass welding tests such as ASME IX requirements.

Two possible material grades were identified for the pipeline, SA-516 Grade 65 and SA-516 Grade 60.

In order for the welded joint to have passed the tensile tests, the following criteria needed to be met if the material grade is assumed to be SA-516 grade 65:

1. If the material fails in the weld metal, the minimum allowable tensile strength must match the minimum tensile strength of the base material. In this case, the minimum tensile strength of the base material is 450 MPa. Additionally the material must display a minimum elongation of 22%.
2. If the material fails in the base metal, the minimum allowable tensile strength is dictated by the minimum tensile strength of the base metal, but allows a concession of -5% in tensile strength. This allows material that fails in the base material to have a minimum tensile strength of 428 MPa and still pass the tensile test as prescribed by ASME IX section QW-153.1(d) (2).

If the material was assumed to be SA-516 grade 60, the following criteria needed to be met.

1. If the material fails in the weld metal, the minimum allowable tensile strength must match the minimum tensile strength of the base material. In this case, the minimum tensile strength of the base material is 415 MPa. Additionally the material must display a minimum elongation of 22%.
2. If the material fails in the base metal, the minimum allowable tensile strength is dictated by the minimum tensile strength of the base metal, but allows a concession of -5% in tensile strength. This allows material that fails in the base material to have a minimum tensile strength of 394 MPa and still pass the tensile test as prescribed by ASME IX section QW-153.1(d) (2).

Table 29 is a replica of Table 16

Table 29: Full section tensile test results for samples 1-4. The tensile strength and elongation required as prescribed by ASME IX has also been inserted for SA-516 Grade 60 and Grade 65

Sample #	Yield strength 0.2% offset (MPa)	Tensile strength (MPa)	Total elongation (%)	Location of failure
1	263	410	42	Base material
	245	416	38	Base material
2	268	416	45	Base material
	269	418	44	Base material
3	259	418	52	Base material
	277	419	47	Base material
4	272	451	48	HAZ
	277	450	46	HAZ
SA-516 Grade 65	240	450	23	-
SA-516 Grade 60	220	415	25	-

Table 30 summarises the acceptance criteria of samples 1-4 based on the tensile strengths of SA-516 grade 65 and grade 60 respectively.

Table 30: Summary of tensile test results using SA-516 grade 65 and SA-516 grade 60 respectively

Variable	Sample 1	Sample 2	Sample 3	Sample 4
Failure location	Parent metal	Parent metal	Parent metal	Weld
Required tensile strength for grade 65 (MPa)	428	428	428	450
Pass/Fail for grade 65	Fail	Fail	Fail	Fail
Required tensile strength for grade 60 (MPa)	396	396	396	415
Pass/Fail for grade 60	Pass	Pass	Pass	Pass

All welded joints (samples 1-4) consistently met the requirements of SA-516 Grade 60.

4.2. Sample Selection

The samples were selected by analysing the material metallographically in order to determine which material had experienced the most graphitization prior to any further processing. The reason for this was that any subsequent attempts to increase the graphite content in a particular sample would have a higher chance of success when working with a material that demonstrated to have a tendency to graphitize faster than other material that was available for use in this project.

Despite literature indicating that material with elevated concentrations of carbon, silicon, and aluminium, and reduced concentrations of manganese would preferentially form graphite, the

146

microstructural investigation indicated that the chemistry was not the only contributing factor. It was determined that, based on the chemistries, sample W 23 DS should have been the least susceptible to form large amounts of graphite (14), but instead formed the most graphite of the samples that were analysed (Figures 24 - 29). Due to the findings from the metallographic investigations, the final decision was made to use material from the sample identified as W 23 DS.

4.3.   Heat treatment

The initial graphitization heat treatment study was performed in a laboratory furnace at the University of Pretoria, while the full scale pre and post weld heat treatments were performed in a larger furnace in Secunda.

4.3.1.   Initial heat treatment

The initial goal of the prolonged heat treatment was to increase the graphite content in the samples as much as possible before continuing with the project. The initial graphitization heat treatment study proved that this was possible to deteriorate the microstructure further by spheroidizing the pearlite (transformation of the lamellar structure of pearlite, to the spherical structure of spheroidized iron carbide). The spheroidization of carbides can be seen in Figure 136.
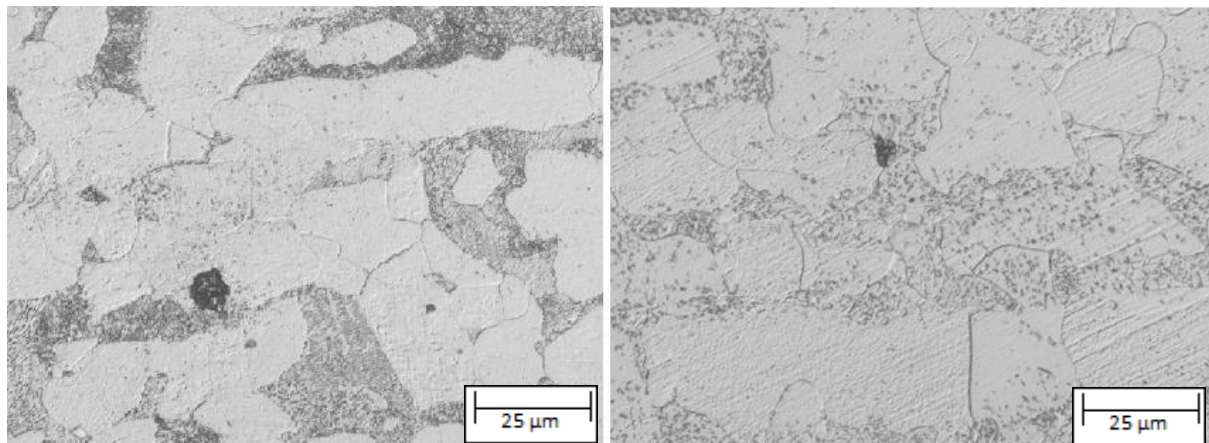
Figure 136: Light microscopy image of sample W 13 DS where microstructural degradation occurred as a result of prolonged exposure (500h) to 635°C. Left image is the As-received microstructure while the right hand image is the same sample after 500 hours of exposure to 635°C. Note the spheroidization.
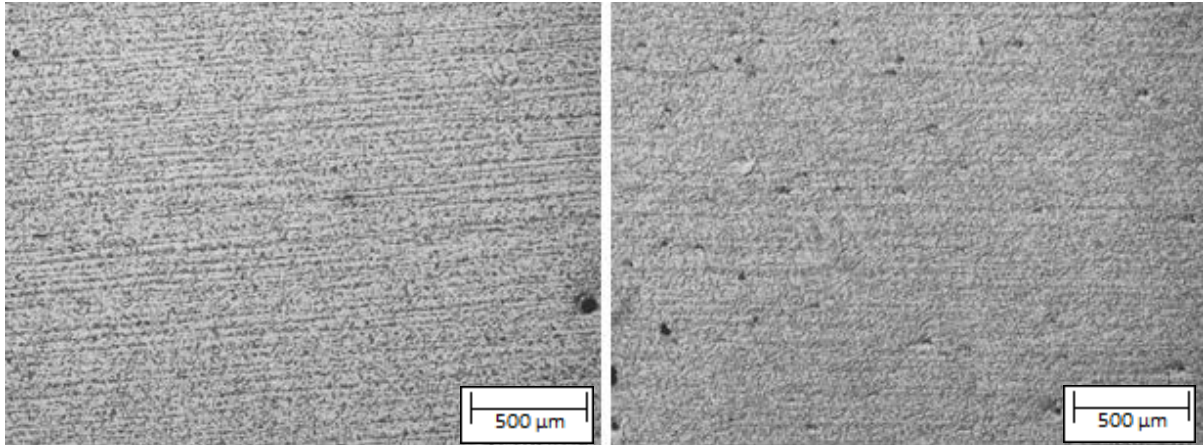
Figure 137: Light microscope images of sample W 24 DS which is chemically sensitive to graphitization according to literature in the as-received condition (Left) and after 500 hour of exposure to elevated temperature (Right)
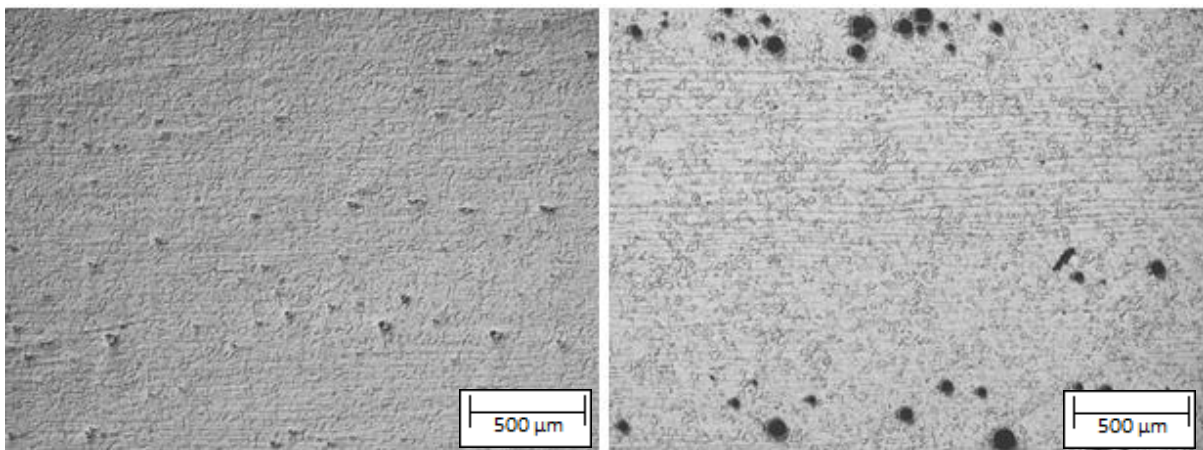
Figure 138: Light microscope images of sample W 23 DS which is chemically insensitive to graphitization according to literature in the as-received condition (Left) and after 500 hour of exposure to elevated temperature (Right)

These results also proved that steel chemistry in C-Mn steel has little to no effect on the tendency for steel to graphitize as seen in Figure 136 and Figure 137.

While spheroidization was not an outcome that was anticipated to occur in pipelines that are currently in operation, the process is known to reduce the tensile strength of carbon steels and thus, a more severe 'worst case scenario' was developed. Spheroidization typically occurs at higher temperature (6) such as at 635°C.

4.3.2. Pre-weld heat treatment

The pre-weld heat treatment was performed in order to replicate the results found in the initial graphitization heat treatment study. The largest possible graphite content prior to welding would qualify more severely graphitized material and therefore be of more value.

Several disruptions in power supply were experienced during the post weld heat treatment. It is likely that the disruption did however have little to no effect on the final outcome of the heat treatment.

148

This is because the graphite content in steel is a cumulative function of time at temperature. Because the heat treatment occurred at a temperature below the Ac_1 temperature, there were no massive phase transformations such as austenitization, and therefore the most important factors that needed to be maintain within acceptable ranges where the time at temperature and the maximum temperature. Both of these criteria were met and three interruptions were experienced (Table 12). Thus the pre-weld heat treatment was performed to a satisfactory level.

4.3.3. Post weld heat treatment

The PWHT experienced approximately 8 interruptions. The time at temperature was the main focus of the PWHT and thus an additional amount of time was added to ensure that the minimum requirement of 600 hours at temperature was obtained. Based on the recorded response of the furnace to previous interruptions in the pre-weld heat treatment, it was assumed that a similar furnace response could be expected in the PWHT.

The PWHT was performed in an attempt to produce new graphite in the new HAZ. The prolonged heat treatment was performed in order to test the hypothesis that graphite forms in the low temperature HAZ. After 672 hours of PWHT, no conclusive evidence of the formation of new graphite in the HAZ was identified. This demonstrates the low rate of graphite nucleation and growth and merely illustrates the slow kinetics that graphitization displays.

4.4. Tensile Test

In total, 3 samples of the 22 tensile tests that were performed (8 full section tensiles, 8 reduced section round tensiles, and 4 reduced section hot round tensiles) failed through the graphitized HAZ. The remaining 19 samples failed in the base metal away from the welded joint (see Table 16, Table 17 and Table 18)

Samples that were exposed to 635°C for periods of time in excess of 600 hours did display a lower tensile strength, however, the drop in tensile strength appears to plateau at a minimum of roughly 410MPa as seen in Figure 120. This is most likely due to the fact that at 600 hours of exposure, all the pearlite has already transformed to spheroidized carbides.
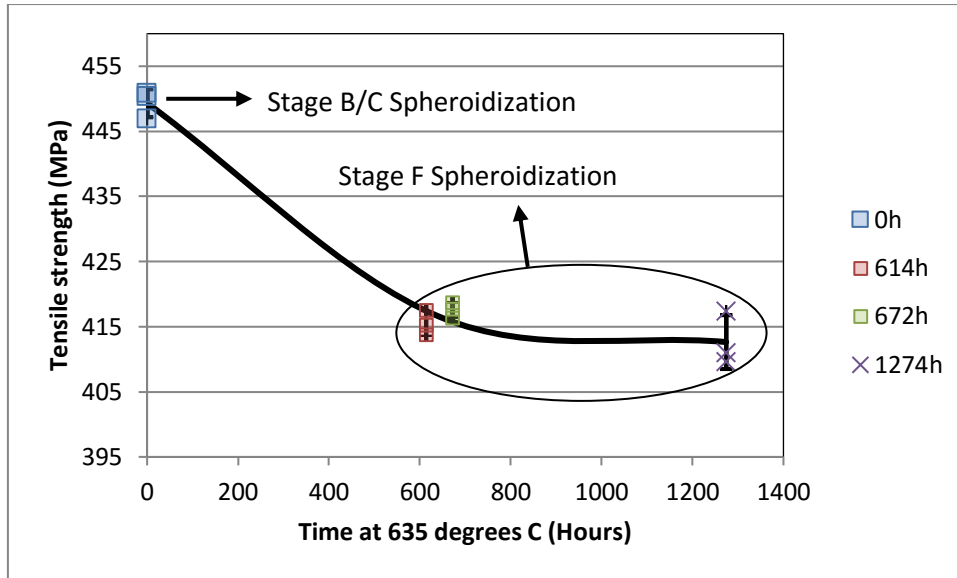
Figure 139: Tensile strength at room temperature of samples 1-4 as a function of time exposed to 635°C of both full section and reduced section tensile test samples.

4.4.1. Full section tensile tests

Full section tensile tests are valuable because they characterise the full thickness of a welded joint. This is in contrast to reduced section tests that only test a portion of the joint.

The disadvantage of a full section tensile test with regards to sample with large wall thicknesses is that it is difficult to extract precise data from the information that is returned by the test. An example of this can be seen in Figure 32, which shows that the elastic regions of all the graphs vary significantly. This could partially be contributed to misalignment of the sample during cutting or if the sample was distorted due to the welding process. This will have an effect on the elastic modulus reading that the test equipment reads and is therefore not a true reflection of the material properties but rather of the material geometry. For these reasons, the most valuable data that can be extracted from these tests are the tensile strength, and the location of the fracture.

Samples 1 and 2 were tensile tested by applying the load in a direction which was perpendicular to the original rolling direction, whereas samples 3 and 4 were tensile tested by applying the load in a direction which was parallel to the original rolling direction (refer to 2.4.1). It was initially suspected that the direction of tensile loading with regards to the original rolling direction would affect the mechanical properties of the samples, but due to the spheroidization of samples 1, 2 and 3, there was no noticeable effect due to tensile load orientation. This can be seen in the full section tensile test results of sample 2 and 3 (see Table 16) which both experienced a total of about 600 h of heat treatment at 635°C.

The tensile strength of all the samples were considered acceptable to qualify a welding procedure for SA-516 Grade 60. It must be noted that sample 4 (the as-received sample) consistently displayed the highest tensile strength during the full section tests. This result was expected, due to the fact that sample 4 did not experience any additional rapid thermal cycling (from welding) or, more importantly,

any additional heat treatment for prolonged periods of time. The effect of the extended heat treatment that samples 1 (1274 hours at 635°C), 2 (614 hours at 635°C) and 3 (672 hours at 635°C) experienced is that the pearlite in the microstructure transformed to spheroidized carbides as seen in Figure 136. The cementite lamella which is present in pearlite acts as a barrier to plastic deformation which occurs mainly in ferrite. Therefore if material contains lamella of cementite as is the case in pearlitic material, the tensile strength of the material will be higher than that of the same material that contains spheroidized carbides (7). It was found that the tensile strength of the material that contained pearlite was consistently 35 MPa higher than that of material that did not contain pearlite as seen in Figure 139.

The true stress at fracture was not calculated on the full section tensile samples due to their irregular geometry. The shape of the fracture surface is largely rectangular with parabolic sides sloping inwards. Therefore the cross sectional area could not be measured accurately. It was noted that there was a much smaller reduction in cross sectional area in sample 4 due to the fact that these samples failed through the graphitic HAZ. It was also observed during test witnessing that the samples that failed through the HAZ did not fail in a brittle manner, as the reduction in cross sectional area would suggest, but instead tore slowly along the HAZ.

The quantity and location of the graphite are two important factors that determine the fracture type. Sample 4 displayed large quantities of graphite in a preferred plane and subsequently failed in the HAZ. Similarly, sample 3 also displayed graphite in a preferred plane, however due to the removal of some of the graphitized material from the HAZ and replacement of this material with new, graphite free weld metal, the quantity of graphite was not sufficient to induce HAZ fracture. The remedial action was therefore at least partially vindicated.

4.4.2. Reduced section round tensile tests

As stated in section 4.3.1 the full section tensile test has a large amount of merit but has limitations in sensitivity. Therefore reduced section round tensile test were performed in order to obtain a more accurate flow curve. Figure 140 is a diagram of true stress vs. true strain, shows a more accurate result for the elastic modulus of the four samples. The true stress – true strain graphs are plotted up to the tensile strength of the material. It can be seen that material that experienced prolonged heat treatments are in general more ductile than material that did not undergo any further heat treatments. Additionally, all samples that experienced a prolonged heat treatment performed very similarly in the tensile test where only sample 4 performed differently with slightly lower uniform elongation and high tensile strengths.
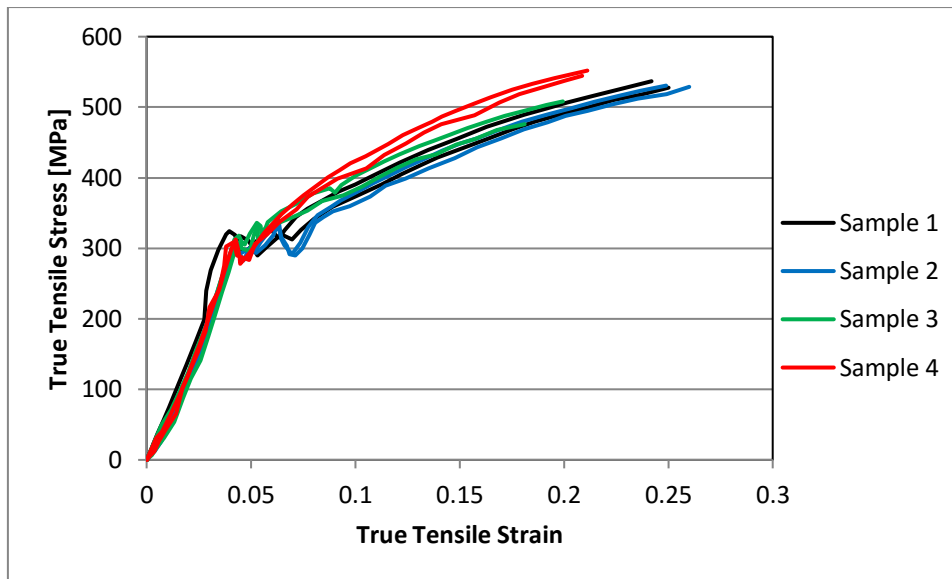
Figure 140: True stress vs true strain graph up the tensile strength (and point of necking) for the reduced section round tensile test samples 1-4

The true stress that each sample experienced at fracture can be seen in Table 31. It is clear that for samples that fail through the graphitized HAZ, the true stress is significantly reduced and is able to resist approximately 680 MPa of stress whereas samples that failed in the base metal could withstand true stresses ranging from 960 to 1200 MPa.

Table 31: Table summarizing the true stress at fracture for samples 1-4 of the reduced section round tensile test samples

Sample No.	Original cross sectional area (mm²)	Final cross sectional area (mm²)	Force at fracture (kN)	True stress at fracture (MPa)	Failure position
1	123.1	36.6	37.6	1026	Base material
	123.5	37.7	37.7	1027	Base material
2	123.5	36.6	37.1	1012	Base material
	124.5	36.4	36.3	997	Base material
3	122.5	70.1	47.5	678	HAZ
	124.5	36.5	35.2	964	Base material
4	121.5	31.8	38.2	1202	Base material
	120.0	36.7	39.8	1084	Base material

The results of the reduced section round tensile tests do not agree with the full section tensile test results with regards to the location of the failure. In the full section tensile test, both tests of sample

4 failed in the graphitized HAZ while for sample 3, both samples failed in the base material as seen in Table 16. However in the reduced section round tensile test, for sample 4, both samples failed in the base material while for sample 3, one failed in the graphitized HAZ and one failed in the base material as seen in Table 17. The cause for the erratic failure locations of sample 3 is due to the locations from which the reduced section tensile tests were machined. Because the repair welding only took place in the top half of the sample, and new weld/old weld overlap only occurred in the top 5-10mm of the sample and it was suspected that the reduced section round tensile sample was machined in such a way that HAZ graphite remained in the sample while the reinforcing material was machined away. This was confirmed by etching the round tensile samples with 3% Nital to reveal the welds in sample 3 as seen in Figure 141 and thus can be concluded that the experimental weld was not tested with this sample.

Figure 141: Sample 3 reduced section round tensile test that failed through the HAZ. The image contains markings to assist with region identification ('W' refers to welds while 'B' refers to base metal)

Table 32: Uniform reduction in area of each reduced section round tensile sample as well as the true strain at necking.

Sample No.	% Uniform reduction in area	True % strain at necking	Failure position
1	15.2	25	Base material
1	17.7	27	Base material
2	14.0	25	Base material
2	19.4	27	Base material
3	7.7	20	HAZ
3	9.9	20	Base material
4	11.5	23	Base material
4	10.4	21	Base material

Sample 3 fractured through the graphitized HAZ and it can be seen in Table 32 that graphitized HAZ material possesses a much lower true stress at fracture than material that fractures through the base metal. It can be seen that true stress vs. true plastic strain extrapolated slopes for samples 1-3 are

essentially identical, while this slope for sample 4 is slightly steeper. This indicated that sample 4 hardens more rapidly as a result of strain than the other three samples. The higher strain hardening observed in the Sample 4 round tensile test specimens was probably due to the low degree of spheroidization in the as-received material. The true plastic strain that can be accommodated in sample 3 is lower than any other samples due to the material fracturing through the graphite. Additionally, the true stress at fracture is 334 MPa lower than the other samples that were tested.

Based on the information obtained from the true stress – true strain (σ_T – ϵ_T) diagram up to the UTS, it is possible to determine the strain-hardening exponent (n) and strength coefficient (K) for each sample from each respective Hollomon plot as seen in Figure 142 (45).

The Hollomon equation is valid for uniform plastic elongation and relates the true stress to true strain via the following equation from the yield point, up to the tensile strength:

$$\sigma_T = K\epsilon_p^n$$

Where: K = Strength coefficient
 n = Strain hardening exponent
 σ_T = True stress
 ϵ_p = True plastic strain

The strain hardening exponent (n) can range from 0 to 1, where 0 describes a perfectly plastic solid while 1 describes an elastic solid. The typical n values for carbon steel range from 0.19-0.26 (45). The strain hardening exponent is defined by the slope of the log-log graph of true stress vs. true plastic strain. As n approaches 0, the true stress in the sample approaches the value of the strength coefficient. Additionally, as n approaches 0, the material becomes less sensitive to strain hardening.

The strength co-efficient (K) is defined as the true stress of a material at a theoretical true plastic strain of 1. The higher the strength co-efficient, the more rapidly the true stress rises with regards to strain. The strength co-efficient is equal to the theoretical true stress that the material experiences at 100% true plastic strain.
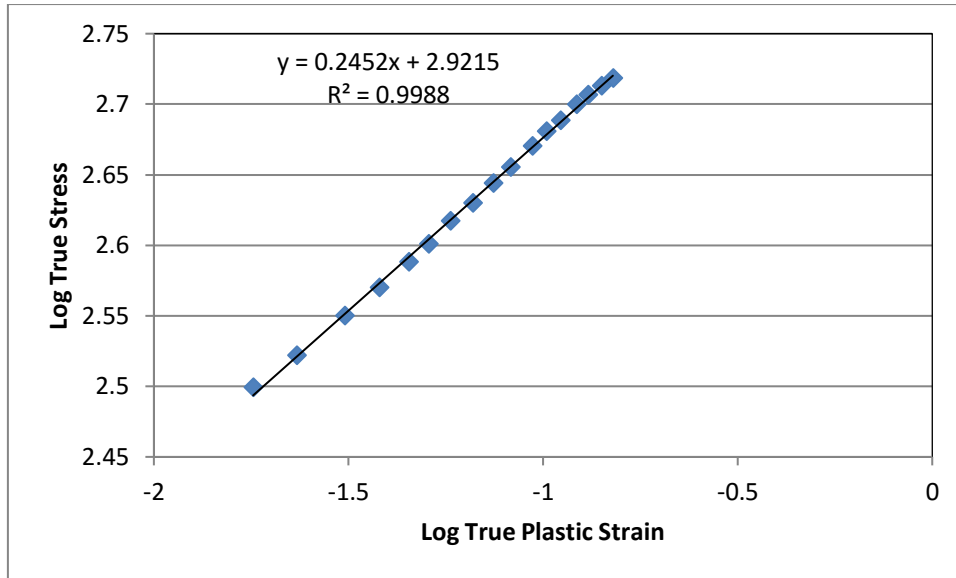
Figure 142: Log true stress - Log true strain graph of reduced section round tensile sample 1. Similar analysis were performed for each sample in order to obtain the strength coefficient and strain hardening exponent.

Table 33 shows the strain hardening exponent and strength coefficient of all 8 full section tensile samples, as well as all 8 reduced section round tensile samples. It can be seen that the average value for the strain hardening exponent (n) falls within the normal limits for carbon steels as quoted by Dieter, with three samples falling outside of normal range of 0.19-0.26 (45). The average value for the Strength Coefficient (K) falls within the normal limits of 530-1230 for carbon steels as quoted by Dieter for all samples.

Table 33: Strain hardening exponent and strength coefficient for each sample

Sample No.	Sample Section	Strain Hardening Exponent, n	Strength Coefficient, K (MPa)
1	Full Section	0.24	805
		0.25	839
	Reduced Section	0.25	806
		0.27	803
2	Full Section	0.23	817
		0.24	856
	Reduced Section	0.25	821
		0.26	816
3	Full Section	0.29	914
		0.24	886
	Reduced Section	0.22	790
		0.23[1]	781
4	Full Section	0.26[1]	1002
		0.29[1]	1062
	Reduced Section	0.22	846
		0.23	865
	Minimum	0.22	781
	Maximum	0.29	1062
	Average	0.25	857

(1) Samples fractured in the HAZ. All other samples fractured in the base material

155

The strain hardening rate was also determined from the yield point, up to the tensile strength as a function of true stain according to the following proposed relationship:

$$\frac{\Delta\sigma}{\Delta\varepsilon} = ke^{-C\varepsilon}$$

Where: Δσ/Δε = strain hardening rate

k = strain hardening pre-exponential

C = Plasticity coefficient

ε = True Plastic Strain

This relationship was derived empirically from the data of the 16 room temperature tensile tests that were performed. It can be seen that the strain hardening rate increases linearly with the increase in the strain hardening pre-exponential. The material becomes less effective at strain hardening (approaches perfect plasticity) as the plasticity coefficient increases.

Table **34** summarises the results obtained from the strain rate vs. log true plastic strain diagrams. This relationship is represented graphically in Figure 143.
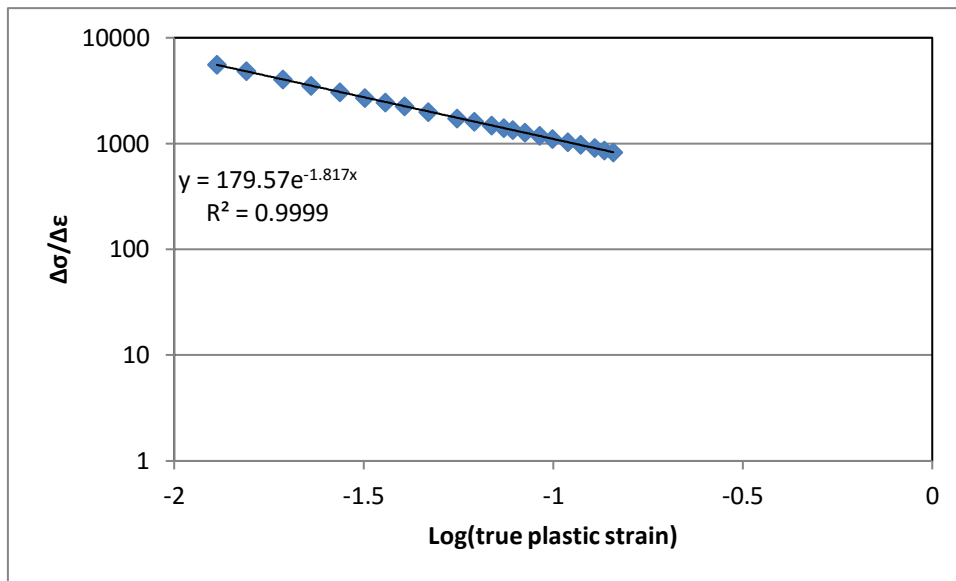
Figure 143: Strain hardening rate as a function of the log of true plastic strain

Table 34: List of calculated strain hardening pre-exponential values as well as the plasticity coefficient for all samples tensile tested at room temperature

Sample No.	Sample Section	Strain Hardening pre-exponential (k)	Plasticity Coefficient (C)
1	Full Section	186	1.78
		203	1.74
	Reduced Section	194	1.78
		186	1.80
2	Full Section	175	1.83
		183	1.86
	Reduced Section	187	1.80
		184	1.82
3	Full Section	240	1.74
		200	1.80
	Reduced Section	168	1.89
		152	1.91
4	Full Section	249	1.74
		295	1.67
	Reduced Section	184	1.80
		180	1.82
	Maximum	295	1.91
	Minimum	152	1.67
	Average	199	1.80
	Standard deviation	36	0.06
	95% C.I.	199 ± 19	1.80 ± 0.03

The plasticity coefficient of the second test from the full section tensile test of sample 4 deviates from the trend that develops across the other samples that were tested. This deviation most likely occurred from an undetected irregularity during testing as the same sample in Table 33 displays the highest strength coefficient and stain hardening exponent.

4.4.3. Reduced section round hot tensile tests

The reduced section round hot tensile tests revealed that the samples experienced reduction in tensile strength as well as yield strength when compared to the samples tested at room temperature. A percentage loss in yield strength can be calculated and these results can be compared with the maximum allowable stresses that are allowed by ASME II at certain temperatures for the relevant material. Table 35 shows the average percentage loss in yield strength as well as allowable loss in strength according to API 579-1.

Table 35: Recorded yield strength values compared to calculated values according to API 579-1

Sample No.	Average actual recorded σ_y at 25°C	Actual σ_y at 420°C	Fraction of σ_y available at 420°C vs. 25°C as measured from hot tensile tests	Average theoretical σ_y according to API 579-1	Fraction of σ_y required at 420°C vs 25°C as calculated from API 579-1
1	272	212	0.78	190	0.70
2	279	236	0.84	196	0.70
3	280	230	0.82	196	0.70
4	279	251	0.90	196	0.70

The equation used in API 579-1 to calculate the theoretical yield strength at temperature is as follows:

$$\sigma_y \text{ at } 420^oC = (\sigma_y \text{ at } 25^oC) \times Exp(C_0 + C_1T + C_2T^2 + C_3T^3 + C_4T^4 + C_5T^5)$$

Where: C0 = 3.7934 X 10^{-2}
C1 = -1.86386 X 10^{-3}
C2 = 6.6947 X 10^{-6}
C3 = -1.82518 X 10^{-8}
C4 = 2.31521 X 10^{-11}
C5 = -1.22947 X 10^{-14}
T = 420

According to ASME II part D, the material that is in use, will enter the creep regime when operating temperatures exceed 350°C. Due to this note, creep is also a factor that could exacerbate the problems experienced with graphitization. Creep is however outside the current scope of work.

4.5. Bend Test

In order for a process to be qualified for a PQR, four samples must undergo the bend test and observed surface defects may not exceed 3mm in size (2).

The bend test is also used as a measure of severity of graphitization (31). The angle through which the sample bends before it cracks as a result of graphite in the HAZ is the measure used to qualitatively measure the degree or severity of graphitization. As mentioned in the section 1.2.3, the test method is not consistent from one researcher to the next, and therefore, an accurate scale cannot be developed for severity of graphitization. The samples in this study are an example of this point, as none of the samples fractured as a result of graphite, however the graphitized zone was not placed at the point that experienced the highest degree of deformation, nor was the graphitized zone aligned with the plunger as depicted in Figure 11. Under very close inspection it was possible to detect multiple sub-millimetre defects in the HAZ region of the original welds in both samples 3 and 4 and seen in Figure 144 and Figure 145.
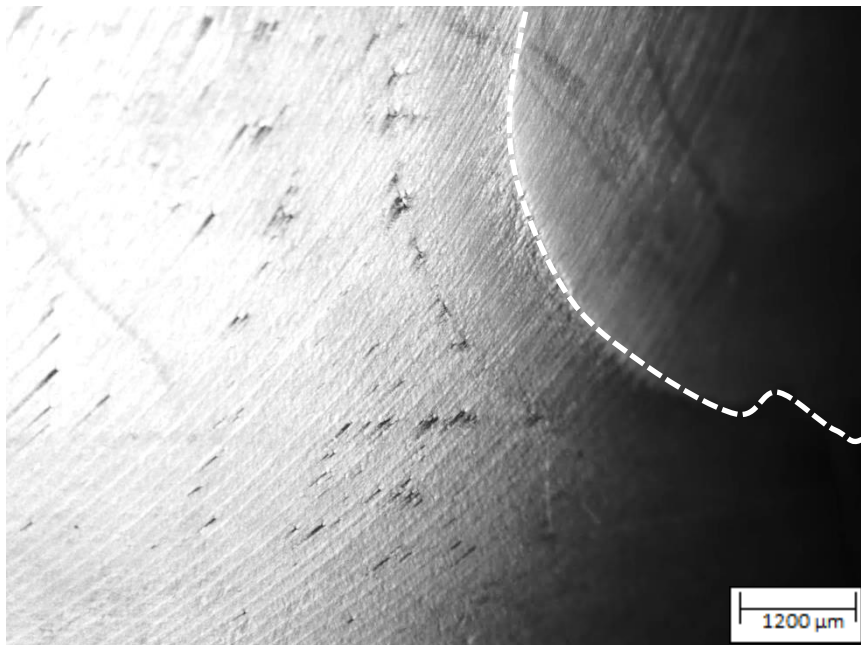
Figure 144: Stereoscopic image of the tensile surface of the bend test (See Figure 41) of sample 3 showing sub-millimetre defects adjacent to the original fusion line. Fusion line is demarcated by the dotted line and the weld metal is located in the top right of the image.
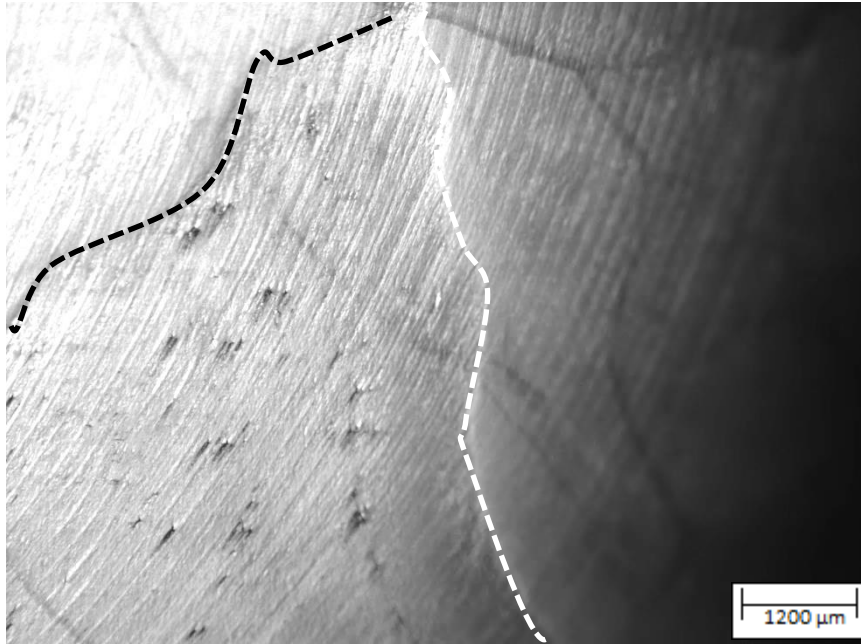
Figure 145: Stereoscopic image of the tensile surface of the bend test (See Figure 41) of sample 3 showing sub-millimetre defects adjacent to the original fusion line. Original fusion line is demarcated but the dotted line on the right with original weld metal on the right of this line. The dotted line on the left demarcates the experimental repair weld and the material in the top left side of the image is the experimental welds' weld metal.

The defects that are observed are consistent with the position of HAZ graphite, however due to the bend test method not conforming to the most severe method for testing HAZ graphite, the results cannot be compared to other published results that use a different specimen orientation for the bend test. In the current study, no deleterious effects of heat affected zone graphite on the mechanical behaviour of any bend test specimen could be observed.

4.6. Charpy Impact Test

The Charpy impact tests revealed that all samples displayed energy absorption which is significantly higher than 27 J. Samples that absorb less than 27 J of energy are deemed to be brittle while samples absorbing more than 27 J are deemed to have sufficient toughness. The minimum recorded value (82 J) is 3 times higher than the 27 J threshold, therefore it can be concluded that graphitization does not significantly affect the impact toughness of material.

In general, the weld metal displayed much higher toughness values than the base metal, this can most likely be attributed to the very low carbon content of the weld metal when compared to the base metal.

4.7. Hardness Tests

The hardness tests displayed the typical expected results associated with weld metal, HAZ material, and base material profiles (See Table 20 and Table 21). There were no abnormalities that were detected. An additional check that can be performed to ensure that the hardness readings are correct and acceptable is to relate the hardness to the tensile strength of the material and compare these results to the hardness vs. tensile strength relationships that are published in ASTM A370 table 7B (46) as seen in Figure 146. The outliers of sample 3 and 4 (also coloured red) indicate the samples that failed through the HAZ.
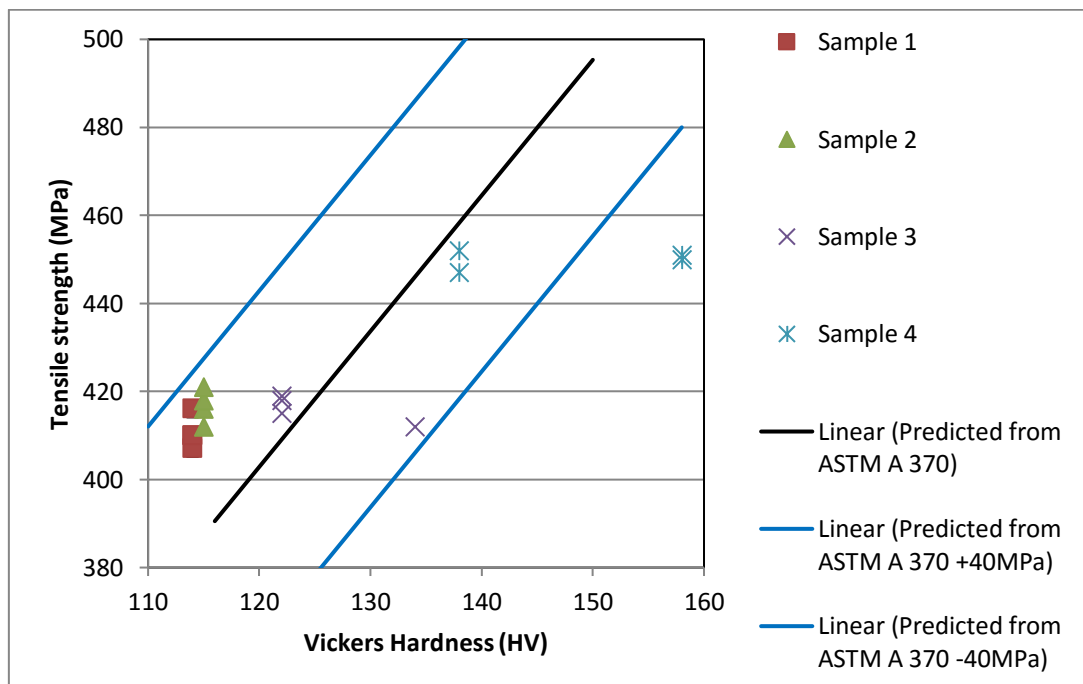
Figure 146: Figure showing the correlation of the tensile strength of material with its hardness at the failure location, and how experimental results correspond to published values.

It can be seen that the data coincides well with the predicted values obtained from the ASTM table. The data that is provided in the ASTM A370 table 7B is most likely for new material that has not experienced prolonged heat treatments. This explains the deviations (less than 40MPa) of the recorded data from the predicted values obtained from ASTM.

4.8. Mechanical test summary

Table 36 shows the effects of graphite on the mechanical properties of the material.

Table 36: Effects of graphitization on the mechanical properties of C-Mn steel

General class of properties	Mechanical property	Effect of graphite on mechanical property
Strength	Yield strength (σ_Y)	None
	Tensile Strength (σ_{TS})	None
	Engineering Stress at fracture (σ_F)	None
	True stress at fracture ($\sigma_{True\ F}$)	Decrease (from 960 to 680MPa)
	Elevated temperature yield strength (σ_Y)	None
	Elevated temperature tensile strength (σ_{TS})	None
	Hardness (HV)	None
Ductility	Total elongation (ε)	None
	Reduction in area	Decrease (from 77% to 44%)
Work hardening behaviour	Strength coefficient (K)	None
	Strain hardening exponent (n)	None
Impact toughness	Impact toughness (J)	None

Based on the experimental values obtained from: engineering tensile strength; fracture strength; engineering strain; strain hardening exponent; and strength coefficient, it is clear that graphite does not negatively affect the tensile properties, hardness, or impact toughness at room temperature of SA-516 Grade 60 carbon steel.

The PQRs developed from the mechanical tests that were performed in section 3.5 and 3.6 can be seen in Appendix D.

4.9. Microstructural analysis

4.9.1. Partial pearlite transformation during welding

As discussed in section 0, the position of graphite is linked to the partial transformation of pearlite that occurs when material is heated to just above the Ac_1 temperature, and subsequent rapid cooling to below the Ac_1 temperature. These circumstances will arise in every weld at a critical distance from the weld which is determined by preheat, and heat input into the weld pool.

The following variables were recorded for every run and the results can be seen in appendix B: Maximum current; minimum current; maximum voltage; minimum voltage; welding time; weld bead length; remaining electrode length/tab length (only applicable for SMAW); preheat/interpass temperature.

Based on the actual data that was recorded during the welding of the samples used in this project (see Appendix B) it is possible to apply the Rosenthal equation to every run and determine the position in the base material (in relation to the weld) that experienced a peak temperature that correlates to the Ac_1 temperature for that steel. The Rosenthal equation was applied to every weld run and the results are available in Appendix C. The results indicate that the material that experienced a peak temperature of 719°C (as calculated from section 0 on pg. 18) falls within a relatively narrow window ranging from 2.7 – 7.2 mm from the fusion line in all cases.

The thick-plate Rosenthal equation was used:

$$T_p - T_0 = \left(\frac{2}{\pi e}\right)\frac{q/v}{\rho r^2}$$

Where: T_p = Peak temperature (K)
      T_0 = Starting (or preheat temperature) (K)
      q/v = Heat input (J/m)
      ρ = Volume thermal capacity ($J/m^3.K$) Assumed to be 4.5×10^6 $J/m^3.K$
      r = Distance of T_p from the centre of the heat source (m)

The equation was re-written to make r the subject as follows:

$$r = \sqrt{\left(\frac{2}{\pi e}\right)\frac{q/v}{(T_p - T_0)\rho}}$$

r was then calculated for the melting temperature of the steel (1534°C) (47), and for the Ac_1 temperature of the steel (720°C) in order to determine the distance that the graphite should form from the fusion line.

An example of the calculations performed can be seen below. Note that all variable values were obtained from recorded data (see Appendix B & C).

T_p where peak temperature is the melting point (Fusion line calculation)

$$r = \sqrt{\left(\frac{2}{\pi e}\right)\frac{1067074}{(1807 - 438){\times}4.5{\times}10^6}}$$

$$r = 6.37 \; mm$$

T_p where peak temperature is the Ac_1 temperature (Graphite position calculation)

$$r = \sqrt{\left(\frac{2}{\pi e}\right)\frac{1067074}{(993 - 438){\times}4.5{\times}10^6}}$$

$$r = 10 \; mm$$

Thus the distance from the fusion line to the graphite would be 3.63 mm.

Table 37 summarises the results of the Rosenthal equation.

Table 37: Summary of the results of the estimation of the position of graphite formation based on the last material to experience the Ac_1 temperature

Sample No.	1	2	3 (Groove 1)	3 (Groove 2)
Maximum distance from fusion line of last material to experience the Ac_1 temperature (mm)	7.2	5.5	6.5	6.8
Minimum distance from fusion line of last material to experience the Ac_1 temperature (mm)	2.7	3.6	4.0	3.4
Average distance from fusion line of last material to experience the Ac_1 temperature (mm)	4.5	4.3	5.3	4.9
Number of runs	37	30	42	36
Standard deviation of the Average (mm)	0.9	0.6	0.7	0.7
95% Confidence interval of the Average (mm)	0.31	0.21	0.23	0.25

A weighted average from the data in Table 37 was calculated in order to determine the average distance from the fusion line of the last material to experience the Ac_1 temperature as follows.

For sample 1

$$\# \ Runs \times Average \ distance \ from \ fusion \ line$$
$$37 \times 4.5 = 166.5$$

Repeated for sample 2, and both grooves of sample 3

- 2: $30 \times 4.3 = 126$
- 3 (Groove 1): $42 \times 5.3 = 222.6$
- 3 (Groove 2): $36 \times 4.9 = 176.4$

Weighted average calculation

$$\frac{Sum \ of \ previous \ 4 \ calculations}{Total \ number \ of \ runs}$$
$$\frac{691.5}{145} = 4.8$$

This material is the most likely to graphitizing preferentially to the rest of the material and is, on average, 4.8 mm from the fusion line.

Figure 147 shows the distribution curve of the distance from the fusion line of material that experienced a peak temperature equal to the Ac_1 temperature. This curve indicates that the highest frequency of weld runs experienced a peak temperature equal to the Ac_1 temperature at a distance of 5 mm from the fusion line. This result is very consistent with the result obtained from the weighted average calculation.
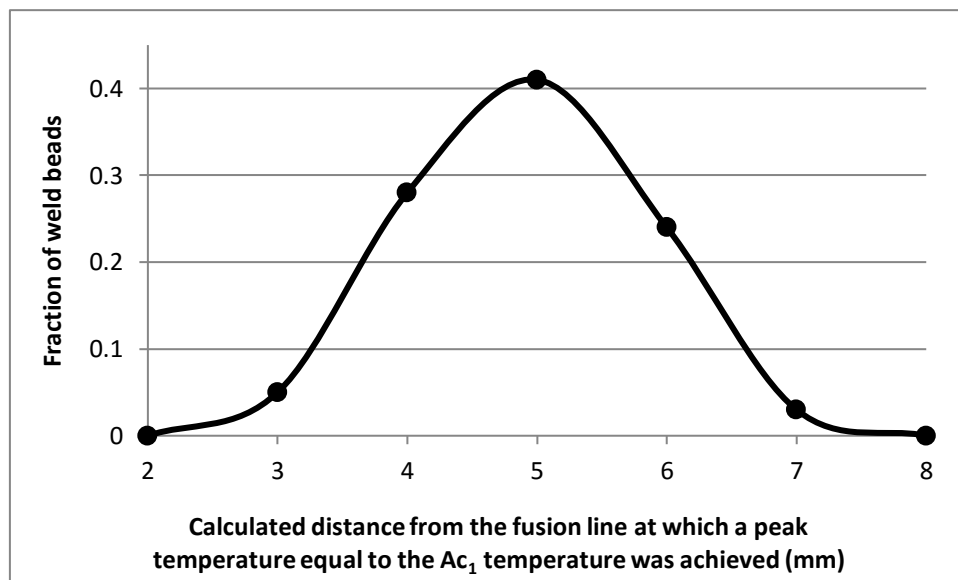
Figure 147: Distribution curve of the frequency of weld runs that experience a peak temperature equal to the Ac_1 temperature at varying distances from the fusion line

As mentioned previously, the WPS that was used to weld these samples was the same WPS that was originally used on sample 4 (the service exposed material). Based on this fact, the heat input and ultimately the last material to experience the Ac_1 temperature should be located at approximately the same distance from the fusion line in all samples. Therefore the region which is graphitized in sample

4 should correspond to the Ac_1 temperature which, according to the calculations from the Rosenthal equation, should fall approximately 4.8 mm from the fusion line.

Figure 148 graphically represents the effect of the preheat/interpass temperature on the distance from the fusion line at which material will be exposed to a peak temperature of 719°C. It can be seen that if the material is welded at room temperature, the heat input required to result in material that is 4.8mm away from the fusion line to experience a peak temperature of 719°C is between 2.75 and 3 kJ/mm. However, for material that has been preheated to 150°C (Minimum preheat temperature) or 280°C (Maximum interpass temperature), the heat input required is only between 1.75 - 2.25 and 1.25 - 1.5 kJ/mm respectively. This data further supports the results obtained in Figure 147.
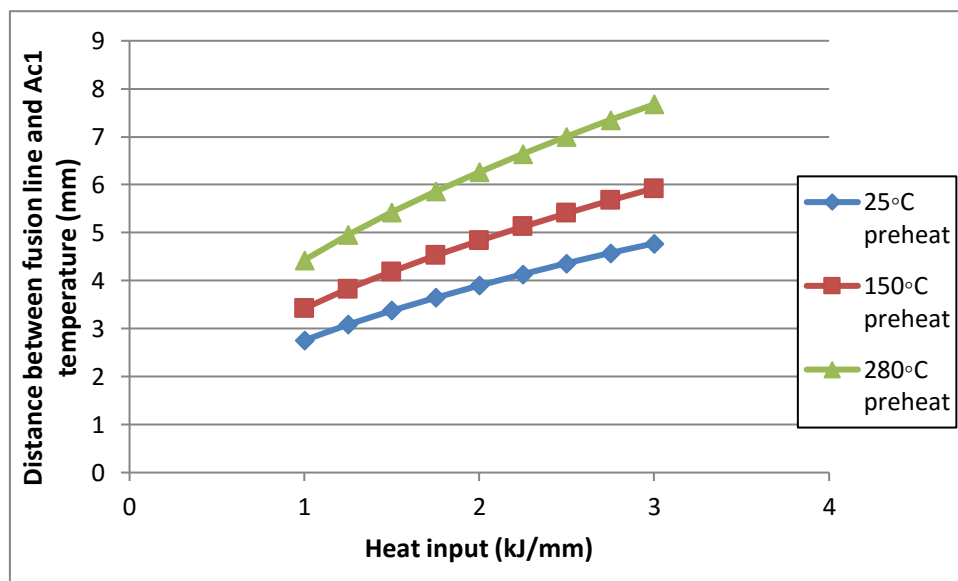
Figure 148: Effect of preheat/interpass temperature on the distance from the fusion line that a peak temperature equal to the Ac_1 temperature is achieved at various heat inputs according to the Rosenthal equation.

4.9.2. Effects of planar graphite on fracture behaviour of carbon steel

Ductile fracture is witnessed in samples that failed through HAZ graphite as can be seen in Figure 90 and Figure 108. The definition of ductile fracture is a slow tearing of material through the expenditure of significant amounts of energy (45). The mechanism of ductile fracture is through a coalescence of voids on a preferred plane within the defusing neck of a sample. The forces that form the initial central crack are concentrated shear forces acting on the edges of the crack and are referred to as the shear band. Voids tend to form within this shear band and as the material is strained, the voids subsequently elongate and the material separating the voids elongate to the point where the material cannot elongate any further. At this point the crack grows, and it zig-zags from one void to the next. When the fracture surface is observed, the final result under high magnification, is a series of voids separated by thin walls of material to produce the 'dimpled' effect commonly associated with ductile fracture (Figure 108). Void nucleation is a heterogeneous process that occurs on inclusions, second phase particles, or fine oxide particles. In the particular case of carbon steels, it is found that carbides that

are orientated in the direction parallel to the applied load are the first carbides to crack and tend to do so at roughly a 50° angle to the tensile load. Thus the voids coalesce along parallel carbides to form the fracture surface (45).

In the context of graphite, the above description of ductile fracture appears to coincide well with what is being observed in mechanical testing. The most important observation is that the graphite has no noticeable effect on the tensile strength of material. This is justified by the tensile properties of sample 3 from Table 17. In this event, one sample fractured through the planar graphite, while the other sample fractured in the base material, and yet the tensile strength of the samples are within 3 MPa of one another (412 MPa for the HAZ failure and 415 MPa for the base metal failure). When the fracture surfaces are observed, the typical signs of ductile tearing can be seen in the metallic sections of both samples. This suggests that the planar graphite failures that have been witnessed in the current study assume a ductile type of fracture behaviour. Samples that fractured through the planer graphite do so in accordance to the description in the previous paragraph, where the graphite is considered a very weak second phase particle that tends to form in the direction that coincides with the tensile load. Thus, if a diffuse neck develops across the graphitized plane, it will result in a shear force developing across the graphite particles in much the same way that is described by Dieter when he refers to this mechanism for pearlite. Ultimately, the void formation and coalescence is greatly accelerated through the presence of a phase that displays low ductility. It is also mentioned that the crack tends to, on a macro scale, form roughly perpendicular to the tensile load, however on a micro scale, the crack will not travel in a straight line but rather jump from one void to the next.

It is clear that graphite appears to, in the location and quantity observed in this study, have no effect on the tensile strength of the material under conditions of tensile loading. When the material is severely affected by planer graphitization (HAZ graphite) and the diffusion neck forms across this plane, the fracture behaviour of the material is affected.

In cases where the graphite is randomly distributed through the material, the tearing mechanism follows the same basic principles that are discussed in Dieter. The crack will zig-zag through the material, moving from one void to the next. If there is a randomly distributed graphite particle that is located in a position near to the crack, and a void is generated on the graphite particle, there is a high chance of the crack running to, and through the graphite particle as seen in Figure 74 and Figure 99. All samples that did not fracture through a graphite plane, fracture in the typical 'cup-and-cone' ductile fracture.

Graphite is considered an embrittling phase that allows cracks to form and grow between graphite nodules that occur in a planar manner (28). Almost all graphite related failures have been as a result of mechanical or thermal shock or fatigue (31). Some researchers have thus found it important to attempt to investigate the change in subcritical and critical crack growth characteristics as the graphite content in material changes (12).

4.9.3. Spheroidization

The aim of this project was to examine the effects of graphitization on the mechanical properties of C-Mn steel. The first step that was taken was to increase the graphite content on the steel by performing a prolonged heat treatment. In addition to increasing the graphite content of the steel, any material that was exposed to 635°C for 600 hours or longer was discovered to be fully spheroidized. According to the qualitative stages of spheroidization proposed by Toft, samples 1-3 display stage F spheroidization while sample 4 displayed stage B or C (48). Figure 149 is a reproduction of Figure 146 with the stages of spheroidization added in order to illustrate the effects of spheroidization on the tensile strength and hardness as well as the relationship between these two parameters.
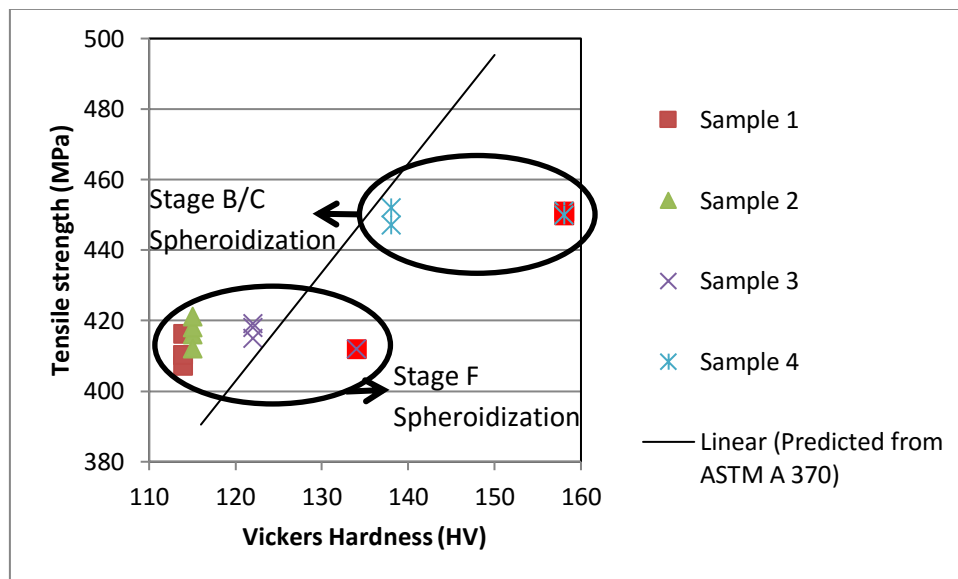
Figure 149: Figure showing the correlation of the tensile strength of material with its hardness at the failure location, and how experimental results correspond to published values.

Spheroidization is the process whereby the alternating cementite – ferrite lamella in the pearlite structure transform into small spherical cementite particles surrounded by a ferrite matrix (6). The effects of spheroidization on the mechanical properties have been such that the spheroidized samples tend to display lower tensile strengths than that of unspheroidized material (Table 16).

Despite sample 1-3 having undergone full spheroidization, the tensile strength obtained during full section as well as reduced section tensile testing was still considered acceptable according to ASME IX assuming SA-516 grade 60 was used. This will therefore allow the material to become fully spheroidized and still be considered safe to operate. As noted previously, if it was assumed that SA-516 grade 65 was used, none of the samples (including the service exposed material) display acceptable tensile strengths.

4.9.4. Analysis of graphitized HAZ geometry and fracture surfaces

The results obtained from the image analysis of the fracture surface of sample 4 in conjunction with the results obtained from the quantitative metallography of sample 4 indicate the following:

1. The fracture surface analysis indicated that approximately 50% of the fracture surface consisted of graphite.
2. The quantitative metallography performed on a polished cross section of the partially transformed region of the HAZ indicated that the volume fraction of graphite is approximately 2.2%. This is significantly higher than any other area in the material and indicates that there are favourable conditions for graphite formation and growth in these regions.

Based on these findings, it can be concluded that a crack that forms in the HAZ displays a strong preference towards cracking through the graphite which only contributes a small volume fraction of the total HAZ microstructure.

It has been demonstrated that samples that fail through the HAZ follow a specific path that correlates strongly with the angle of the fusion line. Figure 106 also indicated that the graphite nodules appear to rupture in the direction that is parallel to the tensile load when the HAZ is observed in the through thickness direction of the pipe.

In an effort to quantitatively estimate the percentage graphite that should be visible on a fracture surface if the material fails through the HAZ, Figure 106 was measured using the following rationale. It has been observed that when a crack propagates through the HAZ, there are two distinct crack directions – the direction that is parallel to the tensile force and the direction that is perpendicular to the tensile force. When the crack travels in the direction which is parallel to the tension force, it is observed that the crack is running along clusters of graphite nodules. Therefore, the ratio of crack length in the parallel direction to the total length of the crack should produce a similar percentage to the total graphite on the fracture surface as measured by ImageJ. The results of these measurements indicated that the percentage graphite on the fracture surface in Figure 103 should be 59%. This corresponds very well with the ImageJ data which suggested that the same fracture surface contained 55% graphite.

Based on the PQR, the edge preparation of the original welds consisted of a single V groove with an open angle of 90°. This means that on each side of the pipe, a 45° bevel was machined onto each edge that was to be welded. According to Pythagoras, a 45-45-90° triangle will have two equal length sides and one hypotenuse that is 1.414 times the length of the other sides.
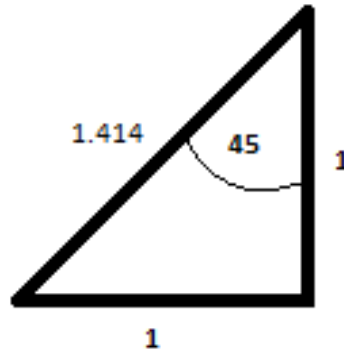
Figure 150: Pythagoras theorem for a 45-45-90° triangle

The relevance that this has to the percentage of graphite that is observed on the HAZ failure fracture surface is that, due to the step wise crack path, the original joint preparation will dictate the amount of graphite that is observed on the fracture surface. According to the geometry used in the PQR, the amount of observed graphite should have been approximately 50% based on the 1 to 1 relationship between the horizontal length (graphite containing) and vertical length (graphite free) planes.

 The density of a graphite nodule can be measured through the use of x-ray tomography, the results of which can be seen Table 38 (49).

Table 38: Estimated density of the bulk sample and of graphite nodules using x-ray tomography (49).

	Carbon Steel	Graphite Nodule
Density (g/cm³)	7.85	5.84

By measuring the density of the nodule, a volume fraction of graphite and ferrite can be calculated in what can be concluded to be a two phase (graphite-ferrite) nodule. Based on the results in Table 38, a volume fraction can be calculated for ferrite and graphite as indicated below.

$$(Volume\ fraction\ \alpha) \times (Density\ of\ \alpha)$$
$$+ (Volume\ Fraction\ Graphite) \times (Density\ of\ Graphite)$$
$$= Density\ of\ the\ nodule$$

Simplified to solve for the volume fraction of α, the equation is a follows:

$$(V_\alpha)(\rho_\alpha) + \left(1 - \rho_{Graphite}\right) = Density\ of\ the\ nodule$$

$$V_\alpha \times 7.85 + (1 - 2.226) = Density\ of\ the\ nodule$$

The estimated average density of a graphite nodule was 5.84 g/cm³ as seen in Table 38. Based on this estimated density and the calculation above, it can be concluded that the volume fraction of graphite in the nodule was 40%.

By carefully examining micrographs such as Figure 81 it is possible to see the ferrite phase dispersed in the nodule. The appearance of the nodule changes significantly once the ferrite is etched away and only the graphite remains in the nodule as seen in Figure 121 - Figure 123. In these images it would appear that the graphite is positioned in between ferrite lamella. It is possible that the graphite is

171

formed as a result of the decomposition of cementite inside pearlite colonies (and thus diffusion over a short distance is required to form graphite).

4.9.5. Graphite nucleation, growth and composition

The graphite nodules present in the base metal and the HAZ appear to contain more carbon in the form of graphite than the amount that would be supplied by locally decomposing cementite in pearlite colonies. Therefore it can be concluded that diffusion takes place across a larger distance than only the size of a pearlite colony.

In general, base metal graphite and HAZ graphite can be differentiated by the following characteristics. Base metal graphite tends to result in larger, less frequent and randomly distributed nodules while HAZ graphite tends to result in many smaller and highly heterogeneously distributed nodules as seen in Figure 151. The proposed mechanism for this observation is as follows:

Figure 151: HAZ and Base metal graphitization as reported by Foulds (17).

Base metal graphitization occurs solely as a result of Fe_3C decomposition and precipitation of carbon in the nodule as graphite. Due to Fe_3C being more stable than other carbide phases, this process occurs slower than the HAZ graphitization. Subsequently, few nucleation sites are active in the base metal and it seems that existing nodules grow rather than new nodule formation taking place.

HAZ graphitization occurs first as a result of the decomposition of carbides other than Fe_3C that were formed during the weld thermal cycle. The rapid decomposition (rapid relative to that of Fe_3C) results in a larger number of graphite nucleation sites becoming active and thus a greater number of graphite nodules form in the HAZ. This explains the larger number of nodules in the HAZ that are in general significantly smaller than those observed in the base metal. Once the rapidly decomposing carbides (relative to that of Fe_3C) have been depleted, nodule growth progresses in a manner similar to that of

172

the base metal graphite, where nodule growth is now solely dependent on the decomposition of Fe_3C and subsequent diffusion of the carbon to the graphite nodules.

An alternative theory exists that suggests that the nucleation sites forms at a position in the HAZ that correlates to temperatures below the Ac_1. These sites are reported to form from isolated carbides or cementite in pearlite (19).

Both theories on the position of HAZ graphitization (that is, where the peak temperature is slightly below the Ac_1 temperature or between the Ac_1 and Ac_3 temperature) are consistent with the formation of graphite in a narrow region in the HAZ. As the primary objective of this study was to establish the effect of HAZ graphite on the mechanical properties of the welded joint, the precise position of the HAZ graphite has no effect on the outcomes of this study.

Long term diffusion of carbon will be possible with the mechanism proposed in the schematic presentation in Figure 152. At 450°C, the solubility of carbon in ferrite in equilibrium with graphite is 1 ppm. The solubility of carbon in ferrite in equilibrium with Fe_3C is 6 ppm (50). This means, at the interface between Fe_3C and ferrite, the carbon content of the ferrite will be six times higher than the carbon content in ferrite at the graphite – ferrite interface. Thus a concentration gradient is established along which carbon will diffuse.
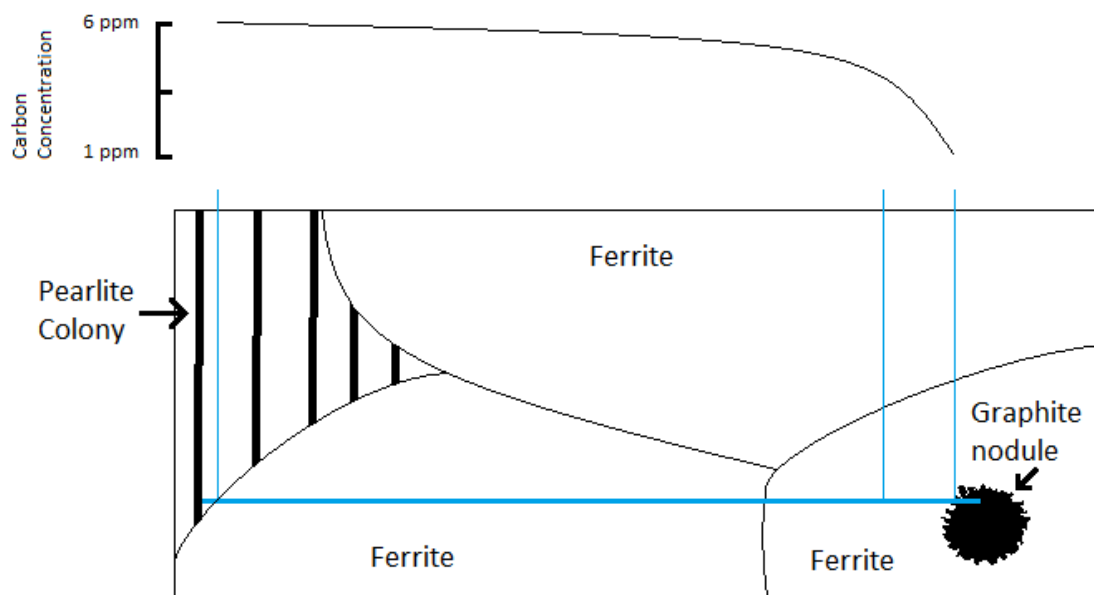
Figure 152: Schematic presentation of the change in carbon concentration near to and at the interface of both Fe_3C and graphite nodules

Graphite nodules have been confirmed to contain at least graphite and ferrite. Figure 153 shows cementite plates that were liberated from ferrite via chemical etching and Figure 154 shows graphite nodules that were liberated from a second phase within the nodule using the same etching process. It can therefore be concluded that the second phase that is present in the nodule is ferrite. As a result, the actual carbon present in the graphite is less than the volume of the nodule.
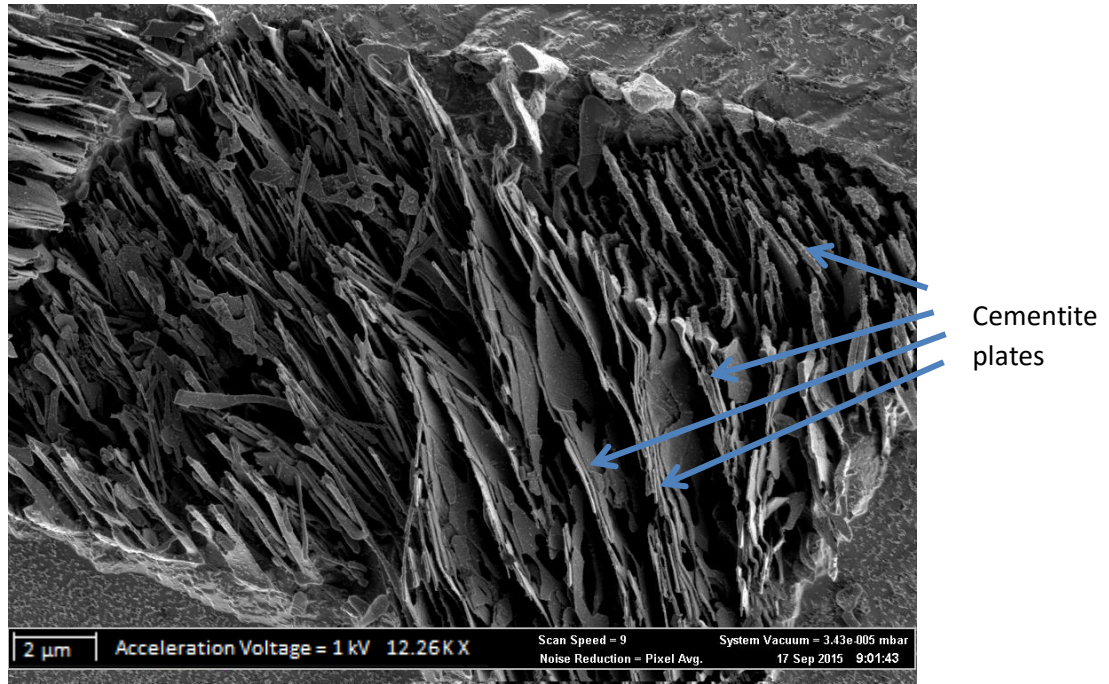
Cementite plates

Figure 153: Cementite plates of a pearlite colony liberated from ferrite via prolonged etching. The sample was a polished cross section of the full section tensile test of sample 4 on the side of the weld where the HAZ remained intact. (Material was tested in the service exposed condition with no further welding or heat treatments performed in order to establish a test baseline).
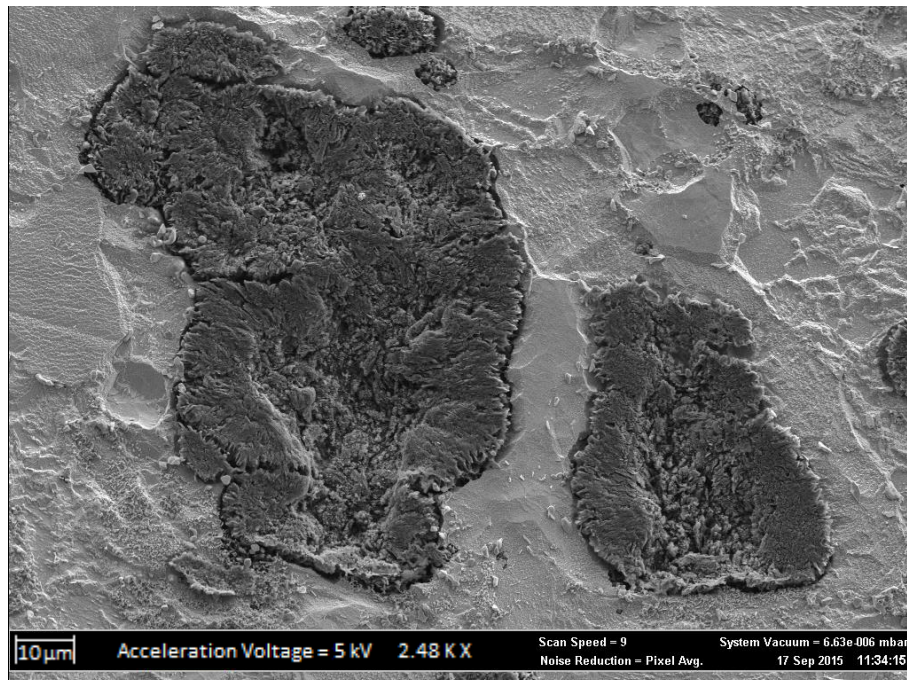
Figure 154: Graphite nodules liberated from ferrite via prolonged etching. The sample was a polished cross section of the full section tensile test of sample 4 on the side of the weld where the HAZ remained intact. (Material was tested in the service exposed condition with no further welding or heat treatments performed in order to establish a test baseline).

4.10. Degradation mechanisms acting in the graphitized material

In addition to graphitization, pipelines that operate in similar conditions as the pipelines that have, to date, failed as a result of graphite are also at risk of several other contributing factors which are discussed further in this section. Graphite is ultimately a slow, continuously growing weak second phase (27). Graphite changes the fatigue and creep behaviour of material (28).

4.10.1. Mechanical fatigue

Mechanical fatigue is a well-documented, but complex mechanical degradation mechanism associated with cyclic loading and unloading of material. With regards to a pipeline, a typical mechanical fatigue mechanism would be mechanical vibration. In this instance, defects such as graphite nodules will act as stress concentrations (45) and allow the fatigue crack to initiate from these sites.

There are a large number of variables that affect the mechanical fatigue behaviour. These factors include the tensile strength, yield strength, defect shape, defect size, loading direction, component size, and mean applied stress.

For steels that have a tensile strength < 1400 MPa, the endurance limit (the highest stress at which material can theoretically withstand an infinite number of cycles) is typically 0.5 σ_{TS}. However the endurance limit disappears entirely when a material is cyclically loaded at elevated temperatures (45).

The implications of mechanical fatigue on the current study is that the areas that are exposed to high levels of cyclic loading and high degrees of restraint must be investigated. If graphite is present in areas with high cyclic loads compared to the bulk of the pipeline, there is a high possibility that these areas are at risk of forming fatigue cracks first.

4.10.2. Thermal Fatigue

Thermal fatigue is a process whereby stresses are repeatedly induced in a material as a result of restrained members that experiences thermal expansion on heating and contraction on cooling (51). Similarly to mechanical fatigue, graphite will act as a stress concentrator in the material and provide crack initiation sites from which the fatigue crack will grow. The factors that determine the amount of stress that is applied to a material in thermal fatigue is dependent on the level of restraint and the thermal gradient within the material. As the level of restraint increases, so do the applied stresses. Similarly, as the thermal gradient increases, so do the applied stresses.

The implications of thermal fatigue, much the same as mechanical fatigue, are that areas of the pipeline that experience large temperature fluctuations coupled with high degrees of restraint during start-up and shutdown are most at risk of forming thermal fatigue cracks.

4.10.3. Creep

As mentioned in 4.4.3, C-Mn steel that is in service at temperatures that exceed 350°C are considered to be in the working envelope for creep. Creep is defined as the deformation of material under a constant load at elevated temperature (51). Due to the fact that the operating temperature of many C-Mn steels that have undergone graphitization is above 350°C, creep could play a role during failure.

Chapter 5 – Conclusions

1. Graphite forms in C-Mn steels that are exposed to elevated temperatures for prolonged periods of time as a result of metastable carbides such as Fe_3C and Fe_5C_2 decomposing to form $C_{(Graphite)}$ and $Fe_{(\alpha)}$. This decomposition reaction is a well-documented phenomenon that occurs homogeneously in the base metal as well as heterogeneously in the heat affected zone of welded joints. Graphite formation appears to be restricted to pearlite colonies.

2. While the phenomenon is well documented, many aspects such as a reliable prediction of graphite incubation times and nodule growth rates are still impossible. This study has concluded that graphite forms heterogeneously in the HAZ of welded joints due to a number of factors. These factors include: a susceptible microstructure in the intercritical region of the HAZ; an ideal temperatures at which to form graphite; and residual tensile stresses. All these factors serve to increase thermodynamic driving forces that favour the formation of graphite.

3. The rate of graphite formation is coupled to the rate of carbide decomposition. The rate of decomposition of the carbide is thought to be related to the carbide stability, which explains the increased graphitization rate of carbides that fall in a narrow temperature band in the Heat Affected Zone (HAZ) of welded joints known as the intercritical zone. This band correlates to a peak temperature during welding that falls between the A_1 and A_3 lines of the C-Mn steel in question. This results in a partial transformation where cementite transforms to an austenite that is rich in carbon. Because the material is only above the Ac_1 temperature for a brief time, the subsequent cooling results in the formation of less stable carbides which decompose more readily.

4. After welding, HAZ graphitization forms a plane of graphite parallel to the fusion line and in the through thickness direction of the pipe that is welded. This renders the pipeline vulnerable to cracking in this plane which may occur through axial loading of the pipeline if sufficient graphite is present in a joint.

5. It was therefore necessary to develop a method that could easily and quickly be employed that would mitigate the risk of catastrophic failure of a pipeline by means of a graphitized HAZ failure. Repair welding proved to be a viable method by which pipelines could be repaired and thus the appropriate PQRs were developed for use in repair welding procedures.

6. The metallurgical evaluation used in this study confirmed several theories that had been suggested in literature (Graphite nucleation sites, graphite position within the HAZ, a correlation between welding cooling rates a tendency for C-Mn steels to graphitize) that must be considered for both repair welding of graphitized material and welding of C-Mn steels in the future that will be exposed to graphitizing service temperature.

7. In the practical failures reported in the literature, graphitized carbon steel pipelines failed through the graphitized HAZ as a result of fatigue mechanisms, rather than tensile overload.

8. Due to the fact that the tests that were conducted only tested the effects that graphite has on steel during gross plastic deformation, few parallels can be drawn between the tests that were conducted in this project and the failure mechanism that is typically observed in industry. The conclusion that can be drawn is that graphite has little to no effect on most

mechanical properties with regards to the tensile strength, yield strength, hardness and impact toughness.

9. The need to understand the change that graphite makes to the crack growth characteristics of material is of vital importance in order to accurately evaluate the embrittling effect of graphite in C-Mn steel.

Chapter 6 – Recommendations

6.1. Implications for installed pipelines

Based on tests that were performed in the current study, it was concluded that the presence of graphite in the HAZ does not affect the tensile properties of the material. This suggests that there could be two scenarios that would explain the failures of the pipelines referenced in sections 1.3:

1. The pipelines that failed through the HAZ would have failed regardless of the presence of graphite (based on the fact the presence of graphite does not alter the tensile strength of material).
2. If graphite was a cause of failure, it would stand to reason that the cause of failure was not purely due to plastic collapse (as is experienced during the tensile test).

Most pipelines have an operating stress that falls well below the yield strength of the material. With regards to the current study, the average pressure in the pipeline from which the sample material was obtained was 4160 kPa (3). Based on the size of the pipe and wall thickness, it was determined that the average hoop stress experienced by the pipeline is approximately 54 MPa. This falls well below the yield strength of the material. Therefore it is highly unlikely that the material will fail as witnessed in the current study due to exceeding the tensile strength and failing as a result of tensile overload.

6.1.1. Proposed repair strategies

Based on the results obtained in this study, it has been concluded that accurately predicting the time to failure is not solely based on the graphite content of a particular plane, but rather a combined effect of graphite content and fatigue (thermal and mechanical). The magnitude of fatigue is also variable through the length of any pipeline due to the variable levels of restraint and thermal gradients during start up and shutdown. By using computer modelling it would be possible to model the thermal fatigue and mechanical fatigue and to superimpose these results in order to determine the areas in the pipeline that contain welds that are at greatest risk of experiencing HAZ graphite failure from the combined effects of these failure mechanisms. These results will allow for the identification of problem areas that could be repaired or monitored via a fitness for service model in order to determine the remaining life of the weld.

There are currently three possible repair strategies for such pipeline, namely: replacement, refurbishment, or reinforcement.

Replacement

Replacement is an extreme approach that should only be considered if the material appears to be approaching end of life. Due to the large number of variables that affect true end of life, the calculations are generally conservative and therefore sections could be scrapped well before it is necessary to do so.

If replacement is the route that is taken, it is important to ensure that a more appropriate material is used in the new section. Typically the grades that should be considered contain small amounts of carbide stabilizers (typically ¼ or ½ chromium) (52).

This process requires the removal of a section of the line and can therefore only be performed while the pipeline is offline.

Refurbishment

Refurbishment involves the rehabilitation of the line in an attempt to increase the integrity of the graphitized region of the original weld HAZ. The proposed refurbishment requires approximately 50% of the wall thickness to be cut away, and ensuring that the graphitized HAZ is removed. The process then requires the resultant groove to be filled up using a welding process.

If refurbishment is the route that is chosen, the groove preparation will be performed in-situ which will be extremely labour intensive, and additionally can only be performed while the pipeline is offline due to the fact that 50% of the wall thickness will be removed in this specific joint preparation. By removing and rewelding the outer 50% of the pipe, the area exposed to the highest bending moment will be free of planar graphite, and as one moves through the neutral axis on the pipe (in the through thickness direction) the remaining planar graphite will be in compression is only the bending moment is considered.

Reinforcement

Reinforcement focuses on increasing the strength on the pipeline in the regions where the material is suspected to be at risk of failing. The proposed method is to fillet weld a reinforcing band around the welds and their graphitized HAZ regions as illustrated in Figure 155.

This repair strategy requires minimal joint preparation, and will only require the removal of the oxide layers from the regions on the band and pipe that are to be welded together. Because this strategy does not require removal of large amounts of material from the pipeline, the process could be performed on the line while it is in operation. An image of the reinforcement suggested can be seen in Figure 155.
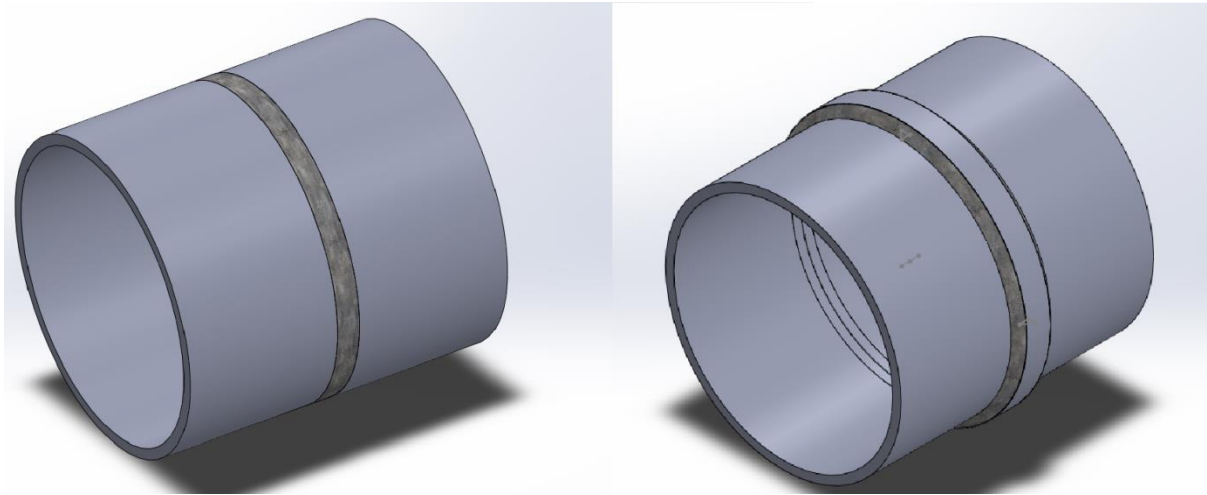
Figure 155: Proposed reinforcement which required a steel band to be fillet welded to the pipeline across the weld (Left image is the weld without reinforcement and the right image is the reinforced weld

Due to the fact that there will be an air gap between the pipeline and the reinforcement, there will be a difference in thermal expansion between the two components.

Assuming steel has a thermal expansion of 12μm/m. °C and the yield strength of the steel is assumed to be 200 MPa at 420°C (see Table 35) and Young's modulus for steel is 210 GPa, the following calculation holds.

$$\frac{\Delta \varepsilon}{Degree\ C} = \frac{12 \times 10^{-6}/1}{1}$$
$$\frac{\Delta \varepsilon}{Degree\ C} = 1.2 \times 10^{-5}$$

The strain that carbon steel before yielding can roughly be calculated as follows

$$\varepsilon_y = \frac{\sigma_y}{E}$$
$$\varepsilon_y = \frac{200}{210\ 000}$$
$$\varepsilon_y = 9.52 \times 10^{-4}$$

Therefore, the strain the material can withstand without yielding is equal to the thermal expansion associated with a temperature difference of 79°C. Assuming Young's modulus does not change with a rise in temperature, the steel will not plastically deform unless there is a temperature difference greater than 79°C.

Table 39 lists the advantages and disadvantages for the possible repair techniques.

Table 39: List of advantages and disadvantages for three proposed repair techniques for graphitized C-Mn steel pipelines

Repair technique	Advantages	Disadvantages
Section replacement	• Can replace old, graphitized material and ensure that no graphite is present in the new section. • ½ % Cr steel can be used in order to prevent future graphitization.	• Can only be implemented when the pipeline is offline. • If joint preparation of the old section is required, the process will be very slow. • The time implications of this solution translate to high implementation costs.
Weld refurbishment as detailed in 2.4.4 titled 'Half thickness groove preparation	• No new sections need to be placed in the pipeline. • Welding consumables required are reduced.	• Can only be implemented during offline times • Joint preparation will have to be performed in-situ • Placement of the groove to ensure it falls within the graphitized HAZ is practically difficult.
Reinforcing band	• Can be performed while the pipe is online • Joint preparation is kept to a minimum • Process is fast, and easy to implement • Witness hole can be drilling into the band to allow the steam to vent if a weld fails, the joint can then be replaced if necessary or the witness hole can be filled	• Graphite remains intact. • There will be a difference in thermal expansion between the reinforcement and the pipeline material due to the air gap between the reinforcement and the pipeline.

While graphite has historically been linked to several catastrophic failures in industry, the mechanisms by which graphite assists in such failures are still largely unexplained.

Several possible repair solutions have been suggested in this study, however because of the highly heterogeneous formation of graphite through a pipeline, the repair solutions would be most effective in combination with an understanding of the failure mechanisms that are associated with graphite in high temperature and pressure applications. It has been concluded in this study that plastic collapse due to tensile overload is not a likely cause of failure for such pipelines and that other mechanisms such as thermal and mechanical fatigue should be investigated.

References

1. **ASM International Handbook Committee.** Service Characteristics of Carbon and Low-Alloy Steels. [book auth.] ASM International Handbook Committee. *ASM Handbook 1 - Properties and Selection: Irons, Steels, and High Performance Alloys.* s.l. : ASM International, 1990, pp. 617-653.

2. **ASME Boiler and Pressure Vessel Committee on welding, Brazing and Fusing.** *ASME IX Welding, Brazing and Fusing Qualifications.* New York : ASME, 2013.

3. **Orsmond, Charl.** *Mr.* [interv.] Kristian Kruger. February 2015.

4. **ASME II Committee.** Specification for electric-fusion-welded steel pipe for high-pressure service at moderate temperatures. [book auth.] ASME Section II Committee. *ASME Section II, Part A.* 2007, pp. 1213-1219.

5. **Fletcher, FB.** Carbon and Low-Alloy steel Plate. [book auth.] ASM Handbook Committee. *ASM Handbook, Volume 1: Properties and Selection: Irons, Steels, and High-Performance Alloys.* s.l. : ASM International, 1990, pp. 226-239.

6. **Samuels, Leonard E.** Spheroidization and Graphitization. *Light Microscopy.* 1999, pp. 165-183.

7. **Stumpf, Waldo.** *The strengthening mechanisms of pearlite.* [interv.] Kristian Kruger. 4 September 2015.

8. **Stumpf, WE.** Phase Transformations in Metals and thier Alloys. Pretoria, Gauteng, South Africa : University of Pretoria, 01 01 2014.

9. **Callister, William.** *Material Science and Engineering.* s.l. : John Wiley & Sons, 2011.

10. **Bhadeshia, H.K.D.H.** The Structure of Cementite. *University of Cambridge.* [Online] [Cited: 28 9 2015.] http://www.msm.cam.ac.uk/phase-trans/2003/Lattices/cementite.html.

11. **Asbury Graphite Mills Inc.** Graphite. *mindat.org.* [Online] [Cited: 28 9 2015.] http://www.mindat.org/min-1740.html.

12. *Graphitization of Steels in Elevated-Temperature Service.* **Foulds, J R and Viswanathan.** 2000, Journal of Materials Engineering and Performance, p. 9.

13. *Graphitization of Weld Heat-Affected Zone in Carbon Steel.* **Okada, Minoru.** 1982, Transaction of the Japan Institute of Metals, pp. 353-359.

14. *Nucleation of Graphite in Steel.* **Brown, Floyd.** 1954, Welding Journal, pp. 257-261.

15. *An electron microscopic study of spheroidal graphite nodules formed in a medium-carbon steel by annealing.* **He, K.** 2007, Acta Materialia, pp. 2919-2927.

16. *Graphitization in high purity Iron-Carbon Alloys.* **Wells, C.** Ohio : American Society of Metals, 1938, Vol. 26.

17. *An Updated Assessment of Graphitization of Steels in Elevated Temperature Service.* **Foulds, J and Shingledecker, P.** 2015, Journal of Materials Engineering and Performance, pp. 586-597.

18. *Factors controlling graphitization of carbon steels at subcritical temperatures.* **R, Charles, Austen and Fetzer.** Ohio : American Society of Metals, 1945, Vol. 35.

19. **Bharadwaj, Maneel.** Study of Graphitization in Carbon Steel Weldments for Remaining Life Assessment. Knoxville : s.n., 14 November 2016.

20. *Heterogeneous Nucleation of Graphite in Hypo-Eutectoid Steel.* **Dennis, W.E.** 1952, Iron and Steel Instatute, pp. 59-64.

21. **Thielsch, Helmut.** *Interpreting Graphitization.* Rhode Island : Grinnell Company, 1954.

22. *Subcritical decomposition of carbide phase in some low-carbon silicon steels.* **Harry, E.D.** 1954, The Journal of the Iron and Steel Institute, pp. 109-112.

23. *Reactions to annealing above the eutectoid temperature of quenched hypereutectoid steels.* **R, Charles, Austin and Fetzer.** Ohio : American Society of Metals, 1939, Vol. 27.

24. *Grphitization of low-carbon-molybdenum Steel.* **Kerr, H and Eberle, F.** New York : Babcock & Wilcox co., 1945.

25. *Graphitization in type A201 carbon steel in petro-chemical plant after long term service.* **Moss, C.J.** 1994, Australian Nuclear Science and Technology Organisation, pp. 351-359.

26. *Numerical Simulation of Residual Stress and Strain Behavior After Temperature Modification.* **Soul, Farag.** Intech.

27. *Graphitization effects on high temperature ductwork.* **Meier, Austin, Hammerschmidt, Dain and Skibbe, Eric.** 2014, Energy-Tech, p. 5.

28. *Evaluation of an unsusual superheated steam pipe failure.* **Furtado, HC.** 2003, Materials Characterization, p. 6.

29. **Committee, AMS International Handbook.** Properties and Selection: Irons, Steels, and High-Performance Alloys. *ASM Handbook Volume 1.* s.l. : ASM International, 1990, p. 642.

30. **AWS C3 Committee on Brazing and Soldering.** *Brazing Handbook 5th edition.* s.l. : American Welding Society, 2012.

31. *Considerations in the evaluation of graphitization in piping systems.* **Thielsch H, E.R. Jerome.** 1955, The Welding Journal, p. 9.

32. **Leslie, William.** *The Physical Metallurgy of Steels.* Michigan : McGraw-Hall International Book Company, 1981.

33. **Orsmond, C.** *Detection of graphite during service.* [interv.] KJ Kruger. 03 2015.

34. **ASTM International.** Standard Test Method for Conducting Temperature Uniformity Surveys of Furnaces Used to Heat Treat Steel Products. *Standard Test Method for Conducting Temperature Uniformity Surveys of Furnaces Used to Heat Treat Steel Products.* s.l. : ASME International, 2004.

35. **AWS B4 Committee on Mechanical Testing of Welds.** *Standard Methods for Mechanical Testing of Welds (7th Edition): (AWS B4.0:2007).* s.l. : American Welding Society (AWS), 2007.

36. **Vander Voort, George.** Table of Chemicals and Etchants. *ASM Handbook, Volume 09 - Metallography and Microstructures.* s.l. : ASM International, 2004, p. 21.

37. **Scientific Multidimensional Images.** ImageJ. *ImageJ.* [Online] 3 2 2015. http://imagej.net/ImageJ.

38. *Quantitative Metallography.* **Ervin, E.**

39. **British Standards.** Non-destructive testing of welds. Ultrasonic testing. Techniques, testing levels, and assessment. s.l. : British Standards, January 2010.

40. **Becker, William and Shipley, Roch.** *ASM Handbook Volume 11 - Failure analysis and prevention.* s.l. : ASM International, 1986.

41. **Vander Voort, George.** ASM Handbook volume 9 - Metallography and Microstructures. s.l. : ASM International, 2004.

42. **Underwood, Ervin.** *Quantitative Stereology.* Marietta, Georgia : Addison - Wesley Publishing Company.

43. **French, John.** *Metallurgical Filures in Fossil Fired Boilers.* s.l. : John Wiley & Sons, 1993.

44. **Orsmond, CPM.** *Void formation in Carbon Steel.* [interv.] PGH Pistorius. 04 11 2016.

45. **Dieter, George.** *Mechanical Metallurgy.* Singapore : McGraw-Hill Book Co, 1961.

46. **ASTM International.** Standard Test Methods and Definitions for Mechanical Testing of Steel Products. s.l., United States : ASTM International.

47. **FactSage.** Fe-C Binary Phase Diagram.

48. *The Structure and Properties of 1%Cr-0.5%Mo Steel.* **Toft, L.H. and Marsden, R.A.** 1963, The Iron and Steel Institute, pp. 276-294.

49. **Hoffman, J. and Weys, J.** South African Nuclear Energy Corporation (NECSA) Unpublished research. 2016.

50. *Thermodynamics and Phase Diagram of the Fe-C System.* **Chipman, John.** 1972, Metallurgical Transactions, pp. 55-64.

51. **ASM International.** *Dictionary of Metals.* s.l. : ASM International, 2012.

52. **Viswanathan, R Nutting, J.** *Advanced Heat Resistant Steels for Power Generation.* London : IOM Communications Ltd, 1999.

53. **ASM International Handbook Committee.** *ASM Handbook, Volume 01 - Properties and Selection: Irons, Steels, and High-Performance Alloys.* s.l. : ASM International, 1990.

54. **O'Brien, A.** Composition and strength requirements of typical ASTM carbon steels. *Welding Handbook, Volume 4 - Materials and Applications, Part 1 (9th Edition).* s.l. : American Welding Society (AWS), 2011, p. 1.

55. **IHS Inc.** ASTM A106/A106M: Standard Specification for Seamless Carbon Steel Pipe for High-Temperature Service. *Industry Standards & Regulations.* [Online] 2014. [Cited: 26 09 2014.] http://engineers.ihs.com/document/abstract/XTKGCAAAAAAAAAAA.

56. **Moosbrugger, Charles.** *Atlas of Stress-Strain Curves (2nd Edition).* s.l. : ASM International, 2002.

57. **Semiatin, S.** *ASM Handbook, Volume 14A - Metalworking: Bulk Forming.* s.l. : ASM International, 2010.

Appendix A – Welding parameters as per ASME IX

Table 40: Welding Variables Procedure Specifications (WPS) – Gas Tungsten Arc Welding (GTAW)

Paragraph		Brief of Variables	Essential	Supplementary Essential	Nonessential	Actual Value
		Welding Variables Procedure Specifications (WPS) – Gas Tungsten Arc Welding (GTAW)				
QW – 402 Joints	.1	φ Groove Design			X	Double V
	.5	+ Backing			X	None
	.10	φ Root Spacing			X	3 mm
	.11	± Retainers			X	None
QW – 403 Base Metals	.5	φ Group Number		X		1
	.6	T Limits Impact		X		16mm
	.8	φ T Qualified	X			N/A
	.11	φ P-No. qualified	X			1
QW – 404 Filler Metals	.3	φ Size			X	2mm
	.4	φ F-Number	X			1
	.5	φ A-Number	X			
	.12	φ Classification		X		ER70S-6
	.14	± Filler	X			Filler added
	.22	φ Consum. insert			X	None
	.23	φ Filler metal product form	X			Bare
	.30	φ t	X			2-3mm
	.33	φ Classification			X	SFA – 5.1
	.50	± Flux			X	None
QW – 405 Positions	.1	+ Position			X	G1
	.2	φ Position		X		None
	.3	φ↑↓ Vertical Welding			X	None
	.1	Decrease > 100ºF (55°C)	X			150°C min

Category	No.	Description				Value
QW – 406 Preheat	.3	Increase > 100ºF (55°C) (IP)		X		280°C Max
QW – 407 PWHT	.1	φ PWHT	X			635°C
	.2	φ PWHT(T & T range)		X		508-635°C 9.6-600h
	.4	T limits	X			N/A
QW – 408 Gas	.1	± Trail or φ comp			X	None
	.2	φ Single, mixture or %	X			Ar
	.3	φ Flow rate			X	15-20L/min
	.5	± or φ backing flow			X	None
	.9	- backing or φ comp	X			None
	.10	φ Shielding or trailing	X			None
QW – 409 Electrical Characteristics	.1	> Heat input		X		0.8-2.5kJ/mm
	.3	± Pulsing current			X	No
	.4	φ Current or polarity		X	X	DCEN
	.8	φ I & E range			X	190A & 10-12V
	.12	φ Tungsten Electrode			X	1% Th
QW – 410 Technique	.1	φ string/weave			X	String
	.3	φ orifice, cup or nozzle size			X	15mm
	.5	φ Method cleaning			X	Brushing
	.6	φ Method back gouging			X	Grinding
	.7	φ Oscillation				None
	.9	φ Multiple or single pass/side		X	X	Single
	.10	φ Single or multi electrodes		X		N/A
	.11	φ Closed to out chamber	X			N/A
	.15	φ Electrode spacing			X	N/A
	.25	φ Manual or automatic			X	Manual
	.26	± Peening			X	None

	.64	Use of thermal processes	X			N/A
	Legend : + Addition > Increase/greater than ↑ Uphill ← Forward φ Change - Deletion < Decrease/less than ↓ Downhill → Backward					

Table 41: Welding Variables Procedure Specifications (WPS) – Shielded Metal Arc Welding (SMAW) as defined by ASME IX

Welding Variables Procedure Specifications (WPS) – Shielded Metal Arc Welding (SMAW)							
Paragraph		Brief of Variables	Essential	Supplementary Essential	Nonessential	Actual Value (double V-groove)	Actual Value (V-groove)
QW – 402 Joints	.1	φ Groove Design			X	Double V	Single V
	.4	- Backing			X	None	None
	.10	φ Root Spacing			X	None	None
	.11	± Retainers			X	None	None
QW – 403 Base Metals	.5	φ Group Number		X		1	1
	.6	T Limits Impact		X		16mm	16mm
	.8	φ T Qualified	X			N/A	N/A
	.9	t Pass > ½ in. (13mm)	X			N/A	N/A
	.11	φ P-No. qualified	X			1	1
QW – 404 Filler Metals	.4	φ F-Number	X			4	4
	.5	φ A-Number	X				
	.6	φ Diameter			X	3.15,4,5mm	3.15,4,5mm
	.7	φ Diameter > ¼ in. (6mm)		X		N/A	N/A
	.12	φ Classification		X		E7018-1	E7018-1
	.30	φ t	X			2-5mm	2-5mm
	.33	φ Classification			X	SFA 5.1	SFA 5.1
QW – 405 Positions	.1	+ Position			X	G1	G1
	.2	φ Position		X		N/A	N/A

	No.	Variable				Value	Value
	.3	φ↑↓ Vertical Welding			X	None	None
QW – 406 Preheat	.1	Decrease > 100°F (55°C)	X			N/A	N/A
	.2	φ Preheat maintained			X	150-280°C	150-280°C
	.3	Increase > 100°F (55°C) (IP)		X		N/A	N/A
QW – 407 PWHT	.1	φ PWHT	X			635°C	635°C
	.2	φ PWHT(T & T range)		X		508-635°C 480-600h	508-635°C 480-600h
	.4	T limits	X			N/A	N/A
QW – 409 Electrical Characteristics	.1	> Heat input		X		1.5-4kJ/mm	1.5-4kJ/mm
	.4	φ Current or polarity		X	X	DCEP	DCEP
	.8	φ I & E range			X	45-130A & 22-29V	45-130A & 22-29V
QW – 410 Technique	.1	φ string/weave			X	Both	Both
	.5	φ Method cleaning			X	Brushing and slag hammer	Brushing and slag hammer
	.6	φ Method back gouging			X	Grinding	Grinding
	.9	φ Multiple or single pass/side		X	X	Single	Single
	.25	φ Manual or automatic			X	Manual	Manual
	.26	± Peening			X	None	None
	.64	Use of thermal processes	X			N/A	N/A
Legend : + Addition > Increase/greater than ↑ Uphill ← Forward φ Change - Deletion < Decrease/less than ↓ Downhill → Backward							

Appendix B – Additional welding information

Welding Data

Sample 1

Welding Process	Layer No.	Run No.	Preheat/ Interpass ()	Volts (V)		Amps (A)		Run length (mm)	Weld time (s)	Tab (mm)	Heat input method 1[3] (kJ/mm)	Heat input method 2[4] (kJ/mm)
				Min	Max	Min	Max					
GTAW	1	1	160	10.9	11.9	198	200	200	544		1.76	
GTAW	1	2	150	11.5	12	198	207	207	180		0.86	
GTAW	1	3	150	10.5	11.5	226	227	227	211	55	2.63	
SMAW	2	4	160	21	23.5	135	138	138	59	70	0.90	0.86
SMAW	2	5	150	22.3	24.5	134	137	137	61	120	0.86	0.73
SMAW	2	6	150	22.2	25.6	132	137	137	53	250	1.14	0.90
SMAW	2	7	150	22.7	24.4	134	139	139	24	50	1.12	0.85
GTAW	3	8	150	21.7	23	183	185	185	65	70	1.16	1.22
SMAW	4	9	180	22.5	27.4	189	190	190	66	100	1.32	1.11
SMAW	4	10	190	21.7	25	184	191	191	61	75	3.05	2.70
SMAW	4	11	200	23.3	27.1	243	247	247	96	105	1.69	1.58
SMAW	5	12	200	23.7	27.2	242	246	246	90	70	1.86	1.70
SMAW	5	13	230	23	24.9	139	143	143	57	70	1.03	0.87
SMAW	5	14	240	23.8	25.7	139	144	144	57	70	1.06	0.87
SMAW	6	15	250	24.1	25.7	136	143	143	57	170	0.99	0.82
SMAW	6	16	240	25	29	134	142	142	40	60	1.49	1.05
SMAW	6	17	240	21.9	24	190	194	194	62	70	1.46	1.46
SMAW	6	18	250	23.1	26.4	193	200	200	65	110	1.40	1.17

[3] Electrical properties method
[4] Run out length method

SMAW	7	19	250	22.3	24.7	190	194	194	58	250	1.31	1.13
SMAW	7	20	230	24	31.1	189	194	194	23	100	1.94	1.51
SMAW	7	21	240	21.9	24.7	246	250	250	90	130	1.66	1.65
SMAW	8	22	230	22.7	30	242	250	250	85	360	1.92	1.64
SMAW	8	23	200	24	28	227	245	245	24	60	2.14	1.93
SMAW	8	24	200	21.7	25	248	251	251	99	120	1.92	1.92
SMAW	9	25	250	23.1	25.5	247	249	249	93	290	1.95	1.69
SMAW	9	26	260	29	34	221	239	239	43	80	3.12	2.36
SMAW	9	27	240	21.7	24.8	241	249	249	97	370	1.05	1.04
SMAW	Cap	28	280	21.8	23.9	242	249	249	25	95	1.25	1.05
SMAW	Cap	29	160	21.4	26.4	237	242	242	95	240	1.28	1.23
SMAW	Cap	30	170	22.4	25.6	239	243	243	51	50	1.47	1.55
SMAW	Cap	31	200	22.1	24.9	240	247	247	105	300	1.26	1.24
SMAW	Cap	32	210	22.2	26.1	238	243	243	43	60	1.43	1.26
SMAW	Cap	33	220	22	26.1	241	244	244	101	260	1.35	1.31
SMAW	Cap	34	240	22.2	25	240	245	245	58	85	1.66	1.40
SMAW	Cap	35	240	22.8	25.3	240	244	244	98	285	1.38	1.31
SMAW	Cap	36	260	22.7	26.9	241	245	245	48	140	1.36	1.15
SMAW	Cap	37	260	23.1	26.1	242	245	245	84		0.96	

Sample 2

Welding Process	Layer No.	Run No.	Preheat/ Interpass (°C)	Volts (V)		Amps (A)		Run length (mm)	Weld time (s)	Tab (mm)	Heat input method 1 (kJ/mm)	Heat input method 2 (kJ/mm)
				Min	Max	Min	Max					
GTAW	1	1	165	10.1	12	190	Max					
GTAW	1	2	165	10.4	12.1	191	190					
GTAW	1	3	165	10.5	12	191	191		138			
SMAW	2	4	180	21.4	24	135	191	140	191	65	1.02	0.95
SMAW	2	5	230	22.7	24.7	137	137	115	58	100	1.23	1.02
SMAW	2	6	190	22	24	134	134	145	55	65	1.07	0.92
SMAW	2	7	160	22	25.6	133	130	115	64	90	1.28	1.06
SMAW	3	8	200	10.4	12.4	200	134	470	58		1.51	0.87
SMAW	4	9	180	22.5	25	130	200	135	390	100	1.04	0.73
SMAW	4	10	205	22.2	25.1	131	135	160	56	100	0.91	0.84
SMAW	4	11	195	22.9	26.1	132	135	145	58	90	1.04	0.84
SMAW	4	12	195	22	25	132	134	75	58	215	1.13	1.30
SMAW	5	13	190	22.8	24.7	179	134	165	34	65	1.39	1.18
SMAW	5	14	210	22.2	26	180	181	170	67	85	1.36	1.28
SMAW	5	15	210	22	27.7	181	188	165	65	70	1.45	1.25
SMAW	6	16	200	22	27.7	208	184	260	66	80	1.72	1.22
SMAW	6	17	200	22.6	27.9	219	216	240	106	120	1.80	1.61
SMAW	7	18	220	23.5	28.7	219	223	230	97	120	1.89	1.68
SMAW	7	19	240	23.2	25.5	219	224	270	94	80	1.68	1.62
SMAW	8	20	240	23.7	26.1	217	225	440	105	60	0.91	1.69
SMAW	8	21	265	23.5	27.1	215	225	30	91	50	1.48	1.62
SMAW	9	22	200	23.5	24.3	215	224	440	10	60	1.12	1.05
SMAW	10	23	160	21.6	24.3	178	224	185	117	45	1.33	1.57
SMAW	10	24	160	21.6	24.3	178	184	185	74	50	1.28	1.05
SMAW	10	25	160	22.1	24.4	180	184	145	71	40	1.21	1.18
SMAW	11	26	200	24.7	26.4	239	183	390	52	60	1.28	3.54

Welding Process	Layer No.	Run No.	Preheat/ Interpass (°C)	Volts (V) Min	Volts (V) Max	Amps (A) Min	Amps (A) Max	Run length (mm)	Weld time (s)	Tab (mm)	Heat input method 1 (kJ/mm)	Heat input method 2 (kJ/mm)
SMAW	11	27	220	24.6	27.1	231	241	140	102	30	1.23	1.54
SMAW	12	28	240	22.7	24	240	243	280	35	85	1.55	1.28
SMAW	12	29	235	22.7	25.5	240	244	230	96	200	1.40	1.07
SMAW	13	30	180	22.2	26	238	245	390	69	95	1.12	1.26
SMAW	13	31	175	22.8	26.1	235	243	140	94	300	1.37	1.21
SMAW	14	32	180	22.8	25.7	239	242	360	41	80	1.27	1.79
SMAW	14	33	220	21.9	26.6	239	243	165	98	200	1.98	1.95

Sample 3 Groove 1

Welding Process	Layer No.	Run No.	Preheat/ Interpass (°C)	Volts (V) Min	Volts (V) Max	Amps (A) Min	Amps (A) Max	Run length (mm)	Weld time (s)	Tab (mm)	Heat input method 1 (kJ/mm)	Heat input method 2 (kJ/mm)
SMAW	1	1	175	23.7	24	179	181	180	71	60	1.35	1.22
SMAW	1	2	190	22.8	25.1	179	183	180	68	70	1.31	1.17
SMAW	1	3	160	22.1	24.1	180	184	180	69	70	1.29	1.17
SMAW	1	4	190	22.5	24.4	178	186	160	64	100	1.37	1.18
SMAW	2	5	180	23.7	26.6	234	241	270	107	55	1.89	1.73
SMAW	2	6	210	24.3	28.1	236	244	250	108	55	2.17	1.86
SMAW	2	7	260	23	25.4	238	245	240	88	120	1.71	1.62
SMAW	3	8	180	23.1	27.7	234	244	200	100	85	2.43	2.15
SMAW	3	9	200	23.3	26	238	242	170	96	110	2.67	2.36
SMAW	3	10	180	23.4	26.3	239	245	180	102	70	2.73	2.49
SMAW	3	11	250	23.7	27	237	242	220	102	80	2.25	1.98
SMAW	4	12	250	23.7	26.6	231	237	290	105	65	1.70	1.57
SMAW	4	13	250	23.7	26.9	228	238	240	89	140	1.75	1.52
SMAW	4	14	250	24.6	27	228	237	220	101	85	2.20	1.96
SMAW	4	15	260	23	27	230	233	250	87	140	1.61	1.46

SMAW	4	16	215	22.5	27.8	229	237	185	106	65	2.69	2.46
SMAW	4	17	250	24.1	26.5	232	233	195	103	80	2.49	2.24
SMAW	4	18	200	23.1	28.8	222	240	180	99	75	2.64	2.46
SMAW	5	19	250	24.8	31.1	228	236	200	93	105	2.41	2.04
SMAW	5	20	200	22.9	27.1	228	237	200	100	70	2.33	2.24
SMAW	5	21	250	24.8	28.5	225	236	205	94	100	2.25	2.01
SMAW	5	22	220	22.8	26.6	221	234	165	91	110	2.48	2.43
SMAW	6	23	250	24.1	28	221	232	170	83	140	2.30	2.15
SMAW	6	24	220	22.7	27.7	228	233	170	93	70	2.54	2.64
SMAW	cap	25	240	24.3	28.3	228	234	230	102	70	2.16	1.95
SMAW	cap	26	240	22.9	25	230	235	250	95	90	1.69	1.70
SMAW	cap	27	260	23.2	25.7	229	186	220	73	160	1.35	1.56
SMAW	cap	28	200	22.2	24.9	181	184	160	63	80	1.35	1.27
SMAW	cap	29	230	22.9	24.5	182	185	160	65	60	1.41	1.37
SMAW	cap	30	240	22.8	24.1	182	186	170	65	70	1.32	1.24
SMAW	cap	31	250	21.8	24.7	181	185	170	66	65	1.32	1.27
SMAW	cap	32	270	22.1	24.6	182	185	170	64	60	1.29	1.29
SMAW	cap	33	180	23.8	25.6	181	185	170	66	60	1.40	1.29
SMAW	cap	34	230	23.1	25.1	180	181	130	46	170	1.23	1.05
SMAW	cap	35	240	21.5	25.1	181	185	165	65	70	1.34	1.28
SMAW	cap	36	250	22.8	26.2	180	182	160	64	65	1.42	1.35
SMAW	cap	37	200	21.4	24.4	181	184	130	67	60	1.72	1.68
SMAW	cap	38	230	22.6	25.9	181	183	140	64	75	1.61	1.48
SMAW	cap	39	230	23.7	26	181	184	135	55	125	1.48	1.26
SMAW	cap	40	200	22	24.2	181	184	120	64	60	1.80	1.83
SMAW	cap	41	230	22.7	25.1	181	185	140	63	75	1.57	1.48
SMAW	cap	42	240	21.8	24.5	180	184	165	66	55	1.35	1.35

Sample 3 Groove 2

Welding Process	Layer No.	Run No.	Preheat/ Interpass (°C)	Volts (V)		Amps (A)		Run length (mm)	Weld time (s)	Tab (mm)	Heat input method 1 (kJ/mm)	Heat input method 2 (kJ/mm)
				Min	Max	Min	Max					
SMAW	1	1	165	24.1	25.9	179	182	170	67	65	1.42	1.27
SMAW	1	2	185	22.7	24.4	179	182	210	72	60	1.17	1.04
SMAW	1	3	150	22.9	25.5	179	183	190	70	70	1.29	1.11
SMAW	1	4	180	23.7	27	178	182	130	57	130	1.60	1.28
SMAW	2	5	180	26.1	28	235	242	290	112	40	1.99	1.67
SMAW	2	6	175	23.7	26.6	236	242	270	106	65	1.89	1.68
SMAW	2	7	230	23.3	27.4	237	242	185	70	210	1.84	1.53
SMAW	3	8	160	23.1	26.4	236	243	210	103	85	2.33	2.05
SMAW	3	9	190	23.3	26.7	239	242	190	93	130	2.35	1.99
SMAW	3	10	150	23.1	28	237	241	180	104	65	2.82	2.52
SMAW	3	11	230	23.1	26.1	237	242	190	82	155	2.03	1.83
SMAW	4	12	200	23.9	26.1	231	238	300	105	70	1.64	1.49
SMAW	4	13	190	22.7	26	227	237	215	104	70	2.19	2.09
SMAW	4	14	150	24	26	233	235	210	102	70	2.27	2.14
SMAW	4	15	180	23.5	26.8	231	237	190	96	110	2.38	2.11
SMAW	4	16	150	22.9	27.1	229	234	160	101	70	2.92	2.80
SMAW	4	17	200	23.8	27.2	22	238	180	84	140	1.24	2.03
SMAW	5	18	160	23.3	26.1	229	235	240	100	70	1.91	1.87
SMAW	5	19	200	23.8	28.5	215	236	175	96	100	2.59	2.36
SMAW	5	20	165	23.5	26.7	226	236	185	101	70	2.53	2.42
SMAW	5	21	230	24.7	26.3	228	237	160	73	175	2.16	2.03
SMAW	6	22	200	24.3	27.7	224	234	210	98	80	2.22	2.08
SMAW	6	23	200	22.8	26.7	230	237	240	89	110	1.71	1.67
SMAW	6	24	260	22.9	27.6	224	232	165	91	105	2.54	2.47

SMAW	cap	25	200	23.7	26.4	229	236	220	95	90	2.01	1.93
SMAW	cap	26	230	24.4	27	229	236	200	88	110	2.10	2.01
SMAW	6	27	230	25.7	29.6	228	237	170	71	170	2.15	1.94
SMAW	cap	28	220	23.8	25	181	184	175	64	75	1.30	1.19
SMAW	cap	29	190	21.8	24.5	180	181	130	62	60	1.59	1.68
SMAW	cap	30	200	22.8	25	182	185	150	67	55	1.57	1.49
SMAW	cap	31	180	22.1	23.6	181	184	130	67	70	1.72	1.63
SMAW	cap	32	230	22.8	25	182	184	130	65	80	1.75	1.57
SMAW	cap	33	220	22.9	25	181	184	150	64	80	1.49	1.36
SMAW	cap	34	230	21.8	24.2	180	184	150	64	60	1.43	1.46
SMAW	cap	35	250	23	25	180	183	155	66	70	1.48	1.36
SMAW	cap	36	250	22.9	25	181	184	165	65	85	1.38	1.21

Appendix C – The Rosenthal Equation

Sample 1 distances calculated from the Rosenthal Equation

Average Current (A)	Average Voltage (V)	Heat Input (kJ/mm)	Welding time (s)	Run length (mm)	Distance of fusion line from heat source (mm)	Distance of last material to be heated to the Ac_1 temperature from the heat source (mm)	Distance of the last material to be heated to the Ac_1 temperature from the fusion line (mm)
199.0	11.4	1.76	544	420	5.0	7.9	2.8
202.5	11.8	0.86	180	300	4.9	7.7	2.7
226.5	11.0	2.63	211	120	5.8	9.0	3.2
136.5	22.3	0.90	59	160	6.3	9.9	3.6
135.5	23.4	0.86	61	180	5.8	9.0	3.2
134.5	23.9	1.14	53	120	5.8	9.0	3.2
136.5	23.6	1.12	24	55	9.2	14.3	5.1
184.0	22.4	1.16	65	185	6.5	10.1	3.6
189.5	25.0	1.32	66	190	7.4	11.7	4.3
187.5	23.4	3.05	61	70	7.2	11.4	4.3
245.0	25.2	1.69	96	280	8.6	13.7	5.1
244.0	25.5	1.86	90	240	8.3	13.3	5.0
141.0	24.0	1.03	57	150	7.3	12.0	4.6
141.5	24.8	1.06	57	150	6.8	11.2	4.4
139.5	24.9	0.99	57	160	6.4	10.5	4.2
138.0	27.0	1.49	40	80	6.6	10.8	4.2
192.0	23.0	1.46	62	150	8.1	13.3	5.2
196.5	24.8	1.40	65	180	7.5	12.4	4.9
192.0	23.5	1.31	58	160	7.3	12.1	4.8
191.5	27.6	1.94	23	50	8.6	14.0	5.4
248.0	23.3	1.66	90	250	8.8	14.4	5.6
246.0	26.4	1.92	85	230	9.1	14.9	5.8
236.0	26.0	2.14	24	55	10.1	16.2	6.1
249.5	23.4	1.92	99	240	6.5	10.4	3.9
248.0	24.3	1.95	93	230	7.4	12.2	4.8
230.0	31.5	3.12	43	80	8.1	13.5	5.4
245.0	23.3	1.05	97	420	7.6	12.5	4.9
245.5	22.9	1.25	25	90	7.2	12.1	4.9
239.5	23.9	1.28	95	340	7.3	11.4	4.1
241.0	24.0	1.47	51	160	7.1	11.2	4.1
243.5	23.5	1.26	105	380	8.0	12.9	4.8
240.5	24.2	1.43	43	140	7.4	11.9	4.5
242.5	24.1	1.35	101	350	7.2	11.7	4.5
242.5	23.6	1.66	58	160	6.1	10.0	3.9
242.0	24.1	1.38	98	330	14.7	24.1	9.4
243.0	24.8	1.36	48	170	5.8	9.6	3.8
243.5	24.6	0.96	84	420	10.8	18.0	7.2

Sample 2 distances calculated from the Rosenthal Equation

Average Current (A)	Average Voltage (V)	Heat Input (kJ/mm)	Welding time (s)	Run length (mm)	Distance of fusion line from heat source (mm)	Distance of last material to be heated to the Ac_1 temperature from the heat source (mm)	Distance of the last material to be heated to the Ac_1 temperature from the fusion line (mm)
200.0	11.4	1.51	390	470	6.3	9.9	3.7
136.0	22.7	1.02	58	140	7.0	11.4	4.4
135.5	23.7	1.23	55	115	6.4	10.3	3.8
132.0	23.0	1.07	64	145	7.0	10.9	3.9
133.5	23.8	1.28	58	115	7.7	12.3	4.6
132.5	23.8	1.04	56	135	6.3	10.0	3.7
133.0	23.7	0.91	58	160	6.0	9.6	3.6
133.0	24.5	1.04	58	145	6.4	10.2	3.8
133.0	23.5	1.13	34	75	6.6	10.6	4.0
180.0	23.8	1.39	67	165	7.3	11.7	4.3
184.0	24.1	1.36	65	170	7.3	11.8	4.5
182.5	24.9	1.45	66	165	7.5	12.2	4.6
181.0	23.0	1.33	74	185	8.2	13.1	4.9
181.0	23.0	1.28	71	185	8.4	13.4	5.0
181.5	23.3	1.21	52	145	8.6	14.0	5.4
212.0	24.9	1.72	106	260	8.2	13.5	5.3
221.0	25.3	1.80	97	240	6.0	9.9	3.9
221.5	26.1	1.89	94	230	7.8	13.0	5.2
222.0	24.4	1.68	105	270	6.5	10.5	3.9
221.0	24.9	0.91	91	440	7.1	11.1	4.0
219.5	25.3	1.48	10	30	6.9	10.9	3.9
219.5	23.9	1.12	117	440	6.8	10.6	3.8
240.0	25.6	1.28	102	390	7.1	11.3	4.3
237.0	25.9	1.23	35	140	7.0	11.3	4.3
242.0	23.4	1.55	96	280	7.9	13.0	5.1
242.5	24.1	1.40	69	230	7.5	12.3	4.8
240.5	24.1	1.12	94	390	6.5	10.4	3.8
238.5	24.5	1.37	41	140	7.2	11.4	4.2
241.0	24.3	1.27	98	360	7.0	11.1	4.1
241.0	24.3	1.98	70	165	8.9	14.4	5.5

Sample 3 Groove 1 distances calculated from the Rosenthal Equation

Average Current (A)	Average Voltage (V)	Heat Input (kJ/mm)	Welding time (s)	Run length (mm)	Distance of fusion line from heat source (mm)	Distance of last material to be heated to the Ac$_1$ temperature from the heat source (mm)	Distance of the last material to be heated to the Ac$_1$ temperature from the fusion line (mm)
180.0	23.9	1.02	71	180	7.2	11.4	4.2
181.0	24.0	0.98	68	180	7.1	11.3	4.2
182.0	23.1	0.97	69	180	7.0	10.9	4.0
182.0	23.5	1.02	64	160	7.3	11.6	4.3
237.5	25.2	1.89	107	270	8.5	13.5	5.0
240.0	26.2	2.17	108	250	9.2	14.9	5.6
241.5	24.2	1.71	88	240	8.4	13.9	5.6
239.0	25.4	2.43	100	200	9.7	15.3	5.6
240.0	24.7	2.67	96	170	10.2	16.3	6.1
242.0	24.9	2.73	102	180	10.2	16.2	6.0
239.5	25.4	2.25	102	220	9.5	15.8	6.2
234.0	25.2	1.70	105	290	8.3	13.7	5.4
233.0	25.3	1.75	89	240	8.4	13.9	5.5
232.5	25.8	2.20	101	220	9.4	15.6	6.2
231.5	25.0	1.61	87	250	8.1	13.5	5.4
233.0	25.2	2.69	106	185	10.3	16.6	6.3
232.5	25.3	2.49	103	195	10.0	16.6	6.5
231.0	26.0	2.64	99	180	10.1	16.2	6.1
232.0	28.0	2.41	93	200	9.9	16.3	6.5
232.5	25.0	2.33	100	200	9.5	15.2	5.7
230.5	26.7	2.25	94	205	9.6	15.8	6.2
227.5	24.7	2.48	91	165	9.9	16.1	6.2
226.5	26.1	2.30	83	170	9.7	16.0	6.3
230.5	25.2	2.54	93	170	10.0	16.3	6.2
231.0	26.3	2.16	102	230	9.3	15.3	6.0
232.5	24.0	1.69	95	250	8.2	13.5	5.3
207.5	24.5	1.35	73	220	7.4	12.3	4.9
182.5	23.6	1.35	63	160	7.3	11.6	4.4
183.5	23.7	1.41	65	160	7.5	12.2	4.7
184.0	23.5	1.32	65	170	7.3	12.0	4.7
183.0	23.3	1.32	66	170	7.3	12.1	4.8
183.5	23.4	1.29	64	170	7.3	12.2	4.9
183.0	24.7	1.40	66	170	7.3	11.6	4.3
180.5	24.1	1.23	46	130	7.0	11.4	4.4
183.0	23.3	1.34	65	165	7.3	12.1	4.7
181.0	24.5	1.42	64	160	7.6	12.5	4.9
182.5	22.9	1.72	67	130	8.2	13.1	4.9
182.0	24.3	1.61	64	140	8.0	13.1	5.1
182.5	24.9	1.48	55	135	7.7	12.5	4.8

182.5	23.1	1.80	64	120	8.4	13.4	5.0
183.0	23.9	1.57	63	140	7.9	12.9	5.0
182.0	23.2	1.35	66	165	7.4	12.1	4.7

Sample 3 Groove 2 distances calculated from the Rosenthal Equation

Average Current (A)	Average Voltage (V)	Heat Input (kJ/mm)	Welding time (s)	Run length (mm)	Distance of fusion line from heat source (mm)	Distance of last material to be heated to the Ac$_1$ temperature from the heat source (mm)	Distance of the last material to be heated to the Ac$_1$ temperature from the fusion line (mm)
180.5	25.0	1.07	67	170	6.4	10.0	3.6
180.5	23.6	0.87	72	210	5.8	9.2	3.4
181.0	24.2	0.97	70	190	6.0	9.4	3.4
180.0	25.4	1.20	57	130	6.8	10.7	4.0
238.5	27.1	1.99	112	290	8.7	13.9	5.1
239.0	25.2	1.89	106	270	8.5	13.4	4.9
239.5	25.4	1.84	70	185	8.6	14.0	5.4
239.5	24.8	2.33	103	210	9.4	14.7	5.3
240.5	25.0	2.35	93	190	9.5	15.2	5.7
239.0	25.6	2.82	104	180	10.3	16.0	5.7
239.5	24.6	2.03	82	190	9.0	14.7	5.7
234.5	25.0	1.64	105	300	8.0	12.8	4.8
232.0	24.4	2.19	104	215	9.2	14.6	5.4
234.0	25.0	2.27	102	210	9.2	14.4	5.2
234.0	25.2	2.38	96	190	9.6	15.1	5.6
231.5	25.0	2.92	101	160	10.4	16.2	5.7
130.0	25.5	1.24	84	180	6.9	11.1	4.2
232.0	24.7	1.91	100	240	8.5	13.3	4.8
225.5	26.2	2.59	96	175	10.0	16.1	6.0
231.0	25.1	2.53	101	185	9.8	15.4	5.6
232.5	25.5	2.16	73	160	9.3	15.2	5.9
229.0	26.0	2.22	98	210	9.3	14.9	5.6
233.5	24.8	1.71	89	240	8.2	13.1	4.9
228.0	25.3	2.54	91	165	10.2	16.9	6.8
232.5	25.1	2.01	95	220	8.9	14.2	5.3
232.5	25.7	2.10	88	200	9.2	14.9	5.8
232.5	27.7	2.15	71	170	9.3	15.1	5.8
182.5	24.4	1.30	64	175	7.2	11.6	4.5
180.5	23.2	1.59	62	130	7.9	12.5	4.7
183.5	23.9	1.57	67	150	7.8	12.5	4.7
182.5	22.9	1.72	67	130	8.1	12.9	4.7
183.0	23.9	1.75	65	130	8.4	13.6	5.3
182.5	24.0	1.49	64	150	7.7	12.5	4.8
182.0	23.0	1.43	64	150	7.5	12.3	4.8
181.5	24.0	1.48	66	155	7.8	12.8	5.1
182.5	24.0	1.38	65	165	7.5	12.3	4.9

Appendix D – PQRs developed for welding graphitized C-Mn Steel
Procedure Qualification Record (PQR)

Company Name: <u>Department of Materials and Metallurgical Engineering, University of Pretoria</u>
Procedure Qualification Record No.: <u>Graphite replacement - Sasol PQR CAT 78</u> Date: <u>19/08/2015</u>
WPS No.: <u>Sasol Synfuels (For reference see WPS Sasol WPS CAT 24 (SP-1-1-D-21-1))</u>
Welding Process(es): <u>GTAW, SMAW</u>
Types (Manual, Automatic, Semi-Auto): <u>Manual</u>
JOINTS (QW 402):

BASE METALS (QW-403)
Material Spec: <u>SA-106</u>
Type or Grade: <u>B</u>
P-No.: <u>1</u> to P-No.: <u>1</u>
Thickness of Test Coupon: <u>35mm</u>
Diameter of Test Coupon: <u>N/A</u>
Other:_____

FILLER METALS (QW-404)
SFA Specification: <u>5.1</u>
AWS Classification: <u>ER 70S-6, E7018-1</u>
Filler Metal F-No.: <u>4</u>

Weld Metal Analysis A-No.: <u>1</u>
Size of Filler Metal: <u>2mm, 3.15mm, 4mm, 5mm</u>
Other:_____
Weld Metal Thickness: <u>GTAW- 5mm, SMAW- 20mm, SMAW- 10mm</u>

POSITION (QW-405)
Position of Groove: <u>G1</u>
Welding Progression(Uphill, Downhill): <u>N/A</u>
Other:_____

PREHEAT (QW-406)
Preheat Temp.: <u>150°C (min)</u>

POSTWELD HEAT TREATMENT (QW-407)
Temperature: <u>635°C</u>
Time: <u>12 hours, 600 hours</u>
Other:_____

GAS (QW-408)
Percentage Composition

Gas(es)	(Mixture)	Flow Rate
Shielding: <u>Ar</u> <u>-</u> <u>N/R[5]</u>
Trailing: _____ _____ _____
Backing: _____ _____ _____

ELECTRICAL CHARACTERISTICS (QW-409)
Current: <u>DC</u>
Polarity: <u>DCEN (GTAW), DCEP (SMAW)</u>
Amps: <u>190-191 (GTAW), 130-45 (SMAW)</u>
Volts: <u>10-12 (GTAW), 22-29 (SMAW)</u>
Tungsten Electrode Size: <u>N/R</u>
Other:_____

TECHNIQUE (QW-410)
Travel Speed: <u>130-290 mm/min (SMAW)</u>
String of Weave Bead: <u>String & Weave</u>
Oscillation: <u>None</u>
Multipass of Single Pass (Per side): <u>Multi</u>
Single or Multi-pass Electrodes: <u>Single</u>

---

[5] Not Recorded

Interpass Temp: 280°C (max)_____   Other:_____

Other: Oxy-acetylene Flame heated_____

WELDING PROCEDURE

Pass or weld layers	Process	Filler metal diameter (mm)	Type and polarity	Current (A)	Voltage (V)	Travel speed (mm/min)	Heat Input (kJ/mm)
1-2	GTAW	2.00	DC-	190-191	10-12	N/R	N/R
3-6	SMAW	3.15	DC+	132-144	21-26	137-177	0.8-1.2
7-10	SMAW	4.00	DC+	183-194	21-31	68-173	1.1-3
11-19	SMAW	5.00	DC+	221-251	21-28	110-213	1.2-2.2

TENSILE TEST (QW-150)

Specimen No.	Width (mm)	Thickness (mm)	Area (mm^2)	Ultimate Tensile Load (kN)	Ultimate Tensile Strength (MPa)	Type of Failure & Location
1 (12h PWHT)	19.33	33.42	646.01	268.8	416	PM-Ductile
2 (12h PWHT)	19.30	32.85	634.01	264.8	418	PM-Ductile
3 (600h PWHT)	19.31	32.65	630.47	258.7	410	PM-Ductile
4(600h PWHT)	19.06	30.35	578.47	240.8	416	PM-Ductile

Guided – Bend Tests (QW-160)

Sample No. (PWHT) Type and Figure No.	Results
1-4 (12h PWHT) Side Bend QW-462.2	No indications
5 (600h PWHT) Side Bend QW-462.2	Acceptable indication (1mm)
6-8 (600h PWHT) Side Bend QW-462.2	No indications

TOUGHNESS TESTS (QW-170)

Specimen No. (PWHT)	Notch Location	Specimen Size (mm)	Test Temp.	Impact Values		
				J	% Shear	LE (mm)
1 (12h PWHT)	Weld	10 x 10	25°C (room temp.)	293	100	2.14
2 (12h PWHT)	Weld	10 x 10	25°C (room temp.)	268	100	2.11
3(12h PWHT)	Weld	10 x 10	25°C (room temp.)	268	100	2.17
4 (12h PWHT)	HAZ	10 x 10	25°C (room temp.)	96	70	1.17
5 (12h PWHT)	HAZ	10 x 10	25°C (room temp.)	82	60	1.18
6 (12h PWHT)	HAZ	10 x 10	25°C (room temp.)	136	70	1.57
7 (600h PWHT)	Weld	10 x 10	25°C (room temp.)	182	90	2.11
8 (600h PWHT)	Weld	10 x 10	25°C (room temp.)	252	100	2.30
9 (600h PWHT)	Weld	10 x 10	25°C (room temp.)	208	100	1.87
10 (600h PWHT)	HAZ	10 x 10	25°C (room temp.)	104	80	1.72
11 (600h PWHT)	HAZ	10 x 10	25°C (room temp.)	90	70	1.73
12 (600h PWHT)	HAZ	10 x 10	25°C (room temp.)	104	70	1.69

OTHER TESTS

Chemical Analysis

Metallographic Evaluation

Hardness Tests

Welder's Name: Dennis (SAIW)
Tests conducted by: MetLab Boksberg

Procedure Qualification Record (PQR)

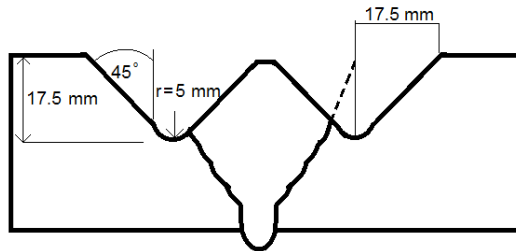Company Name: Department of Materials and Metallurgical Engineering, University of Pretoria _____

Procedure Qualification Record No.: Graphite repair - Sasol PQR CAT 78 Date: 19/08/2015_____

WPS No.: Sasol Synfuels (For reference see WPS Sasol WPS CAT 24 (SP-1-1-D-21-1))_____

Welding Process(es): SMAW_____

Types (Manual, Automatic, Semi-Auto): Manual_____

_____

JOINTS (QW 402):

_____

BASE METALS (QW-403)

Material Spec: SA-106_____

Type or Grade: B_____

P-No.: 1_____to P-No.: 1_____

Thickness of Test Coupon: 35mm_____

Diameter of Test Coupon: N/A_____

Other:_____

POSTWELD HEAT TREATMENT (QW-407)

Temperature: 635°C_____

Time: 500 hours_____

Other:_____

GAS (QW-408)

Percentage Composition

	Gas(es)	(Mixture)	Flow Rate
Shielding:	_____	_____	_____
Trailing:	_____	_____	_____
Backing:	_____	_____	_____

FILLER METALS (QW-404)

SFA Specification: 5.1_____

AWS Classification: E7018-1_____

Filler Metal F-No.: 4_____

Weld Metal Analysis A-No.: 1_____

Size of Filler Metal: 4mm, 5mm_____

Other:_____

Weld Metal Thickness: SMAW- 18mm

ELECTRICAL CHARACTERISTICS (QW-409)

Current: DC_____

Polarity: DCEP (SMAW)_____

Amps: 178-245 (SMAW)_____

Volts: 21-31 (SMAW)_____

Tungsten Electrode Size: N/A_____

Other:_____

POSITION (QW-405)

Position of Groove: G1_____

Welding Progression(Uphill, Downhill): N/A_____

Other:_____

PREHEAT (QW-406)

Preheat Temp.: 150°C (min)_____

TECHNIQUE (QW-410)

Travel Speed: 104-181 mm/min_____

String of Weave Bead: String & Weave_____

Oscillation: None_____

Multipass of Single Pass (Per side): Multi___

Single or Multi-pass Electrodes: Single____

Interpass Temp: <u>280°C (max)</u>_____   Other:_____

Other: <u>Oxy-acetylene Flame heated_____</u>

TENSILE TEST (QW-150)

Specimen No.	Width (mm)	Thickness (mm)	Area (mm^2)	Ultimate Tensile Load (kN)	Ultimate Tensile Strength (MPa)	Type of Failure & Location
1	19.29	33.07	637.92	266.5	418	PM-Ductile
2	19.14	33.16	634.68	265.9	419	PM-Ductile

Guided – Bend Tests (QW-160)

Type and Figure No.	Results
Side Bend QW-462.2	No indications
Side Bend QW-462.2	No indications
Side Bend QW-462.2	No indications
Side Bend QW-462.2	No indications

TOUGHNESS TESTS (QW-170)

Specimen No.	Notch Location	Specimen Size (mm)	Test Temp.	Impact Values		
				J	% Shear	LE (mm)
1	Weld	10 x 10	25°C (room temp.)	264	100	2.30
2	Weld	10 x 10	25°C (room temp.)	272	100	2.51
3	Weld	10 x 10	25°C (room temp.)	260	100	2.08
4	HAZ	10 x 10	25°C (room temp.)	220	100	2.11
5	HAZ	10 x 10	25°C (room temp.)	182	100	2.16
6	HAZ	10 x 10	25°C (room temp.)	176	100	2.04

OTHER TESTS

Chemical Analysis

Metallographic Evaluation

Hardness Tests

Welder's Name: <u>Dennis (SAIW)</u>
Tests conducted by: <u>MetLab Boksberg</u>